UNIVERSITÀ DEGLI STUDI DI TRIESTE

UNIVERSITÀ DEGLI STUDI DI UDINE

XXXVI CICLO DEL DOTTORATO DI RICERCA INTERATENEO IN INGEGNERIA CIVILE-AMBIENTALE E ARCHITETTURA CURRICULUM: STRUTTURE

ADVANCED MODELLING OF MASONRY WALL STRUCTURES UNDER EARTHQUAKE LOADING

Settore scientifico-disciplinare: **ICAR/09 - Tecnica delle Costruzioni**

DOTTORANDO	**LUCA BOMBEN**	
COORDINATORE	**Prof. ALBERTO SDEGNO**	
SUPERVISORE	**Prof. CHIARA BEDON** **Università degli Studi di Trieste**	
CO-SUPERVISORE	**Prof. LORENZO MACORINI** **Imperial College London**	
CO-SUPERVISORE	**Dr. CORRADO CHISARI** **Università degli Studi della Campania "Luigi Vanvitelli"**	

ANNO ACCADEMICO 2022/2023

UNIVERSITÀ DEGLI STUDI DI TRIESTE

UNIVERSITÀ DEGLI STUDI DI UDINE

XXXVI PhD PROGRAM IN
CIVIL-ENVIRONMENTAL ENGINEERING AND ARCHITECTURE
CURRICULUM: STRUCTURAL ENGINEERING

ADVANCED MODELLING OF MASONRY WALL STRUCTURES UNDER EARTHQUAKE LOADING

Scientific-disciplinary sector: **ICAR/09 – Structural Engineering**

CANDIDATE	**LUCA BOMBEN**
COORDINATOR	**Prof. ALBERTO SDEGNO**
SUPERVISOR	**Prof. CHIARA BEDON** **Università degli Studi di Trieste**
CO-SUPERVISOR	**Prof. LORENZO MACORINI** **Imperial College London**
CO-SUPERVISOR	**Dr. CORRADO CHISARI** **Università degli Studi della Campania "Luigi Vanvitelli"**

ACADEMIC YEAR 2022/2023

ABSTRACT

Masonry structures are widespread globally, especially in regions with high seismic hazard. Notably, unreinforced masonry (URM) buildings were mainly constructed before the knowledge acquired in the last decades in the field of seismic engineering, therefore potentially exhibiting significant vulnerability to seismic events. Furthermore, in modern structures, masonry panels are frequently utilised as infills for framed buildings. While widely recognised to significantly influence the seismic performance, the contribution of masonry infills is often neglected, and this oversight may not always be in favour of safety. For these reasons, ensuring a reliable prediction of these structures is essential in order to protect human lives, minimise economic losses and preserve historical building heritage.

Masonry is a heterogeneous material characterised by a complex structural response, strongly nonlinear and dependent on the properties of its constituents and their arrangement. Furthermore, when analysing masonry-infilled frames, the complexity even increases, as it involves the representation of the ever-changing interaction between the frame and the infill. Therefore, the modelling of these structures represents a particularly challenging task.

This PhD thesis focuses on addressing the critical issue of modelling the complex behaviour of masonry wall structures under earthquake loading, assessing the application of refined strategies for the analysis of URM and masonry-infilled frame structures while proposing a reliable yet efficient tool, which can be applied for accurate evaluations of the structural response of real-sized structures.

The research work begins with a comprehensive literature review, outlining the response characteristics of URM and infilled-frame structures, along with a review of the more common modelling strategies.

Subsequently, a numerical comparison between two nonlinear finite element descriptions is conducted, employing an advanced mesoscale and a continuum macroscale strategy, investigating the nonlinear response under seismic loading of masonry wall structures up to collapse. The simulation results are compared against experimental findings to assess the ability to represent the cyclic hysteretic response. Great emphasis is placed on the objectivity of the definition and calibration of the model material parameters, with the aim of critically assessing how the response predictions are affected by the inherent uncertainty of their selection.

The research then progresses to modelling of masonry-infilled frames under horizontal actions, employing a sophisticated multidimensional approach, where masonry infills are represented using either mesoscale or continuum macroscale methods. The implemented models are assessed against experimental data, demonstrating their capability in capturing the complex frame-infill interaction and successfully replicating both global responses and local mechanisms. The objective calibration of material parameters is examined, accompanied by parametric analyses aimed at identifying the most

influential characteristics. Furthermore, the influence of openings is evaluated, offering valuable insights into how their presence affects the response, particularly in terms of strength and stiffness variations.

Since the strategies previously employed may not be suitable for analysing real-sized structures due to their computational cost, an enhanced three-dimensional macroelement is proposed to provide a tool that combines reliability and computational efficiency. The modelling strategy is developed upon the groundwork laid by the original work of (Minga et al., 2020), which has already been proven to ensure satisfactory results while maintaining high computational efficiency. The introduced advances address a number of drawbacks of the original implementation, resulting in a substantial improvement in the accuracy of response predictions. A comprehensive validation of the enhanced macroelement is conducted, focusing on applications to both URM and masonry-infilled frame structures under monotonic, cyclic and earthquake loadings. The validation extends to the evaluation of the out-of-plane response, crucial for a comprehensive assessment of the seismic performance of existing masonry buildings. Additionally, the model's ability to account for the presence of openings in masonry-infilled frames is assessed by comparing its outcomes against those obtained from continuum macro-scale models.

The enhanced macroelement strategy is finally applied to assess the seismic vulnerability of a real 4-story irregular reinforced-concrete structure, originally designed without seismic provisions. The structure is analysed within the nonlinear dynamic analysis framework, under the application of natural spectrum-compatible accelerograms and considering various configurations of infills. The significant influence of infills on the overall response of structures is emphasised, with effects that can widely vary, potentially improving seismic performance but also introducing further vulnerabilities. It is highlighted that, for an accurate description of the response in existing RC structures, infill panels must be carefully considered within the seismic assessment through the adoption of a reliable modelling strategy.

Keywords: Unreinforced Masonry – Masonry-Infilled frames - Mesoscale Modelling – Macroscale Modelling – Macroelement – Cyclic response – Seismic Vulnerability

ACKNOWLEDGEMENTS

The research reported in this thesis has been conducted within the Computational Structural Mechanics group of Imperial College London since September 2022, when I began my research period as visiting PhD student.

The work was performed under the supervision of Prof. Lorenzo Macorini and Dr. Corrado Chisari, for whose invaluable guidance throughout the research I am deeply thankful. In particular, their continuous suggestions, motivation and thorough review of the final manuscript significantly contributed to the successful completion of this thesis.

I want to express my deepest gratitude to Prof. Claudio Amadio. I thank him for everything he taught me, not only as a researcher and engineer, and for always being someone I could count on. I hope he will be satisfied with this work.

Special thanks are extended to Prof. Bassam Izzuddin for his priceless advice and insights throughout the development of the work.

Furthermore, I would like to express my gratitude to Prof. Chiara Bedon for the great encouragement and support.

I want to thank the reviewers, Prof. Bartolomeo Pantò and Prof. Mislav Stepinac, for their comprehensive review and for providing essential feedback, which significantly contributed to enhancing the quality of this thesis.

I would like to express my gratitude to the Department of Civil and Environmental Engineering of Imperial College for providing the computational resources used for all calculations. In particular, I acknowledge the HPC service for carrying out a significant portion of the numerical analyses.

Moreover, I want to thank all my colleagues in Trieste and in London for the unforgettable memories we have shared, their genuine friendship, and the engaging and fruitful conversations we have had.

Most importantly, I am deeply grateful to my family and my partner, for being my reference point and constant support.

Luca

Trieste, April 8, 2024

TABLE OF CONTENTS

LIST OF FIGURES

LIST OF TABLES

CHAPTER 1

INTRODUCTION

1.1 Research background

Unreinforced masonry (URM) is a heterogeneous material formed by arranging block units together through mortar joints. This simple building technique has been widely employed worldwide for centuries, making masonry structures particularly widespread and characterising the majority of historical building heritage, in Italy and abroad. Masonry is also frequently employed in modern structures as secondary component, as infill panel within reinforced concrete or steel frame structures.

Masonry material presents a composite mechanical behaviour, wherein units and mortar exhibit markedly distinct characteristics. Despite its relatively simple constructional technique, masonry exhibits a highly complex and markedly nonlinear response, even at low load levels. Cracks can propagate either in the mortar joints, which represents the conjunction of mortar layers and brick-mortar interfaces, or within the units. Furthermore, the response of masonry can significantly vary based on factors such as the mechanical characteristics of its constituents, the geometry of the units and their arrangements, environmental conditions, and workmanship.

As a result, numerical modelling of masonry represents a challenging task. Masonry modelling techniques can be typically categorised into three strategies: micro-modelling, where each constituent is explicitly represented; meso-scale modelling, which lumps mortar layers and brick-mortar interface into a single interface element; and macro-scale modelling, which depicts masonry as a single homogeneous material. Within the macro-scale level strategy, a further distinction can be made between continuum finite element strategies, where the geometry is discretised by 2D or 3D elements using a specific masonry material law, and macroelement strategies, involving the assembly of basic mechanical components like beams or nonlinear springs. The more sophisticated approaches, namely

micro and mesoscale, despite their ability to accurately predict the actual response of masonry, are generally applicable only to small masonry components due to their prohibitive computational cost. On the contrary, macro-scale approaches, although generally more computationally efficient, may lack reliability. Moreover, the calibration of the macroscopic material properties from individual constituents is generally not straightforward, and the prediction of the final response can be significantly influenced by the analyst choices.

The modelling complexity even increases when considering masonry as infill panels. As mentioned, in modern buildings masonry wall are frequently employed as infill elements within frame structures. Despite their significant influence on the overall response is widely recognised, they are often neglected in evaluating the primary structural system. Inspections of damage patterns after past earthquakes have clearly revealed that the influence of URM panels on the responses was significant, in some cases beneficial, enhancing the frame strength, while in others detrimental, triggering unexpected brittle failure. The influence of masonry infills depends on various factors, including the relative mechanical properties of the frame and infill, as well as the geometrical layout and distribution of the infill. To realistically evaluate the global performance of infilled frames under earthquake loading, it is therefore crucial to properly consider their presence. An accurate modelling of masonry-infilled frames necessitates the representation of not only the behaviour of the masonry infill and the surrounding frame but also the complex and ever-changing interaction at the interfaces between the two components.

Considering the number of challenges posed, the numerical modelling of masonry represents an open research topic. Given the ultimate goal of protecting human lives, minimising economic losses and preserving cultural heritage, the development of sufficiently accurate yet efficient modelling techniques, together with the establishment of reliable material calibration methodologies, is essential for accurate predictions of the response of real structures.

1.2 Aims and scope

This PhD thesis tackles the challenging task of modelling the complex behaviour of brick masonry wall structures under earthquake loading. The dual aim of this thesis is evaluating advanced finite-element methodologies for analysing URM and infilled-frames structures, while also proposing a reliable and efficient tool for the assessment of real-scale structures.

The initial phase of the research focuses on modelling masonry wall structures using two distinct strategies characterised by different levels of refinement. The first strategy involves a detailed

mesoscale approach proposed in (Macorini and Izzuddin, 2011) and subsequently refined in (Minga et al., 2018). At a lower level of refinement, a continuum finite element approach is considered, employing the continuum damage plasticity material law, as presented in (Chisari et al., 2020), a slight modification of the original model proposed in (Lee and Fenves, 1998). Considerable importance is given to the objective calibration of material characteristics, with the assumption of unawareness of the final response of the structure. Objectively calibrating the material parameters is crucial for a genuine assessment of the model applicability. Indeed, while a model may accurately predict the response of experimental outcomes, it is important to verify if the material characterisation employed aligns with appropriate values for the considered case. Therefore, the question to be addressed in this phase is how reliable these techniques are for accurately a-priori predicting the actual response of masonry wall structures. Additionally, considering the large dispersions of material properties inherent in masonry structures, the study explores how sensitive their responses are to variations within suitable parameter ranges. Furthermore, the investigations aim to identify the mechanical characteristics that predominantly influence the response within these refined methodologies.

First, experimental tests on URM structures are simulated utilising the two modelling approaches. The assessment includes the evaluation of both monotonic and cyclic responses, the capability of predicting the actual failure mode, and the evaluation of hysteretic dissipative capacity. The focus then moves to the modelling of infilled-frame, employing a sophisticated multidimensional framework (Jokhio, 2012), wherein masonry infill is represented through either mesoscale or continuum macroscale modelling. The aim is to assess the employed strategies against experimental outcomes, evaluating their capability to predict both the global response and the local mechanisms typical of infilled frame structures while maintaining a focus on the objectivity of material calibration. The assessment also involves evaluating the mechanical characteristics that most significantly affect the numerical predictions. Furthermore, the impact of openings within infills is examined, as they may represent a crucial source of structural irregularities, largely affecting the response of infilled frames. The analyses outcomes provide valuable insights into the decay in strength and stiffness associated with their presence, serving as a reference for subsequent evaluations and analyses with the macroelement proposed in the following chapters.

Despite their potential accuracy, the computational demand of mesoscale models generally restricts their application to small-scale structures. Furthermore, even in finite element macroscale modelling, simulating large-scale URM and infilled-frame structures under realistic dynamic loading conditions, often requiring an extensive number of numerical analyses, can be prohibitive. Consequently, the second part of the thesis focuses on providing a more efficient yet reliable macroelement strategy for modelling of masonry structures.

The macroelement model developed in (Minga et al., 2020) represents the existing foundation for the current study. In this approach, each single element represents a rectangular portion of a masonry structure. These elements consist of deformable blocks, featuring cohesive frictional interfaces at the borders (allowing the interaction with adjacent elements) and internal in-plane and out-of-plane nonlinear springs. This formulation enables the model to represent all the basic in-plane and out-of-plane failure modes of rectangular URM walls. However, certain drawbacks can be identified in the original implementation. Specifically, the cyclic constitutive law governing in-plane and out-of-plane springs is overly simplified, lacking consideration for stiffness and strength degradation. Additionally, the post-peak branch definition does not ensure mesh objectivity. Moreover, another drawback regards the impossibility to mechanically differentiate the material characteristics of all the boundary interfaces, particularly important within the modelling of infilled-frames. These drawbacks are addressed in the present work. Furthermore, the enhanced macroelement is in-depth evaluated by simulating several experimental tests, including monotonic, cyclic and dynamic responses. Finally, the potential of the macroelement is assessed within a practical scenario, involving the analysis of a real-size infilled-frame building within the nonlinear dynamic analysis framework.

1.3 Thesis outline

Following the opening introduction, the research work is outlined with a general overview provided below, including a summary of the content in each chapter.

Throughout the work, all finite element implementations and numerical analyses are executed within ADAPTIC (Izzuddin, 1991), a general finite element program for nonlinear structural analysis. The preliminary numerical modelling is conducted through the implementation of Gmsh (Geuzaine and Remacle, 2009) and Matlab R2022b (MathWorks, 2022) scripts. Additionally, Matlab scripts are employed for the post-processing phase within the macroelement modelling, specifically for the visualisation of damage and deformed shapes.

Chapter 2: Literature review

This chapter deals with literature review relevant to the research topics, focusing on the general behaviour and numerical modelling of unreinforced masonry and masonry-infilled frame structures. Initially, the key characteristics of the nonlinear behaviour of unreinforced masonry structures are outlined. The focus then shifts to describing the unreinforced masonry (URM) modelling approaches for nonlinear analysis adopted in this research. Two finite element modelling approaches are initially

detailed. The first involves a mesoscale (or simplified microscale) model, as proposed by (Minga et al., 2018), explicitly considering material heterogeneity and implemented within a partitioning framework. Furthermore, a continuum macroscale strategy is considered, adopting the isotropic concrete damage plasticity material as provide in (Chisari et al., 2020), which represents a slight modification of the original model of (Lee and Fenves, 1998). Subsequently, a comprehensive review is provided on relevant simplified discrete element strategies, as part of the present work involve the development of an enhanced three-dimensional macro-element, built upon the existing model of (Minga et al., 2020). Finally, the mechanics of masonry-infilled frames are reviewed, detailing the typical response of infilled frame structures under lateral loading conditions resulting from earthquake actions. Governing mechanisms, along with typical monotonic and cyclic behaviour, and significant influencing factors, are outlined. Following this, the review delves into the state-of-the-art exploration of both simplified and advanced modelling strategies for the analysis of this structural typology.

Chapter 3: Mesoscale and macroscale modelling for cyclic analysis of URM structures

This chapter investigates the nonlinear response up to collapse of unreinforced masonry wall components and structures under horizontal cyclic loading. Finite element descriptions formulated according to different scales of representation for masonry - specifically mesoscale and continuum macroscale, previously described - are compared. The purpose is to evaluate their capacity on the prediction of the hysteretic response under in-plane cyclic loading representing earthquake actions. The results of macro and mesoscale simulations are compared against experimental findings to assess the ability to represent strength and stiffness degradation and the amount of dissipated energy. Great emphasis is placed on the objectivity of the definition and calibration of the model material parameters with the aim of critically assessing how the response predictions are affected by their selection.

Chapter 4: Advanced modelling of masonry-infilled frame structures

This chapter focuses on the modelling of infilled reinforced concrete frames using two sophisticated strategies. These approaches involve representing masonry infills through either a mesoscale or a continuum macroscale approach, while the frame is modelled using cubic elasto-plastic 3D beam-column elements. To ensure effective coupling between the 3D masonry representation and the 1D beam/column elements, a multi-dimensional partitioned strategy has been employed (Jokhio, 2012). Experimental tests from literature are simulated, starting with the calibration of the bare reinforced concrete frame and then, following an accurate and objective calibration of the material, progressing to the calibration of the masonry infilled-frame models. The results demonstrate, for both modelling

strategies, a high level of accuracy compared to experimental outcomes, providing a faithful representation that precisely captures both the global response, namely the capacity curve, and the local behaviour, including the failure mechanisms of the infill, frame, and frame-infill interfaces. Additionally, sensitivity analyses are conducted to identify parameters that significantly impact the response. Finally, an assessment is conducted on the calibrated continuum-infill model to evaluate the impact of openings within the infills, either door or windows of various dimensions. The outcomes of this investigation provide valuable insights into the structural response of infilled reinforced concrete frames, serving as a reference point for subsequent analyses in the following chapters with the enhanced macroelement.

Chapter 5: A novel enhanced 3D macroelement for URM and infilled-frame structures modelling

This chapter introduces an enhanced macro-element model, building upon the groundwork laid by the element introduced in (E. Minga et al. 2020). This element has already proven to ensure accurate results while maintaining high computational efficiency. The introduced amendments focus on addressing certain limitations of the original implementation, resulting in a substantial improvement in the accuracy of response predictions. Changes are focused on the constitutive law governing the phenomenological evaluation of both in-plane and out-of-plane macroelement springs. The previous simplified representation lacked the capability to account for strength and stiffness degradation. To overcome this, the enhanced macroelement incorporates a more sophisticated constitutive law for both in-plane and out-of-plane springs, through the implementation of the cyclic hysteretic model of (Tomaževič and Lutman, 1996), capable of realistically capturing shear strength and stiffness degradation. A significant change also regards to the post-peak branch definition in the skeleton curve, ensuring mesh objectivity. Additionally, to realistically predict the actual response of frame-infilled frames, the possibility to distinguish mechanical properties between external, generally weaker, and internal frame-infill interfaces is introduced.

Chapter 6: Macroelement simulations of URM and masonry-infilled frame structures

The enhanced macroelement undergoes an accurate validation against several experimental outcomes, encompassing both unreinforced masonry and infilled-frame structures. The structural components under investigation include the masonry structures subjected to in-plane loadings, as previously evaluated in Chapter 3. Additionally, the crucial out-of-plane response is examined, essential for a comprehensive assessment of the seismic performance of existing masonry buildings. Furthermore, the response of a 3D structure subjected to earthquake loading is analysed. Concerning infilled-frame

structures, the specimens investigated in Chapter 4, utilising advanced mesoscale and continuum macroscale modelling techniques for the infills, are revisited herein. Moreover, the model's capacity to account for the presence of openings in masonry-infilled frames is evaluated by comparing its outcomes against those obtained from continuum macro-scale models. Eventually, cyclic analyses are performed, revealing the enhanced model's capability to predict the hysteretic response. The analyses conducted demonstrate the macroelement's ability to accurately represent both monotonic and cyclic behaviours observed in URM structures and masonry-infilled frames while maintaining high computational efficiency, making it applicable also in the domain of real-size buildings analysis.

Chapter 7: Seismic assessment of a real RC masonry-infilled frame building

The concluding chapter focuses on applying the enhanced macroelement strategy to assess the seismic vulnerability of a real 4-story irregular RC existing building, not designed to withstand earthquake loading. Nonlinear dynamic analyses are conducted using a set of spectrum-compatible accelerograms. The assessment of the RC concrete frames includes both scenarios, neglecting and considering the presence of masonry infills, with various configurations. The analysis results highlight the significant impact of masonry infills on the final vulnerability assessment and emphasise the importance of properly considering them through the use of a reliable modelling strategy.

Chapter 8: Conclusions and future work

The final section summarises the main conclusions drawn in each chapter and highlights the main achievements of the thesis. Furthermore, suggestions for future work are presented, with the aim of extending the outcomes of the research.

The flowchart in Figure 1 illustrates the various stages of the research, highlighting key steps.

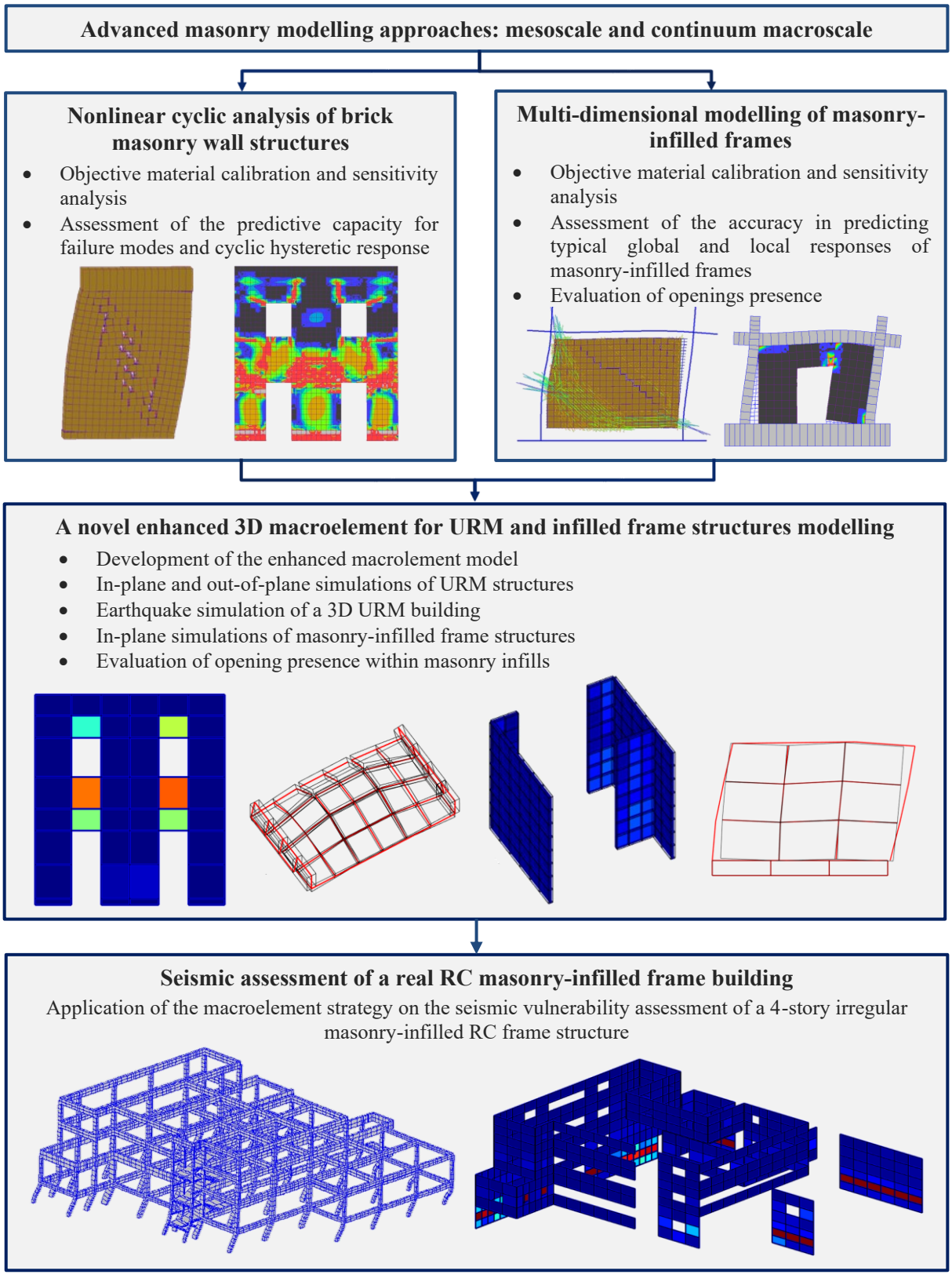

Figure 1 Flowchart presenting the research methodology

CHAPTER 2

LITERATURE REVIEW

2.1 Introduction

In this chapter, a literature review on the general behaviour and numerical modelling of unreinforced masonry (URM) and masonry-infilled frame structures is presented, with emphasis placed on the topics that are in-depth explored throughout the present research.

Initially, the review provides a general description of the key characteristics of the nonlinear behaviour of URM structures that numerical models need to replicate. It then delves into the URM modelling approaches adopted in this research. Specifically, it explores a simplified microscale (or mesoscale) modelling, which explicitly considers material heterogeneity, and a continuum macroscale strategy, which treats the material as a single isotropic entity at the macroscale level. A comparative analysis of these two strategies will be undertaken in Chapter 3, with the aim of assessing the objective calibration parameters of masonry wall structures subjected to cyclic loading. Subsequently, a review regarding the use of simplified discrete macro-elements for masonry modelling is presented, as Chapters 5, 6, and 7 of the present work will involve the application of a novel three-dimensional masonry macro-element.

Following this, the focus shifts to the mechanics of masonry-infilled frames, outlining the peculiarities and complexities of this structural typology. The governing mechanisms, together with the typical monotonic and cyclic responses, and the significant influencing factors are outlined. The review then explores the state-of-the-art of simplified and advanced modelling strategies for the analysis of masonry-infilled frame structures.

2.2 Structural response of URM wall structures

The majority of the existing building heritage in Italy and globally is predominantly constructed using masonry, often employing techniques that precede the era of construction industrialization. As a consequence, masonry structures exhibit a significant heterogeneity, with their characteristics influenced by cultural, geographical, material, workmanship, and functional factors. Therefore, each historical masonry construction should be viewed as a unique prototype, making it impractical to extend findings to apparently similar buildings. Thus, to ensure a reliable structural analysis, a detailed and site-specific structural survey is always necessary, along with the application of a suitable modelling approach.

Masonry is a heterogeneous material consisting of an assembly of units and mortar joints. Units, which can be either artificial or natural elements, such as clay bricks, calcium-silicate blocks or stones, are arranged in a more or less regular manner and stacked upon each other. Mortar layers serve as binding substance, and can be lime/cement based, polymer-based or other materials. In some cases, units are assembled without any mortar (so-called dry-joint masonry). Countless masonry combinations can be generated from the geometry, origin, and arrangement of units, along with the characteristics of mortar. However, they all share in common a low tensile strength. Despite this, masonry has been widely used for thousands of years due to its durability and the simplicity of its construction technique. Masonry can be generally utilised for a variety of purposes; in particular, it can serve as a load-bearing element or be employed as an internal or perimeter dividing element, simultaneously providing thermal and acoustic insulation. Figure 2 illustrates various masonry arrangements, encompassing both ancient and more contemporary masonry practices. In the present research, the focus is on the unreinforced masonry (URM), i.e. masonry not including steel reinforcement.

Masonry presents a composite mechanical behaviour, wherein units and mortar exhibit markedly distinct characteristics. Figure 3 presents an example of stress-strain curves from compressive tests performed independently on bricks, mortar and masonry specimens, as reported by (Binda et al., 1995). Generally, bricks and most units in historical buildings exhibit higher compressive strength than mortar. Moreover, as the compressive strength of units increases, they may show a progressively more brittle behaviour, in contrast with the more ductile nature of traditional mortars. The overall masonry may demonstrate strength smaller than that of the unit but greater than that of the mortar. However, different behaviours among the components may be possible. Furthermore, bricks and mortar generally have tensile strength significantly lower than their compressive strength, while the tensile strength of masonry as a whole is generally more related to the bond at the interface between units and mortar.

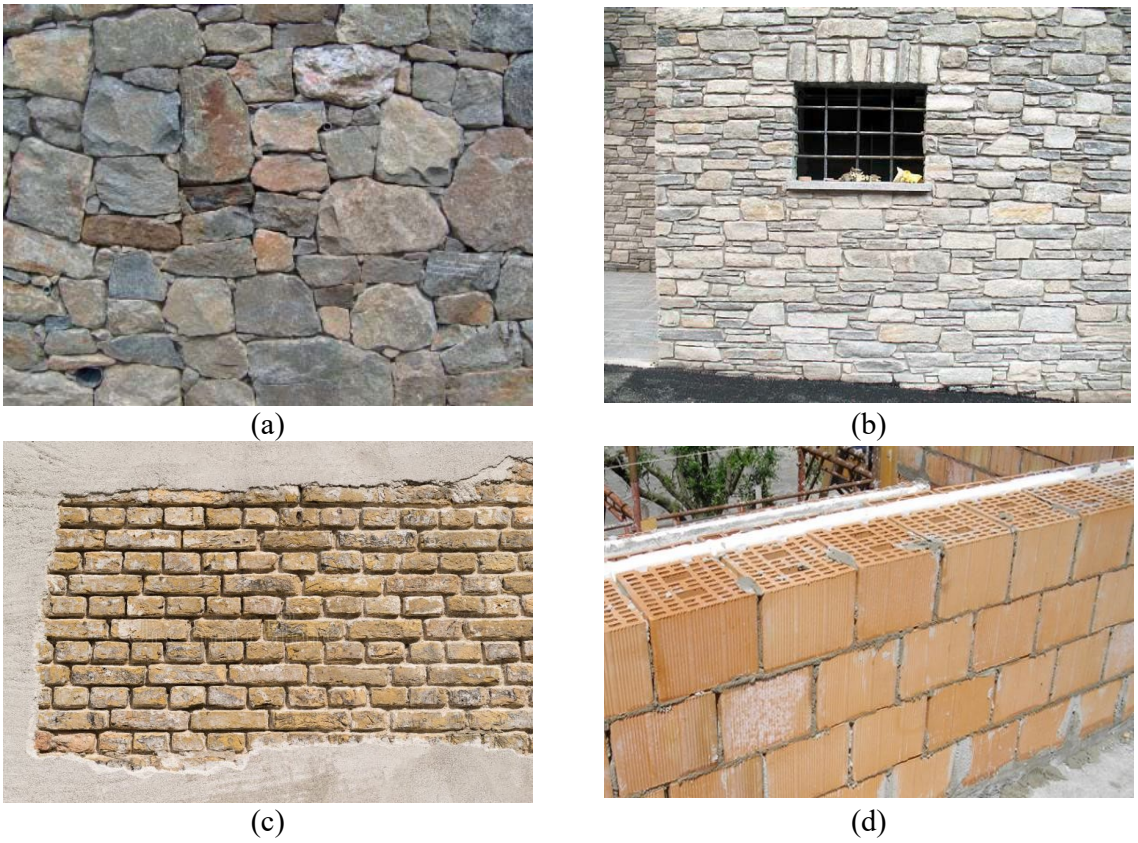

Figure 2 Example of masonry typologies: (a) dry stone wall; (b) irregular masonry with squared stone blocks; (c) regular clay brick-masonry wall in English bond pattern; (d) Single-layer semi-solid blocks masonry

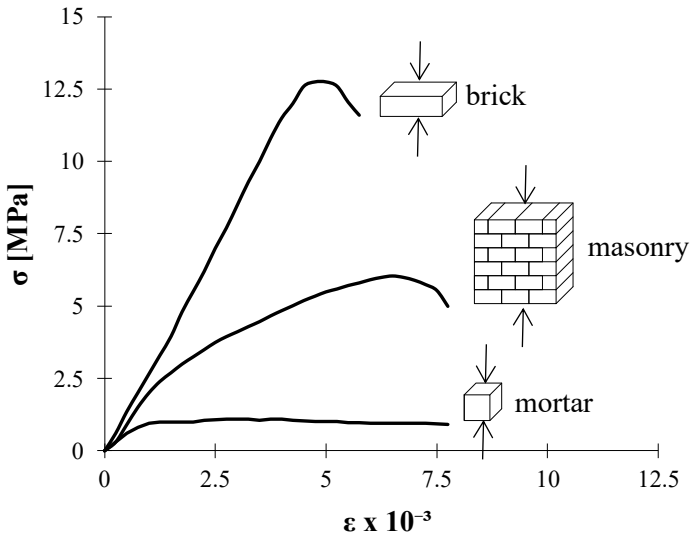

Figure 3 Stress-strain compressive response of brick, mortar and masonry (from Binda et al., 1995)

The measurement of material properties for each constituent within a URM assembly is generally achievable through relatively simple methods. However, the determination of local properties does not yield a direct estimation of the macroscopic nonlinear properties. This is due to the dependence of macroscopic properties on factors such as boundary conditions, units arrangement and geometry. As a result, establishing a straightforward link between individual properties and macroscale characteristics proves challenging. Typically, structural-scale (or macroscale) tests become necessary for a more comprehensive understanding of the masonry response as a whole, although at the expense of a higher invasiveness.

URM components, such as piers or spandrels, may exhibit various failure modes, generally categorised into in-plane and out-of-plane mechanisms. An illustrative example of activation of both in-plane and out-of-plane failures is presented in Figure 4, depicting the damage of a masonry building following the earthquake of Central Italy (2016). It is noteworthy that the ultimate failure mechanism of a masonry component may also be given by the interaction between more failure modes.

Figure 4 Damage on a URM structure after the Central Italy earthquake (2016): localised in-plane shear damage in the masonry piers of the upper floor and out-of-plane expulsion of the left-corner wall (Da Porto et al., 2016)

Typical in-plane mechanisms for brick-masonry walls are summarised in Figure 5 and presented below. The occurrence of one or the other depends on the characteristics of the components, the panel dimensions, and the applied vertical load.

- Diagonal shear failure:

  This failure may occur in two distinct ways. At one side, it can affect only the mortar layers, leading to detachment and sliding of bed and head mortar joints, resulting in the typical stepped crack (illustrated in Figure 5a), which is common in regular masonry with mortar joints weaker than unit strength. Alternatively, the failure may involve the conjunction of mortar and brick when the principal tensile stress exceeds the masonry's tensile strength (Figure 5b), leading to a straight cracking pattern. This type is more common in irregular masonry and regular masonry with strong mortar joints. Diagonal failures are generally observed in squat panels and for intermediate values of normal stress.
- Sliding shear failure (Figure 5c):

  Failure occurs due to shear failure of bed-joints, commonly observed in the presence of less resistant mortar layers. This failure may occur at low normal stresses, especially for squat elements.
- Flexural failure (Figure 5d) and toe crushing (Figure 5e):

  These two failure modes are often associated and typically occur in slender elements with high normal stress values. Horizontal cracks develop at the top and bottom of the wall due to flexural bending. Rocking may induce a concentration of compressive stresses in a small area, leading to compression crushing.

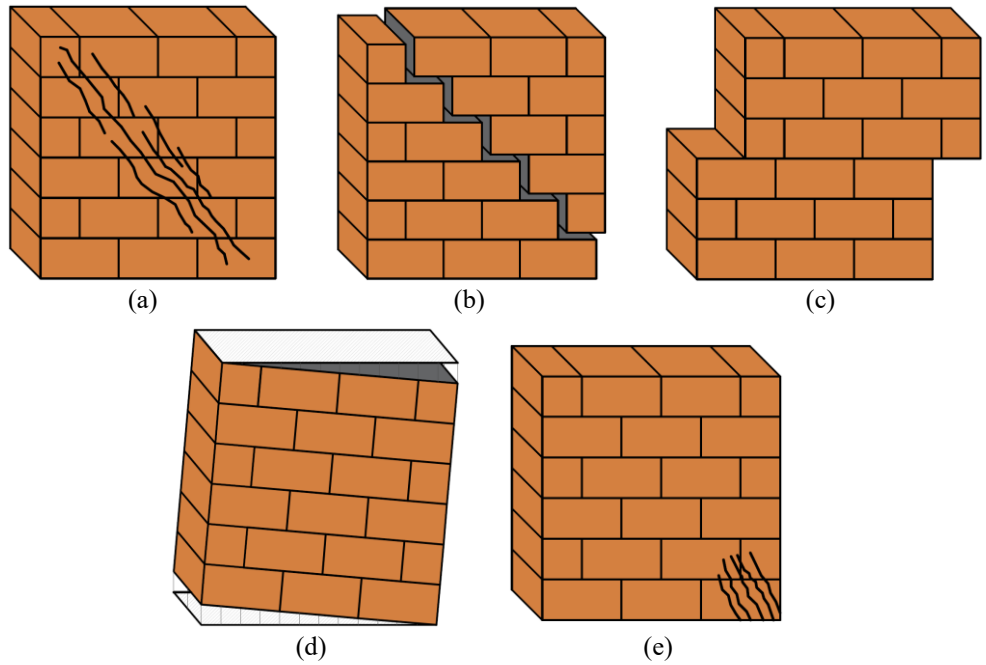

Figure 5 In-plane failure modes of URM components: shear diagonal cracking – (a) stepped cracking and (b) straight cracking; (b) shear sliding; (c) flexural failure; (d) toe crushing

The seismic vulnerability assessment of masonry buildings must be conducted not only with reference to the in-plane seismic response of URM components but also considering the out-of-plane mechanisms. Out-of-plane collapses can be linked to various kinematics and may be triggered by inadequate or insufficient boundary conditions. Illustrative examples of out-of-plane kinematics are depicted in Figure 6.

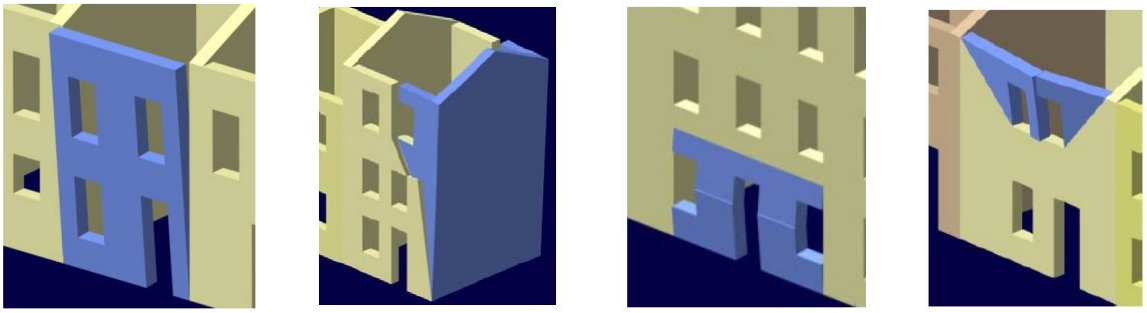

(a) (b) (c) (d)

Figure 6 Example of out-of-plane kinematic motions: (a) simple wall overturning; (b) composite wall overturning; (c) vertical flexure; (d) horizontal flexure (ReLUIS, 2013)

Excluding potential rigid body mechanisms resulting from insufficient boundary conditions, possible out-of-plane mechanisms at the scale of individual structural elements are enumerated below and visually depicted in Figure 7:

- Flexural failure (Figure 7a):
  Cracks manifest along one of the primary directions of the wall due to one-way flexural bending.
- Sliding shear failure (Figure 7b):
  Comparable to in-plane sliding shear, the sliding takes place in the out-of-plane direction.
- Two-way bending failure mechanism with diagonal cracking (Figure 7c):
  Occurs when the wall is connected to other parts of the structure along all its boundaries and may lead to the complete expulsion of the masonry component.

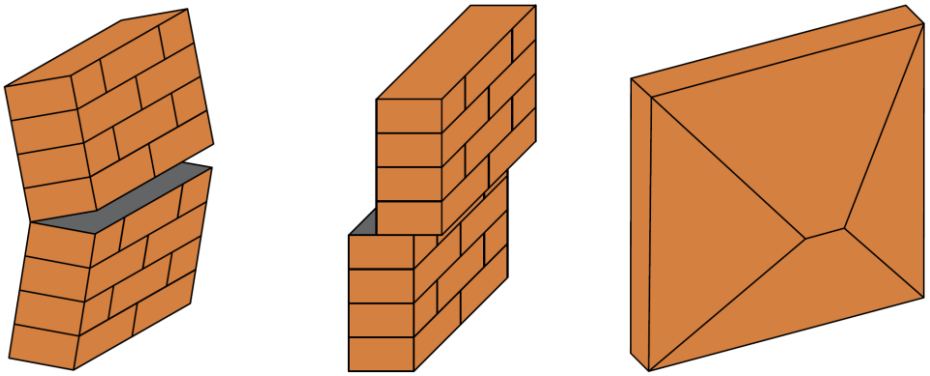

(a) (b) (c)

Figure 7 Out-of-plane failure modes of URM components: (a) flexural failure; (b) sliding shear failure; (c) two-way bending failure

2.3 URM modelling approaches

2.3.1 Overview

The behaviour of masonry structures is affected by several factors, as the mechanical properties of the constituents, the interaction among them and their spatial arrangement. Each of these characteristics has a distinct effect on the macroscopic behaviour of the masonry material. For these reasons achieving accurate prediction of the response of URM components and structures under extreme loading is a particularly challenging task.

The modelling of masonry can generally follow four main computational strategies according to the level of accuracy desired:

- Detailed micro-modelling (Figure 8a): units and mortar joints are represented by nonlinear continuum elements, while unit-mortar physical interfaces are modelled by nonlinear interface elements.
- Simplified micro-modelling or mesoscale modelling (Figure 8b): expanded units are modelled by elastic continuum elements, while mortar joints and unit-mortar interfaces are lumped together in zero-thickness nonlinear interface elements. More accurate approaches also take into account the potential occurrence of crack surfaces within the units.
- Finite elements macromodelling (Figure 8c): units, mortar and unit-mortar interfaces are not explicitly modelled since masonry is assumed as a homogeneous material employing isotropic or anisotropic nonlinear material models. A proper definition of the constitutive law is crucial within this strategy, and various choices can be considered, including phenomenological or

micro-mechanical approaches. The geometry of the structure may be discretised by 2D or 3D finite elements.

- Structural macromodels: masonry macroelements are defined by an arrangement of basic mechanical components, like beams or nonlinear springs, which are linked together to reproduce the resisting mechanisms typical of masonry components. These elements are widespread and used in the current engineering practice for their simplicity and computational efficiency. Two main typologies of macroelement can be found in the literature:
  - 1D macroelements, typical of the equivalent frame (EF) approach (an example of this representation is reported in Figure 17, Chapter 2.3.4), which require an a-priori simplification of the actual structural geometry.
  - 2D and 3D macroelements, which offer an alternative strategy to overcome certain limitations, such as the possibility of modelling different geometries and, in some cases, to reproduce the out-of-plane behaviour, while keeping the computational efficiency high (examples are given by Figure 20 and Figure 21, Chapter 2.3.4).

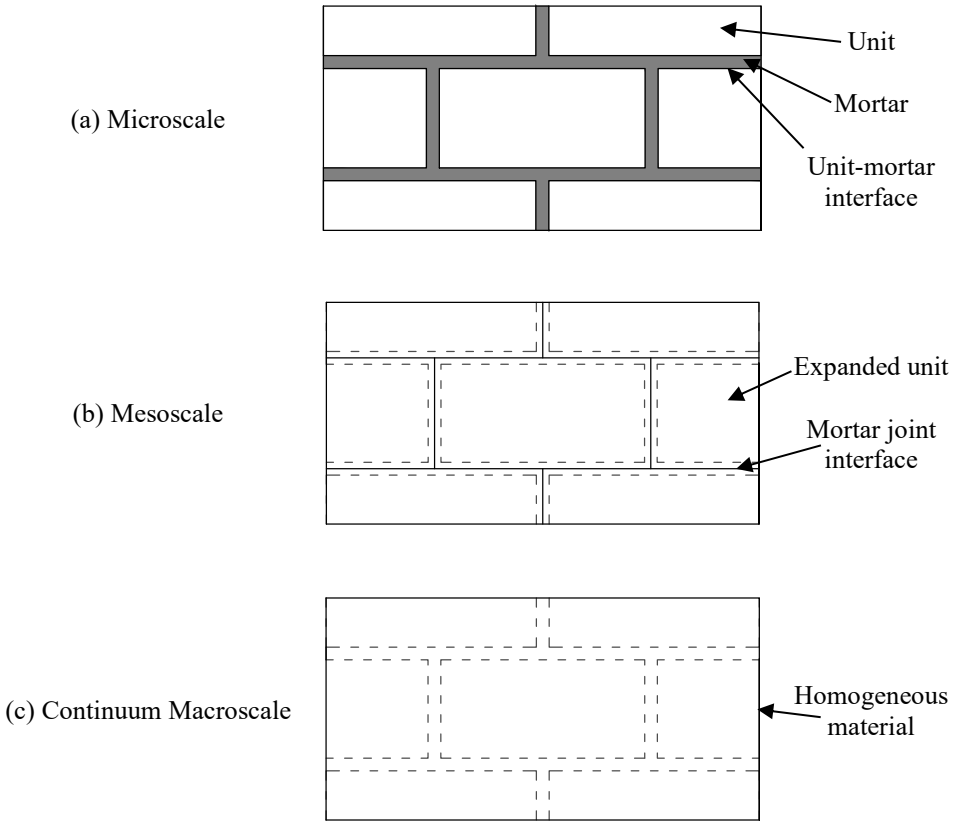

Figure 8 Different scales of representation for finite element modelling of masonry components

As pointed out in (Lourenco and Gaetani, 2022), the selection of an appropriate modelling strategy is linked to the level of knowledge of the material properties. Besides, different application fields require specific modelling approaches. Cost and time of the analyses, together with user knowledge and expertise, are other key aspects.

A mesoscale modelling strategy is usually associated with a simpler calibration of material properties, requiring straightforward tests on individual units and mortar joints. This is important when dealing with existing structures of historical and architectural value, where only low-invasive in-situ tests can be performed. On the other hand, mesoscale models or more detailed microscale models generally involve a significant computational cost and a time-consuming pre-processing stage, making this strategy not always feasible, particularly for the analysis of full-scale structures.

As a result, microscale approaches can be generally employed for analysing small-scale problems, such as individual assemblages of units and mortar layers up to single structural elements (e.g., piers or spandrels). Mesoscale approaches can be applied for larger problems, such as analysing parts of buildings like façades, although applications to entire buildings have also been made by creating some assemblage of masonry units into a larger equivalent unit. However, the analysis of large real URM structures under extreme loading are typically conducted using macroscale strategies, which offer computational efficiency but are often characterised by more challenging material calibration, potentially resulting in inaccurate response predictions.

Experimental data are essential in setting both micro and macro-modelling analyses. The investigations should cover information on the material response up to failure, including potential softening branch. Table 1 presents a synthesis of the required parameters for each approach.

Table 1 Synthesis of the main parameters needed for nonlinear static analysis of masonry structures (Lourenço and Gaetani, 2022)

Strategy	Elements	Linear parameters	Nonlinear parameters
Detailed micro-modelling	Unit (usually assumed isotropic)	Young's modulus Poisson's ratio	• Compressive and tensile strengths • Fracture energies in tension and compression • Hardening-softening criteria for compression and tension (σ-ε diagrams)
	Mortar (isotropic)		
	Interface for bed and head joint	Dummy normal and shear stiffness (to avoid interpenetration)	• Bond tensile strength • Cohesion • Friction coefficient • Dilatancy coefficient • Tensile and shear softening criteria (evolution of stresses vs. crack opening and slipping) • Mode I fracture energy • Mode II fracture energy
Simplified micro-modelling	Expanded units (usually assumed isotropic)	Young's modulus Poisson's ratio	No need as all nonlinearities are lumped at the interfaces (masonry joints and potential cracks in the units)
	Interface for bed and head joint	Normal stiffness Shear stiffness	Equal to detailed micro-modelling but, in addition: • Compressive strength of masonry • Hardening-softening criterion for compression (evolution of stresses vs. crushing) • Fracture energy in compression
	Interface for potential cracks in the unit	Dummy normal and shear stiffness (to avoid interpenetration)	• Tensile strength of unit • Cohesion • Friction coefficient • Dilatancy coefficient • Tensile and shear softening criteria (evolution of stresses vs. crack opening and slipping) • Mode I fracture energy • Mode II fracture energy
Macro-modelling	Isotropic	Young's modulus Poisson's ratio	• Tensile and compressive strengths of masonry • Fracture energies in tension and compression • Hardening-softening criteria for tension and compression (σ-ε diagrams)
	Ortotropic	Similar to isotropic but referring to both horizontal and vertical directions as material axes	

As mentioned, different modelling strategies necessitate distinct types of material tests, where macroscale characterisation may depend on more invasive tests compared to the less invasive tests required by mesoscale or microscale modelling. Typical tests necessary for mesoscale modelling include the following for characterising mortar interfaces: shear triplet tests (Figure 9a) for joint cohesion and joint coefficient of friction, cross joint tests (Figure 9b) for joint tensile strength (bond strength), and compressive tests on masonry prisms (Figure 9c) or, alternatively, less invasively, through flat-jack tests (Figure 10), for assessing compression strength. For interfaces representing brick failures (if they are represented), compression tests on whole units are performed to evaluate compression strength (Figure 9d) while splitting tests (Figure 9e) or tensile tests (Figure 9f) on whole units are conducted to assess tensile strength. In the case of microscale modelling, mortar must also be characterised for compression (through compression tests on mortar specimens) and tensile strength (typically through bending tests). Regarding the characterisation of macroscale models, as mentioned, since the link between properties of individual components and those of masonry as a whole is generally not straightforward, it may be necessary to conduct more invasive tests to characterize the shear-tensile response of the masonry, such as diagonal compression tests (Figure 11) or shear compression tests (Figure 12), while the compressive response may be determined through compressive tests on prisms or flat-jack tests.

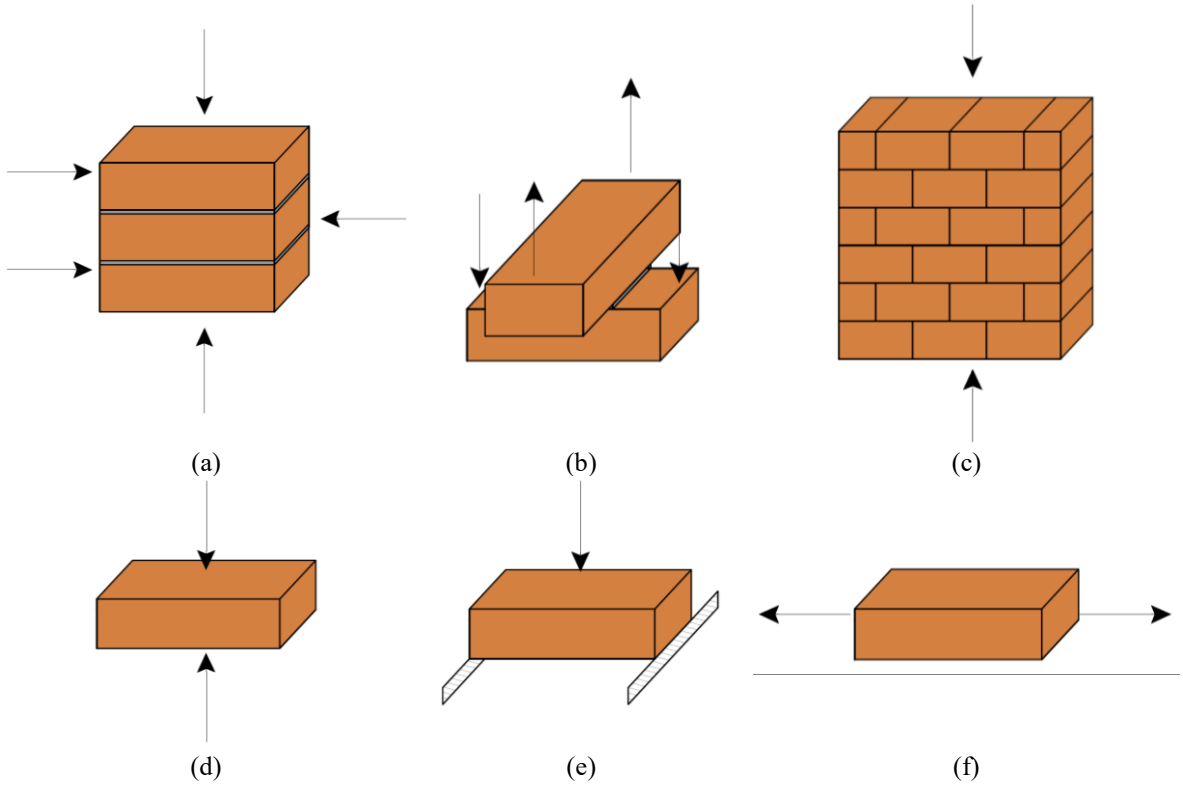

Figure 9 Tests on components: (a) triplet shear test; (b) cross joint test; (c) compressive test on masonry prism; (d) compressive test on unit; (d) splitting test on unit; (e) tensile test on unit.

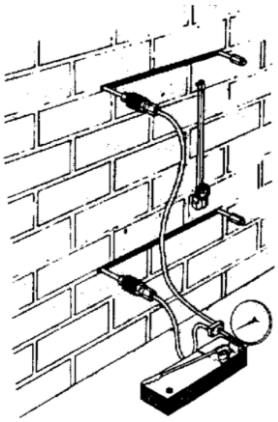

Figure 10 Typical test set-up for two flat jacks test (image taken from Gregorczyk and Lourenço, 2000)

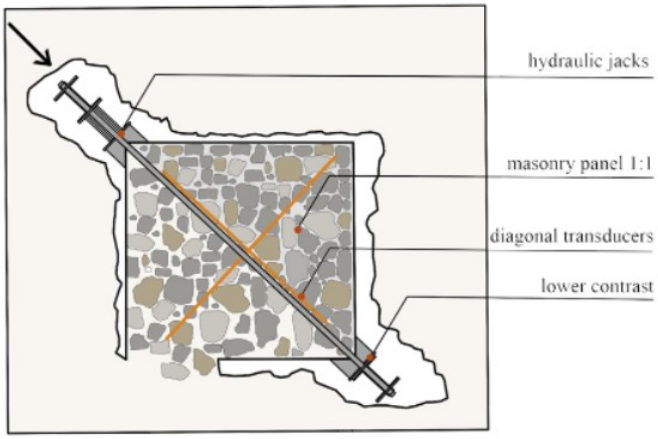

Figure 11 In-situ diagonal compression test (image taken from Croce et al., 2018)

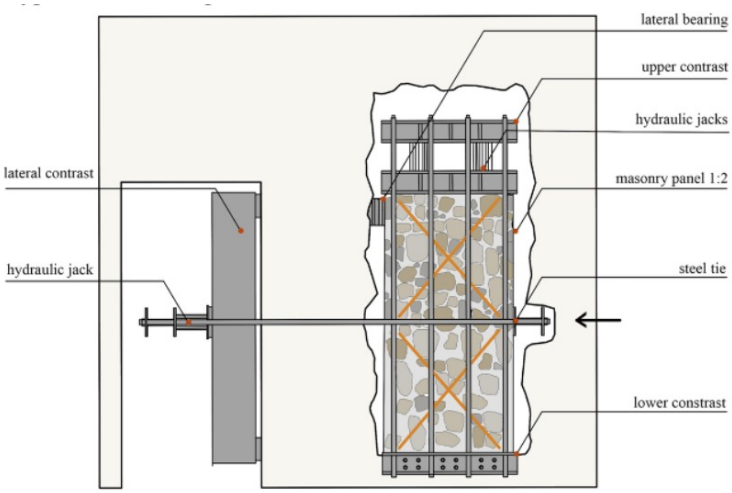

Figure 12 In-situ shear compression test (image taken from Croce et al., 2018)

The following sections provide a description of the modelling strategies for URM adopted throughout the present research.

2.3.2 Mesoscale approach

The 3D mesoscale description for URM structures, previously implemented in the FE software ADAPTIC (Izzuddin, 1991) and adopted in the present research (Macorini and Izzuddin, 2011), is based on the use of 20-noded elastic solid elements in combination with 16-noded zero-thickness nonlinear cohesive interface elements (Figure 13a). The former represent masonry units while the latter mortar joints and possible fracture interfaces within the units. The solid elements are expanded to fill the volume of the mortar joints. According to experimental observations, potential cracking paths in URM develop mainly in mortar joints. However, once formed, cracks can pass also through bricks and blocks. For this reason, brick failure surfaces are also arranged within masonry units. The behaviour of the brick-mortar and brick-brick interfaces determines the global nonlinear response of masonry and it is modelled by the refined constitutive model presented in (Minga et al., 2018), which combines plasticity and damage theories. A simplified multi-surface Coulomb yield criterion (Figure 13b) in the stress domain governs the development of permanent plastic strains. The conical surface simulates the behaviour in shear, corresponding to Mode II failure, and it is governed by cohesion c and friction angle φ. This surface is capped by two planar surfaces, which represent fracture in tension and compression. Stiffness and strength degradation are given through the evolution of an anisotropic damage tensor, as a function of the plastic work produced. The consideration of geometric nonlinearity, essential for evaluating the out-of-plane response, involves employing Green strains for the solid elements and a co-rotational approach in the interface elements, where the local reference system of the zero-thickness interface moves together with the mid-plane of the element (Izzuddin, 2005). For further information the reader is referred to (Macorini and Izzuddin, 2011; Minga et al., 2018).

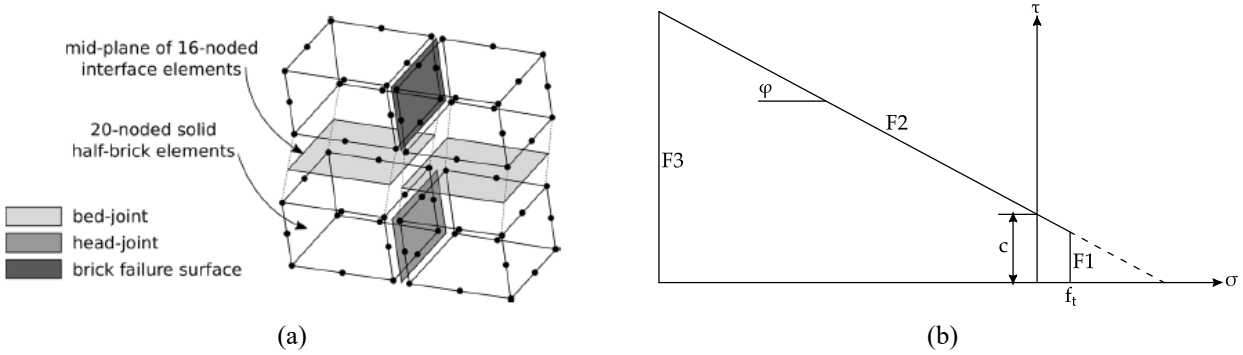

(a) (b)

Figure 13: (a) Mesoscale modelling of brick masonry (Macorini and Izzuddin, 2011); (b) Multi-surface yield criterion of plastic problem

The 3D mesoscale description allows for the representation of any regular masonry bonding pattern, defined by the in-plane and through-thickness brick arrangement; it also enables modelling non-planar brick/block masonry components, such as arches, vaults, and domes. The main drawback of the mesoscale strategy is the high computational burden, which normally limits its application to small structures. One way to mitigate this issue is through domain partitioning, as developed in (Jokhio and Izzuddin, 2015, 2013). The original (monolithic) structure is divided into *n* partitions, each representing a distinct section of the overall domain, referred to as "child" partitions in accordance with Jokhio and Izzuddin (2013). These partitions undergo separate analyses, each one solved in a different processor. The so-called "parent" structure is formed by dual super-elements identified by the boundary nodes of the child partitions. It controls the two-way communication between the sub-domains, allowing the parallelisation of the analysis. An illustrative example of a decomposition strategy is depicted in Figure 14, extracted from the research conducted by Macorini and Izzuddin (2013a) focusing on the nonlinear analysis of URM structures. In the figure, the original wall is partitioned into four child mesoscale sections. The dual super-element, denoted by the set of red nodes, serves as the parent structure. One side of this super-element is incorporated into the parent process, while the other side acts as a covering around the partitioned boundary in the child process. To further enhance computational efficiency, multiple levels of hierarchical partitioning can be considered, as shown in Figure 15 (Macorini and Izzuddin, 2013b), involving a recursive partitioning of each sub-domain.

To define a mesoscale model, it is necessary to characterise the material parameters of both units and interfaces. For the units, only the elastic modulus and Poisson's ratio must be provided. Meanwhile, cohesive-frictional interfaces must be detailed by specifying the normal and tangential stiffnesses, along with the strength parameters, namely cohesion, coefficient of friction, tensile bond strength and compressive strength, which define the multi-surface elastic domain (Figure 13b). The compressive strength for the nonlinear interfaces representing mortar joints is generally assumed equal to the whole masonry compressive strength, as suggested in (Lourenço and Gaetani, 2022). The post peak and cyclic response can be affected by other properties more difficult to quantify, i.e., fracture energies related to tensile, shear and crushing failure modes, and the stiffness degradation parameter (defined as the ratio between normal strain at which full damage in Mode I is attained under pure tension and the plastic strain at unloading (Minga et al., 2018). These main properties, with typical values for clay brick masonry (masonry typology examined in the comparison of Chapter 3), are listed in Table 2.

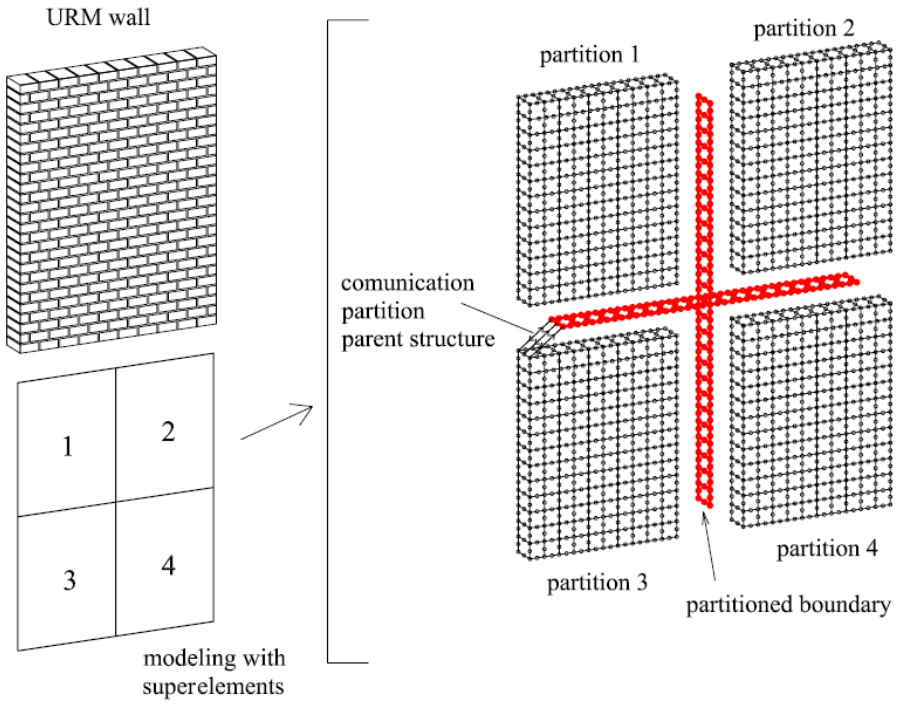

Figure 14 Partitioned approach (flat partitioning) for modelling URM components (Macorini and Izzuddin, 2013a)

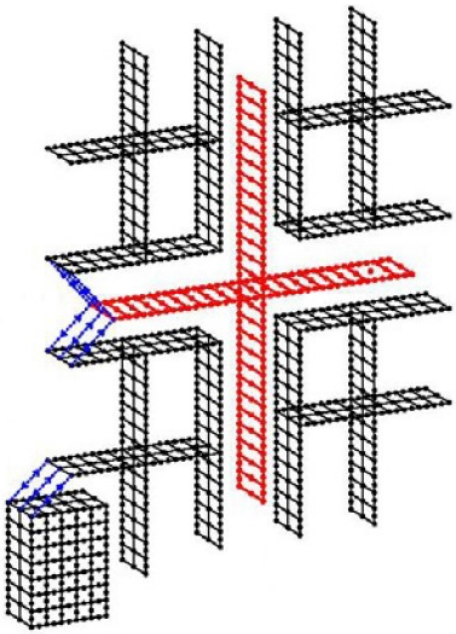

Figure 15 Schematic hierarchic partitioning of the URM wall (Macorini and Izzuddin, 2013b)

Table 2 Typical material properties for a mesoscale modelling approach for clay brick masonry walls (subscripts: b: brick; j: mortar joint; n: normal direction; t: tangential direction)

Parameter			Symbol	Unit	Typical values	Source
Units elastic parameters	Elastic modulus		E_b	N/mm^2	4000÷18000	(NZSEE, 2006)
	Poisson's coefficient		ν_b	-	0.2÷0.35	(NZSEE, 2006)
Interfaces elastic parameters	Mortar joints	Normal stiffness	$K_{n,j}$	N/mm^3	10÷250	(Minga et al., 2018)
		Tangential stiffness	$K_{t,j}$	N/mm^3	5÷105	(Minga et al., 2018)
	Internal bricks	Normal stiffness	$K_{n,b}$	N/mm^3	10^4	(Chisari et al., 2020)
		Tangential stiffness	$K_{t,b}$	N/mm^3	10^4	(Chisari et al., 2020)
Interfaces mechanical parameters	Mortar joints	Cohesion	c_j	N/mm^2	0.13÷0.38	(EN 1996-1-1, 1995)
		Friction coefficient	$\tan\varphi_j$	-	0.3÷0.8	(NZSEE, 2017)
		Tensile bond strength	$f_{t,j}$	N/mm^2	0÷0.1	(Lourenço and Gaetani, 2022)
	Internal bricks	Tensile strength	$f_{t,b}$	N/mm^2	1.4÷4.2	(NZSEE, 2017)
	Compressive strength		f_c	N/mm^2	2.6÷4.3	(MIT, 2019)
Interfaces fracture energies	Mortar joints	Mode I	$G_{I,j}$	N/mm	0.005÷0.035	(Van der Pluijm, 1999)
		Mode II	$G_{II,j}$	N/mm	0.01÷0.25	(Van der Pluijm, 1992)
	Internal bricks	Mode I	$G_{I,b}$	N/mm	0.1	(Chisari et al., 2020)
	Crushing mode		G_c	N/mm	$(0.88÷5.3)\cdot f_c$	(Jafari et al., 2022)
Interfaces stiffness degradation	Mortar joints		μ_j	-	0.1	(Minga et al., 2018)
	Internal bricks		μ_b	-	0.1	(Minga et al., 2018)

2.3.3 Continuum finite element macroscale

The FE continuum macroscale strategy adopted throughout the thesis is characterised by the use of the concrete damaged plasticity (CDP) material law (Lee and Fenves, 1998; Lubliner et al., 1989), an isotropic model that combines the concepts of damaged elasticity with tensile and compressive plasticity. A scalar isotropic damage, which comprises separate damage variables in tension (d_t) and compression (d_c), is assumed. The nonlinear response is defined through a uniaxial nonlinear constitutive law, with softening in tension and compression as shown in Figure 16a, where the stiffness recovery parameters w_c and w_t for compressive and tensile behaviour varying from 0 to 1 for zero and full stiffness recovery, are also indicated. The model makes use of the yield surface proposed by Lubliner et al. (1989), with the modifications put forward in (Lee and Fenves, 1998) to account for

different evolution of strength under tension and compression. The typical form of the yield function in the two-dimensional space of the principal stresses is sketched in Figure 16b.

In the present work, the concrete damaged plasticity model developed in (Chisari et al., 2020) is considered, which is a slightly modified version of the one proposed in (Lee and Fenves, 1998; Lubliner et al., 1989). The difference between them regards the specification of the damage laws d_c and d_t. In the Lee & Fenves's model, the parameters are directly defined by the user, as a function of inelastic deformation, while in Chisari's model they are defined as functions of nominal and effective strength, which are, in turn, functions of state variables related to plastic strain. For further information on the description of the material law, the reader can refer to (Chisari et al., 2020).

It is noteworthy that the CDP model has been originally developed for modelling the behaviour of concrete structures and isotropic quasi-brittle materials, but has also been widely adopted in the modelling of masonry structures (Cattari et al., 2021; Chisari et al., 2020; Zizi et al., 2022, 2021). Some anisotropic damage or plasticity-damage models have been developed but specifically for masonry (Berto et al., 2002; Chisari et al., 2023).

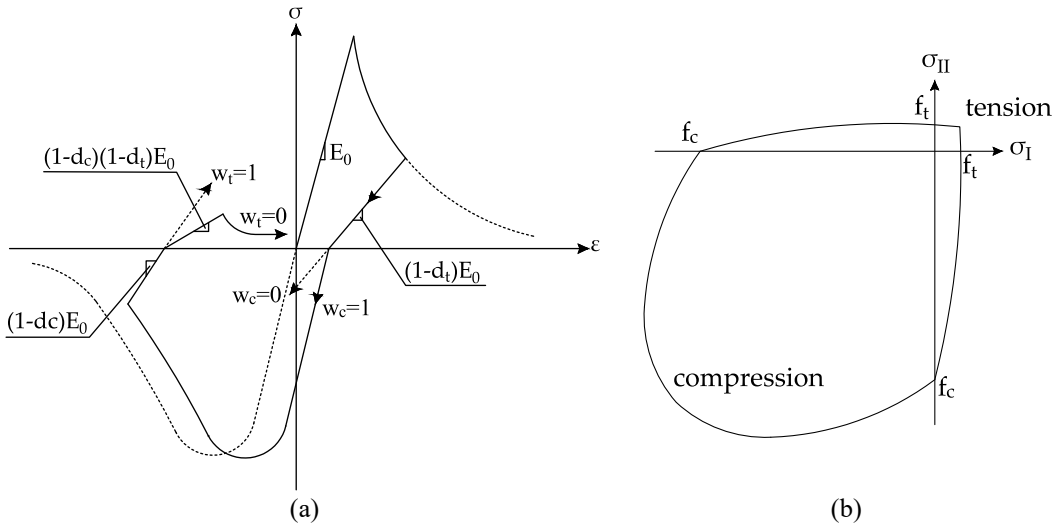

Figure 16 (a) Typical uniaxial load cycle (tension-compression-tension) for damaged plasticity, assuming total stiffness recovery for crack closure (w_c=1) and null recovery for crack reopening after crushing (w_t=0); (b) typical elastic limit function for damaged plasticity model, in the two-dimensional space of principal stresses

The CDP material model must be defined through many parameters (as detailed in Table 3, with typical values provided for clay brick masonry walls), characterising:

- the elastic behaviour: Young's modulus E, Poisson's coefficient ν;

- the uniaxial post-elastic behaviour in tension: uniaxial tensile strength f_t, fracture energy G_t, stiffness degradation in tension parameter μ;
- the uniaxial post-elastic behaviour in compression: uniaxial compressive strengths f_c, ratio between uniaxial yielding stress and maximum strength f_{yr}, plastic strain at the peak compression strength $k_{c,fmax}$;
- the multi-axial cyclic behaviour: dilatancy ψ, ratio between biaxial and uniaxial compressive strength f_{b0}, flow potential eccentricity ε, ratio of the second stress invariant on the tensile meridian to that on the compressive meridian at initial yield K_c, stiffnesses recovery parameters in tension w_t and in compression w_c.

The calibration of the material parameters for the macroscale model is not straightforward when only the properties of the masonry constituents are available. In addition, some parameters that may greatly affect the response cannot often be explicitly and objectively quantified. These aspects will be investigated in Chapter 3.

Table 3 Typical material properties for a continuum macroscale CDP modelling approach for clay brick masonry walls

Parameter	Symbol	Unit	Typical values	Source
Elastic modulus	E	N/mm^2	690÷5600	(MIT, 2019)
Poisson's coefficient	ν	-	0.2	(Lourenço and Gaetani, 2022)
Dilatancy angle	ψ	°	0÷35	(Van der Pluijm, 1993)
Ratio between biaxial and uniaxial compressive strength	f_{b0}	-	1.16	(ABAQUS Inc, 2014)
Flow potential eccentricity	ε	-	0.1	(ABAQUS Inc, 2014)
Ratio of the second stress invariant on the tensile meridian to that on the compressive meridian at initial yield	K_c	-	0.66	(ABAQUS Inc, 2014)
Global tensile strength	f_t	N/mm^2	0.075÷0.195	(MIT, 2019)
Fracture energy	G_t	N/mm	0.005 ÷ 0.035	(Van der Pluijm, 1999)
Parameter controlling stiffness degradation in tension	μ	-	0÷1	(Chisari et al., 2020)
Maximum compression strength	f_c	N/mm^2	2.6÷4.3	(MIT, 2019)
Ratio between uniaxial yielding stress and maximum strength in compression	f_{yr}	-	0.01÷1	(Chisari et al., 2020)
Plastic strain at maximum compressive strength	$k_{c,fmax}$	-	$1\cdot10^{-5}$÷$1\cdot10^{-2}$	(Chisari et al., 2020)
Tensile stiffness recovery	w_t	-	0	(ABAQUS Inc, 2014)
Compressive stiffness recovery	w_c	-	1	(ABAQUS Inc, 2014)

2.3.4 Macroelements

The second approach within the macroscale framework is based on the use of an arrangement of basic mechanical components, like beams or nonlinear springs, linked together to generate macroelements. The material nonlinearity of macroelements is usually given by phenomenological constitutive laws

attributed to the specific components, by distinguishing the resistant mechanisms of masonry structures to be represented. These elements are widespread and used in the current engineering practice for their simplicity and computationally efficiency. Many modelling approaches have taken place over time, ranging from Equivalent Frame modelling (EF) to usage of macroelement to represent an entire panel. Thus, two main typologies of macroelements can be recognised in literature, roughly distinguished whether they are mono-dimensional or bi- or tri-dimensional.

Within the so-called Equivalent Frame Approach (Bracchi et al., 2021; Bracchi and Penna, 2021; Brencich et al., 1998; Lagomarsino et al., 2013; Rinaldin et al., 2016), 1D macroelements represent single structural members, piers and spandrels, connected to each other through rigid offsets (Figure 17a). Macroelements can be defined through rigid or elastic beams with lumped plasticity located on springs, which allows the simulation of masonry resistant mechanisms, such as shear-diagonal cracking, shear-sliding and axial-flexural failure modes. The main advantage is due to its simplicity and computational efficiency. Indeed, they can also include the possibility to represent the cyclic strength and stiffness degradation, as in (Rinaldin et al., 2016). However, this strategy has some clear limitations. Replacing a masonry portion with a frame element leads to some intrinsic inaccuracies, related to the imprecise simulation of interactions among macro-elements, difficulties arising from complex geometries characterised by irregular openings dispositions and lack of representation of the out-of-plane response.

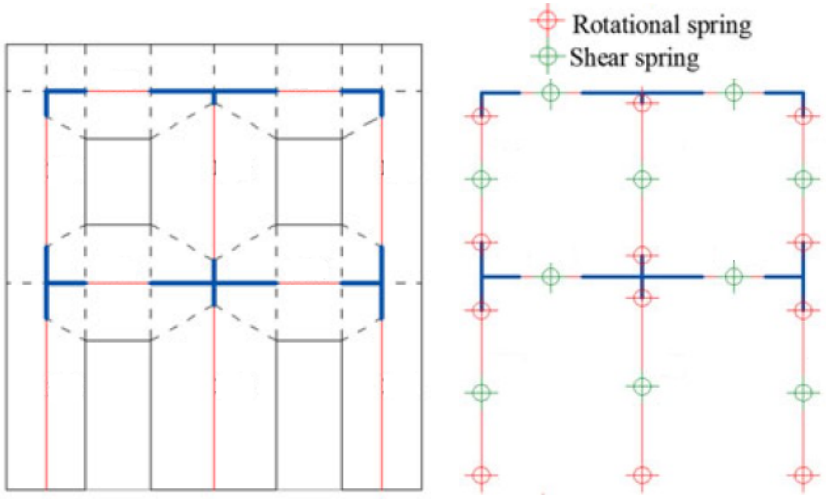

(a) (b)

Figure 17 (a) Equivalent frame discretisation (piers and spandrels macroelements are depicted in red, while rigid offsets are in blue) and (b) location of shear and flexural rotational springs (images taken from Rinaldin et al., 2016)

Bi- or tri-dimensional macroelements represent a reliable alternative capable of facing certain limitations, such as the possibility of model different geometries and to reproduce the out-of-plane behaviour, while keeping the computational efficiency high. Over the years, various models have been developed. Some of them are briefly described in the following.

One of the first two-dimensional macroelement development was proposed by D'asdia and Viskovic (1995), in which the masonry portion was modelled by a plane assemblage of linear elastic frame elements of variable shape. The nonlinearity was represented by a nonlinear step-by-step updating of the geometry of the element, varying the resisting section of the wall by excluding volumes experiencing tensile stress.

Foraboschi and Vanin (2013) proposed an analytical approach for the pushover analysis of masonry structures. Their method consists in splitting the structure into stories, and then subdividing each story into plane masonry panels, consistently with the geometry. The masonry panels are modelled using an evolutive strut-and-tie model, by means of a system of articulated struts exhibiting elastic-perfectly plastic response in compression and zero strength in tension. The behaviour of each panel under lateral loading can simulate the in-plane response until the development of failure mechanisms, such as shear diagonal cracking or flexural failure (Figure 18). The evolutive strut-and-tie model generates the capacity curve of the single panels, contributing then to the overall pushover response of the structure.

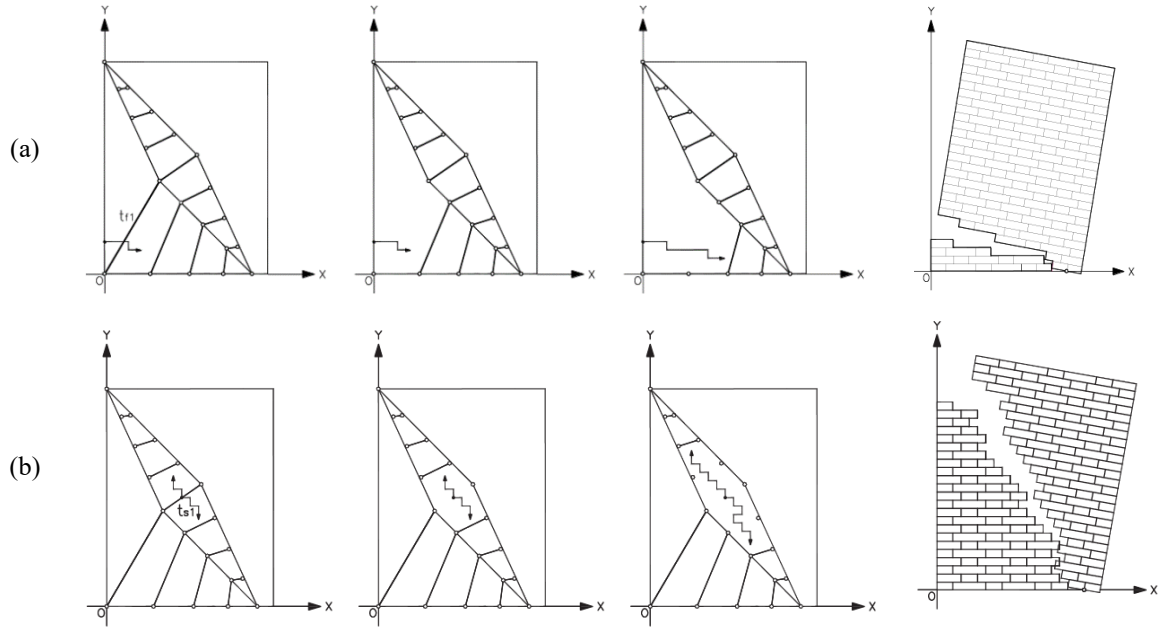

Figure 18 Progressive modification of the equivalent evolutive strut-and-tie due to the (a) flexural failure and (b) shear failure with diagonal crack (images taken from Foraboschi and Vanin, 2013)

Casolo and Peña, (2007) presented a mechanistic ‘rigid body spring model’, in which masonry elements are discretised through ‘unit cell’, which are plane quadrilateral rigid elements, linked together with uncoupled normal and shear springs at each side (Figure 19). The constitutive laws of these springs are defined to simulate in a phenomenological way the in-plane cyclic and dynamic hysteretic response, specifically reproducing diagonal cracking, in-plane flexural and crushing failure modes of masonry.

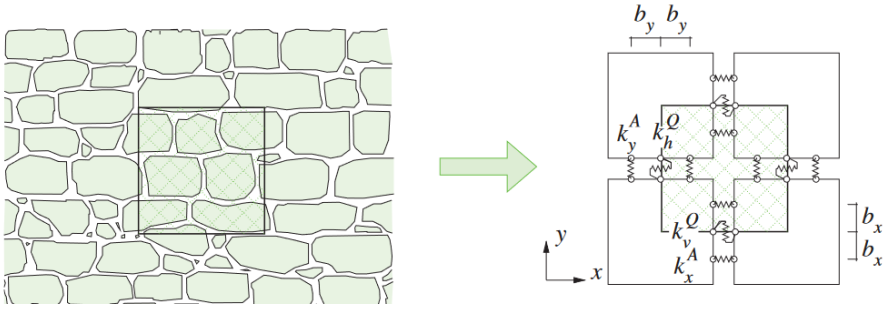

Figure 19 Rigid body spring model: scheme of an irregular masonry and ‘unit cell’ defined by four rigid elements (image taken from Casolo and Peña, 2007)

In (Bertolesi et al., 2016) a comparable approach was utilised to examine the in-plane response. Holonomic constitutive laws are adopted for the springs connecting the rigid elements, specified through homogenization principles. These laws are derived separately and subsequently incorporated into a standard commercial finite element software. The model was lately deepened in (Da Silva et al., 2017), allowing also the out-of-plane behaviour. Both the implementations do not incorporate the representation of cyclic hysteretic response.

In the model proposed by Caliò, Marletta, and Pantò (2012), the representation of masonry medium involves the utilisation of pinned articulated quadrilaterals with rigid edges, surrounded by interfaces given by uncoupled nonlinear axial and shear springs, which allow the interaction through adjacent elements (Figure 20a). The deformable internal block is governed by a couple of additional diagonal nonlinear springs. Hence, each plane macro-element exhibits three degrees-of-freedom, corresponding to in plane rigid-body motion, along with an additional degree-of-freedom required to characterize in-plane shear deformability. Thus, the model is capable of simulating all in-plane failure modes, since the border springs govern shear sliding and axial-flexural response, while the diagonal springs enable the simulation of diagonal cracking failure mode. A single macroelement can be employed to represent an entire structural member (as illustrated in Figure 20c, which displays a basic mesh discretisation of a wall with openings) or a portion of it, in a more refined mesh discretisation. The macroelement model, firstly implemented for the representation of the in-plane behaviour only, was then enhanced

incorporating also the out-of-plane response (Pantò et al., 2017, 2016). In the original plane model, the interfaces were characterised by one single row of orthogonal nonlinear springs along with a single additional longitudinal spring. To account for the out-of-plane response, the 3D border interface of the enhanced formulation considers multiple rows of orthogonal nonlinear links and additional transversal sliding springs, as illustrated in Figure 20b. The latter are necessary for controlling the out-of-plane sliding mechanisms and the torsion around the axis perpendicular to the plane of the interface. Overall, the upgraded three-dimensional macroelement considers three further degrees of freedom, allowing to comprehensively capture the out-of-plane response.

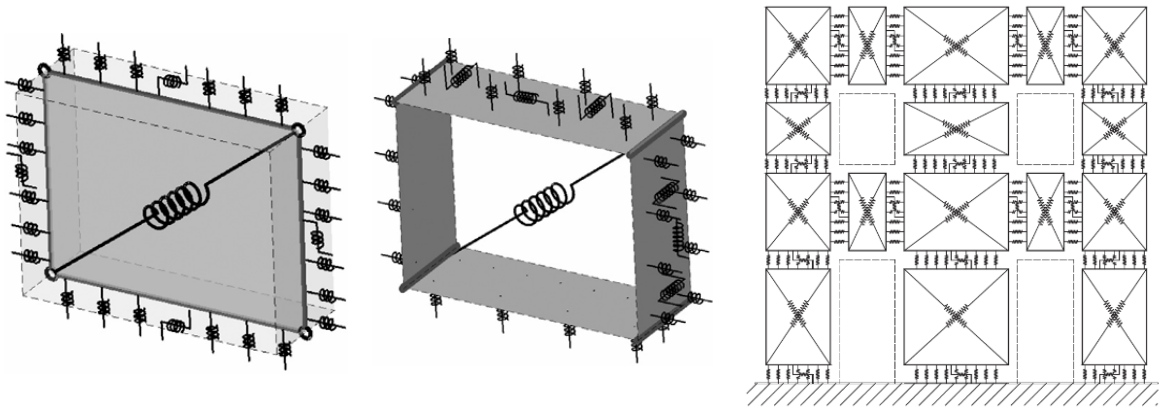

(a) (b) (c)

Figure 20 (a) Mechanical representation of the plane macroelement and (b) spatial macroelement; (c) basic discretisation of a wall with openings (images taken from Pantò et al., 2016, and Caliò et al., 2012)

E. Minga et al. (2020) presented a three-dimensional macroelement approach for the cyclic analysis of unreinforced masonry structures subjected to in-plane and out-of-plane actions, used to represent large portions of masonry walls. The macroelement is characterised by an internal deformable block surrounded by four external edges, that are connected through zero-thickness cohesive-frictional interfaces (Figure 21a), for which the sophisticated constitutive model for the description of unified joint interfaces under cyclic loading proposed in (Minga et al., 2018) was employed. Hence, instead of considering uncoupled springs, the implementation of the sophisticated interfaces directly couples normal and tangential behaviour. Furthermore, the in-plane shear and the out-of-plane bending modes are defined through non-linear springs, governed by two independent Lagrangian parameters (Figure 21b and Figure 21c). Therefore, all the failure modes typical of masonry buildings can be represented within a highly computationally efficient model. Flexural cracking, shear-sliding and toe crushing are represented along the macroelement interfaces, allowing them to interact together within a single interface joint model, while in-plane and out-of-plane diagonal cracking are phenomenologically depicted through the nonlinear springs associated with the deformation modes of the inner block.

Additionally, unlike previous macroelement strategies (e.g., Caliò et al., 2012; Pantò et al., 2016, 2017), the model is developed within a finite element framework. This enables flexible connectivity through its boundary edges with adjacent elements, such as quadratic beams or shells.

This element will be thoroughly investigated in the present work, in Chapters 5, 6, and 7, where original drawbacks will be addressed, and a novel enhanced macroelement will be proposed.

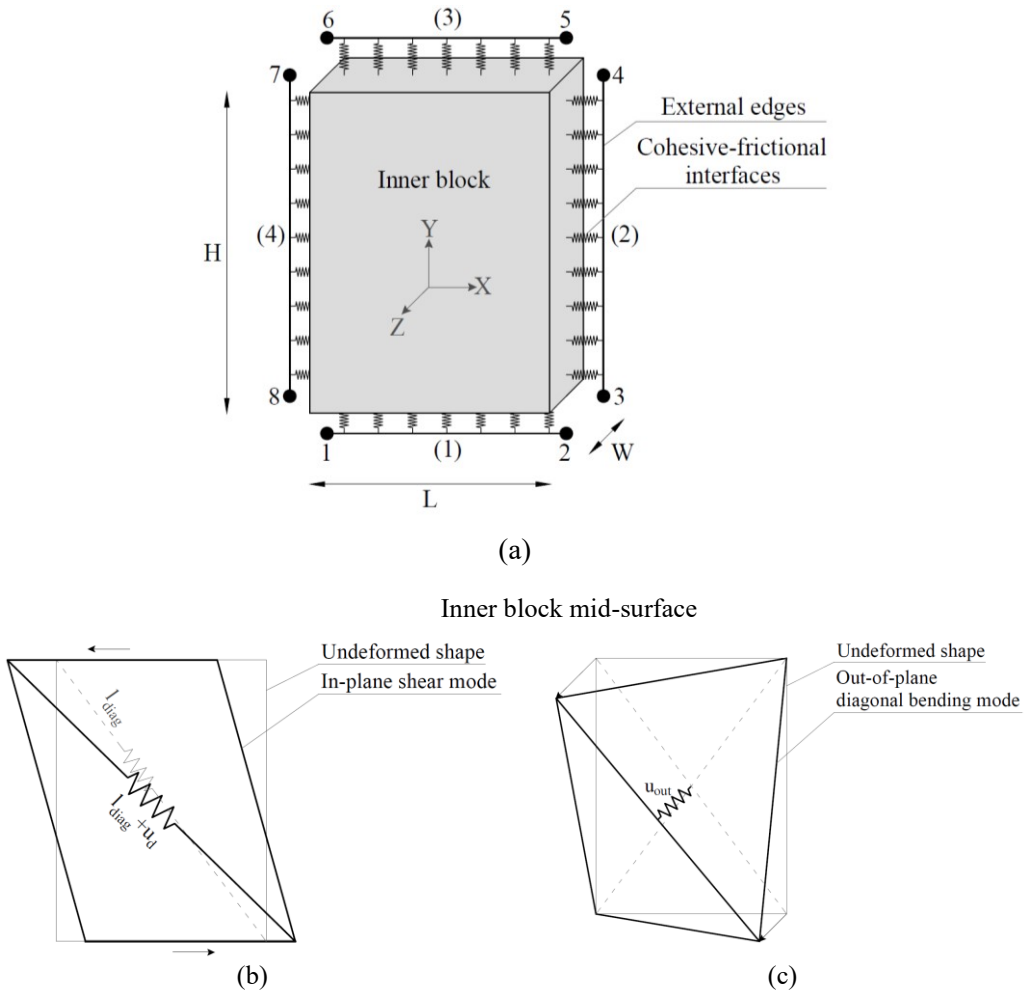

Figure 21 (a) URM macroelement; (b) in-plane shear and (c) out-of-plane diagonal bending deformation modes of inner block

2.3.5 Safety assessment and knowledge levels

The reliability of structural analysis is not only influenced by the link between material characteristics and modelling approaches, which must align with the typology of parameters known and the structure being analysed, but also by the quantitative level of knowledge about the structure. Masonry structures, particularly those constructed with irregular stone masonry, can exhibit significant heterogeneity, leading to variations in properties across different parts of the structure Therefore, conducting more experimental tests may be necessary to ensure sufficient reliability regarding the overall characteristics of the structure. The specific values used in the analysis must account for this inherent uncertainty, which varies based on the depth of knowledge of different aspects. Essentially, a less detailed investigation leads to conservative estimates with lower mechanical properties.

In this context, both Eurocode 8 and the Italian code (MIT, 2019) encompass the concepts of knowledge levels (KL) to consider varying degrees of investigation concerning geometry, construction details and material properties. Additionally, they define the confidence factor (CF), which is applied to reduce the material strength based on the level of knowledge reached.

The knowledge level KL serve as an indicator of the completeness of the investigation conducted, which in turn determines the confidence factor (CF). The factors contributing to the appropriate knowledge level include: (1) geometry of structural and non-structural elements (such as masonry infills, which can impact the structural response); (2) constructive details (including morphology of masonry and connections between masonry infills and the surrounding frame); (3) material characterisation. Based on the level of knowledge attained in each of these aspects, three knowledge levels are recognised, each associated with a different confidence factor: limited knowledge (KL1, with CF=1.35), normal knowledge (KL2, with CF=1.2) and full knowledge (KL3, with CF=1).

Based on the knowledge level, the Italian code (MIT, 2019) provides guidelines for calculating the mechanical properties required for analysis. In nonlinear analysis, these values are determined by dividing the mean value by the confidence factor (CF). The mean values of the material parameters are obtained from the recommendations outlined in Table 4 of the Italian code and are based on the knowledge level attained. Specifically:

- For KL1: Minimum strength and average Young's modulus are derived from the specified ranges of values.

- For KL2: Average strength and average Young's modulus are derived from the specified ranges of values.
- For KL3: Strength and Young's modulus are determined by combining the values recommended in the code with the results obtained from experimental tests, using statistical expressions that consider the number of experimental tests conducted.

Table 4. Recommended masonry material characteristics according to Italian regulation (MIT, 2019)

Masonry typology	f_c [MPa] min-max	τ_0 [MPa] min-max	f_{v0} [MPa] min-max	E [MPa] min-max	G [MPa] min-max	w [kN/m^3]
Irregular stone masonry (pebbles, erratic, irregular stones)	1.0÷2.0	0.018÷0.032	-	690÷1050	230÷350	19
Uncut stone masonry with inhomogeneous thickness of leaves	2.0	0.035÷0.051	-	1020÷1440	340÷480	20
Regular stone masonry with good bonding	2.6÷3.8	0.056÷0.074	-	1500÷1980	500÷660	21
Soft stone masonry (tuff, limestone, etc.)	1.4÷2.2	0.028÷0.042	-	900÷1260	400÷600	13÷16
Regular soft stone masonry (tuff, limestone, etc.)	2.0÷3.2	0.04÷0.08	0.10÷0.19	1200÷1620	400÷500	
Dressed rectangular (ashlar) stone masonry	5.8÷8.2	0.09÷0.12	0.18÷0.28	2400÷3300	800÷1100	12
Solid brick masonry with lime mortar	2.6÷4.3	0.05÷0.13	0.13÷0.27	1200÷1800	400÷600	18
Hollow bricks (void < 40%) with cement mortar	5.0÷8.0	0.08÷0.17	0.20÷0.36	3500÷5600	875÷1400	15

2.4 Structural response of masonry-infilled frames

2.4.1 Overview

The seismic events of the past have revealed significant structural implications arising from the presence of infilled frames in reinforced concrete or steel structures. The infills, serving as external claddings or internal partitions, heavily impact the overall response of such frames. While offering benefits in terms of increased base strength and hysteretic capacity, they concurrently introduce an increase in stiffness leading to reduced vibration periods (Asteris et al., 2011; El-Dakhakhni et al., 2003). Consequently, structures with infills generally face higher spectral acceleration compared to bare structures. Moreover, infills greatly impact on the overall economic losses. In fact, as indicated by Tiedeman (1980), approximately 80% of the economic costs associated with earthquakes can be attributed to damages sustained by infills, including harm to windows, doors, and various installations (Figure 22).

Figure 22 Infill damages after L'Aquila (IT) earthquake in 2009 (Dipartimento della Protezione Civile, 2009)

Infilled-frames structures are particularly widespread in earthquake prone regions, particularly where masonry remains a common construction type due to historical and cost-related considerations. Many of these structures were constructed before the advent of modern seismic codes, designed to resist gravity loads without adequate consideration for lateral loads and lacking seismic ductile detailing (Al-Chaar et al., 2002; Crisafulli et al., 2000).

In current engineering practice, structural engineers often neglect the significant impact of masonry infills when analysing both new and existing buildings. In particular, vulnerability analysis and subsequent retrofitting necessitate a comprehensive assessment of the structural behaviour. Overlooking the presence of masonry infills may easily result in inaccurate predictions of the structural response in terms of lateral stiffness, strength, and ductility (Crisafulli et al., 2000). This neglect can be attributed to a combination of limited knowledge on the topic and the absence of practical and reliable methods for evaluating the complex composite behaviour of infilled-frames. Additionally, the mechanical characteristics of masonry infills exhibit significant variability, primarily due to workmanship, making them challenging to quantify with precision and reliability.

The response of infilled frame structures is complex and markedly nonlinear due to the brittle behaviour of infill masonry, the ductile nonlinear behaviour of frame, the different stiffnesses of the two components and the ever-changing conditions of the border interfaces (Crisafulli, 1997). The overall strength and stiffness of these structures are typically higher than the sum of their single components (Klingner and Bertero, 1976).

The seismic responses of infilled frames and bare frames exhibit significant distinctions. The composite structure is characterised by elevated stiffness and strength in comparison to the bare counterpart. However, this increased stiffness results in a reduction of the fundamental vibration period, subjecting the infilled frame structure to higher seismic demands. Furthermore, the hysteretic dissipative capacity of the infilled frame is greater, with energy dissipation occurring not only through individual components but also through the slip resistance opposed by the border interfaces, driven by cohesive-frictional behaviour. Nevertheless, the cyclical response of infilled frames is generally marked by rapid and substantial degradation in strength and stiffness. This can be attributed primarily to the brittle behaviour of masonry infills and the cessation of interface contributions when large displacements are reached.

Over the years, numerous researchers and engineers have delved into the study of this construction type, debating whether the presence of infills may be beneficial or detrimental. As emphasised in (Crisafulli, 1997), the often observed poor response of infilled frames to seismic events can be attributed to the irregular distribution of masonry infills. Indeed, irregular distributions of infills, whether in the horizontal plan or vertically, may lead to detrimental torsional vibration modes and give rise to the so-called soft-storey mechanisms (an example of soft-story mechanism activation is given in the post-earthquake damage depicted in Figure 23). Beyond the overall distribution within the building, the presence of openings - whether for windows, doors, or the passage of pipes - introduces structural irregularities, compromising the overall strength. This can lead to unexpected failures in frame elements, as the short-column phenomenon, which manifests following an increase of shear forces within the column at the locations of openings (typical phenomenon with ribbon windows).

The response of Infilled Frame structures is affected by a number of variables, as highlighted by Dawe et al., /2001). These factors include mechanical parameters and geometric features of the components (such as masonry, beams, columns, and eventual connections). Constructive techniques and interface conditions, including bond tensile strength, cohesion, friction angle, and the possible presence of gaps, also have a great contribution. As per Dhanasekar et al. (1985), the overall distribution of forces within the frame and infill under seismic action, especially the maximum force borne by the frame, is strongly influenced by the relative stiffness of the components. Moreover, the research conducted by Dolsek and Fajfar (2008) and Zarnic et al., (2001), emphasise the critical role of the strength properties of masonry in significantly impacting the overall response.

Figure 23 Soft-story mechanism in a masonry-infilled reinforced concrete building – Syria and Turkey earthquake, 2023 (ReLUIS and Eucentre, 2023)

2.4.2 Monotonic response

When subjected to monotonic loading (Figure 24a), an infilled frame structure typically undergoes four distinct phases (Crisafulli, 1997). Initially, the structure behaves monolithically, owing to the bond strength of interfaces. Maximum stresses concentrate at the four corners, with the panel's centre characterised by an approximately pure shear stress state (Figure 24b). As horizontal load and displacement increase, a gradual detachment of the infill from the frame occurs due to tensile-shear failure of the cohesive-frictional interfaces (Figure 24c). According to Esteva (1966), this separation happens between 0.01% and 0.3% of lateral drift, highly dependent on boundary interface characteristics. Generally the separation point does not affect the maximum strength attained, but only the overall stiffness decay at the first phase (Klingner and Bertero, 1976). After the separation (Figure 24d), stresses become zero on the detached corners and increase on the compressed ones, leading to the formation of a compressive strut along the compressed diagonal. Therefore, the infilled frame behaves as a braced frame with a single diagonal active. In the compressed corners, both principal stresses are compressive, while in the middle, tensile stress occurs in the perpendicular direction, ranging from 7 to 10 times lower than the compressive one (Crisafulli, 1997).

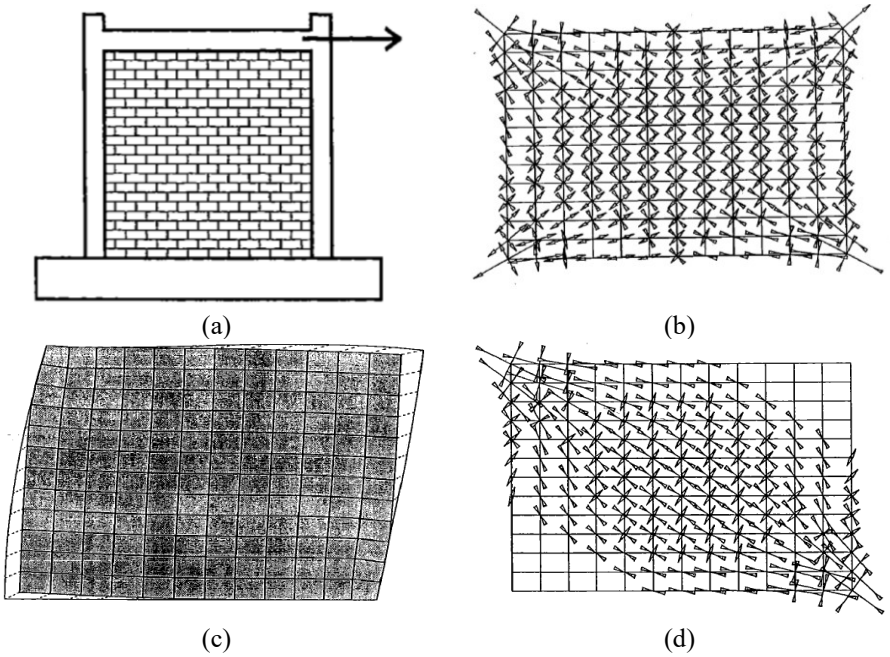

Figure 24 (a) Infilled frame subjected to in-plane monotonic loading; (b) principal stress distribution before frame-infill detachment; (c) frame-infill detachment; (d) principal stress distribution after frame-infill detachment and development of diagonal compressive strut (Crisafulli, 1997)

As the lateral force increases, a further separation between infill and frame may occur, accompanied by masonry cracking, leading to a gradual reduction in stiffness until the maximum shear strength is attained. Beyond this peak, the response is primarily governed by the frame. The features of the softening branch depend on the failure mode of infilled frames. Weak panels typically exhibit a smoother strength decrease (Comitè Euro-International du Béton, 1994), whereas stronger panels tend to have a steeper softening branch (Schuller et al., 1994).

The response of infilled frames is significantly influenced by the characteristics of the infill material but also its level of confinement. To illustrate this, Figure 25 presents several experimental load-displacement curves extracted from a study conducted by (Mehrabi et al., 1996), where specimens of both bare-frames and infilled-frames were tested. The analysed infilled-frame specimens were characterised by different infill typologies, with specimens 2 and 8 featuring hollow brick masonry (denoted as “weak infill”), and specimens 3 and 9 employing solid brick masonry (denoted as “strong infill”). Additionally, the specimens were subjected to distinct vertical load distributions; specimens 2 and 3 had loads applied exclusively on the top of the columns, while in specimens 8 and 9, one-third of the total load was applied on the top beam, with the remaining portion distributed on the columns. This variation in infill type and load distribution is observed to impact not only the response in terms of

maximum strength and stiffness but also the overall shape of the curves. Furthermore, the difference in the responses compared to the bare frame is evident.

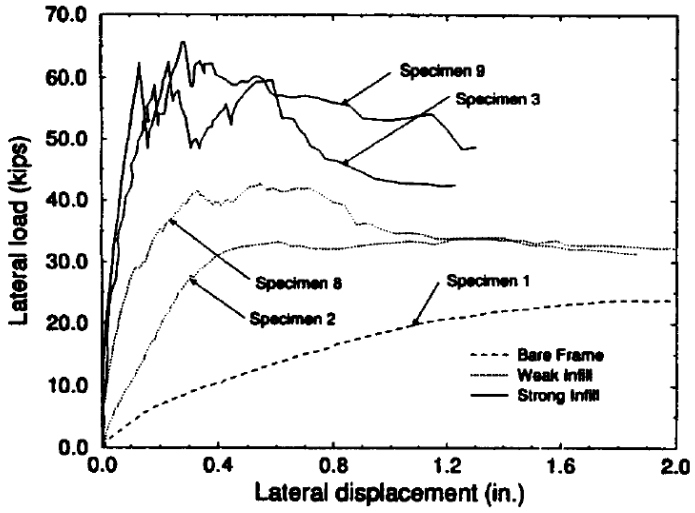

Figure 25 Load-displacement curves for monotonically laterally loaded specimens (Mehrabi et al., 1996)

The typical failure modes of masonry-infilled frames are illustrated in Figure 26 and can be categorised into five distinct typologies (El-Dakhakhni et al., 2003):

1. Corner Crushing Mode (Figure 26a): Involves the crushing failure in at least one of the loaded corners, typically associated with weak infills surrounded by a frame with strong members and weak joints.
2. Sliding Shear Mode (Figure 26b): Characterised by the development of a horizontal sliding crack through bed joints, often related to infills featuring weak mortar bed joints and a strong frame.
3. Diagonal Compression Mode (Figure 26c): Depicts the crushing failure of the infill within its central region, associated with slender infills, where failure results from the out-of-plane buckling of the infill.
4. Diagonal Cracking Mode (Figure 26d): Represents the development of a crack along the compressed diagonal, usually linked to a weak frame or a frame with weak beam-column joints and strong members infilled with a rather strong infill.
5. Frame Failure Mode (Figure 26e): Involves plastic hinges in the members or in the beam-column connections, related to a weak frame or a frame with weak beam-column joints and strong members infilled with a rather strong infill.

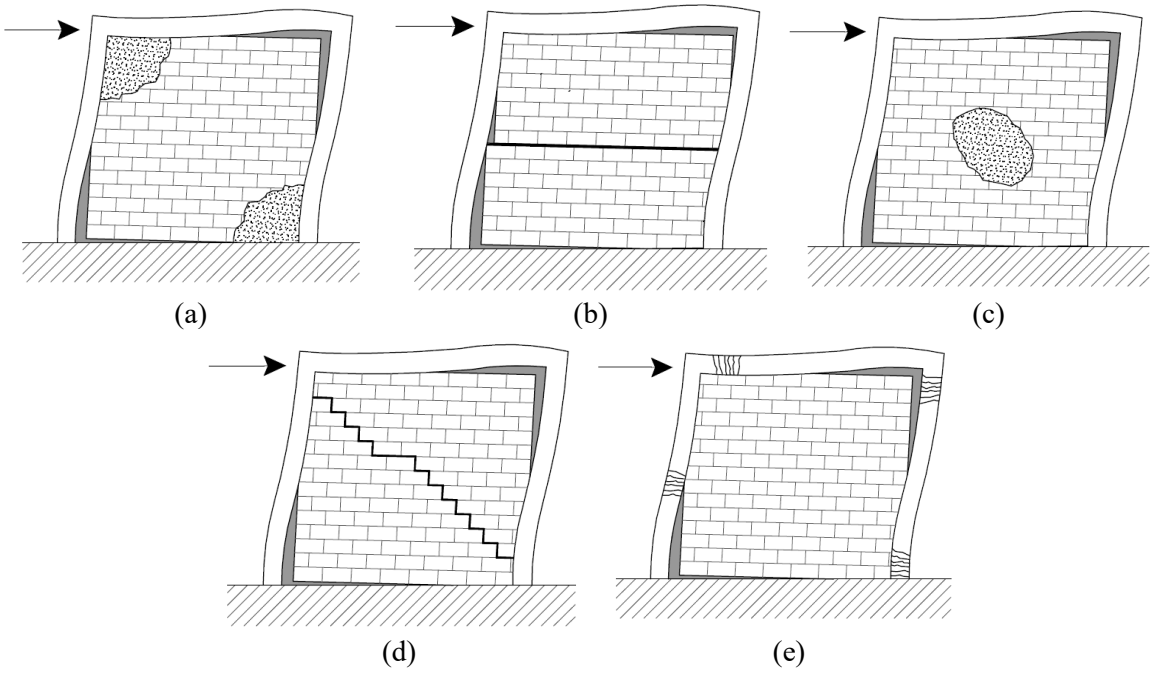

Figure 26 Different failure mode of masonry-infilled frames: a) corner crushing; b) shear sliding; c) diagonal compression; d) diagonal cracking; e) frame failure (taken from El-Dakhakhni et al., 2003)

According to (Comitè Euro-International du Béton, 1996), only the first two infill failure modes are of practical importance, since the third failure mode may occur only with high and uncommon slenderness ratios, leading to out-of-plane buckling failure due to in-plane loading, while the diagonal cracking should not be considered an ultimate failure mode since the infill can still carry additional load after the development of cracking. Frame failure is particularly important in existing structures, often characterised by frame weakness (Asteris et al., 2011). The diagonal strut configuration may vary throughout the application of the action. Indeed, although initially the resultant force points towards the corner of the beam-column joint, it may then move, causing substantial increases in force magnitude on the members. It is finally emphasised that infilled frame response could often result from the combination of multiple failure modes developing subsequently or simultaneously (Crisafulli, 1997).

2.4.3 Cyclic response

The dissipation capacity of infilled frames typically is significantly higher than that of bare frames, primarily attributed to the progressive cracking of the masonry infill and, notably in the initial phases, to the frictional resistance at the interfaces. However, hysteresis loops exhibit pronounced pinching effects owing to the detachment at the frame-infill borders and the opening-closure of cracks in masonry and reinforced concrete members.

Under cyclic loading conditions, infilled-frames manifest significant stiffness degradation, as depicted in Figure 27, taken from (Crisafulli, 1997). In this figure, the author analysed stiffness degradation based on findings from various researchers (Sánchez et al., 1991; Valiasis and Stylianidis, 1989; Zarnic and Tomazevic, 1988) who conducted tests on masonry infilled RC frames. Stiffness decay was assessed as the ratio of K_S, secant stiffness between two consecutive peaks, to K_0, the initial stiffness (evaluated at a drift of 0.05%, approximated as the frame-infill separation point). Despite the authors used different masonries, the decay curves are similar and characterised by a rapid decrease in stiffness at low displacements. For a story drift of 1%, the secant stiffness is approximately ten times smaller than the initial value.

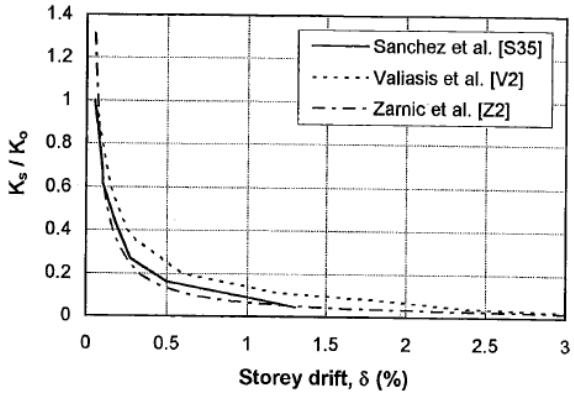

Figure 27 Stiffness degradation against storey drift; image taken from (Crisafulli, 1997) and based on the results of (Sánchez et al., 1991; Valiasis and Stylianidis, 1989; Zarnic and Tomazevic, 1988)

Cyclic loading conditions can also result in a significant degradation in terms of strength. In the study conducted by (Stylianidis, 1988), two reversal cycles of progressively increasing displacements were applied to two specimens, with and without the application of vertical load. The strength loss in the second cycles relative to the first cycles was approximately 16% and 12% for the cases with and without vertical load, respectively. Figure 28 depicts the cyclic curve for one of the specimens.

Several authors have experimentally investigated the loss of strength in infilled frames subjected to cyclic loading (Comitè Euro-International du Béton, 1994; Zarnic and Tomazevic, 1988). However, a general consensus on how to estimate strength degradation in infilled frames has not been reached, highlighting the need for further research to better predict the actual envelope in the softening branch (Crisafulli, 1997).

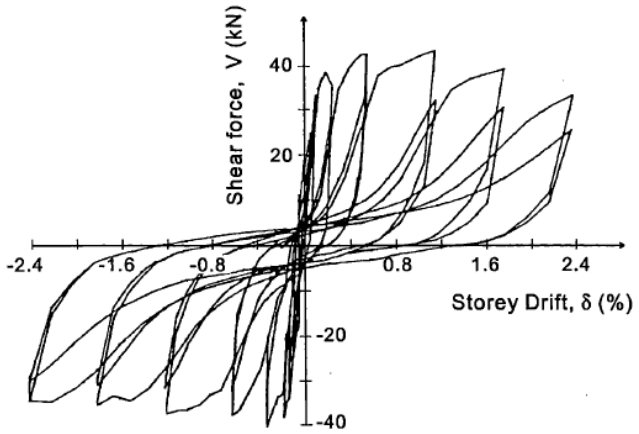

Figure 28 Shear force – storey drift experimental curve (Stylianidis, 1988)

2.4.4 Effects of openings on the behaviour of masonry-infilled frames

Masonry infills may present openings for functional and architectural purposes, introducing a notable decrease in stiffness, ultimate strength, and energy dissipation capacity. The presence of openings in infill walls introduces considerable uncertainty in seismic assessments, contributing to structural irregularities that adversely affect the seismic response. Additionally, the presence of openings can accelerate out-of-plane phenomena, preventing the development of arching mechanisms observed in solid infill walls. Thus, the presence of openings in infilled framed structures should be accurately evaluated.

In presence of small openings, a single diagonal compressive strut may still develop, while with larger openings the stress state generally becomes more complex. Typically, cracks initiate at the corners of the openings and propagate towards the compressed corners. The overall crack pattern is mainly influenced by the position and size of the openings (Mosalam et al., 1997).

The influence of openings has been evaluated by many researchers, by furnishing several suggestions about the assessment of strength and stiffness reduction resulting from their presence (Asteris et al., 2012, 2016; Decanini et al., 2014; Demetrios and Karayannis, 2007). The key parameters influencing the overall response are the dimensions and positions of the openings, along with the potential reinforcement at the edges (such as lintels or steel bars). According to (Decanini et al., 2014), the presence of reinforcing elements can be particularly beneficial, minimising the opening effects. Indeed, the impact of opening size on reduction diminishes with an increasing presence of reinforcements.

2.5 Modelling of Infilled-Frame structures

Essentially, there are two main approaches for modelling of infilled-frame structures, micro-models and macro-models. On one hand, sophisticated micro-models, implemented through finite elements, can accurately represent the complex interaction among the frame, infill, and boundary interfaces. When correctly implemented, these models can simulate the behaviour of infilled frames with high fidelity. However, due to their inherent complexity, these models demand a substantial amount of information and, if not developed meticulously, may yield inaccurate results (Shing and Mehrabi, 2002). On the other hand, simplified macro-models, which are more computationally efficient, use a reduced number of elements to capture the global response of masonry infills without representing local complex phenomena. These models are formulated based on observations derived from actual experimental responses, recognising that, under in-plane horizontal loading, the compressive path in the masonry panel predominantly follows its diagonal. Macro-models are often calibrated though the employment of refined micro-models. Reviews of various proposed macro-models can be found in (Asteris et al., 2011; Moretti, 2015).

2.5.1 Simplified modelling approaches

In the early 1950s, pioneering experimental investigations into the in-plane response of infilled frame structures were conducted at the Building Research Station in Watford, revealing the inherent complexity of the issue (Thomas, 1953; Wood, 1958). Polyakov (1960) was the first to suggest considering the effect of infill panels through diagonal bracings.

Subsequently, Holmes, (1961) suggested employing a pin-jointed diagonal strut composed of the same material as the infill, with a width equivalent (denoted as w) to 1/3 of the diagonal length of the infill (denoted as d), without accounting for the actual relative stiffness of the frame and infill. Following a series of experimental tests, Smith (1962) demonstrated that the ratio w/d typically falls between 0.10 and 0.25. Further experimental work in the latter half of the 1960s (Smith, 1967, 1966; Smith and Carter, 1969) led to the establishment of a relationship between the strut width and frame-infill contact length. This was achieved through the derivation of an equivalent width (denoted as λ_h), which is a function of the relative stiffness of the frame and infill:

$$\lambda_h = h \sqrt[4]{\frac{E_w t_w \sin 2\theta}{4EIh_w}} \tag{1}$$

where E_w is the Young's modulus of the masonry panel, EI is the flexural stiffness of the columns, t_w is the thickness of the panel, h is the height of the column, h_w is the height of the panel and θ is the angle subtended by the diagonal and the horizontal:

$$\theta = \tan^{-1}\left(\frac{h_w}{L_w}\right) \tag{2}$$

where L_w is the length of the panel. The involved parameters are depicted in Figure 29.

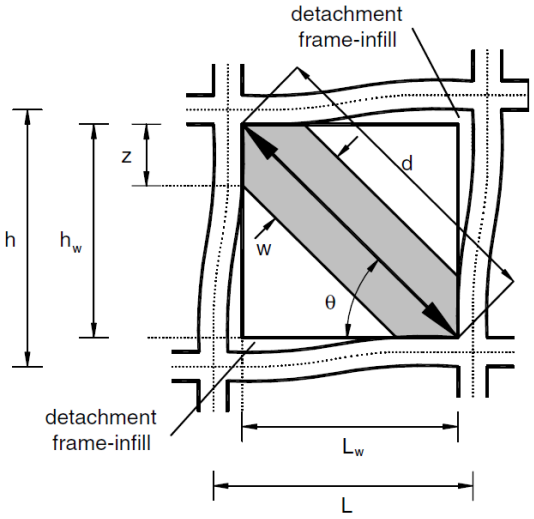

Figure 29 Geometrical parameters characterising masonry infilled frames (Asteris et al., 2011)

Many authors proposed several correlations to calculate the width of the equivalent strut as a function of diagonal length and equivalent width. Mainstone (1974) and Mainstone and Weeks (1970), on the basis of experimental and analytical results, proposed the relation (3), which was also included in the American codes (FEMA 274, 1974; FEMA 306, 1999). Liauw and Kwan (1984) also proposed a semiempirical expression, given by the relation (4), considering the adoption of angle θ equal to 25° and 50°, common values in engineering practice. Paulay and Pristley (1992) suggested to consider a conservative ratio w/d equal to 1/4.

$$\frac{w}{d} = 0.175\,\lambda_h^{-0.4} \tag{3}$$

$$\frac{w}{d} = \frac{0.95\,\sin 2\theta}{2\sqrt{\lambda_h}} \tag{4}$$

Single-strut models, while effective in capturing the overall response of infilled frames, often do not adequately capture the actual distribution of bending moments and shearing forces within the frame

members. To address this limitation, more sophisticated macro-models featuring multiple struts have been developed.

A notable contribution in this direction was made by Thiruvengadam (1985), who introduced a model that integrates a moment-resisting frame with numerous pin-jointed diagonal and vertical struts. Figure 30 illustrates the model both before and after the detachment between the frame and infill. This model, recognised for its comprehensive representation, was adopted for the evaluation of infilled frames with openings within the FEMA 356 (2000) guidelines.

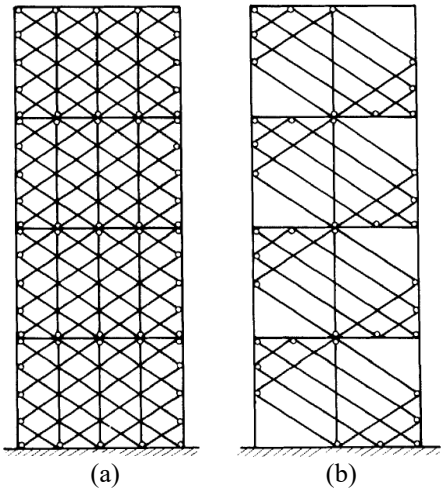

Figure 30 Modelling of frames through multiple struts through Thiruvengadam model (Thiruvengadam, 1985): (a) before frame-infill separation; (b) after frame-infill separation

Chrysostomou (1991) and Chrysostomou et al. (2002) proposed a model featuring six compression-only diagonal struts that are active only when compressed (Figure 31), with the aim of analysing also the cyclic response. The off-diagonal members were strategically positioned at critical locations along the frame members, associated with the development of plastic hinges.

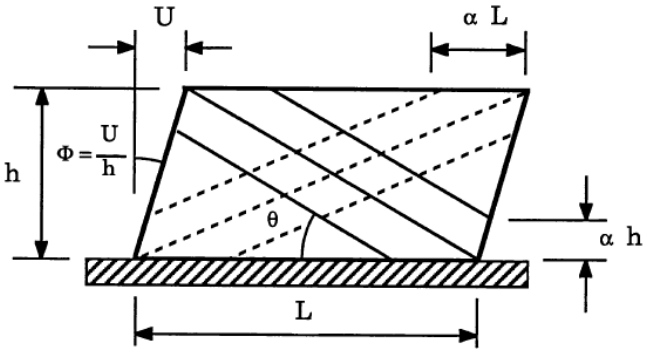

Figure 31 Six-strut model for masonry infilled frames (Chrysostomou, 1991)

A similar model was proposed in (El-Dakhakhni, 2000; El-Dakhakhni et al., 2003), given by a six compression-only diagonal struts (Figure 32) for the modelling of concrete masonry steel infilled frames, characterised by a different evaluation of the contact lengths on columns and beams.

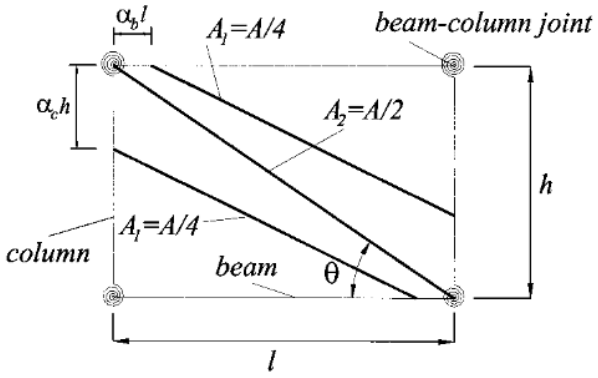

Figure 32 Proposed concrete masonry-infilled steel frame model (El-Dakhakhni et al., 2003) (only the struts active in one direction are represented)

Crisafulli and Carr (2007) proposed a four-node panel element, by considering separately its compressive and shear behaviour, using two compressive struts and one shear spring per direction respectively. This configuration allows to properly consider the strength of the masonry when failure is expected through shear sliding or diagonal cracking.

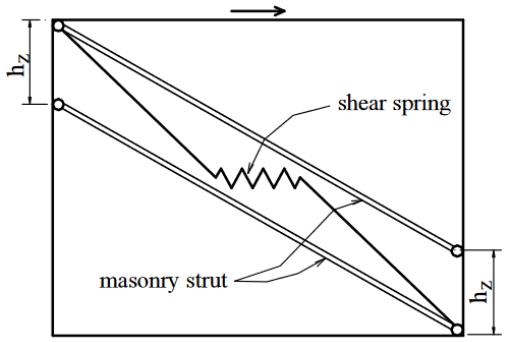

Figure 33 Multistrut model proposed by Crisafulli and Carr (2007; only the struts and the shear spring active in one direction are represented)

Crisafulli (1997) highlighted that the distribution of forces within the frame members can significantly vary with the macro-model considered, after comparing the monotonic response of a single-strut, two-strut, and three-strut models, with a refined finite element model serving as a benchmark (Figure 34a). Despite similarities in lateral stiffness, the induced actions on the surrounding frame varied significantly

(Figure 34b). The single-strut model, characterised by a truss mechanism, generally led to an underestimation of bending moments with the respect of FEM model. In contrast, two-strut models tended to slightly overestimate the actions. The three-strut model provided the best approximation.

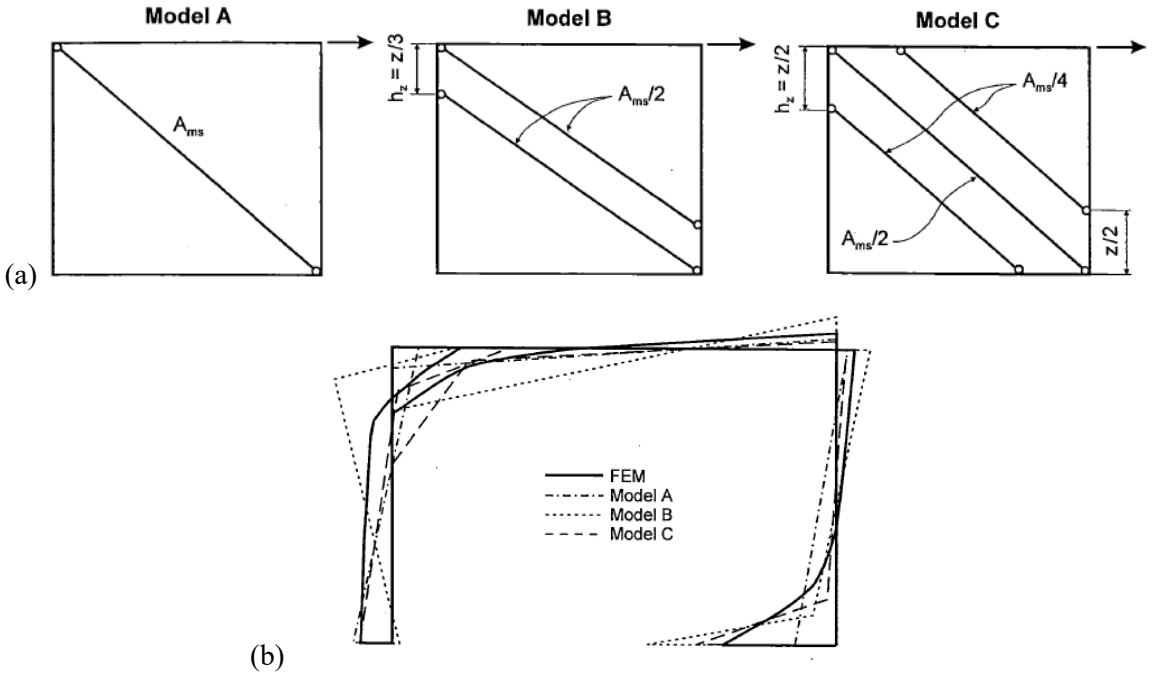

Figure 34 Comparison among different strut models in (Crisafulli, 1997): (a) representations of the models and (b) comparison of the bending moments diagrams

2.5.2 Advanced modelling approaches

Advanced modelling approaches are conceived to represent the local phenomena that may characterise the behaviour of infilled frames subjected to in-plane lateral loading, such as cracking and crushing of the masonry, and ever-changing contact interactions at the interfaces between frame and infill. This strategy necessitates the precise definition of three distinct elements: the masonry infill, the surrounding frame, and the border interfaces essential for simulating the contact interactions between the frame and infill.

Generally, the modelling approaches applicable to unreinforced masonry structures can be extended for the representation of masonry infills. In a macro-scale approach, the masonry material can be conceptualized as an isotropic and homogeneous medium, defined by specific stress-strain relationship and failure criterion. Various criteria, such as the Von-Mises criterion with tension cut-off (Page, 1992) or the Drucker-Prager criterion (Mosalam et al., 1993), have been utilised. Masonry infills may also be meticulously modelled through a micro-scale approach, wherein bricks and mortar layers are

represented by continuum elements, separated by interface contact elements. Some examples of micro-scale modelling of infills were provided in (Ali and Page, 1987; Mohyeddin et al., 2013; Mosalam et al., 1993, 1993; Page, 1992). Ultimately, the meso-scale approach (or simplified micro-scale method), presents a compromise in balancing accuracy and computational efficiency. This method is characterised by the incorporation of interface contact elements, allowing for the specific consideration of mortar layers and mortar-brick interfaces. This approach was extensively used for the modelling of masonry infills, as evidenced by studies conducted in (Chen and Liu, 2015; Dhir et al., 2021; Di Trapani et al., 2022; Kareem et al., 2022; Koutromanos et al., 2011; Mehrabi and Shing, 1997, 1994; Penava et al., 2016; Xavier, 2015).

The modelling of the surrounding frame can be generally implemented through two approaches: employing beam elements, as demonstrated in studies such as (Chen and Liu, 2015; King and Pandey, 1978; Mallick and Severn, 1967), or utilising continuum 2D or 3D elements, as illustrated in research conducted by (Dhir et al., 2021; Di Trapani et al., 2022; Kareem et al., 2022; Koutromanos et al., 2011; Mehrabi and Shing, 1997, 1994; Mohyeddin et al., 2013; Mosalam et al., 1993; Penava et al., 2016). Regarding the use of beam elements, capturing the inelastic response can be achieved through either lumped or diffuse plasticity.

Interface elements play a crucial role in simulating interactions such as separation and sliding between the frame and infill. Accurately representing these local phenomena is essential for a realistic depiction of the overall behaviour. A first effort to model interfaces was undertaken by Mallick and Severn (1967) who introduced an iterative procedure for calculating contact forces within a finite element model, specifically addressing areas where interfaces were closed, thus where frames and infills were in contact. Subsequently, authors such as Dawe and Yong (1985) and King and Pandey (1978), proposed a tie-link connection (depicted in Figure 35a) between the frame and infill. In this configuration, the nodes of the panel and frame are designed to either remain connected or separate based on specific conditions. The connection element withstands compressive and shear forces but does not provide resistance against tensile forces.

However, the typical approach for the modelling of the behaviour of frame-infill interfaces involves the use of interface contact elements. These elements are characterised by the development of shear and normal stresses between the two surfaces (as illustrated in Figure 35b). The relationship between traction and relative displacement can be defined using various constitutive laws, typically based on Coulomb theory, for which relative sliding between two bodies in contact along plane surfaces initiates when the shear force parallel to the plane reaches a critical value proportional to the normal force.

Moreover, if the interface element experiences a tensile stress exceeding the bond tensile strength, separation between the surfaces may occur. An important requirement for these elements is to ensure the impenetrability between the frame and infill. Typically, a finite yet high normal stiffness is prescribed, allowing for a small but negligible penetration between the bodies during the elastic phase (Mosalam et al., 1993). As highlighted by Crisafulli et al. (2000), there is insufficient experimental evidence to adequately characterise the shear bond strength and tensile bond strength of interface elements.

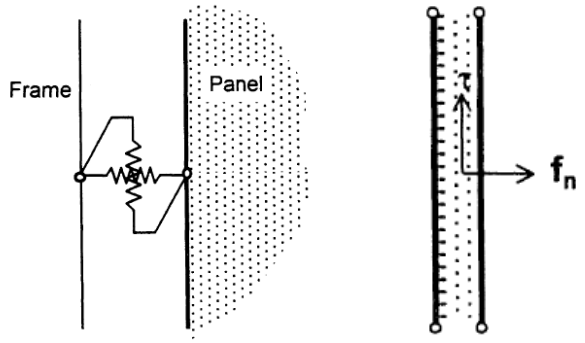

Figure 35 (a) Tie-link element and (b) interface element for the modelling of panel-frame interfaces (taken from Crisafulli et al., 2000)

2.5.3 Evaluation of openings presence

Real reinforced concrete infilled framed buildings could present frames without infills, frames with solid infills, and frames with partial infill presence due to openings, which generally have a detrimental impact on the overall performance. Neglecting openings can result in an unrealistic and generally unsafe assessment of the seismic response of infilled framed buildings.

The openings are frequently overlooked in the analytical assessment of masonry infilled framed structures, primarily due to the absence of a simplified and comprehensive model capable of simulating their effects (Kurmi and Haldar, 2022). Indeed, although the behaviour of solid infilled frames has been extensively studied, those with openings have not received comparable attention. Various analytical methods have been proposed; however, according to Chen and Liu (2015), their effectiveness remains inadequately examined.

Micro-model approaches offer a direct means to model openings, since they are directly modellable with their actual geometries. Among macro-model approaches, the multi-strut model proposed by Thiruvengadam (1985; Figure 30) explicitly accounts for openings geometry, although the evaluation

of strut characteristics such as position and width is relatively complex (Decanini et al., 2014; Kurmi and Haldar, 2022). American codes, including (ASCE/SEI 41-13, 2013; ASCE/SEI 41-17, 2017; FEMA 356, 2000), recommend this approach for the modelling of openings.

The second macro-model approach involves the application of reductive coefficients to modify the width of the strut within a single equivalent strut modelling of infills. Numerous authors have proposed different reduction factors to assess either the decrease in strength (Nwofor, 2012; Tasnimi and Mohebkhah, 2011) or stiffness (Asteris et al., 2012; Imai, 1989; Mondal and Jain, 2008; Polyakov, 1960; Sachanski, 1960) or both strength and stiffness (Al-Chaar et al., 2002; Chen and Liu, 2015; Decanini et al., 2014; Durrani and Luo, 1994; Mansouri et al., 2014; Mohammadi and Nikfar, 2013; NZSEE, 2006).

In the presence of small openings, the diagonal compressive strut can still develop; however, with larger and more common openings, the strut mechanism cannot effectively develop (Durrani and Luo, 1994). Consequently, adopting the single-strut approach to assess infilled frames with openings may not accurately represent the actual stress distribution. Therefore, macro-model approaches can provide only an indirect means to account for the overall behaviour of the frame-infill system.

Decanini et al. (2014) demonstrated that the reduction factor can be considered as a unique value for both strength and stiffness degradation. They proposed analytical expressions to assess the reduction factors, as functions of the area and horizontal length of openings. Distinct analytical expressions were provided based on whether openings are entirely surrounded by reinforcements (such as lintels and reinforcement bars) or only partially or not at all. Notably, they observed that in the absence of reinforcements, infills with openings accounting for more than 40% of the gross panel surface can be neglected. For openings with reinforcements, reduction factors are generally not lower than 0.4. Their assessment covered frames with central openings, while other authors, including Chen and Liu (2015) and Mansouri et al. (2014), also considered the influence of eccentric openings in their proposals of reduction factors.

Mallick and Garg (1971) experimentally studied, through a series of tests on infilled steel frames, the influence of the opening position within the infill. They observed that the performance generally deteriorates when the opening is positioned closer to the compressed diagonal. Consequently, they recommend placing window openings in the mid-height region near the vertical edges of the panel and door openings in the centre of the lower half of the panel. The location of openings in the corners should be avoided also according to (Decanini et al., 2014; NBC-201, 1994). Kakaletsis and Karayannis (2007)

conducted experimental studies on the effects of the shape and location of openings in masonry infilled RC frames. They concluded that openings should be situated as close as possible to the edge of the infill, distant from the corners. Larger piers, allowing for a better distribution of cracks, result in higher energy dissipation, particularly through masonry infill cracking. Additionally, strong infills demonstrated superior performance compared to weak infills in terms of strength, stiffness, and energy dissipation capacity, attributed to a more effective distribution of cracking. In a numerical study, Chen and Liu (2015) found that under monotonic loading, the reduction effect is less pronounced when openings are located away from the loaded side compared to cases where openings are toward the compressed column. They also observed that variations in several masonry infill properties do not significantly affect the response, while the relative stiffness between the frame and infill has a noteworthy impact.

2.5.4 Macroelement modelling of infills

An alternative approach to analyse the in-plane response of masonry infilled-frame is provided by the macroelement method proposed in (Caliò and Pantò, 2014). In this approach, the infilled wall is represented using discrete elements proposed by Calio et al. (2012), detailed in Chapter 2.3.3, while the reinforced concrete frame is modelled employing lumped plasticity beam-column elements, allowing plastic hinges to form at different positions along the beam span. The computational cost of this numerical approach is significantly lower compared to nonlinear finite element modelling. Additionally, the adopted strategy offers several advantages over simplified methods where the infill contribution is represented by one or more diagonal struts, whose characterisation may not be straightforward. Moreover, since each discrete element represents the nonlinear behaviour of the corresponding masonry portion, the presence of openings can be easily represented by considering their actual dimensions and positions within the infill, with a suitable mesh discretisation.

The frame element interacts with the masonry panels through nonlinear links distributed along the interfaces of the macro-elements. Each external interface resembles those between masonry panels (see Figure 20a), consisting of n orthogonal and a single longitudinal nonlinear link. For evaluating the nonlinear behaviour of the frame element, it is assumed that plastic hinges can occur in each sub-beam element between two nonlinear links.

Following the implementation presented in (Pantò et al., 2017, 2016; see Figure 20b), which enables the representation of the out-of-plane response within URM structures, this approach was also employed for modelling the out-of-plane response of infilled frame structures, as in (Pantò et al., 2018a, 2018b).

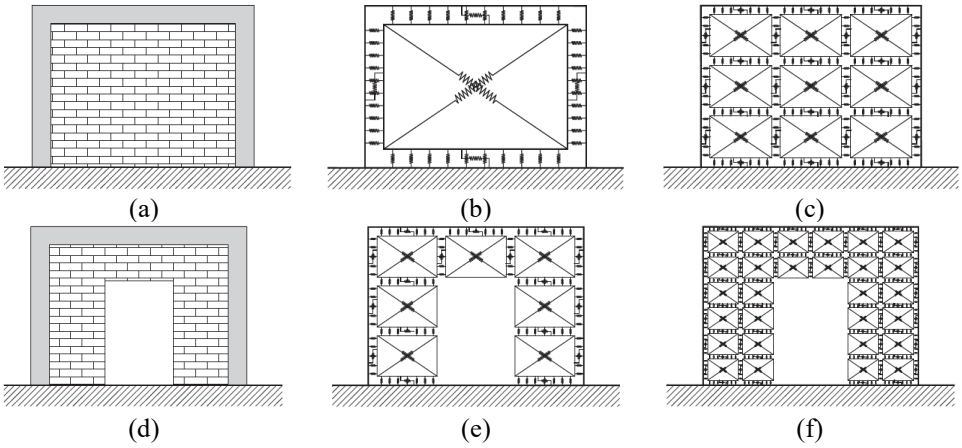

Figure 36 Modelling of infilled frame with and without a central door opening: (a, d) the geometrical layout; (b,e) model corresponding to the basic mesh; (c, f) model corresponding to a more refined mesh resolution (image taken from Caliò and Pantò, 2014)

An application of macroelement utilisation for infilled frame modelling is also presented in (Minga et al., 2020), introduced in Chapter 2.3.3 (refer to Figure 21). In this study, an alternative feature of the macroelement kinematics, specifically developed to enable the interaction with frames, is tested by simulating an experimental in-plane monotonic pushover test. The utilisation of this macroelement approach within infilled frames is discussed in Chapter 5. Following this, the newly enhanced macroelement will undergo testing against several experimental tests related to masonry-infilled frame structures.

2.6 Summary and conclusions

This chapter has provided a comprehensive overview of the responses exhibited by Unreinforced Masonry (URM) and masonry-infilled frames, accompanied by an examination of the modelling approaches.

The typical responses of masonry wall structures, covering both in-plane and out-of-plane failure modes, have been outlined. Exploring refined modelling approaches, the mesoscale strategy introduced in the works of Macorini and Izzuddin (2011) and Eleni Minga, Macorini, and Izzuddin (2018), and the continuum isotropic masonry material presented by Chisari, Macorini, and Izzuddin (2020) have been presented. Additionally, at a lower scale of refinement, various macroelements have been revisited, encompassing both mono-dimensional and bi-dimensional macroelements. The macroelement featured in the study by E. Minga et al. (2020) has been given particular attention, as it forms the groundwork for the enhanced macroelement that will be presented later.

Subsequently, the typical response of masonry-infilled frames has been reviewed. The complexities of this structural typology have been delineated, considering both monotonic and cyclic responses. In general, masonry-infilled frame structures exhibit a notable increase in stiffness and strength, along with enhanced dissipation capacity, compared to the bare frames. However, under cyclic loading conditions, these structures show significant stiffness and strength degradation, and are typically characterised by pronounced pinching effects due to detachment at frame-infill borders and crack opening-closure in masonry and concrete members. Moreover, the presence of irregularities, including openings, has proven to be strongly detrimental, potentially leading to soft-story mechanisms. In particular, the influence of openings in masonry infill may introduce further complexity, causing a decrease in stiffness, ultimate strength, and energy dissipation.

A comprehensive review of infilled-frame modelling has been undertaken, encompassing both simplified (macro-models) and advanced modelling (micro-models) approaches. While micro-models offer a high level of fidelity, they necessitate substantial information and computational resources. On the other hand, macro-models, comprising single-strut and multi-strut models, offer a computationally efficient means to capture global responses, although without detailed attention to local responses. Furthermore, the evaluation of the effects of openings, which is crucial for the seismic assessment of real infilled frames, is generally not straightforward within the single-strut modelling strategy.

In Chapter 4, two advanced modelling strategies will be examined for simulating the response of infilled frames based on the result of an experimental test. Additionally, the presence of openings will be also assessed. The results derived from these simulations not only provide valuable insights into the global and local responses of infilled frames but also serve as a benchmark for evaluating the enhanced macroelement approach within the infilled-frame analysis framework. The macroelement approach effectively addresses specific limitations associated with both micro-models and macro-models, demonstrating its capacity to provide an accurate representation of the actual seismic response of infilled frames while maintaining high computational efficiency.

CHAPTER 3

MESOSCALE AND MACROSCALE MODELLING FOR CYCLIC ANALYSIS OF URM STRUCTURES

3.1 Introduction

Over recent years, a considerable effort has been devoted to the development of numerical models for the simulation of the seismic response of unreinforced masonry (URM) structures. Accurate models are critical for realistic assessment under earthquake loading, where the response is particularly complex due to masonry anisotropic nature and highly nonlinear behaviour.

In current practice, seismic assessment of existing masonry building structures is generally conducted by performing nonlinear static analysis under increasing lateral loading (pushover analysis). While such an analysis procedure provides a satisfactory estimate of load capacity and global ductility, it does not explicitly allow for the distinctive hysteretic behaviour under cyclic loading conditions, which ultimately determines the actual seismic response up to collapse. The energy dissipated during an earthquake is an important parameter for refined structural design and assessment. It is considered by the Capacity Spectrum Method in ATC-40 (Applied Technology Council, 1996) which requires the evaluation of the equivalent damping factor comprising hysteretic and viscous contributions. The latter is obtained by equating the energy dissipated by the analysed system in a single hysteretic cycle to that of an equivalent linear damped system.

Several authors investigated the accuracy provided by different macroscale modelling strategies for URM components and structures, where focus was placed mainly on the load-displacement characteristics under monotonic loading up to collapse. Extensive comparative studies were carried out in (Cattari et al., 2019, 2017) and (ReLUIS, 2020), where differences in the capacity curves provided

by different nonlinear modelling strategies were highlighted. In this previous research, URM structures comprising individual wall panels and a realistic 3D building were analysed by several software packages utilising different macroscale models for masonry, namely (i) the Equivalent Frame (EF) approach with different nonlinear material constitutive relationships for masonry, (ii) 2D macroelement models and (iii) nonlinear continuum finite element (FE) models. (Calderoni et al., 2015) investigated the use of the EF approach with particular attention to the influence of the geometric discretisation of masonry perforated walls and showed how the capacity curves significantly vary depending on the adopted numerical implementation of the method. (De Falco et al., 2017) studied the monotonic nonlinear response of masonry façade walls by varying the material properties within a probabilistic framework and showed how different modelling hypotheses significantly affect the probability of failure. In (Zizi et al., 2022), a comparison among three different material models (i.e. double Drucker Prager (Code_Aster, 2013; Facchini et al., 2017), total strain crack (Midas FEA, 2016; Selby and Vecchio, 1993) and concrete damage plasticity (ABAQUS Inc, 2014; Lee and Fenves, 1998) models) for 3D continuum macroscale simulation of masonry walls was carried out. In this study, numerical comparisons under monotonic loading were also performed to evaluate the suitability of the material property ranges provided by Italian building code (MIT, 2019) for various masonry types. The obtained numerical monotonic curves were compared against experimental results in the literature showing that the application of recommended masonry material properties may lead to unrealistic predictions, as significant discrepancies between the numerical and experimental curves were observed for material properties within the indicated ranges of variation. (Cattari et al., 2021) explored the potential of using macroscale continuum FE descriptions with a concrete damaged plasticity material model (Lee and Fenves, 1998) for masonry and the EF approach (Lagomarsino et al., 2013) to predict the local and global response of masonry panels and of a representative masonry building façade subjected to horizontal monotonic loading. A cross-consistent calibration procedure was also proposed, where the material and geometrical characteristics of the equivalent frame models were calibrated based on the numerical predictions provided the baseline continuum FE models. The nonlinear response of unreinforced masonry wall structures was investigated in (Bomben et al., 2022) using three 1D elasto-plastic models implemented in commercial software for structural assessment. It was shown that the different models provide close monotonic predictions but very different responses under cyclic loading conditions.

As pointed out before, most of previous numerical research investigated the monotonic behaviour of masonry wall structures under in-plane horizontal loading disregarding energy dissipation characteristics, which ultimately determine the response of real structures under earthquake loading. Importantly, it was found that different models for URM may lead to quite different predictions, and

the use of sophisticated model does not necessarily imply more accurate results. More refined models typically require several materials parameters, potentially not all quantifiable through standard material tests. Since numerical predictions are greatly affected by the specific selection of the material properties for URM, the sensitivity of the global response to less known material parameters should be properly assessed, before considering any refined model as a reference.

In the present chapter the ability of different advanced modelling approaches to reproduce the hysteretic behaviour of masonry wall components and structures is investigated, by evaluating the nonlinear response under cyclic loading conditions including the dissipated energy. FE models based on two different scales of representation for masonry are compared: detailed mesoscale models (Macorini and Izzuddin, 2011) accounting for masonry bond explicitly by a separate representation of masonry units and mortar joints, and continuum macroscale models, in which masonry is assumed as a uniform and isotropic material, adopting a damage-plasticity constitutive model for masonry (Chisari et al., 2020). The accuracy guaranteed by the two alternative modelling strategies is assessed through comparisons against experimental tests from the literature. Emphasis is given to the definition of the material properties required by the two modelling approaches on the basis of the results from standard material tests. Extensive parametric studies are conducted by varying the most critical and uncertain parameters within realistic ranges, in order the evaluate their influence on the global response. Final considerations concerning the ease of calibration, the accuracy of the models through either standard or refined calibrations, and the computational cost are outlined together with possible links between material calibration for the adopted macroscale and mesoscale masonry models.

3.2 Experimental tests

The cyclic tests on brick-masonry panels under in-plane horizontal loading performed at the Joint Research Centre in Ispra (Anthoine et al., 1995) are herein considered. Two-wythes thick panels, built with alternate courses of stretchers and headers (English bond), were examined. The specimens are characterised by different aspect ratios: a squat panel (“Short Panel”) and a slender wall (“Tall Panel”). A detailed study on the masonry material properties of the actual specimens is given in (Binda et al., 1995), where an accurate characterisation of the properties of mortar, bricks and brick-mortar joints is provided (Table 5). The geometric characteristics of the wall specimens are given in Table 6.

In the physical tests, the masonry panels were subjected to an initial vertical load of 150 kN, which was uniformly distributed at the top of the wall by a stiff spreader beam. Subsequently, horizontal forces

were applied under displacement control at the top beam, which was maintained horizontal throughout the analysis. The applied horizontal displacement histories are reported in Figure 37.

Table 5. Material properties for the case studies (Binda et al., 1995)

Property	Source	Symbol	Mean value	
Brick tensile strength (*)	Bending test	$f_{fl,b}$	2.44	MPa
		$f_{t,b}$	1.22	MPa
Brick compression strength	Simple compression test	$f_{c,b}$	26.9	MPa
Mortar compression strength	Simple compression test	$f_{c,m}$	3.31	MPa
Brick secant elastic modulus (**)	Simple compression test	E_b	2515	MPa
Mortar tensile strength	Bending test	$f_{t,m}$	0.58	MPa
Joint tensile strength	Cross-tension test	$f_{t,j}$	0.04	MPa
Joint cohesion	Triplet shear test	c_j	0.23	MPa
Joint coeff. of friction	Triplet shear test	$\tan\varphi_j$	0.58	
Masonry compression strength	Compression test on wallets	$f_{c,M}$	6.2	MPa
Masonry secant elastic modulus (***)	Compression test on wallets	E_M	1491	
Brick nominal dimensions		$h_b \cdot l_b \cdot t_b$	55x120x250	mm
Bed joint nominal thickness		h_m	10	mm
Mortar composition		Hydraulic lime/sand = 1/3 in volume		

(*) A reductive coefficient equal to 0.5 is applied to the flexural strength obtained through bending test, in order to determine brick tensile strength, as suggested in the Eurocode 2 for reinforced concrete structures(EN 1992-1-1, 2004, p. 2); experimental tests performed on the solid clay bricks, described in (Binda et al., 1995), proved the acceptability of the correction.

(**) Average secant modulus obtained from compression tests on bricks in the flatwise, lengthwise, and widthwise orientations, each calculated within the range of 30% to 50% of their respective compressive strengths (Binda et al., 1995).

.(***) Average secant modulus derived from compression tests conducted on 5 prisms, with each secant modulus calculated within the range of 30% to 60% of their corresponding compressive strengths (Binda et al., 1995).

Table 6. Geometric features of the panels

Parameter	Unit	Low panel	High panel
Height	[m]	1.35	2
Length	[m]	1.00	1.00
Thickness	[m]	0.25	0.25
Vertical stress	[MPa]	0.6	0.6
Failure mode		shear – diagonal cracking	flexural

The two walls exhibited distinct failure modes, as evidenced by the different experimental cracking patterns reported by Anthoine et al. (1995). The sketches illustrating the cracking patterns of both walls are presented in Figure 38, where the short wall specimen experienced a predominant diagonal shear cracking accompanied by joint openings at the top and bottom of the wall (Figure 38a), while the tall wall specimen exhibited horizontal cracking due to flexural bending and rocking cyclic behaviour (Figure 38b). The distinct response of the specimens is also evident in the experimental shear-displacement curves (Figure 39). The cycle for the short wall is wider, characterised by both strength and stiffness degradation (Figure 39a). In contrast, the tall panel exhibits the typical flexural S-shaped cycle (Figure 39b) with no observed strength degradation and only a slight stiffness degradation,

although an enlargement of the cycle is observed towards the end of the experiment, probably attributed to the initiation of a diagonal cracking damage.

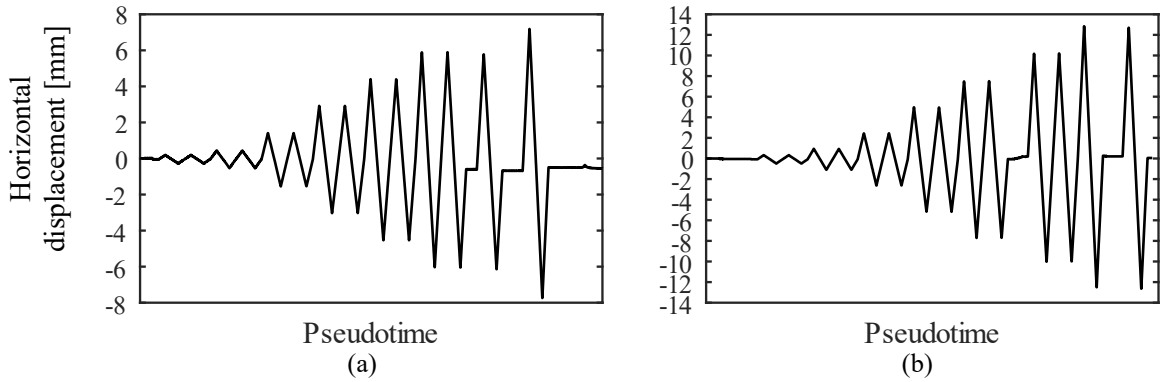

Figure 37. Imposed displacements: a) short panel; b) tall panel

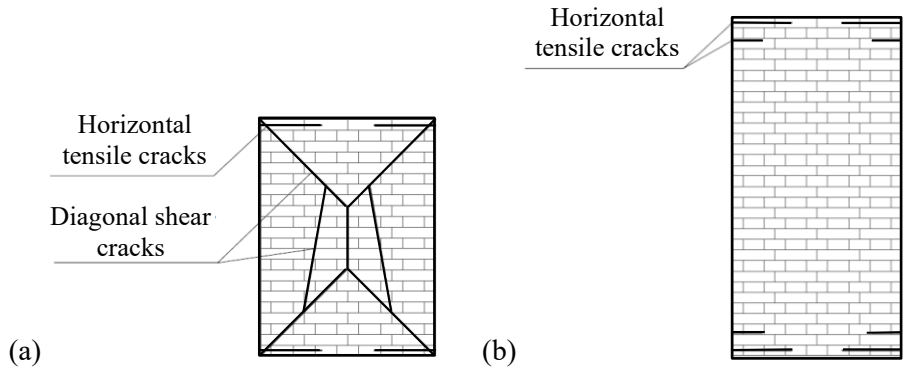

Figure 38. Experimental damage patterns of URM panel specimens tested in (Anthoine et al., 1995): a) short panel; b) tall panel

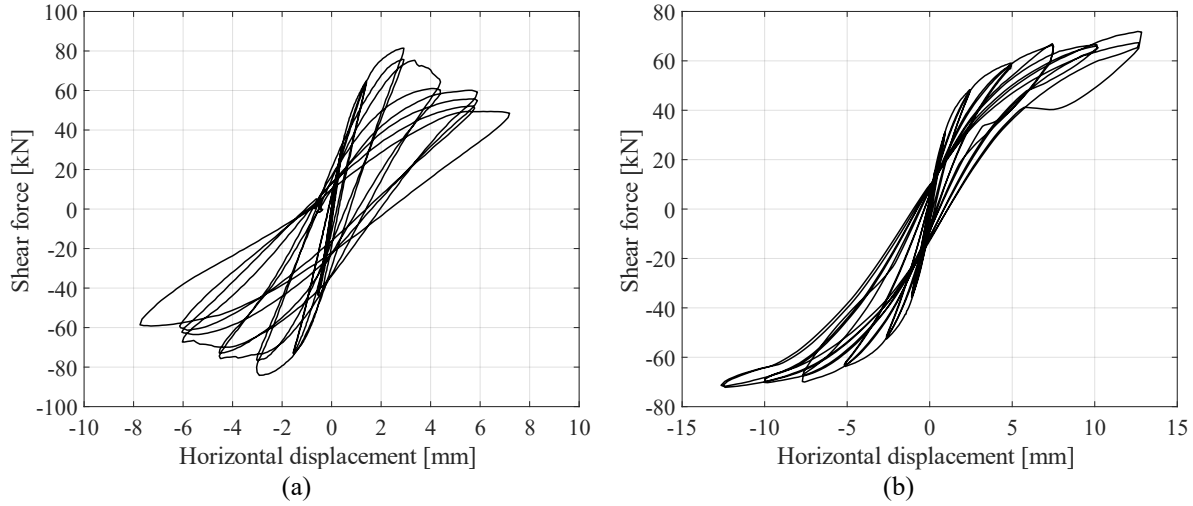

Figure 39 Experimental base shear vs lateral displacement cycles: (a) short panel; (b) tall panel

Furthermore, an entire two-storey perforated wall, which was experimentally tested by Magenes et al. (1995), was also investigated. The façade wall part of full scale two-storey URM building specimen (Figure 40) is named Wall D in (Magenes et al., 1995) and features a regular distribution of openings, with a thickness of 250mm. In the test, Wall D was disconnected from the rest of the building and loaded by vertical loads of 248.4kN and 236.8KN uniformly distributed at to the first and second floor level leading to a precompression of 0.5÷0.6 MPa at the base of the piers. The structure was then subjected to in-plane cyclic loading under displacement control with equal horizontal forces applied at the two floor levels. The resulting displacements at the two floors are reported Figure 41. The two-storey wall is characterised by the same material properties of the single panels (Table 5).

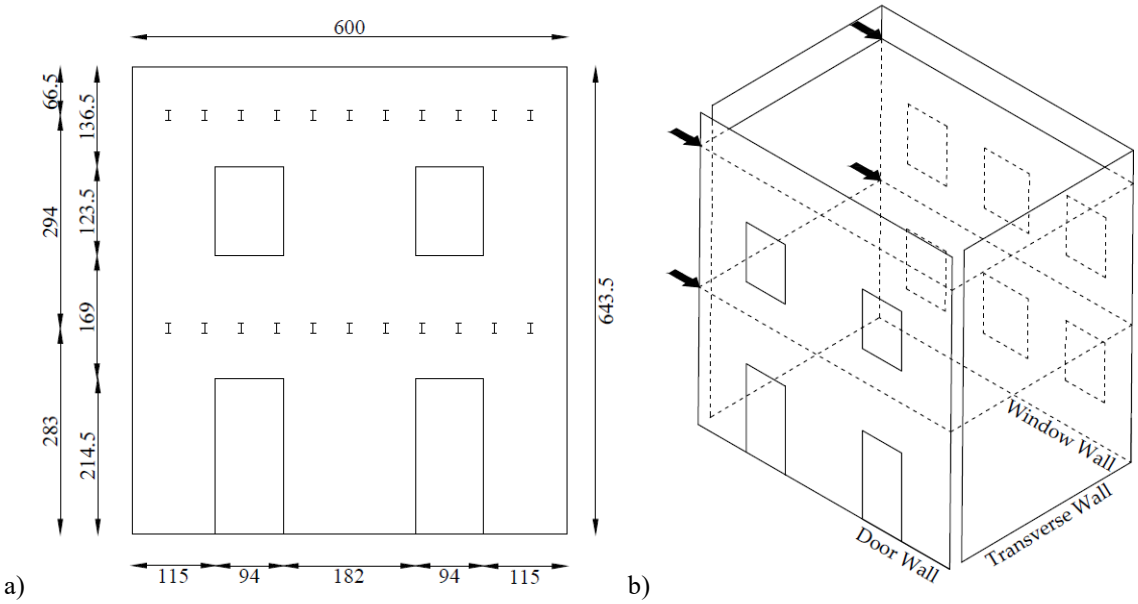

Figure 40 a) Front view of the Door Wall (measurements are in cm); (b) application of the horizontal forces

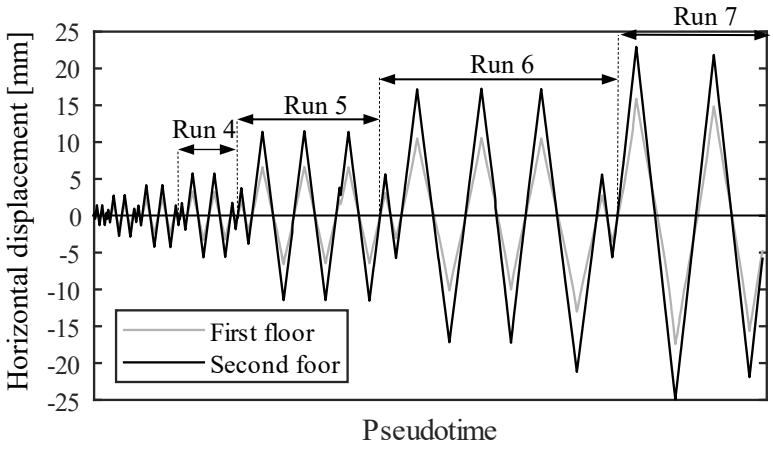

Figure 41 Displacements experimentally measured at the first and second floor of the Wall-D specimen

The progression of damage is depicted in Figure 42. Damage initiates from the spandrels on both floors and with joint openings at the bottom of the piers. Subsequently, it extends involving flexural damage also at the top of the ground-floor piers and on both sides of the lateral first-floor piers. Additionally, increasing damage on the spandrels and shear diagonal cracking on the ground-floor piers are observed, and these are correlated with the widening of the base shear versus first-floor lateral displacement cycle (reported in Figure 43).

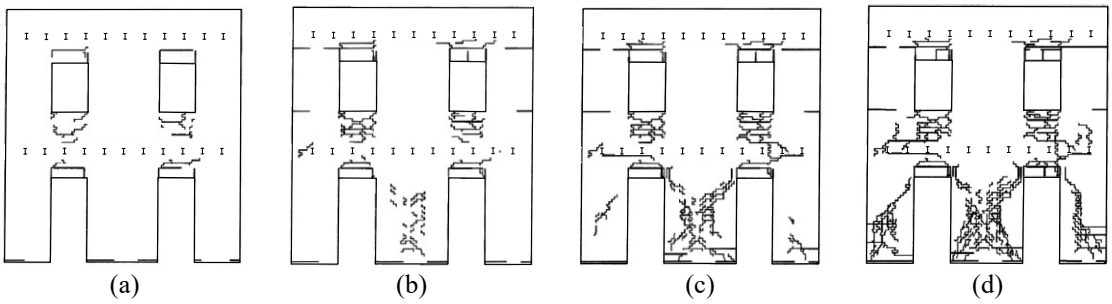

Figure 42 Progression of experimental damage pattern of Wall D: 1) end of run 4 (max. drift 0.10%); 2) end of run 5 (max. drift 0.20%); 3) end of run 6 (max. drift 0.30%); 4) end of run 7 (max. drift 0.40%), from Magenes et al. (1995)

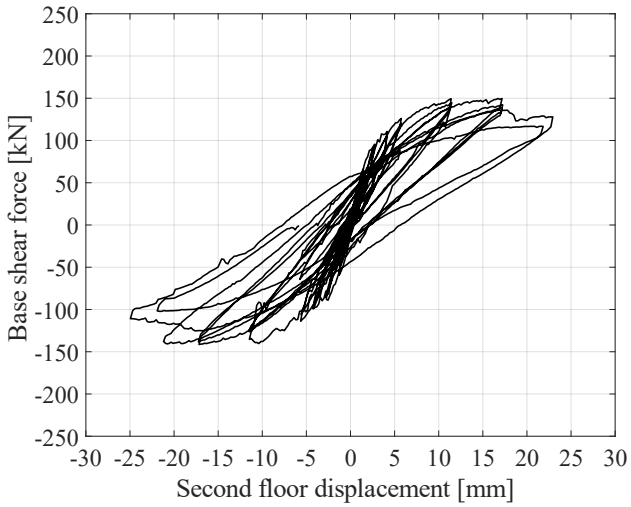

Figure 43 Experimental base shear vs. 2th floor lateral displacement cycle of Wall D

3.3 Mesoscale modelling

In this section, the modelling of the single panels and the two-story façade is presented using the refined mesoscale modelling approach detailed in Chapter 2.3.1. A thorough examination of the material characterisation within the mesoscale framework is conducted. In particular, the elastic stiffness for

both interface and solid elements, along with the mechanical parameters governing the nonlinear interfaces, crucial for the nonlinear response of a mesoscale model, are defined through the results from the physical tests on masonry components (Binda et al., 1995). Moreover, the characterisation includes fracture energy values for the interfaces, which are treated as unknown parameters. Different recommendations from the literature are taken into consideration to assess the sensitivity of the wall response predictions to the variation in these fracture energy values. Furthermore, other uncertainties are taken into account, such as the potential reduction in cohesion in head mortar joints due to mortar shrinkage and the characterisation of fracture energies. As a result, a reference material characterisation and four variants are defined (as outlined in Table 8) and applied in the simulation of both short and tall panels. Finally, based on the panel results, an examination of the perforated wall is conducted, employing a single material characterisation.

3.3.1 Material characterisation

The determination of the normal and tangential stiffnesses of the joint interfaces, respectively denoted as $K_{n,j}$ and $K_{t,j}$, could be approached through elastic considerations by treating the mortar joint as a series of unit-interface-unit springs. In this way, knowing the elastic properties of brick and mortar, $K_{n,j}$ and $K_{t,j}$ would be then determinable. However, as underlined in (Lourenço and Gaetani, 2022), this approach ignores two important aspects. First, the mortar-unit interface is not infinitely rigid but possesses a certain stiffness (or deformability). Second, test on isolated mortar samples might overestimate the actual interface properties, since the real mortar stiffness within the masonry is unknown. For these reasons, stiffnesses can be evaluated as a function of the elastic properties of bricks and masonry at the macroscale, using relations (5) and (6):

$$K_{n,j} = \frac{E_b E_M}{(h_b + h_m)(E_b - E_M)} \tag{5}$$

$$K_{t,j} = \frac{G_b G_M}{(h_b + h_m)(G_b - G_M)} = \frac{K_{n,j}}{2(1+\nu)} \tag{6}$$

where E_b, G_b, and E_M, G_M, represent the normal and tangential elastic modulus for brick and mortar, respectively, h_b denotes the height of the brick and h_m is the thickness of the mortar layers; the subscript “b” refers to brick, “m” to mortar, “M” to masonry, ”j” to mortar joint, “n” to normal direction, “t” to tangential direction. Assuming, then, a common Poisson’s ratio (ν) for both brick and mortar and considering the general linear elastic isotropic relation described in (7), the tangential stiffness can be directly derived from the normal stiffness through (8).

$$E = 2\,G(1+\nu) \tag{7}$$

$$K_{t,j} = \frac{K_{n,j}}{2(1+\nu)} \tag{8}$$

The elastic modulus of masonry E_M and brick E_b are assumed as the initial tangent values, derived from the experimental stress-strain curves reported in (Binda et al., 1995). Specifically, the modulus of masonry is 1980 MPa, and the modulus of brick is 4000 MPa. Additionally, a Poisson's coefficient of 0.2 is considered for both brick and masonry. Elastic stiffnesses of joint interfaces are then calculated using equations (5) and (8) and presented in Table 8, along with other material properties. For brick-brick interfaces, a high value of 10^4 N/mm³ is assigned, both for the normal and tangential directions.

Mechanical parameters of interfaces, including joint tensile strength ($f_{t,j}$), joint cohesion (c_j) and joint coefficient of friction ($\tan \varphi_j$), are experimentally provided for mortar joints and detailed in Table 5. To determine the brick tensile strength ($f_{t,b}$), a corrective factor of 0.5 is applied to the experimental value. This correction is suggested in (Magenes and Calvi, 1997) to account for the indirect evaluation of brick tensile strength through a bending test. Finally, the compression strength is evaluated in a "macroscale" manner, differentiating between horizontal ($f_{c,h}$) and vertical ($f_{c,v}$) interfaces (thus equally considering mortar head joints and internal brick interfaces). For the horizontal interfaces, the compression strength is derived from experimental tests on masonry wallets, while the vertical strength is estimated as the 50% of the value, to account for the orthotropic response of masonry. It is emphasised that in the present context, pertaining to the assessment of URM structures, the differentiation between horizontal and vertical interfaces does not significantly influence the overall response. However, this distinction becomes critical when analysing infilled frame structures (as will be shown in Chapter 4), where the stress state of the masonry infill differs significantly, making the specification of the horizontal compressive strength crucial.

Fracture energies values (referring to mode I, mode II and crushing mode) may represent uncertain parameters within the material calibration. Indeed, as highlighted by Jafari et al. (2022), only a limited number of studies have experimentally characterised the fracture energy of mortar, unit, and masonry under tensile loading. Van der Pluijm (1992, 1993, 1999) experimentally studied the characterisation for mode I ($G_{I,j}$) and mode II ($G_{II,j}$) failures of mortar joints; Table 7 provides the suggested ranges he presented in the research.

Table 7. Mode I and mode II suggested fracture energies values for joint mortar interfaces (energy values expressed in N/mm; c_j in N/mm^2)

Source	Mode I ($G_{I,j}$)		Mode II ($G_{II,j}$)	
	(Van der Pluijm, 1992)	(Van der Pluijm, 1999)	(Van der Pluijm, 1993) (*)	(Van der Pluijm, 1999)
Min	0.005	0.005	0.01	$0.062 \cdot c_j$
Max	0.02	0.035	0.25	$0.147 \cdot c_j$

(*) for c_j between 0.1 and 1.8 N/mm^2

In the present context, to evaluate the sensitivity of the simulations based on their specification, the Mode I and Mode II fracture energies of mortar joint interfaces are assessed by defining a range variation, including a central reference value, a minimum, and a maximum. In particular, the reference value for $G_{I,j}$ is assessed as the average of the values provided in Table 7, resulting in 0.016 N/mm, while $G_{II,j}$ is determined as 10 times higher, as suggested in Jafari et al. (2022), resulting in 0.16 N/mm. The lower and upper range limits are derived from Table 7 by considering the minimum and maximum values of the energies provided.

Regarding the crushing failure energy of masonry ($G_{c,j}$), considered as a whole, scholars such as Lourenço (1996) recommended the use of the parabolic curve proposed by Model Code 90 (provided by relation(9); Comité Euro-International du Béton 1993), originally developed for the modelling of the nonlinear behaviour of concrete in compression:

$$G_{c,j} = 15 + 0.43 \cdot f_{c,M} - 0.0036 \cdot {f_{c,M}}^2 \quad (9)$$

where $f_{c,M}$ represents the compressive strength of masonry, expressed in in N/mm^2, and the crushing energy is given in N/mm.

For the mode I fracture energy of internal brick interfaces ($G_{I,b}$), the following expression is considered, derived from (Lourenço and Gaetani, 2022).

$$G_{I,b} = 0.07 \cdot \ln(1 + 0.17\, f_{c,b}) \quad (10)$$

where $f_{c,b}$ is the brick compression strength.

Finally, four variant characterisations are investigated (refer to Table 8), to address aspects that might introduce uncertainty within a mesoscale modelling framework:

- Variant 1: Head-joints are defined with cohesion and bond strength set to 1/10 of the reference values, aiming to assess potential effects related to mortar shrinkage.

- Variant 2: Mode I and II fracture energies are defined with minimum values of 0.005 and 0.014 N/mm (minimum values of Table 7).
- Variant 3: Mode I and II fracture energies are defined with maximum values of 0.035 and 0.25 N/mm (maximum values of Table 7).
- Variant 4: The stiffness degradation parameter is set to 0.5 instead of 0.1 (the latter considered as reference value), allowing for a higher level of degradation under cyclic actions.

All the interface mechanical parameters, including both reference and variant characterisations, are summarised in Table 8.

Table 8 Reference and variant material characterisations; the variable parameters are reported in shaded cells

Parameter			Symbol	u.o.m.	Ref.	Var. 1	Var. 2	Var. 3	Var. 4
Units elastic parameters	Elastic modulus		E_b	N/mm^2	4000				
	Poisson's coefficient		ν_b	-	0.2				
Interfaces elastic parameters	Mortar joints	Normal stiffness	$K_{n,j}$	N/mm^3	60.3				
		Tangential stiffness	$K_{t,j}$	N/mm^3	25.1				
	Internal bricks	Normal stiffness	$K_{n,b}$	N/mm^3	10^4				
		Tangential stiffness	$K_{t,b}$	N/mm^3	10^4				
Interfaces mechanical parameters	Mortar joints	Cohesion	c_j	N/mm^2	0.23	0.023 (only head joints)	0.23	0.23	0.23
		Friction coefficient	$\tan\varphi_j$	-	0.58				
		Tensile strength	$f_{t,j}$	N/mm^2	0.04	0.004 (only head joints)	0.04	0.04	0.04
	Internal bricks	Tensile strength	$f_{t,b}$	N/mm^2	1.22				
	Compressive strength horizontal interfaces		$f_{c,h}$	N/mm^2	6.2				
	Compressive strength vertical interfaces		$f_{c,v}$	N/mm^2	3.1				
Interfaces fracture energies	Mortar joints (horizontal and vertical)	Mode I	$G_{I,j}$	N/mm	0.016	0.016	0.005	0.035	0.016
		Mode II	$G_{II,j}$	N/mm	0.16	0.16	0.014	0.25	0.16
	Internal bricks	Mode I	$G_{I,b}$	N/mm	0.12				
	Crushing - horizontal interfaces		$G_{c,h}$	N/mm	17.5				
	Crushing – vertical interfaces		$G_{c,v}$	N/mm	16.3				
Interfaces stiffness degradation	Mortar joints		μ_j	-	0.1	0.1	0.1	0.1	0.5
	Internal bricks		μ_b	-	0.1				

3.3.2 Numerical results

The two masonry panels are modelled by restraining the bottom as a fixed surface, while a uniform compressive pressure of 0.6 MPa is applied on the top employing an elastic stiff element, which is supported to remain horizontal. Lateral horizontal displacements, either monotonically or cyclically increasing (Figure 37), are then applied to the top element. As the input data models are only text-based, the structural geometries (composed of bricks, mortar head-joints, mortar-bed-joints, internal brick

interfaces) are first defined through Gmsh scripts (Geuzaine and Remacle, 2009) and then implemented as ADAPTIC data file (Izzuddin, 1991). In particular, an English bond pattern is defined, characterised by the alternating arrangement of header and stretcher rows, resulting in a distinct sequence of mortar head-joints and brick-to-brick internal failure surfaces (see Figure 44). The model, including load and boundary conditions, as well as specifications for cohesive interfaces, is depicted in Figure 45. The short panel model is characterised by 7360 3-DoF nodes, while the tall panel model consists of 10560 3-DoF nodes, resulting in 22080 DoFs and 31680 DoFs, respectively. The experimental displacements are transformed into equivalent accelerations by fitting them with spline curves and subsequently differentiated twice. These accelerations are applied to the nodes on the top beams by performing dynamic nonlinear analysis. This procedure is adopted throughout all the thesis, when performing cyclic analysis since dynamic analysis is generally more stable than displacement-controlled static analysis because inertial terms make the problem better conditioned even in case of loss of stiffness.

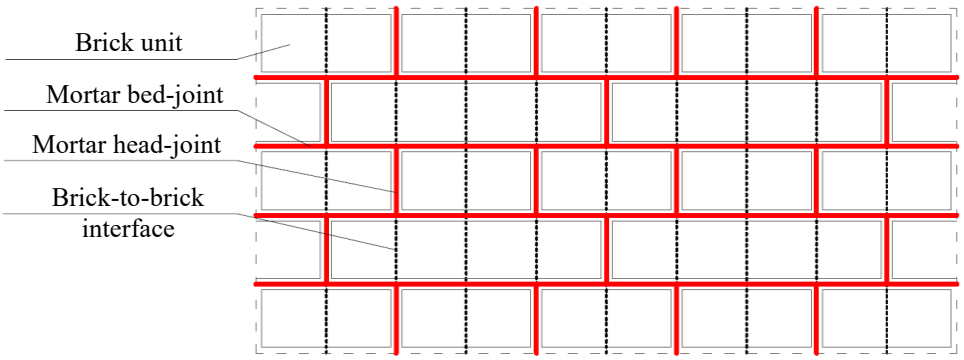

Figure 44 Mesoscale modelling of two-wythe thick English bond pattern

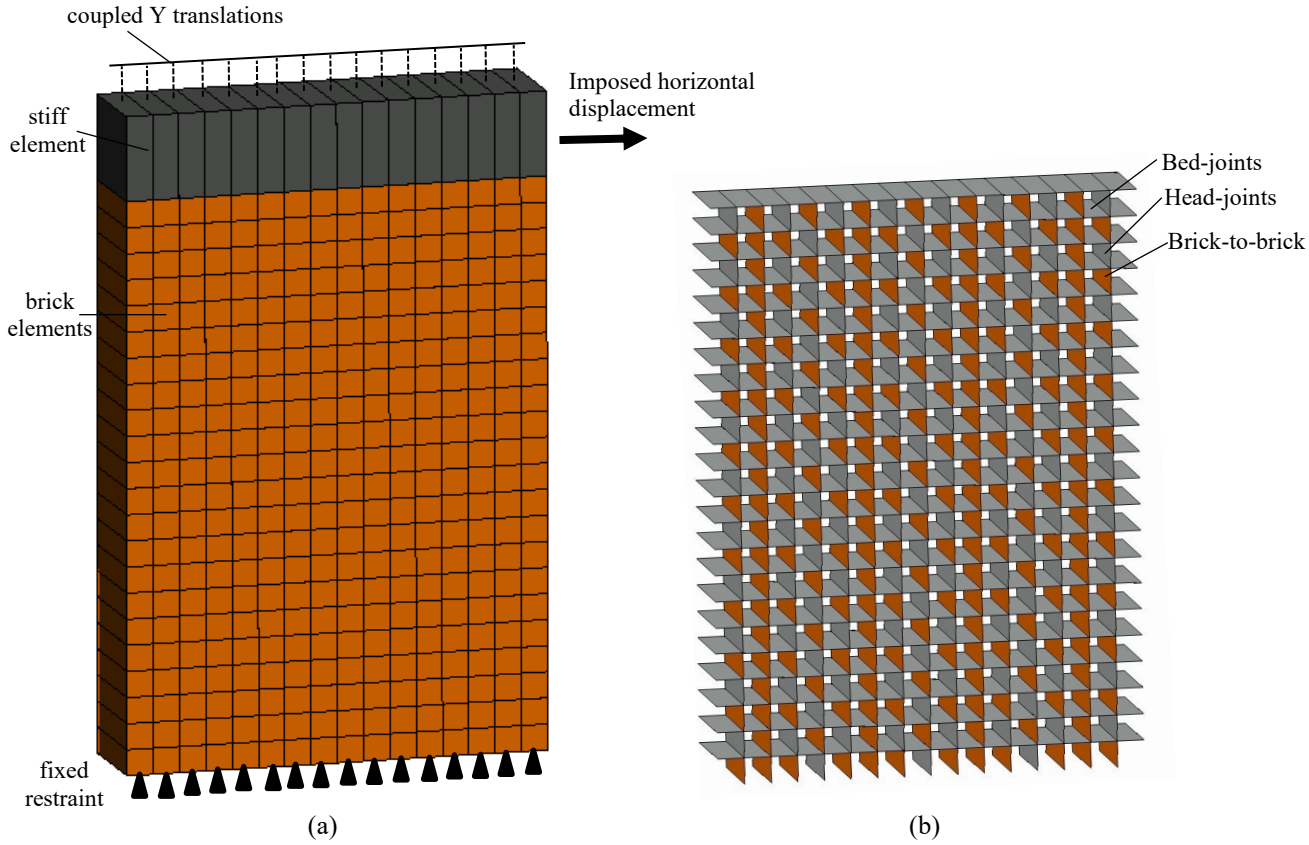

Figure 45 Mesoscale representation of a panel subjected to in-plane loading: (a) brick elements, steel beam, and boundary conditions; (b) interface elements distinct between mortar joints (bed- and head-joint are identically represented) and internal brick-to-brick potential failure surfaces

The results of the reference models subjected to monotonic and cyclic actions are depicted in Figure 46 and Figure 47. These include shear force vs. horizontal displacement curves, tensile damage on the interface elements (which mirrors shear damage on the interfaces), and deformed shapes (highlighting the opening and sliding of interfaces between units). Overall, the results demonstrate good agreement in terms of cracking patterns and shear-displacement curves for both specimens.

In the case of the short panel (Figure 46) subjected to monotonic loading, the damage pattern aligns with the experimental observations. Shear diagonal cracking damage is observable from the tensile damage of the interfaces and the deformed shape, accompanied by flexural horizontal cracks at the corners. The monotonic curve exhibits a good prediction of the initial elastic stiffness and the peak strength. However, the post-peak behaviour does not exhibit the strength softening observed in the experimental cycle. When subjected to cyclic actions, the model exhibits the typical X-shaped damage from shear diagonal cracking. The numerical cyclic curve closely approximate the experimental cycle, with stiffness degradation reasonably replicated. However, similar to the monotonic curve, the post-peak behaviour does not exhibit the strength softening observed in the experimental cycle.

In the case of the tall panel (Figure 47) subjected to monotonic loading, the typical damage associated with in-plane rocking behaviour is observed, characterised by cracking zones at both the bottom and top. The same mechanism is observed during the cyclic analysis. The monotonic shear-displacement curve closely fits the envelope of the experimental cycle. Regarding the cyclic response, the typical S-shaped cycle, indicative of flexural damage in masonry elements, is observable. However, after reaching a certain displacement, the numerical model experiences a loss of symmetry and begins to shift towards one side due to accumulated shear plastic strain at the two extremities of the model. The observed experimental degradation in stiffness is not replicated. One reason for this discrepancy could be attributed to the assumption of simplified elastic unloading-reloading in the constitutive model proposed by Minga et al., (2018), which, in reality, involves a certain level of hysteresis. It should also be noted that during the experimental test, damage within the panel was observed for large displacements, likely leading to the widening of the cycle.

Monotonic and cyclic pushover analyses are subsequently conducted on the variant characterisations defined in Table 8. Remarkably, a low variability in global responses is observed across capacity curves, cyclic diagrams, failure modes, and dissipated energy. The experimental-numerical comparisons in terms of shear vs. displacement curves are reported in Figure 48. In the case of the short panel, the analysis of variant 1 (weak head-joint) terminates earlier, even though its response aligns with that of the reference characterisation. Employing higher but reasonable fracture energies (Variant 3) may facilitate the convergence of the analysis. As for the tall panel, Variant 1 and 2 (low fracture energies) exhibit, at approximately 10 mm of displacement, a change in the slope of the unloading stiffness, leading to an earlier termination of the analysis (for the other cases the analysis are completed). This change is attributed to the spreading of shear-tensile damage of the interfaces within the panel, which in the experimental test is observed for large displacements.

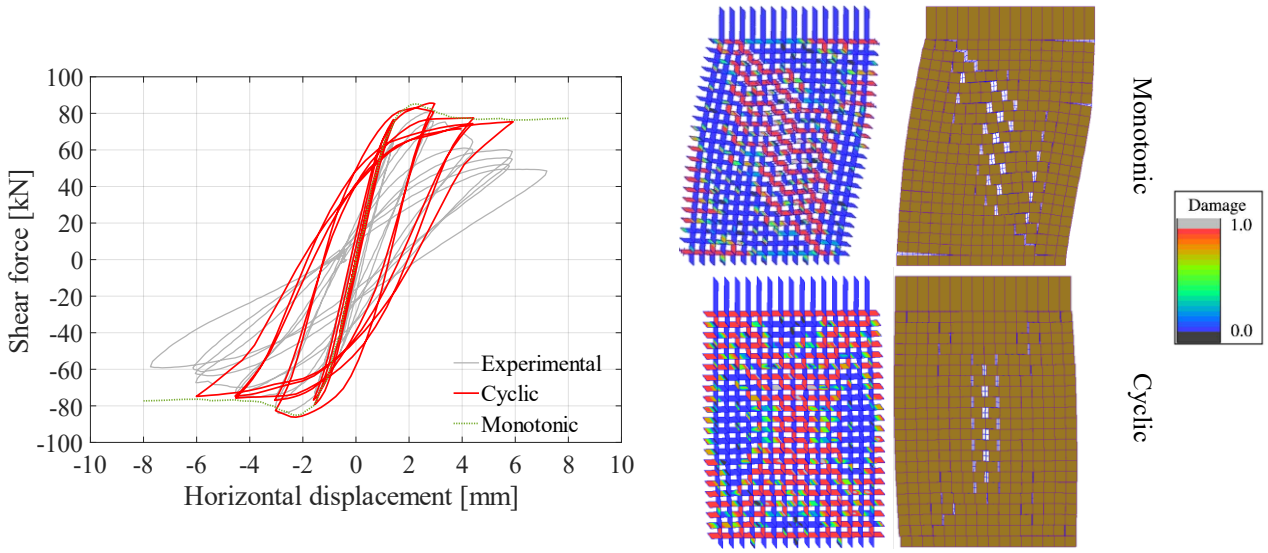

Figure 46 Short panel under in-plane cyclic loading: experimental-numerical shear force vs. horizontal displacement comparison, tensile damage developed in the interfaces and deformed shape at the last step reached in the monotonic and cyclic analysis

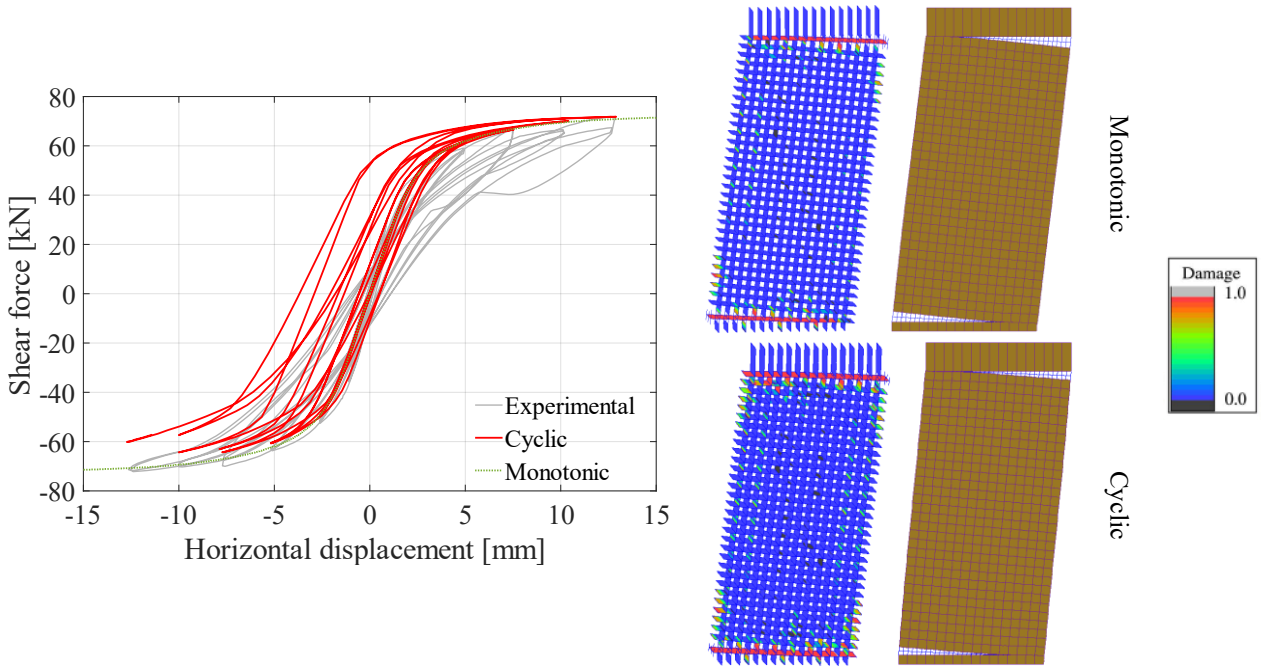

Figure 47 Tall panel under in-plane cyclic loading: experimental-numerical shear force vs. horizontal displacement comparison, tensile damage developed in the interfaces and deformed shape at the last step reached in the monotonic and cyclic analysis

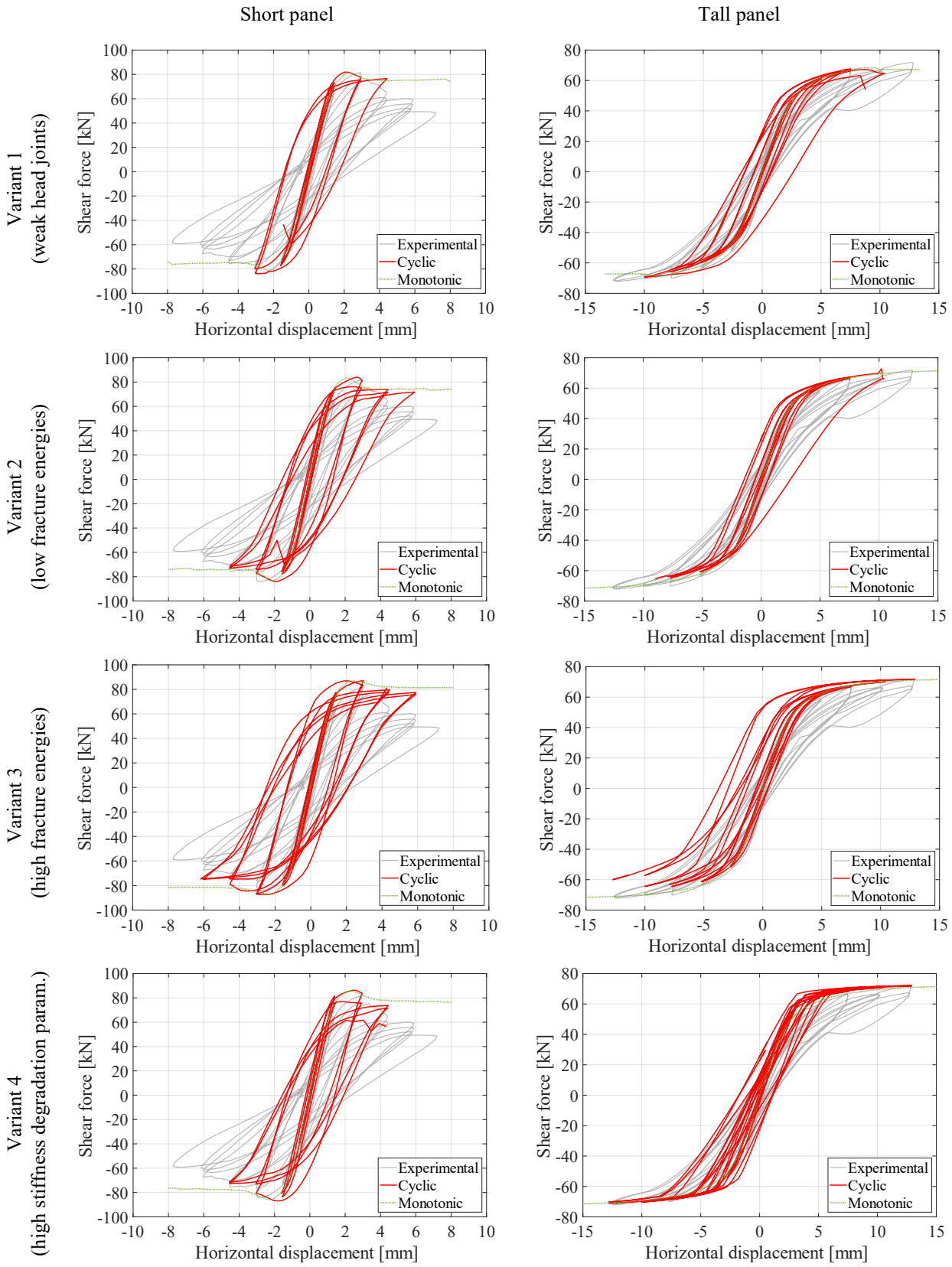

Figure 48 Monotonic and cyclic horizontal displacement vs. shear force curves for each mesoscale variants

Finally, the façade with openings is examined under horizontal cyclic actions (Figure 41). Considering the low variability of the responses from the models of the single panels, the material characterisation with high fracture energy (Variant 3 of Table 8) is employed. The vertical actions are uniformly distributed at the two levels, denoted respectively w_1 and w_2. The model is fully fixed at the base. For the application of the horizontal action, the average of the measured experimental displacements of the two floors, denoted as U, is applied to a master node located between the two floors, as represented in Figure 49. Subsequently, through a spreader element, the corresponding total force (denoted as F in the image) is equally distributed to all the nodes of the two floors (n_{tot} denotes the total number of nodes at the two floors), ensuring the same magnitude of force is applied to both floors, as in the experimental test (as described by Magenes et al., 1995). The model is hierarchically partitioned with 77 partitions to improve the computational efficiency, as proposed by Jokhio and Izzuddin (2015) and detailed in Chapter 2.3.1. In total, the model consists of 15490 3-DoF nodes and 1115 6-DoF nodes (nodes at the boundary partitions), amounting to a total of 156035 nodes and 471450 degrees of freedom. The calculation was carried within the high-performance computing facilities at Imperial College London and was terminated (analysis not completed) after approximately 166 hours.

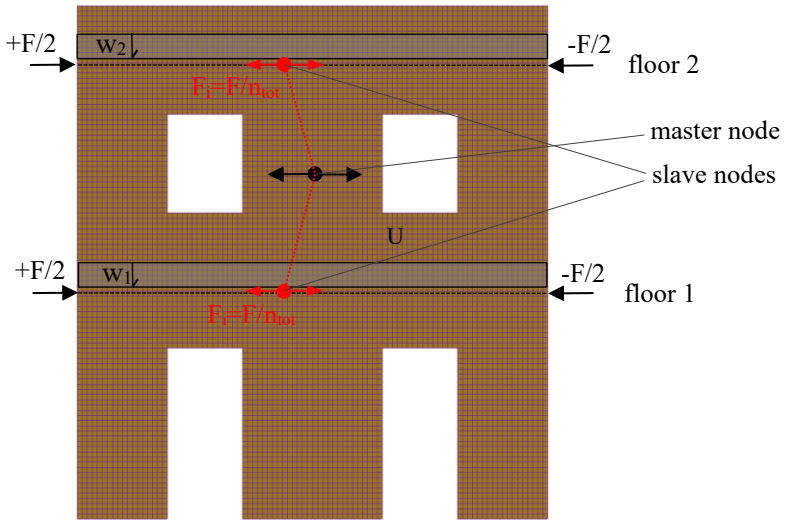

Figure 49 Loading applications and boundary conditions of the Wall D model

The second-floor displacement vs. base shear cycle, along with the experimental response, is reported in Figure 50. A good prediction of the initial stiffness is observed, while the maximum strength appears to be slightly overestimated, within a 10% variation. However, there is significant strength degradation in the first cycles, attributed to the excessively rapid failure of the spandrels (Figure 51). It is noteworthy that no lintels are modelled, as there are no specifications about them in Magenes et al. (1995), although

they were likely present. The rapid collapse of the spandrels on the first floor leads to a cycle with pronounced pinching, caused by the rocking of the piers on both sides.

This prediction does not diminish the reliability of the mesoscale modelling. Since it is a detailed model, when modelling large structures, it is important to appropriately consider construction details, such as lintels, as well as the connections between walls or between walls and floors. The model will be reanalysed by appropriately modelling the lintels.

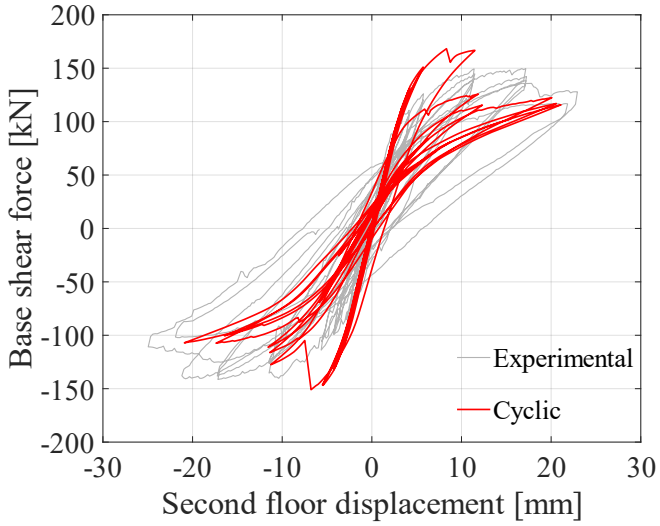

Figure 50 Analysis on the façade with openings

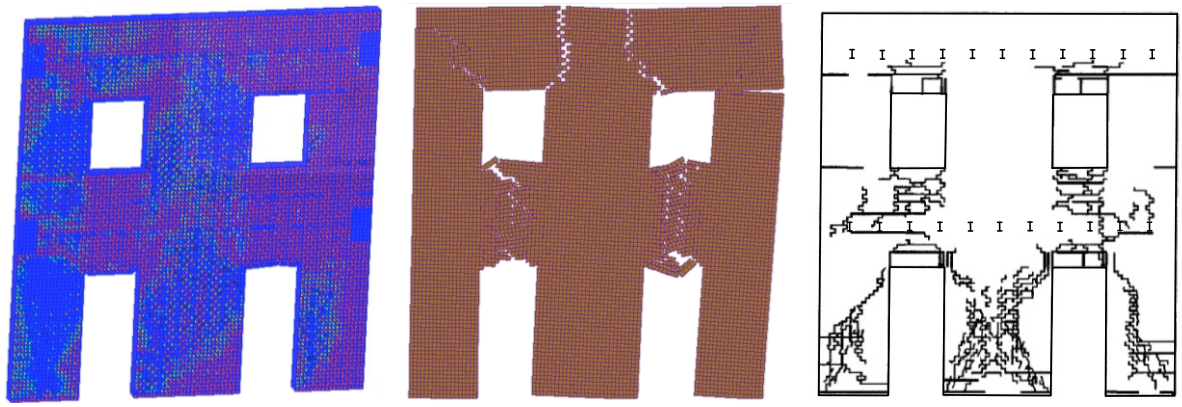

(a) (b) (c)

Figure 51. Perforated wall: a) damage on the interfaces and b) units deformations at the end of the cyclic analysis; c) experimental damage observed with a drift of 0.20% (Magenes et al., 1995)

3.4 Continuum macroscale modelling

This section investigates the application of the continuum macroscale modelling approach (detailed in Chapter 2.3.2), employing the Concrete Damage Plasticity (CDP) model to represent the masonry medium as a nonlinear isotropic material. The material model necessitates definition through numerous parameters, which may not be directly correlated with available experimental material characteristics, which comprise the characteristics of the constituents (bricks and mortar joints) and, at the macroscale level, the compressive strength, but do not include an evaluation of the global tensile strength.

To thoroughly assess the model's sensitivity to the analyst's choice, an extensive series of analyses on the single panels is conducted. This involves considering a set of reference values and 14 additional variants, each derived by individually modifying several defining parameters of the CDP model. The characterisations investigated are summarised in Table 10. A justification for the selection of these parameters is provided later on, followed by the presentation of the principal results derived from the analyses. Finally, the Wall-D is analysed employing a more refined material characterisation, defined based on the insights gained from the single-panel analyses, and compared to results obtained adopting the initial reference values.

3.4.1 Material characterisation

Concerning the stiffness properties, the elastic behaviour is characterised by the initial tangent Young's modulus and a Poisson's coefficient set at 0.2. The same elastic properties are applied to both compressive and tensile responses.

Determining the tensile strength of masonry as a whole within a continuum macroscale approach, for which no results from experimental tests are available (i.e., shear-compression or diagonal-compression test), is challenging and not straightforward. As emphasised by Lourenco and Gaetani (2022), the compressive strength (which in the present case is experimentally evaluated) and tensile strength of masonry significantly differ from each other. The former is generally associated with the composite behaviour of brick and mortar, while the latter is more linked to joint behaviour. Consequently, it is considered unrealistic to establish a direct correlation between the tensile strength of masonry and its compressive strength. In the present context, to assess how the overall response may vary, the specification for the tensile strength is determined by varying its value within a reasonable range, including a reference value and three additional values. The reference value, in accordance with standard engineering practices, is determined by considering mechanical parameters suggested by the

Italian code (MIT, 2019). Specifically, the typology of solid brick masonry with lime mortar, a typology analogous to the masonry evaluated in the experimental tests, is considered, whose mechanical parameter ranges are provided in Table 9. Since the experimental values for the elastic modulus and compressive strength exceed the range limits, the average shear tensile strength with zero vertical stress (denoted as $\tau_{0,M}$) is adopted as the maximum value, set at 0.13 MPa. The evaluation of the tensile strength is then conducted by identifying the maximum stress occurring at the centre of the panel, considering 1.5 times the value of $\tau_{0,M}$, resulting in a global tensile strength of 0.2 MPa.

Table 9. Suggested material characteristics by Italian regulation for Solid brick masonry with lime mortar (MIT, 2019).

$f_{c,M}$ [MPa]	$\tau_{0,M}$ [MPa]	$f_{v0,M}$ [MPa]	E_M [MPa]	G_M [MPa]	w [kN/m^3]
min-max	min-max	min-max	min-max	min-max	18
2.6÷4.3	0.05÷0.13	0.13÷0.27	1200÷1800	400÷600	

Regarding the minimum value of the variation range, this is set by considering the experimental bond strength (Table 5), which is equal to 0.04 MPa. Another value evaluated within the assessed range is determined by considering the lower limit in Table 9 for the shear strength $\tau_{0,M}$, which results in a tensile strength of 0.08 MPa. As for the maximum value of the range, the analytical relation (11) is employed, as proposed by Lourenco and Gaetani (2022). This relation considers the typical behaviour of masonry under tension parallel to the bed-joint, characterised by failure marked by a stepped crack through head and bed-joints. The relation establishes the tensile strength as a function of cohesion (c_j), overlapping length (l_0) – calculated as the average of half-length unit (l_b) and half-width unit (t_b) due to the alternation of header and stretcher – and unit height (h_b), resulting in a tensile strength of 0.39 MPa.

$$f_t = \frac{c_j \, l_0}{h_b} \tag{11}$$

Regarding the fracture energy in tension G_t, a reference value of 0.02 N/mm, as recommended in (Lourenço and Gaetani, 2022) for macroscale modelling, is adopted. The minimum and maximum fracture energy values assessed are established at 0.005 and 0.035 N/mm, respectively, derived from the suggestions reported in Table 7 regarding the Mode I failure, thus linking the tensile failure of the masonry to the mode I fracture energy of the mortar joints.

The parameter governing stiffness degradation in tension, denoted as μ, is assessed using a reference value of 0.2 (taken from Chisari et al., 2020). Sensitivity analyses are conducted with values set at 0.01 and 0.5.

The ratio between biaxial and uniaxial compressive strength $\widetilde{f_{b0}}$, flow potential eccentricity ε, and ratio of the second stress invariant on the tensile meridian to that on the compressive meridian at initial yield (K_c) are assumed as default values from (ABAQUS Inc, 2014), which are equal to 1.16, 0.1, and 0.66, respectively.

The dilatancy angle, denoted as ψ, represents the tendency of certain materials to expand their volume when subjected to shear actions. As emphasised by Lourenco (1996), this phenomenon is directly linked to the magnitude of confining stress. Specifically, lower confining stress levels are generally associated with higher material dilation. The dilatancy angle is defined at the macroscopic level in such a way that its tangent is equivalent to the ratio between normal and shear displacement. Essentially, it quantifies the uplift of one unit over the other when subjected to shear stresses. In Figure 52, provided from (Van der Pluijm, 1993), the outcomes of numerous shear tests on joints in masonry with solid clay units are presented. The figure reports a linear regression, illustrating the relationship between the tangent of the dilatancy angle and the level of confining stress. Given this linear relation and the confinement level of the solid brick masonry panels under consideration (vertical stress equal to 0.6 MPa), the corresponding tangent of the dilatancy angle is approximately 0.3. For the analysis, a reference value of 20° is adopted, and the sensitivity of this parameter is subsequently examined by varying it within a range between 10° and 35°.

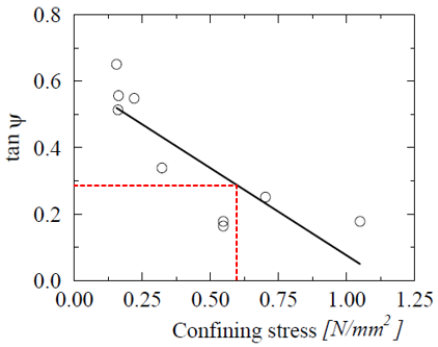

Figure 52. Tangent of dilatancy angle ψ as a function of the normal stress level, adapted from Van der Pluijm (1993); the marked point corresponds to the confinement level of the examined masonry panels

Stiffness recovery parameters are crucial in simulating the cyclic response, with distinction between compression and tension recovery arising from the different failure mechanisms involved, crushing and cracking. In particular, these recovery parameters account for the phenomenon of micro-crack opening and closure. Typically, the recovery is significantly higher when passing from tension to compression than vice versa. Therefore, the adopted reference values are 1 for compression stiffness recovery (w_c), indicating full recovery upon crack closure as the load changes from tension to compression, and 0 for

tension stiffness recovery (w_t), denoting no recovery during the transition from compression to tension once the concrete crushing is initiated. Additionally, two further combinations are considered, with values of 0.8 and 0.2, and 0.16 and 0.87. In particular, the latter combination represents a combination derived from the calibration URM walls conducted by Chisari et al. (2020), using inverse analyses through genetic algorithms. Herein, it is considered an extreme, although "anti-intuitive," case evaluated.

The sensitivity assessment also involves varying the ratio between uniaxial yielding stress and maximum strength in compression (f_{yr}), ranging from a standard value of 0.3 to a minimum of 0.1 and a maximum of 0.5.

Finally, the plastic strain at the compression peak ($k_{c,fmax}$), initially set at a central value of 0.002, typically found in concrete-like materials (Lourenco and Gaetani 2022), is varied from a minimum of 0.001 to an extreme maximum of 0.003.

In summary, material characterisations for reference and variant scenarios adopted in the analysis are provided in Table 10**.**

Table 10. Reference characterisation and variant case studies for the panels analyses; the variable parameters are reported in shaded cells.

Parameter	Symbol	U.o.m.	Reference values	Variants	Case study
Young's modulus	E_M	[MPa]	1980	-	-
Poisson's coefficient	ν_M	[-]	0.2	-	-
Dilatancy angle	ψ	[°]	20	10 – 35	CDP1 - CDP2
Ratio between biaxial and uniaxial compressive strength	f_{b0}	-	1.16	-	-
Flow potential eccentricity	ε	-	0.1	-	-
Ratio of the second stress invariant on the tensile meridian to that on the compressive meridian at initial yield	K_c	-	0.66	-	-
Global tensile strength	$f_{t,M}$	[MPa]	0.20	0.04 - 0.08 - 0.39	CDP3 – CDP4 – CDP5
Fracture energy	G_t	[N/mm]	0.02	0.005 - 0.035	CDP6 – CDP7
Stiffness degradation	μ	[-]	0.2	0.01 - 0.5	CDP8 – CDP9
Maximum compression strength	$f_{c,M}$	[MPa]	6.2	-	-
Ratio between uniaxial yielding stress and maximum strength in compression	f_{yr}	[-]	0.3	0.1 – 0.5	CDP10 - CDP11
Plastic strain at maximum compressive strength	$k_{c,fmax}$	[-]	0.002	0.001 – 0.003	CDP12 - CDP13
Tensile stiffness recovery	w_t	[-]	0	w_t=0.2 & w_c=0.8	CDP14
Compressive stiffness recovery	w_c	[-]	1	w_t=0.87 & w_c=0.16	CDP15

3.4.2 Analysis

Monotonic and cyclic pushover analyses are conducted on the reference model and 14 variants. The boundary and loading conditions of the models are as described in Chapter 3.3.2. The short panel is characterised by 2891 3-DoF nodes, while the tall panel consists of 4178 3-DoF nodes, resulting in 8673 DoFs and 12534 DoFs, respectively.

Figure 53 and Figure 54 illustrate the monotonic and cyclic response obtained from the analysis of both short and tall panels using the reference material characterisation. While initial elastic stiffnesses are accurately captured, maximum strengths are overestimated for the capacity curves of both models. Noteworthy, the monotonic curves deviate significantly from numerical cyclic envelopes. In the cyclic response of the short panel (Figure 53), the initial cyclic phase is characterised by flexural damage, indicating damage concentration at the top and bottom of the panel, but with a shear-lateral displacement curve far from the typical S-shaped cycle of flexural response and, instead, characterised by wide hysteretic cycles. This is reflected also by the high rate of energy dissipation, as illustrated in Figure 55, which shows the progression of the total amount of energy (in comparison with the experimental progression). In a second phase, the spreading of cracks along the panel's height leads to substantial strength and stiffness degradation, accompanied by a decrease in the rate of dissipated energy. This crack spreading does not take place within the monotonic analyses. The tall panel exhibits a similar overall behaviour (Figure 54), notably without reproducing the typical S-shaped cycle experimentally observed.

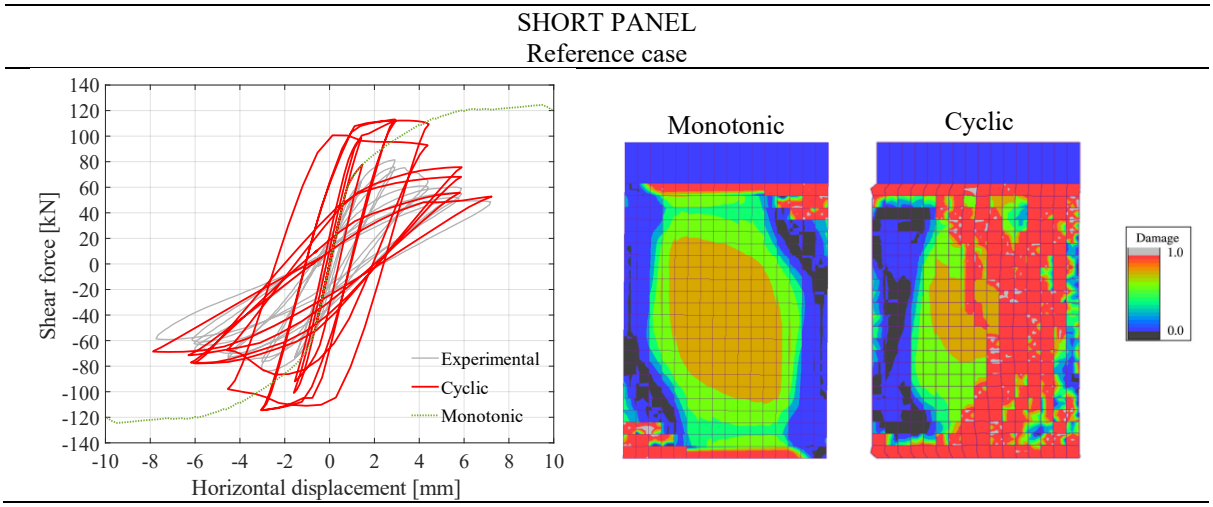

Figure 53. Short panel responses (reference characterisation): experimental-numerical comparison and tensile damage developed in the monotonic (displacement equal to 9mm) and cyclic analysis (last step)

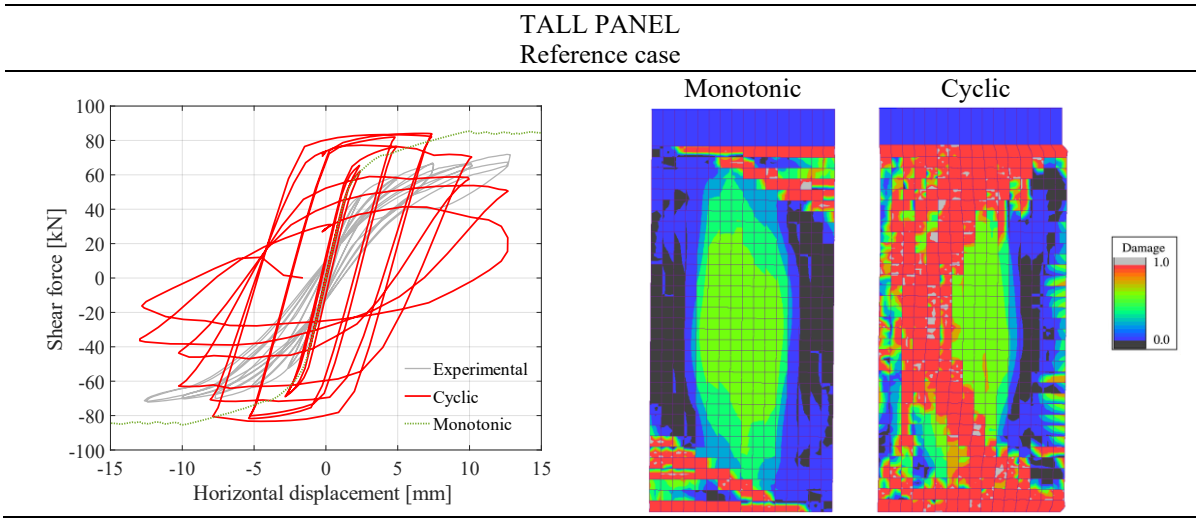

Figure 54. Tall panel responses (reference characterisation): experimental-numerical comparison and tensile damage developed in the monotonic (displacement equal to 14mm) and cyclic analysis (last step)

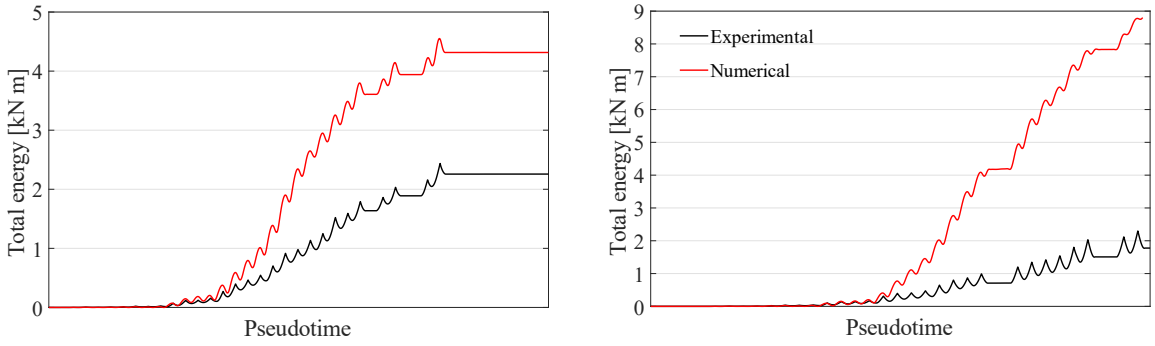

Figure 55. Comparison between experimental and numerical dissipated energy: a) short panel; b) tall panel

The variant models, implemented with the material characterisations of Table 10, exhibit a significant variability in global responses, in terms of capacity curves, cyclic diagrams, failure modes, and the amount of total energy. Notably, significantly different numerical responses arise from varying the global tensile strength, as can be observed in Figure 56 for the short panel and Figure 57 for the tall panel. The variant models, implemented with the material characterisations of Table 10, exhibit a significant variability in global responses, including capacity curves, cyclic diagrams, failure modes, and amount of total energy. Notably, significantly different numerical responses arise from varying the global tensile strength, as observed in Figure 56 for the short panel and Figure 57 for the tall panel. In the case of the short panel, for the two lower value specifications (CDP3 and CDP4 variants), a shear diagonal cracking failure mode is consistently observed throughout the cyclic analysis with no damage at the extremities. The maximum shear force from variant CDP4 is close to the experimental responses, while in CDP3 (where the adopted tensile strength is the bond strength), it is lower. Moreover, the

excessive strength degradation hinders accurate prediction of the total amount of energy, thereby preventing the completion of the analyses for both models. Conversely, the adoption of the highest tensile strength (variant CDP5) does not lead to significant changes compared to the reference case, neither in the monotonic nor in the cyclic response. For the tall panel, similar variations in responses are observed. Notably, again, the typical flexural S-shape cycles are not reproduced in any case.

The results of all the other variant cases are depicted in Figure 58 and Figure 59.

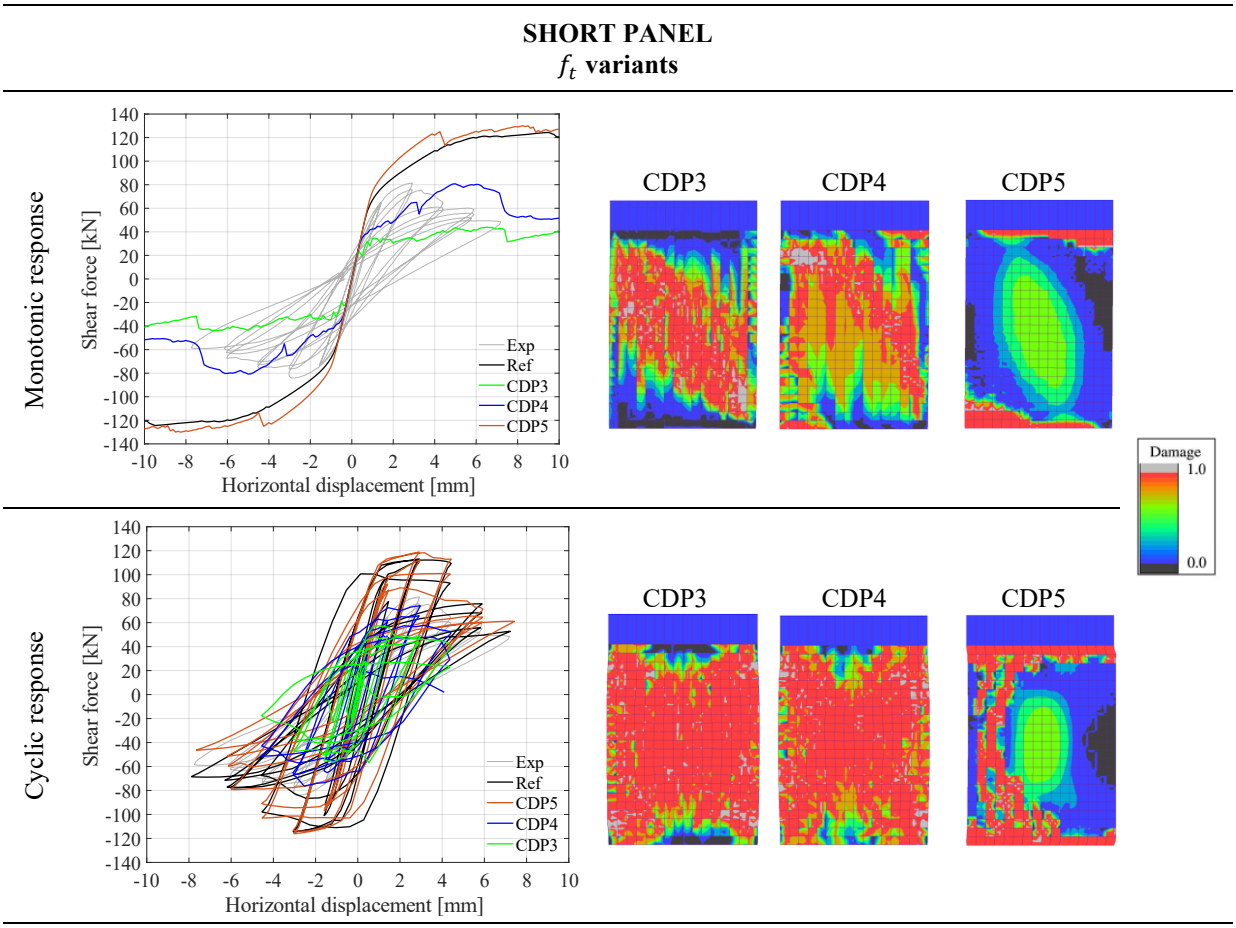

Figure 56. Short panel responses for reference characterisation (f_t=0.2MPa) and variants CDP3 (f_t=0.04MPa), CDP4 (f_t=0.08MPa) and CDP5 (f_t=0.039MPa): experimental-numerical comparison and tensile damage developed in the monotonic and cyclic analysis (last reached step)

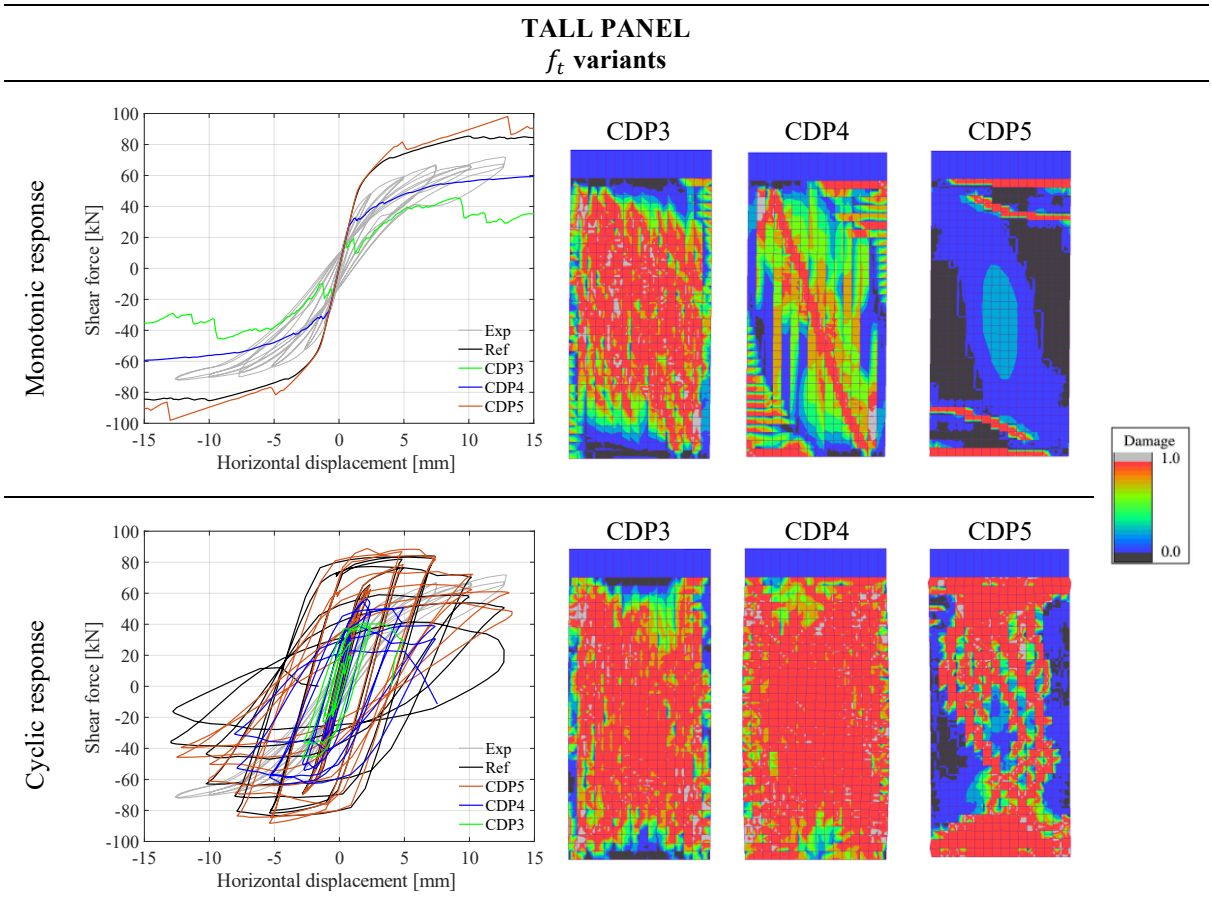

Figure 57. Tall panel responses for reference characterisation (f_t=0.2MPa) and variants CDP3 (f_t=0.04MPa), CDP4 (f_t=0.08MPa) and CDP5 (f_t=0.039MPa): experimental-numerical comparison and damage developed in the monotonic and cyclic analysis (last step)

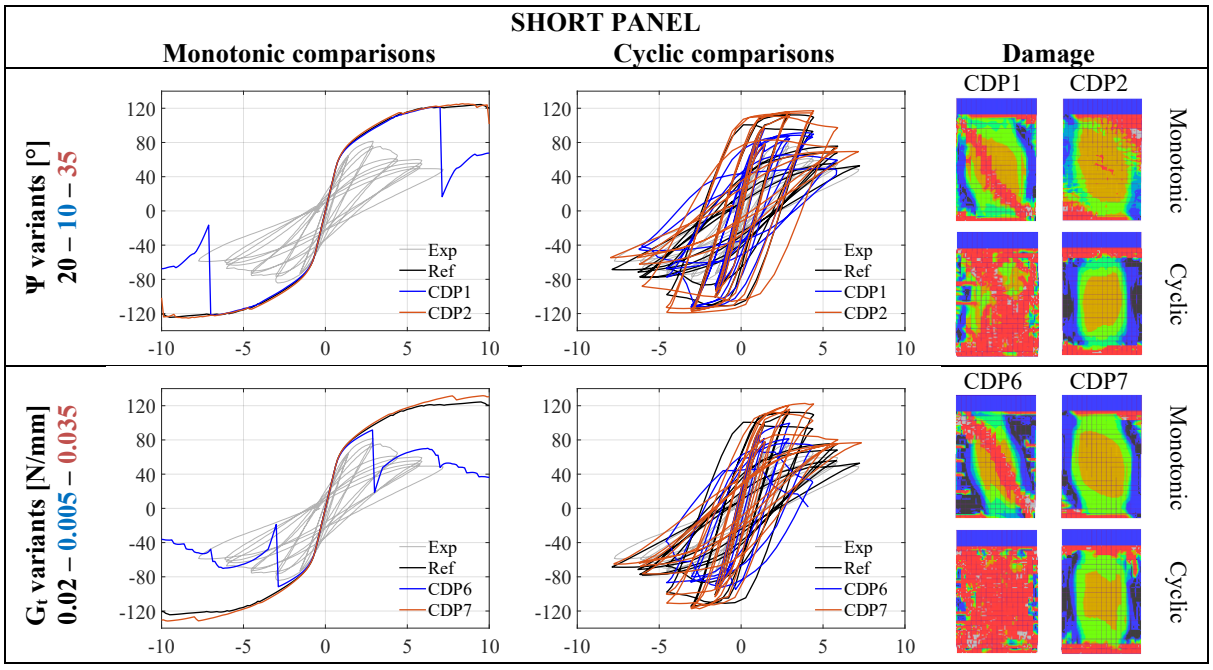

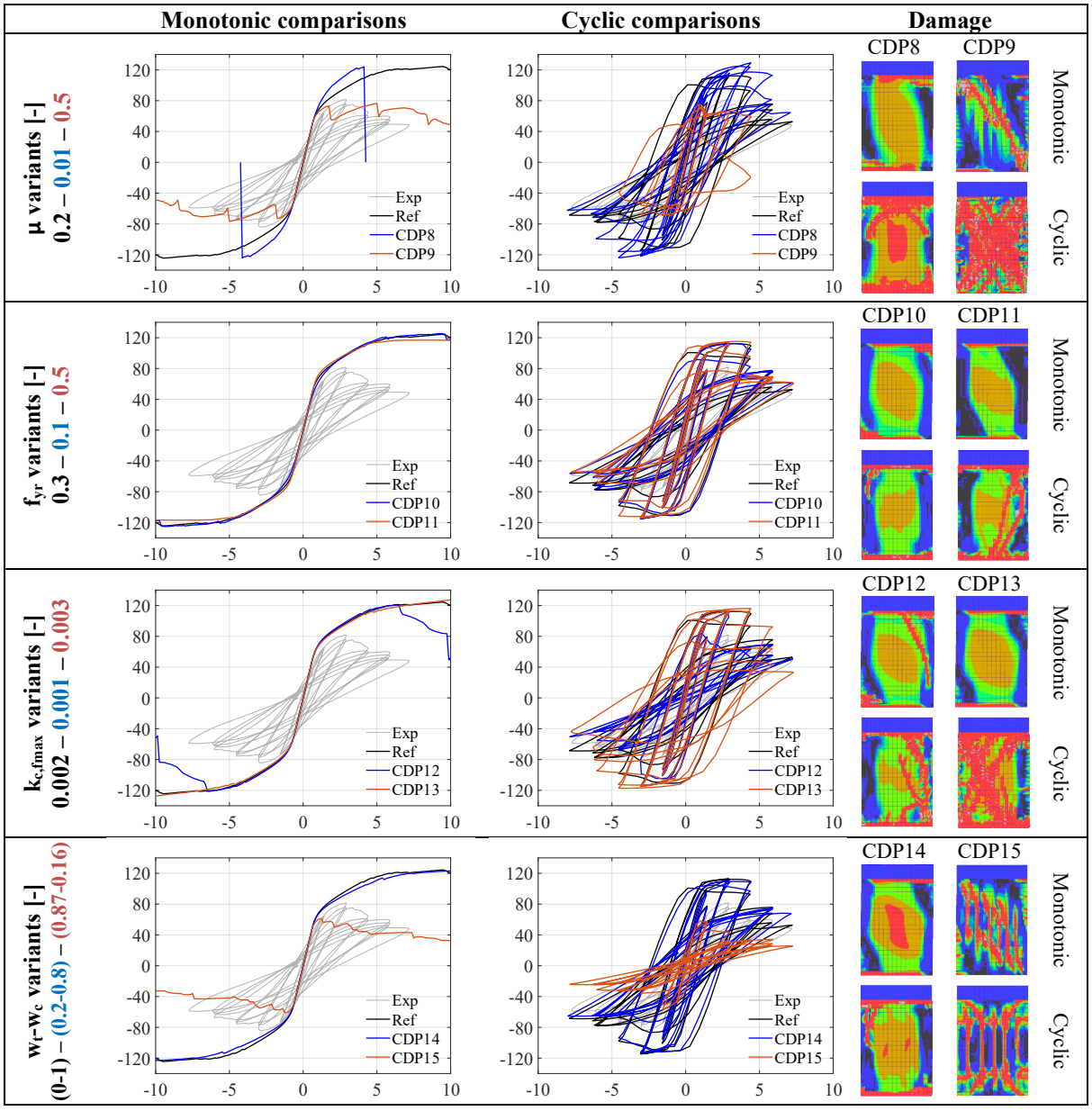

Figure 58. Monotonic and cyclic shear force vs. horizontal displacement responses of short panel models (X-axis in [mm], Y-axis in [kN]) and damage patterns at the last step reached

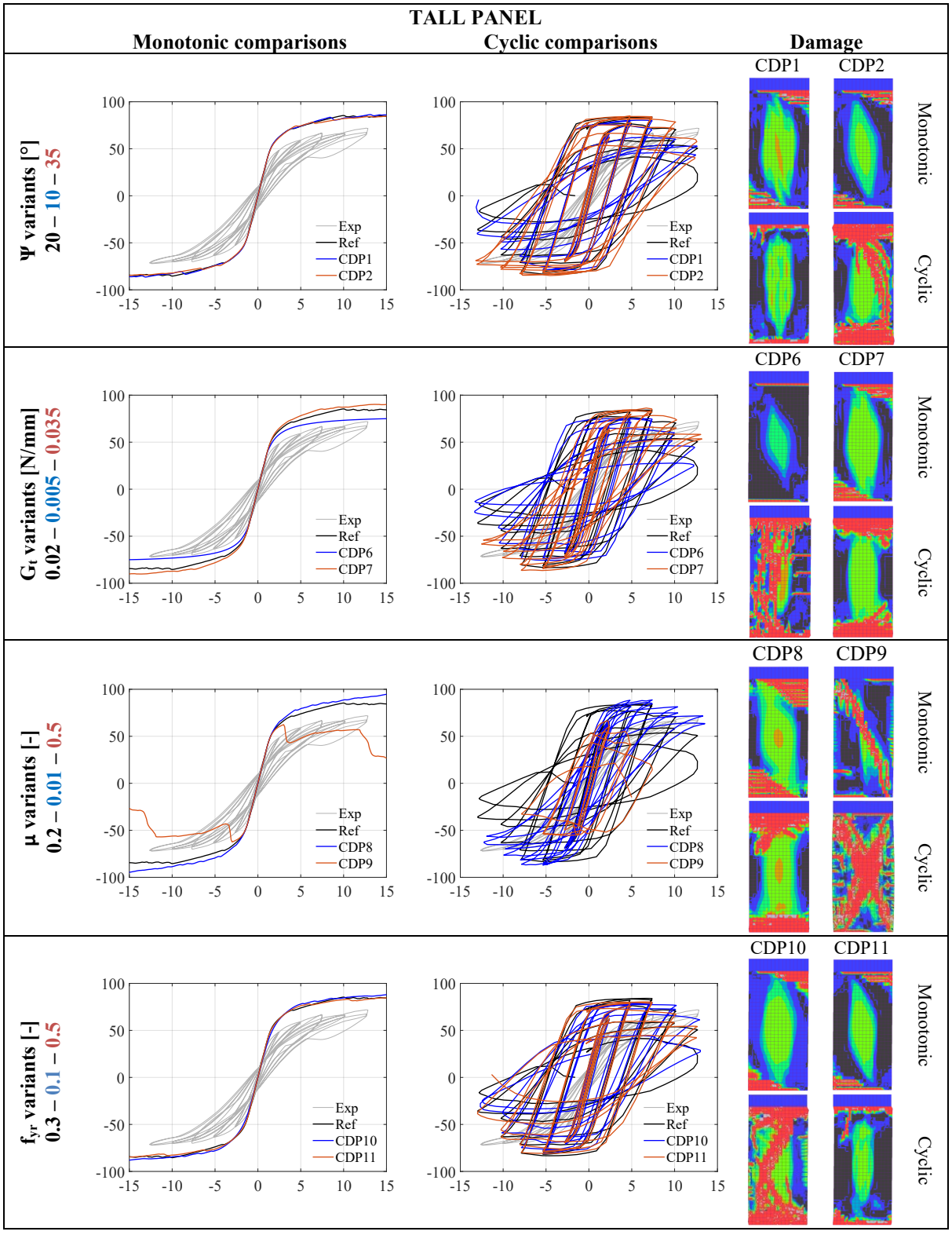
TALL PANEL
Monotonic comparisons
Cyclic comparisons
Damage
Ψ variants [°]
20 – 10 – 35
Gt variants [N/mm]
0.02 – 0.005 – 0.035
μ variants [-]
0.2 – 0.01 – 0.5
fyr variants [-]
0.3 – 0.1 – 0.5
Exp
Ref
CDP1
CDP2
CDP6
CDP7
CDP8
CDP9
CDP10
CDP11
Monotonic
Cyclic

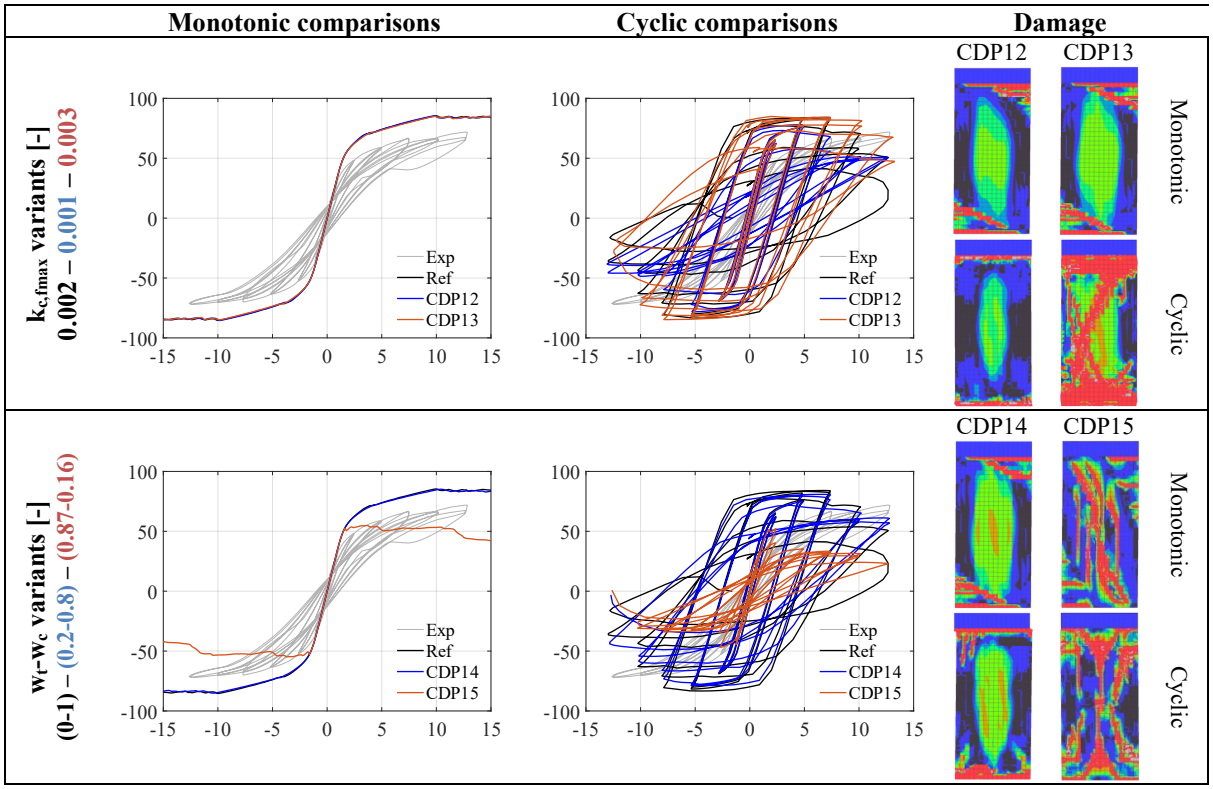

Figure 59. Monotonic and cyclic shear force vs. horizontal displacement responses of tall panel models (X-axis in [mm], Y-axis in [kN]) and damage patterns at the last step reached

The main results from all the cyclic analyses are summarised in Table 11. Due to premature failures, not all the analyses have been completed. Therefore, the percentage variations of final total energy (ΔW_{tot}) between variants and reference configuration, reported in Table 11, are calculated by considering the instant corresponding to the last reached step in the numerical analysis. The differences in dissipation capacity between the models are also represented through the graphs in Figure 60 highlighting the high sensitivity of the responses to variations in the selection of the parameters.

The difference in responses, in terms of dissipated energies and failure modes, among experiments, reference models, and variants, is significant. Specifically (in addition to the tensile strength variation, already discussed):

- Smaller variations (even if still significant) in the dissipated energy are observed when varying dilatancy ψ (CDP1 and CDP2 variants), fracture energy G_t (CDP6 and CDP7 variants), and ratio between uniaxial yielding stress and maximum strength in compression $f_{y,r}$ (CDP8 and CDP9 variants) parameters assumed within realistic ranges.

- A greater variation is observed in the cyclic responses when changing the value $k_{c,fmax}$ from a low value of 0.001 (CDP12 variants), which leads to responses closer to the experimental curves, to the upper limit of 0.003 (CDP13 variants), despite the monotonic responses being similar to each other.
- Both variants related to the stiffness degradation parameter μ result in lower dissipated energies compared to the reference model (μ equal to 0.1), for different reasons. For the upper value (μ equal to 0.5; CDP9 variants), the high degradation leads to premature termination of the analysis (only 51% of the analysis is terminated for the short panel and 59% for the tall panel). On the other hand, for the lower value (μ equal to 0.01; CDP8 variants), the lower stiffness and strength degradation result in significantly narrower cycles.
- Regarding the stiffness recovery parameters, the CDP14 variants (w_t and w_c equal to 0.2 and 0.8, respectively) does not significantly affect the analysis. However, the CDP15 variants, characterised by non-realistic stiffness recovery parameters (w_t and w_c equal to 0.87 and 0.16, respectively), results in substantial strength and stiffness decay, along with distinctive damage patterns.

Table 11. Summary of the results from sensitivity analyses; failure mode: S=shear-diagonal cracking - F=flexural - F→S: flexural first, and then diagonal cracking; W_{tot}: total amount of energy at the last step reached; ΔW_{tot}: percentage variation of total energy with respect to the reference characterisation (for each case the amount of total energy of the reference characterisation is calculated at the last step reached with the variant analysis)

		Short panel				Tall panel			
Changing parameter	Case study	Failure mode	W_{tot} [kN m]	% analysis completed	ΔW_{tot}	Failure mode	W_{tot} [kN m]	% analysis completed	ΔW_{tot}
	Experimental	S	2.26			F	1.78		
	Reference	F→S	4.32	100%		F→S	8.80	100%	
ψ	CDP1	F→S	3.32	65.9%	-8.5%	F	7.29	97.6%	-16.9%
	CDP2	F	5.50	100%	27.5%	F→S	10.82	100%	22.9%
$f_{t,M}$	CDP3	S	1.33	51.4%	-45.3%	S	0.52	47%	56.2%
	CDP4	S	1.94	54.1%	-31.3%	S	2.75	73.1%	-42.3%
	CDP5	F→S	4.39	100%	1.7%	F→S	7.71	100%	-12.4%
G_t	CDP6	S	2.57	54%	-8.9%	F→S	8.55	100%	-2.8%
	CDP7	F	3.84	100%	-11.1%	F	6.54	100%	-25.7%
μ	CDP8	F→S	3.52	100%	-18.4%	F	4.64	100%	-47.2%
	CDP9	S	1.93	51.3%	-18.9%	S	2.29	58.7%	-30.4%
$f_{y,r}$	CDP10	F→S	4.30	100%	-0.4%	F→S	8.50	100%	-3.3%
	CDP11	F→S	4.78	100%	10.9%	F	9.32	97%	6.6%
$k_{c,fmax}$	CDP12	F→S	2.31	100%	-46.5%	F	4.86	100%	-44.8%
	CDP13	F→S	6.42	100%	48.7%	F→S	10.04	100%	14.1%
w_t - w_c	CDP14	F→S	4.04	100%	-6.3%	F	8.37	100%	-4.8%
	CDP15	S	0.97	100%	-77.5%	S	1.99	87.2%	-74.4%

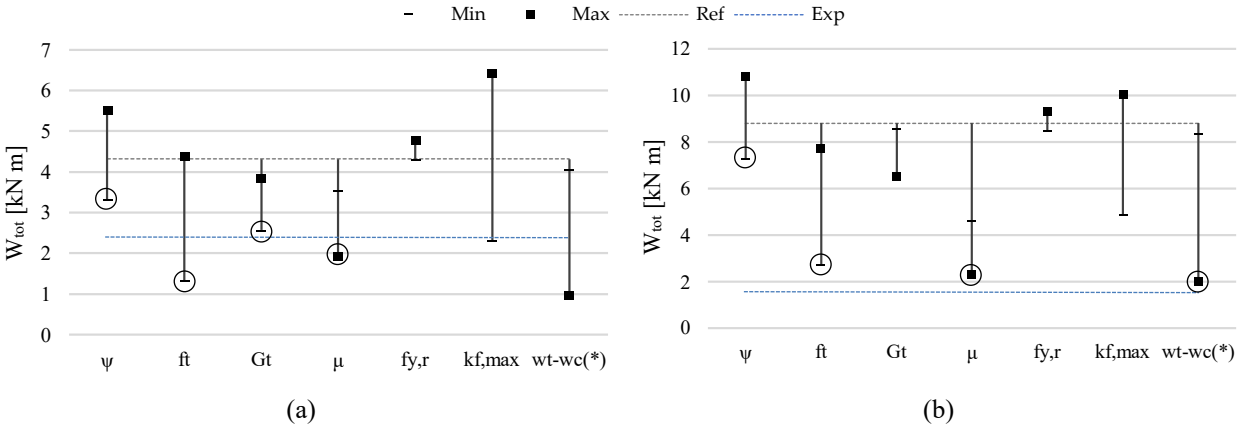

Figure 60 Variation of final total energies for (a) Short Panel and (b) Tall Panel. 'Min' and 'Max' represent the final total energies with the minimum and maximum variants of each range, respectively, while 'Ref' denotes the total energy with the reference models. 'Exp' indicates the experimental total energy, and circled indicators denote analysis not completed. (*) For the wt-wc range, the minimum and maximum cases are assumed as CDP13 and CDP14, respectively

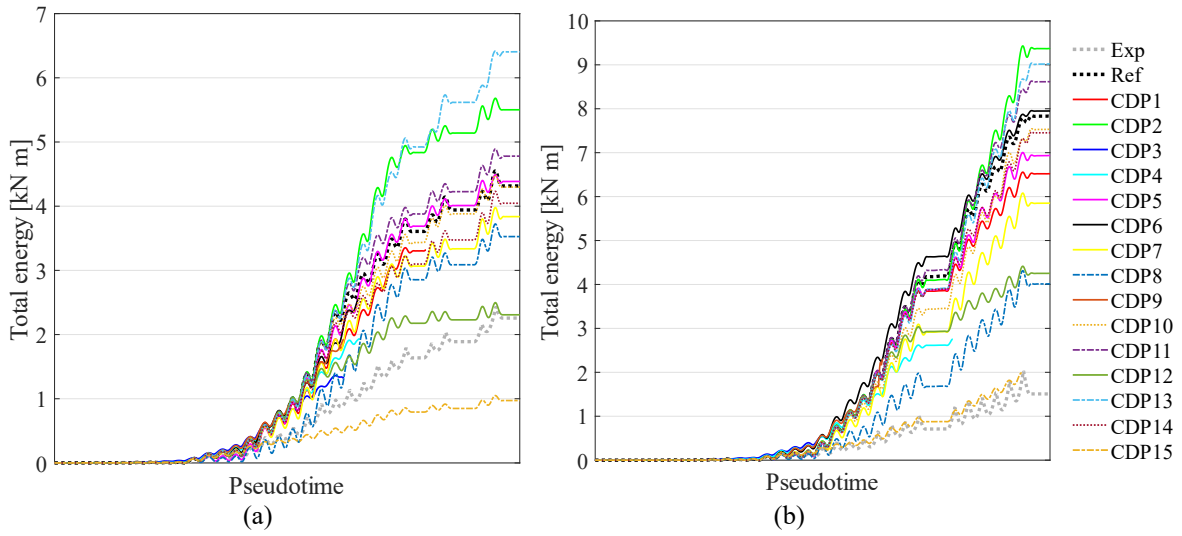

Figure 61 Progression of total energies for each analysis for (a) short panel and (b) tall panel

Based on the results obtained for the single panels, a “refined” material characterisation, is specified for the analysis of the perforated wall, and provided in Table 12. Some parameters are selected with the objective of aligning the numerical model with the experimental hysteretic capacity. Therefore, they are chosen by selecting values within ranges that resulted in cyclic responses closer to the experimental response. These parameters include dilatancy, global tensile strength, stiffness degradation parameter, tensile fracture energy, and peak plastic strain in compression. Meanwhile, other parameters, such as the ratio between yielding and maximum strength and stiffness recovery parameters, are maintained with default reference values, which are considered more common. After conducting analyses to assess

the mesh sensitivity of the models, where it was observed that mesh discretisation has no significant influence on the numerical response of the single panels, the Wall-D model is discretised using a coarser mesh of 125mm x 125mm x 250mm. The same spreader system for applying external loads, utilised in the Wall-D mesoscale model, is employed (Figure 49). The Wall-D macroscale model is characterised by 7371 3-DoF nodes, resulting in 22113 DoFs.

Table 12. Reference and refined characterisations for the Wall-D analysis.

Parameter	Symbol	u.o.m.	Reference	Refined
Young's modulus	E	[MPa]	1980	1980
Poisson's coefficient	ν	[-]	0.2	0.2
Dilatancy angle	ψ	[°]	20	10
Tensile strength	f_t	[MPa]	0.20	0.08
Fracture energy	G_t	[N/mm]	0.02	0.005
Stiffness degradation	μ	[-]	0.2	0.01
Maximum compression strength	f_c	[MPa]	6.2	6.2
Ratio between uniaxial yielding stress and maximum strength in compression	$f_{y,r}$	[-]	0.3	0.3
Plastic strain in compression	$k_{c,fmax}$	[-]	0.002	0.001
Tensile stiffness recovery	w_t	[-]	0	0
Compressive stiffness recovery	w_c	[-]	1	1

The global responses are presented in terms of force-displacement graphs in Figure 62, for both reference and refined characterisations. The selection of different material parameters significantly modifies the overall hysteretic response. The monotonic pushover analyses result in capacity curves characterised by significant overestimations of the overall base strength. Specifically, the maximum forces exhibit an overestimation of +46% with the reference characterisation and +67% with the refined one, in comparison with the experimental response. The cyclic responses also exhibit substantial differences, but noteworthy the refined characterisation provides a better prediction of strength and stiffness degradation, resulting in a progression of total energy remarkably close to the experimental one, as illustrated in Figure 63. The damage pattern (reported in Figure 64) is only partially captured by the models and it is more pronounced by considering the refined characterisation. A widespread flexural damage at the top and bottom of the piers on the first floor is observed in both models. Moreover, the shear-diagonal cracking damage on the piers of the first floor and the spandrel of the first level, as observed experimentally, is only partially reproduced: only the left pier at the base on the reference model collapses through a spreading of damage along the height.

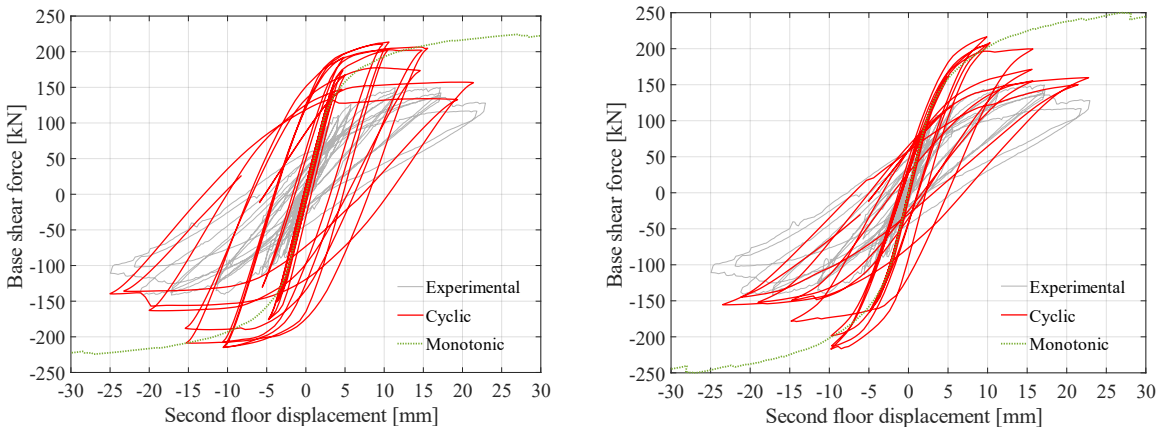

Figure 62. Cyclic responses of Wall D with reference (a) and refined (b) characterisation

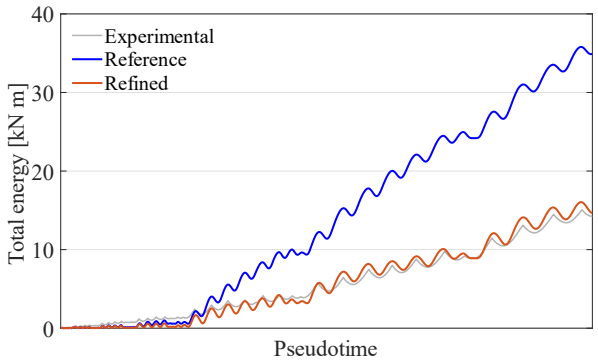

Figure 63 Dissipated energy during the cyclic analysis: comparison between experimental, reference and refined characterisation

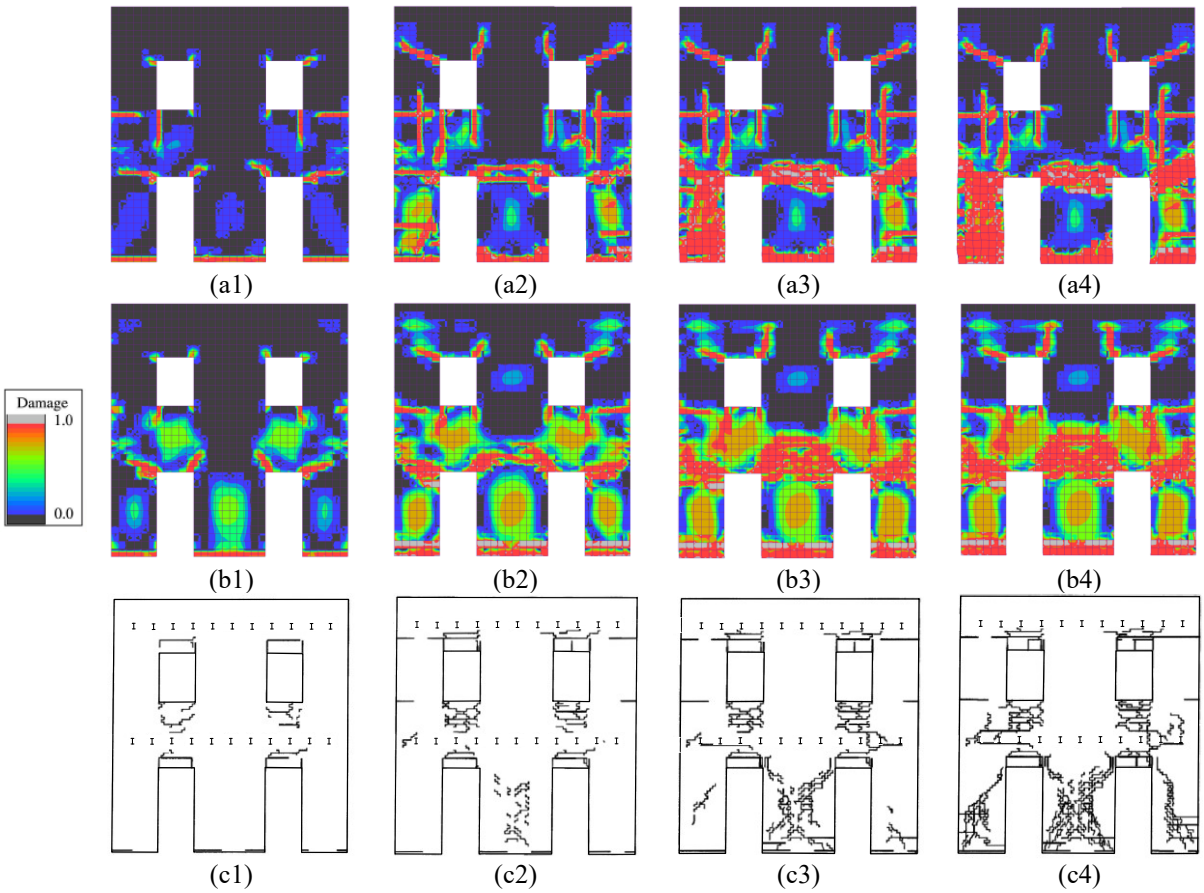

Figure 64. Progression of crack pattern (tensile damage) during the cyclic analysis: a) Reference characterisation; b) Refined characterisation; c) Experimental; 1) end of run 4 (max. drift 0.10%); 2) end of run 5 (max. drift 0.20%); 3) end of run 6 (max. drift 0.30%); 4) end of run 7 (max. drift 0.40%)

3.5 Summary and conclusions

In this chapter, two different approaches for the modelling of URM structures have been compared. Given a common set of material parameters, the modelling representations have been tested on single panels and on an entire perforated wall, subjected to monotonic and cyclic actions. A particular focus has been given to the material characterisation in each of them, a-priori determined, blindly predicted without considering the experimental outcomes. The main observations are below summarised.

The mesoscale approach:

- allows for a generally straightforward calibration of the single panels: monotonic and cyclic responses, in terms of load-displacement diagram and progression of damage pattern, result close to the experimental results, without particular needs of further refinement of material calibration;

- leads to a low variability of the responses with less-known parameters changes: the responses of the panels do not appear significantly affected by eventual variations of uncertain parameters, such as, for instance, fracture energies;
- is characterised by high computational cost making the analysis of larger structure not easy to be performed.

As regards the continuum finite element macroscale modelling, the capability of the concrete damage plasticity model to predict the numerical in-plane seismic response of URM structures has been evaluated by performing several sensitivity analyses, varying many of its defining parameters. The analysis employing the continuum macroscale modelling shows that:

- a "standard calibration", as an initial attempt at material calibration, may lead to a simulation that is significantly distant from the experimental responses, in terms of capacity curve, load-displacement cycles, prediction of failure modes and amount of dissipated energy;
- the variation of not easily quantifiable parameters can substantially affect the response of the models;
- a refined characterisation may allow to better predict, with reasonable approximation, the hysteretic behaviour of a real structure, as the façade with openings analysed;
- the S-shaped typical flexural load-displacement diagram is hardly captured;
- the analyses are medium time-consuming;
- the use of this modelling approach is characterised by greater numerical robustness compared to mesoscale, enabling the completion of the entire cyclic analysis for panels and Wall-D.

Based on the obtained results, some preliminary suggestions on possible links between the two representations, and with the experimental tests carried out, can be made. The material tests (Table 5) regarded the evaluation of single components (bending and compression test on bricks; triplet shear test and cross-tension tests on mortar joints), together with the evaluation of compressive strength and Young's modulus of masonry (compression test on wallets). The suggestions are divided between elastic stiffness parameters, strength parameters and fracture energies.

- Elastic stiffness parameters: The initial tangent elastic modulus, obtained from the experimental stress-strain curve of compression tests on wallets, is adopted as the elastic modulus of the masonry as a whole. This value is utilised in both approaches. In the macroscale approach, the modulus is directly employed as the elastic modulus of the isotropic concrete damage plasticity material. In the mesoscale approach, the elastic modulus is considered when assessing the elastic stiffnesses of the interfaces, which are determined by treating bricks and mortar layers

as connected in series (equations (5) and (8)), depending on the estimated masonry modulus, brick elastic modulus, unit height, and layer thickness.

- Strength: The mechanical parameters of the interfaces (i.e. cohesion, friction coefficient and bond strength), obtained from triplet shear tests and cross-tension tests, enable an accurate prediction of the mesoscale response of the single panels, encompassing failure predictions and shear-displacement curves, both monotonic and cyclic. Regarding the macroscale approach, the specification of the tensile strength significantly influences the response, largely affecting failure mode predictions and overall shear-displacement curves. Given the absence of experimental tests at the macroscale level, determining the masonry tensile strength can be challenging and may be linked to the properties of the individual components. A conservative initial estimate, as also suggested in (Lourenço and Gaetani, 2022), is to consider the bond tensile strength as the global tensile strength of masonry. However, for a more accurate prediction, experimental tests at the macroscale level, which are more invasive and expensive, should be performed. A valid alternative involve employing a small-sized mesoscale model, to be considered as virtual test.
- Fracture energies: In the mesoscale approach, the responses exhibit low variability from fracture energy specifications, allowing for the adoption of relatively high values to enhance analysis convergence. However, in the continuum macroscale, sensitivity is higher and a smaller value can lead to an earlier activation of shear-like mechanisms compared to considering higher fracture energies. In favour of safety, a smaller value (derived from range values provided in literature) may be adopted.

In conclusion, it is emphasised that a multiscale strategy offers an opportunity to reliably employ macroscale models in cyclic analysis, as suggested by Chisari et al. (2020) and Pantò et al. (2022). Through non-invasive tests on mortar joints, coupled with compression strength evaluation (which could be also conducted with a moderately invasive flat-jack test), a mesoscale model can be accurately implemented and used as a virtual test. The mesoscale model can then be employed to calibrate macroscale models, leveraging its higher robustness and computational efficiency to analyse larger structures.

CHAPTER 4

ADVANCED MODELLING OF MASONRY-INFILLED FRAME STRUCTURES

4.1 Introduction

This chapter focuses on modelling of infilled reinforced concrete frames using two sophisticated strategies for masonry-infilled frames. These approaches involve representing masonry infills through either a mesoscale or a continuum macroscale approach, while the frame is modelled using cubic elasto-plastic 3D beam-column elements. The connection between the external cohesive-frictional interfaces, representing the mortar layer at the frame-infill boundary, is guaranteed through a multidimensional coupling element. This element ensures the connection between the 3-degrees-of-freedom (DOFs) nodes of the infill elements and the 6-DOFs nodes of the frame.

A significant focus is placed on the detailed calibration of materials, emphasising the definition of mechanical parameters characterising the interfaces between the frame and infill components. This calibration process undergoes a thorough examination to ensure objectivity, taking into account results from experimental tests, and accuracy in representing actual responses, both globally and locally.

Conclusively, an assessment is conducted on the calibrated continuum-infill model (consistent with the more refined mesoscale-infill model) to evaluate the impact of openings within the infills. This evaluation encompasses an analysis of strength and stiffness decay in response to the presence of openings. The outcomes of this investigation provide valuable insights into the structural response of infilled reinforced concrete frames under various modelling strategies, serving as a reference point for subsequent analyses in the following chapters with the enhanced macroelement approach.

4.2 Experimental tests

The study carried out by Armin B. Mehrabi et al. (1996), focusing specifically on the experimental response of masonry-infilled frames, is considered as reference for evaluating the simulations with the various models implemented in the present work. In their study, twelve single-story, single-bay frame specimens underwent testing. The test specimens were chosen to be half-scale models representing the interior bay at the bottom story of the prototype illustrated in Figure 65. The prototype itself was a six-storey, three-bay reinforced concrete moment-resisting frame. The height-length ratio for each bay was standardised at 1/1.5. The design loads complied with the specifications of the Uniform Building Code (UBC) (1991), with service live load and dead load equal to 2.39 kPa and 6.21 kPa respectively.

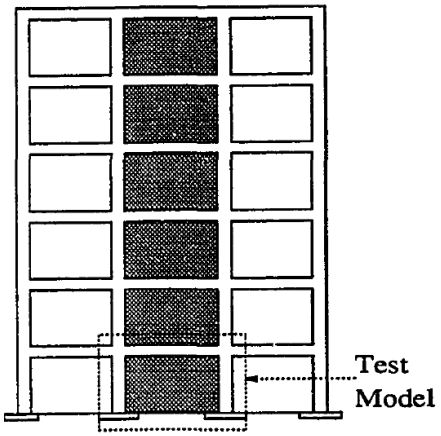

Figure 65 Prototype frame, image taken from (Armin Barzegar Mehrabi 1994)

Two distinct types of frames were tested: a "weak" frame designed solely to withstand wind loads, in addition to vertical loads, and a "strong" frame designed to resist strong earthquake forces. The design specifications for both frames followed the guidelines outlined in ACI 318-89 ("Building" 1989). In either case, the load resistance contributed by infill panels was ignored, as in standard design practice.

In the present research, the focus is on the frame designed to withstand wind loads only. This specific frame is representative of an existing reinforced concrete frame not meeting the detail requirements of seismic design provisions. The frame was designed to withstand a lateral wind pressure of 1.24 kPa, corresponding to a basic wind speed of 44.5 m/s. Figure 66 illustrates the design details of this frame, featuring a typical weak column and strong beam configuration.

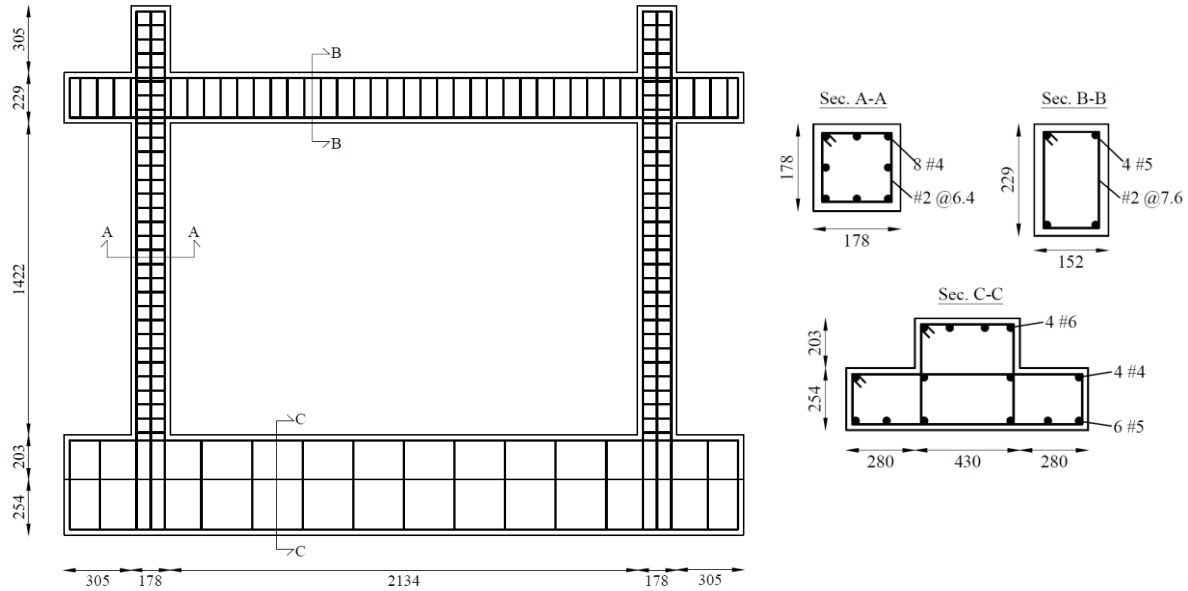

Figure 66 Weak Frame Design Details

In addition to the frame typology, other parameters were also investigated. These included the strength of infill panels in relation to the bounding frame, the distribution of vertical loads, the lateral-load history, and the H/L aspect ratio.

In particular, two types of infill panels were used, considering 92 mm × 92 mm × 194 mm either hollow or solid concrete masonry blocks, with bed and head mortar layer joints 9.5 mm thick. Additionally, two distinct vertical load distributions were examined: one involving vertical loads exclusively applied to the columns, and the other with 1/3 of the total vertical load applied to the beam and 2/3 onto the columns. The vertical load applied to the specimen remained constant throughout each test. Furthermore, two types of in-plane lateral displacement histories were chosen: monotonically increasing and cyclic. Finally, in the analysis of weak frames, a further panel aspect ratio of approximately ½ was considered.

Some of the frame specimens underwent multiple tests. In these cases, the cracks in the frame members were repaired using epoxy injection, and crushed regions were restored with cement paste, comparable in strength to that of the original concrete. A new infill panel was reconstructed for each test, and testing occurred at least 28 days after the construction of the infill.

The characteristics of each experimentally tested specimen are detailed in Table 13. The tests simulated in this chapter and those that will be simulated in Chapter 6, as part of the validation process of the enhanced macroelement, are highlighted. In the context of the present chapter, specimen 1 is considered

for validating the RC bare-frame model, while specimen 3 is chosen for simulating an infilled-frame with either mesoscale or continuum macroscale masonry-infill.

Table 13 Characteristics of the specimens tested by Armin B. Mehrabi et al. (1996): specimens investigated in the present chapter are highlighted in cyan, while those additionally examined in Chapter 6 are highlighted in green

Specimen number	Type of frame	Type of masonry units	Panel aspect ratio (h/L)	Lateral load	Vertical load distribution [kN]	
					Columns	Beams
1	Weak	No infill	0.67	Monotonic	293.7	-
2	Weak (repaired after 1)	Hollow	0.67	Monotonic	293.7	-
3	Weak (repaired after 2)	Solid	0.67	Monotonic	293.7	-
4	Weak	Hollow	0.67	Cyclic	195.8	97.9
5	Weak	Solid	0.67	Cyclic	195.8	97.9
6	Strong	Hollow	0.67	Cyclic	195.8	97.9
7	Strong	Solid	0.67	Cyclic	195.8	97.9
8	Weak (repaired after 4)	Hollow	0.67	Monotonic	195.8	97.9
9	Weak (repaired after 8)	Solid	0.67	Monotonic	195.8	97.9
10	Weak	Hollow	0.48	Cyclic	195.8	97.9
11	Weak	Solid	0.48	Cyclic	195.8	97.9
12	Weak (repaired after 10)	Solid	0.48	Cyclic	-	146.85

Material tests were performed on both concrete and masonry samples for each specimen. The concrete compression test results, performed on standard cylinders with 150 mm diameter, are outlined in Table 14, where the outcomes for specimen 1 and specimen 3 are provided. The secant modulus is determined as 45% of the compressive strength. Additionally, Table 15 presents the compressive strengths of the 3-course masonry prisms and the compressive strength of the single constituents, brick and mortar, specifically for specimen 3. Tensile strengths of the reinforcing bars, common to all tests, are summarised in Table 16. Finally, direct shear tests were conducted on mortar joints under various confinement levels (Table 17). The assessment involved the evaluation of maximum shear stress (τ_{peak}) and residual shear stress (τ_{res}) with respect to vertical stress variations (σ_v).

Table 14 Frame concrete experimental mechanical properties of specimen 1 and 3 (Mehrabi et al., 1996)

Secant modulus (*) [MPa]	Compressive strength [MPa]
21930	30.9

*At 45% of the compressive strength

Table 15 Infill-masonry experimental mechanical properties of specimen 3 (Mehrabi et al., 1996)

Masonry secant modulus (*) [MPa]	Masonry compressive strength [MPa]	Masonry strain at peak stress [-]	Brick compressive strength [MPa]	Mortar compressive strength [MPa]
9520	15.10	0.0029	15.59	16.00

*At 45% of the compressive strength

Table 16 Steel rebars experimental mechanical properties (Mehrabi et al., 1996)

Bar size	Type of bar	Nominal diameter [mm]	Yield stress [MPa]	Ultimate stress [MPa]
no. 2	Plain	6.35	367.6	449.6
no. 4	Deformed	12.7	420.7	662.1
no. 5	Deformed	15.9	413.8	662.1

Table 17 Triplet shear tests results (Mehrabi et al., 1996)

σ_v [MPa]	τ_{peak} [MPa]	τ_{res} [MPa]
0.345	0.483	0.303
0.517	/	0.434
0.690	0.952	0.614
1.035	1.283	0.917

The base shear force vs. horizontal displacement responses of the two specimens under investigation are illustrated in Figure 67. A great difference is noticed in the responses of the bare and infilled frames, both in terms of initial stiffness and maximum strength, and even at considerable displacements, the residual strength of the infilled frame remains significantly higher than that of the bare frame.

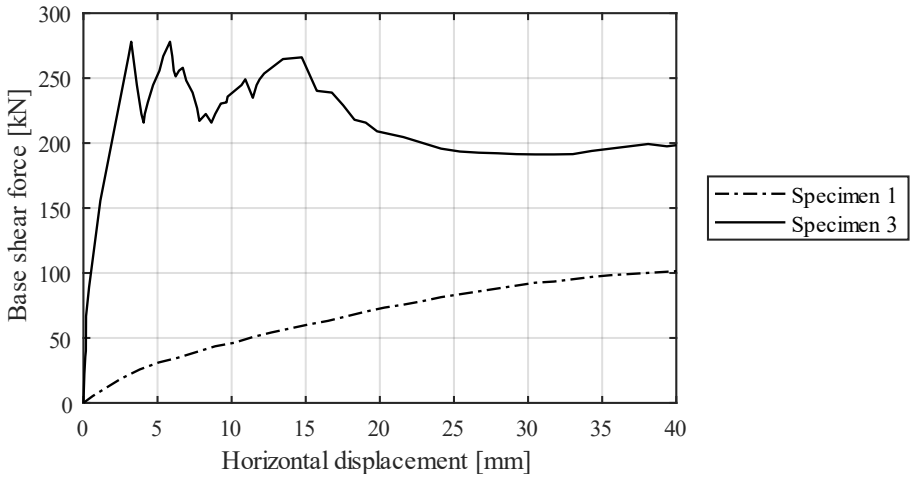

Figure 67 Experimental response of bare frame (Specimen 1) and infilled frame (Specimen 3)

4.3 Reinforced Concrete Bare Frame modelling

The reinforced concrete bare-frame is modelled using 1D elasto-plastic beam-column elements, as developed by B. A. Izzuddin and Elnashai (1993a; 1993b), and implemented in ADAPTIC. These elements utilise a 3D cubic formulation based on Euler-Bernoulli beam theory, which accounts for the interaction between biaxial bending moments and axial force for a generic reinforced concrete (RC) cross-section. The element formulation assumes that plane sections remain flat, while shear strains are neglected, with the section centroid aligning with the shear centre. The element accounts for both material and geometric nonlinearities.

A fibre element strategy (a generic illustration of the approach is given in Figure 68) is employed, where each element is defined by a specific number of Gauss integration points along its length. These points are characterised by the discretisation of the sections into multiple fibre elements, serving as monitoring areas for assessing strains and stresses, and for integrating the virtual work equation. These fibre elements may represent either concrete or steel bars within the sections, each governed by specific material relationships.

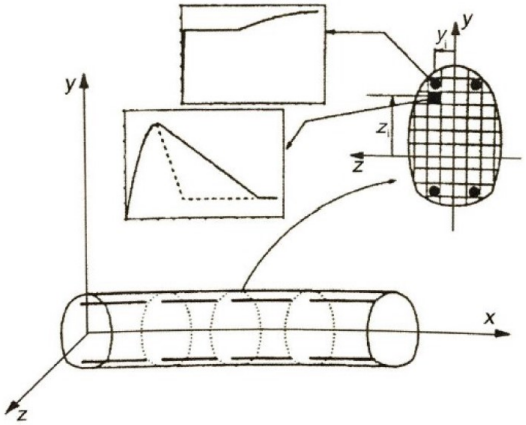

Figure 68 Distributed fibre plasticity approach: Gauss points and fibre discretisation; image taken from (Fardis, 2009)

The formulation proposed by B. A. Izzuddin and Elnashai (1993a; 1993b) involves the inclusion of two Gauss points within each element, as illustrated in Figure 69, where the local freedoms of the element are also depicted. This formulation adopts cubic shape functions for the transverse displacements, v(x) and w(x), and considers a constant centroidal axial strain criterion. The fibre approach allows for the consideration of material nonlinearities, enabling the representation of plasticity spread along the element, due to phenomena such as steel yielding, concrete crushing, and concrete cracking.

Furthermore, the formulation accounts for geometric nonlinearities by incorporating a co-rotational formulation. In this method, the element's local reference system is defined within the deformed configuration, allowing for the consideration of large displacement contributions. Geometric nonlinear effects are represented through transformations between the local and global reference systems.

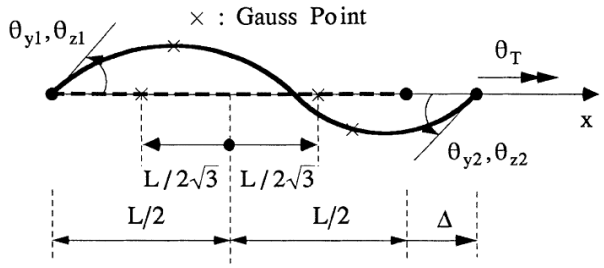

Figure 69 Local freedoms of elasto-plastic cubic formulation and localisation of Gauss points (Izzuddin and Lloyd Smith, 2000)

The RC frame of the experimental test, specifically the Specimen 1 as illustrated in Figure 66, is modelled by adopting a series of elastoplastic beam elements. Each frame element is represented by its centreline, and rigid links are employed for the beam-column joints, while the bottom beam is fixed at the base. The chosen mesh discretisations for the bare frame are linked to the modelling strategies adopted in Sections 4.5 and 4.6; no significant variations with changes in mesh discretisation are observed. The initial loading comprises a vertical application of 146.9 kN on top of the columns, followed by a horizontal displacement applied to the top beam. The model layout is illustrated in Figure 70a, while a 3D view of the extruded numerical model is presented in Figure 70b (the rigid links on the beam-column joints are modelled as elasto-plastic elements with high stiffness and strength, thus they are graphically represented as the other elements).

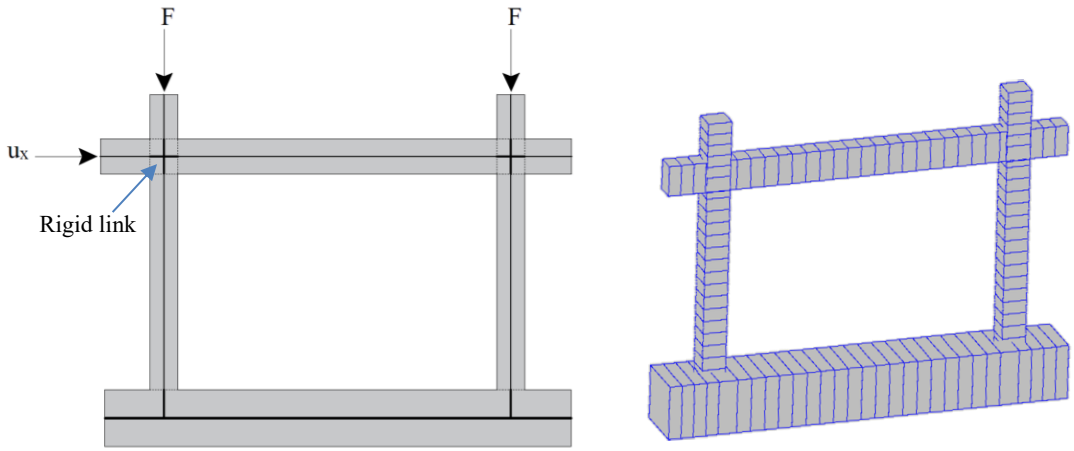

(a) (b)

Figure 70 Bareframe modelling: (a) geometry and external actions; (b) extruded model 3D view

In terms of material specification, concrete is modelled employing an elastic-perfectly plastic law to simulate the uniaxial stress-strain compressive response, with zero tensile strength. For the steel rebars, an elastoplastic model that incorporates strain hardening is employed, assuming same responses in compression and tension. The strain hardening factor, which determines the post-yielding branch stiffness as a percentage of initial stiffness, is set to 0.15. Detailed material characteristics are provided in Table 18, equally considered for columns and beams rebars.

Table 18 Material characteristics of the RC bare-frame model

Concrete		Steel		
Elastic modulus [MPa]	Compressive strength [MPa]	Elastic modulus [MPa]	Yield strength [MPa]	Hardening factor [-]
21930	30.9	210000	400	0.15

The shear-displacement curves, depicted in Figure 71, exhibit a close alignment between the numerical and experimental responses. Additionally, a similar damage pattern is observed (Figure 72), characterised by the formation of plastic hinges at the end sections of the columns and beam. However, shear cracks observed experimentally at the beam-column joints for relatively large displacements cannot be captured with the fibre-element used. Despite this limitation, the overall response is deemed satisfactory, allowing for the evaluation of the reliability of the models after the insertion of the masonry infill.

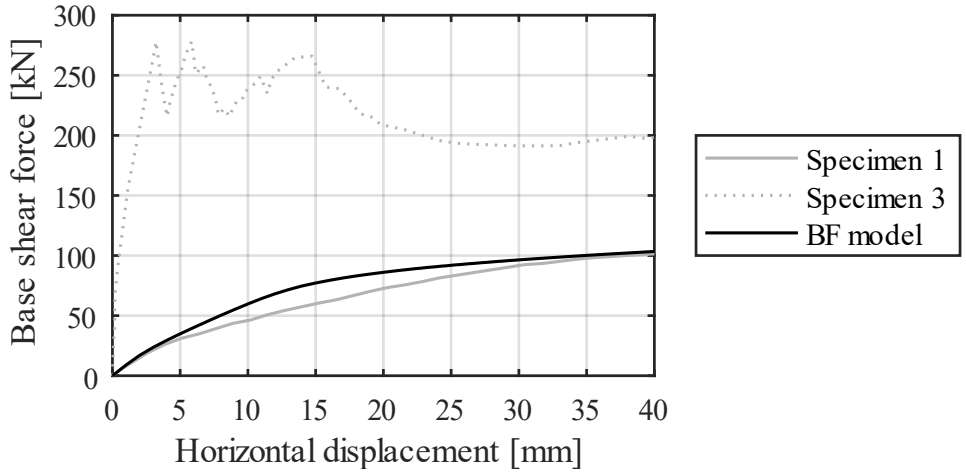

Figure 71 Experimental-numerical comparison for the Bare-Frame model

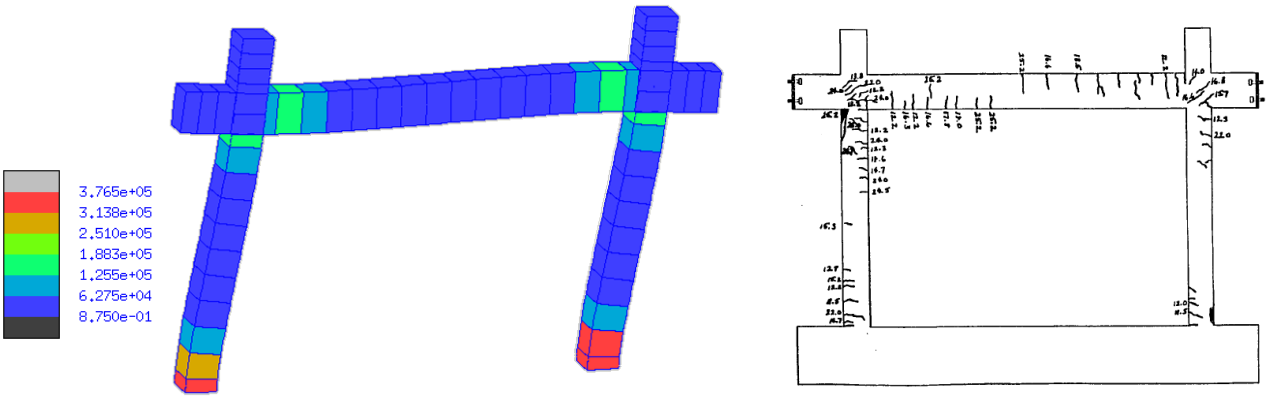

(a) (b)

Figure 72 Damage pattern: (a) numerical (strain energy contour in N mm, deformed shape with 5x amplification); (b) experimental (Mehrabi, 1994)

4.4 Multi-dimensional analysis framework

The complex interaction between the frame and infill plays a key role in the overall response of infilled frames subjected to horizontal loading. This interaction involves a continuous dynamic transfer of forces between the components and is particularly crucial in the early stages of the analysis, determining the infill-frame detachment and the subsequent formation of a compression diagonal strut.

In the infilled-frame models presented in this section, the frame-infill interface is represented using interface elements developed by Minga et al. (2018). These elements were previously utilised in Chapter 3 for URM mesoscale modelling and are characterised by a frictional-cohesive constitutive relationship, which effectively captures opening and sliding mechanisms.

Masonry infills are modelled employing either mesoscale or continuum macroscale strategies, while the surrounding frame is modelled following the strategy of Section 4.3. Notably, the surrounding frame and the masonry infill are characterised by nodes with a different number of degrees of freedom (DoF). Specifically, nodes within the masonry-infill model, whether employing a mesoscale or macroscale approach, are characterised by 3 DoF, while nodes within the frame have 6 DoF. To connect the two components, the multidimensional strategy presented in G. Jokhio (2012) is employed, allowing the coupling of the 3D masonry model with the 1D beam/column finite elements. This approach offers an alternative method, mitigating computational burden, to the typical analysis of infilled frames, where typically structural members are modelled with the same dimensional order as the infill masonry panels, using continuum 2D or 3D solid finite elements.

Figure 73 depicts an illustration of the master-slave procedure as described in G. Jokhio (2012). The 8 nodes located on the outer side of the frame-infill interface, considered as slave nodes, are required to rigidly move, thereby maintaining their relative positions. These slave nodes move accordingly to translations and rotations of the master node, which is either a node rigidly connected to a node within the frame (Figure 74a) or a frame node itself (Figure 74b). The displacement vector U_i of the generic slave node i, given by the translations along the x, y and z directions, as per relation (12), is determined by deriving it from the displacement vector U_m of the master node m, encompassing translations u, v, w and rotations α, β, γ, as per relation (13). This is given by the matrix product involving the rotation matrix (14), which is a function of rotations and is derived in (Izzuddin and Elnashai, 1993), together with the position of the slave node (x_i, y_i, z_i).

$$U_i = \left[U_x\ U_y\ U_z\right]_i^T \tag{12}$$

$$U_m = [u\ v\ w\ \alpha\ \beta\ \gamma]^T \tag{13}$$

$$U_i = \begin{pmatrix} u \\ v \\ w \end{pmatrix} + T_r(\alpha, \beta, \gamma) \begin{pmatrix} x_i \\ y_i \\ z_i \end{pmatrix} \tag{14}$$

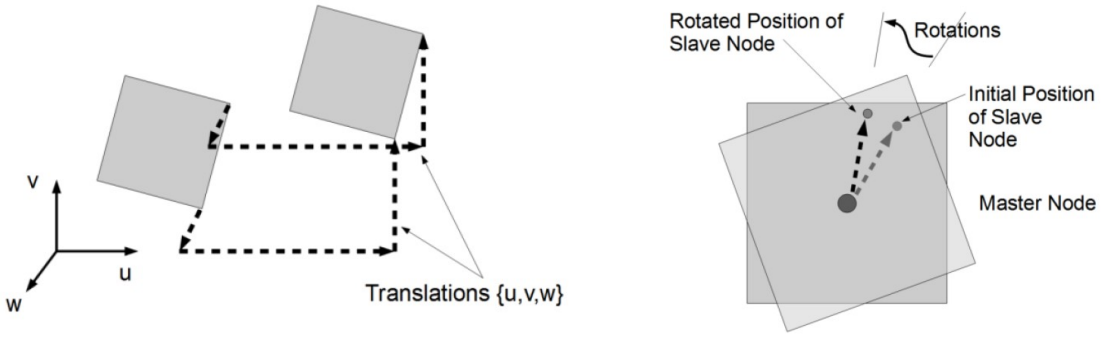

(a) (b)

Figure 73 Master-slave displacement congruence: (a) effect of translation of master node; (b) effect of rotation of master node (images taken from G. Jokhio, 2012)

As mentioned, the master node can be a structural node positioned at the centre of the interface and connected to a node on the frame through a rigid link, following the approach presented in (Macorini and Izzuddin, 2014) and in (Xavier, 2015), as illustrated in Figure 74a. However, in the present study, an alternative approach is adopted wherein the master-slave relations are directly established between the interface nodes and the corresponding frame node, as depicted in Figure 74b. This direct application is preferred due to the observed higher numerical robustness. Notably, the numerical response of the two scenarios closely aligns, as evidenced in Figure 75, which presents shear-displacement curves for the infilled-frame models with and without the rigid link under horizontal loading.

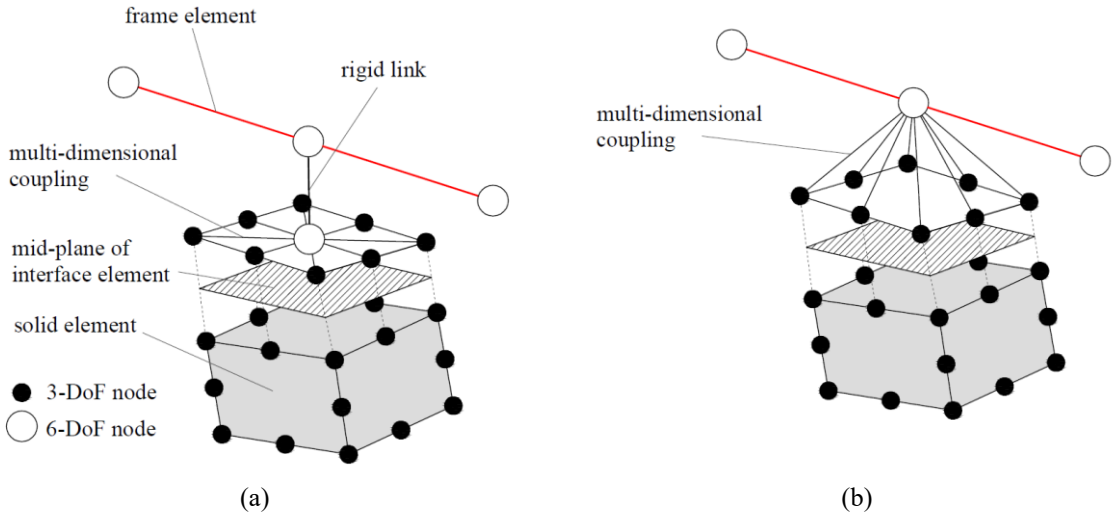

Figure 74 Multi-dimensional coupling for connecting URM components with beam-column elements: (a) with rigid link; (b) without rigid link

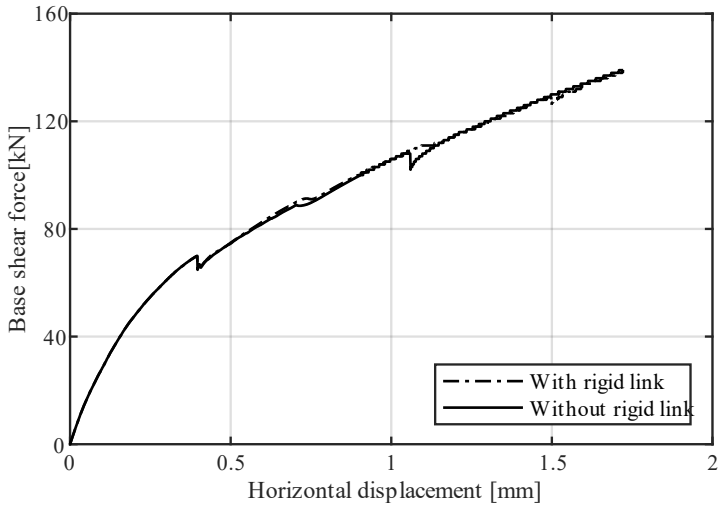

Figure 75 Application of multi-dimensional coupling with and without rigid link

The computational efficiency of these models can be further enhanced by applying a partitioned hierarchical strategy, as detailed in Section 2.3.2. This strategy not only tackles the computational burden but is also necessary to implement together the different components, surrounding frame and infill, characterised by different degrees of freedom.

The two techniques, multi-dimensional coupling along with hierarchical partitioning, have been previously integrated together in the modelling of infilled frames in (Macorini and Izzuddin, 2014) and in (Xavier, Macorini, and Izzuddin, 2014). In this approach, the RC frame is considered as the primary parent structure, while the masonry infill is assigned to a lower partitioning rank. Furthermore, the infill

can be either modelled as a monolithic element or can undergo hierarchical partitioning itself. In the latter case, there is a "child-rank 0" structure, which is considered as the "parent" structure of the infill. This structure enables the two-way communication between the frame and infill, incorporating also the external frame-infill interfaces. The infill can be then recursively partitioned into multiple partitions. In the example depicted in Figure 76, the infill is divided into four partitions. This particular specification will be applied for modelling infilled frames with mesoscale infill (Chapter 4.5), thus incorporating one "child-rank 0" element and four additional "child-rank 1" elements. On the other hand, when dealing with macroscale infill (Chapter 4.6), which is computationally less demanding, the infill will be treated as monolithic, representing a hierarchical partitioning with only one "child-rank 0" structure.

For illustrative purposes, the flowchart in Figure 77 outlines a scenario where the infill wall is initially partitioned into n child domains at the first level (rank 1). Each of these partitions is subsequently divided into m sub-partitions (where m may vary among the partitions), and this procedure may continue further at lower levels.

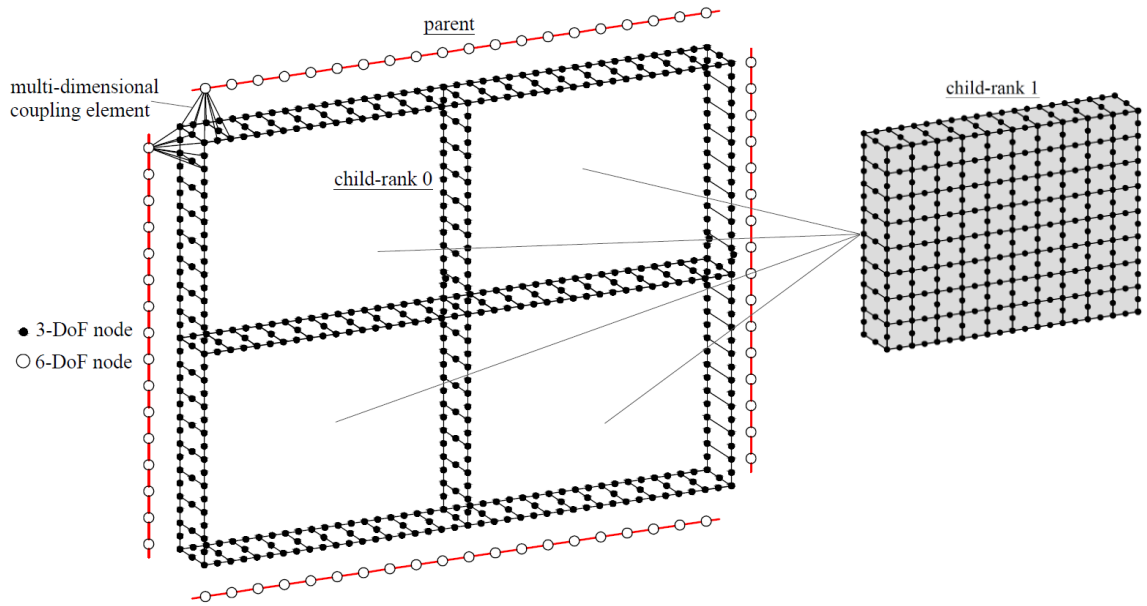

Figure 76 Application of parallel computing procedure with dual partition super-elements to the modelling of infilled-frames

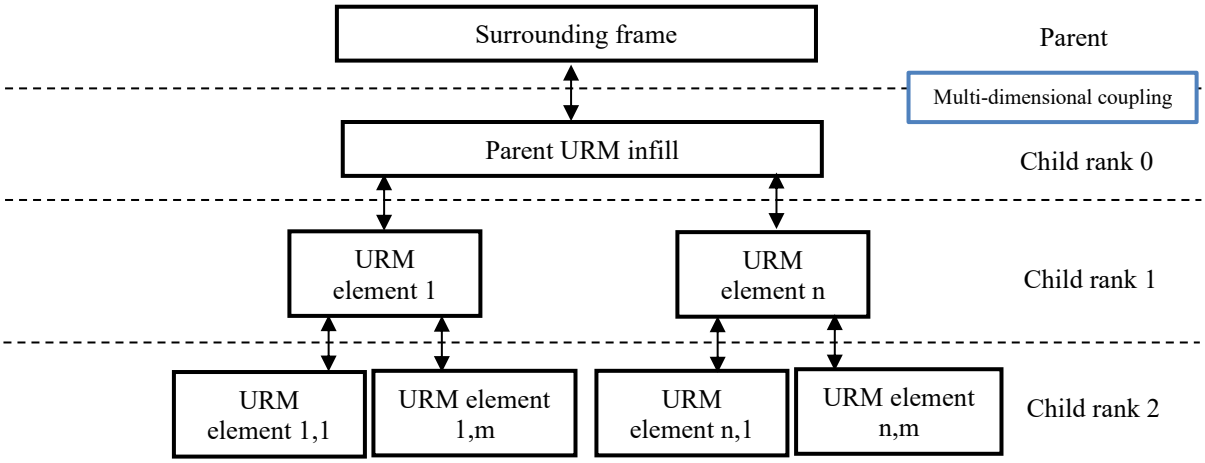

Figure 77 Flowchart for the computational processes in a parallel analysis with frame-infill multi-dimensional coupling and 2-level hierarchic partitioning

4.5 Mesoscale modelling

In this section, a mesoscale approach is implemented for the model of infilled-frame corresponding to Specimen 3, presented in Section 4.2. The infill dimensions are 2096 x 1423 mm², comprising solid concrete blocks measuring 92 mm × 92 mm × 194 arranged in a running pattern. The bed and head mortar layer joints are 9.5 mm thick. The mesoscale representation follows the exact texture of the masonry. Second-order linear elastic brick elements, defined by 20 nodes, are employed in conjunction with cohesive-frictional interfaces, the latter adopting the model developed by (Minga et al., 2018). Interface elements are differentiated into mortar head-joints, mortar bed-joints, and brick-brick interfaces. Moreover, the external frame-infill interfaces are represented using the same cohesive-frictional model. The connection to the external frame is established through the multi-dimensional coupling element as described in Section 4.4. The bare-frame model validated in Section 4.3 is adopted for representing the surrounding RC frame. Overall, the developed mesh comprises 300 solid elements, 635 interface elements, and 112 beam elements, with 6560 3-DoF nodes and 109 6-DoF nodes. Moreover, the partitioning approach is employed by considering four rank-1 partitions representing the infill. The infilled-frame model is subjected to the same external actions as the bare-frame, illustrated in Figure 70. Figure 78 visually represents the infilled-frame model.

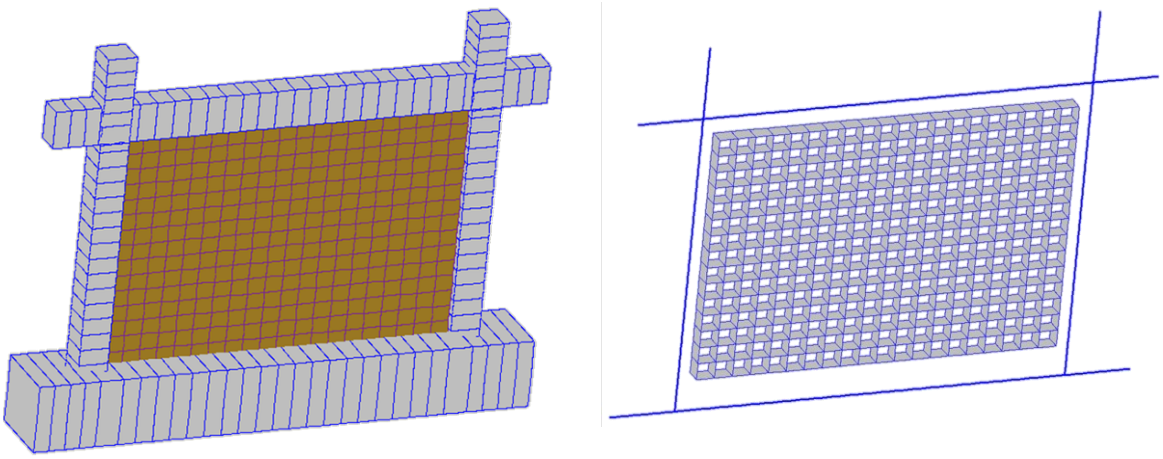

(a) (b)

Figure 78 Views of the infilled-frame mesoscale model: (a) extruded frame and infill brick elements, and (b) infill interfaces

4.5.1 Material characterisation

An objective calibration of the mechanical characteristics of the infill and frame-infill boundary interfaces is carried out. The calibration details for the various parameters involved are provided below, with the adopted values for analysis presented in Table 19.

- Internal interfaces stiffnesses

  These interfaces are assessed based on the tangent elastic modulus of masonry, estimated at 14300 MPa, derived from the results of the compression test (the stress-strain experimental curves are provided by Mehrabi, 1994). Considering an elastic modulus of the concrete bricks as 20000 MPa, a Poisson's coefficient of 0.2, and dimensions including bricks height of 92 mm and mortar layer thickness of 9.5 mm, the determination of joint interfaces, both normal ($k_{n,ji}$) and tangential ($k_{t,ji}$), is conducted through relations (5) and (8). High stiffnesses are set for brick-brick interfaces ($k_{n,b}$ and $k_{t,b}$).
- External frame-infill interfaces stiffnesses

  To ensure the impenetrability condition between the frame and infill, a high value should be assigned to the normal stiffness, allowing for a small but negligible penetration between the bodies during the elastic phase (Mosalam et al., 1993). The normal stiffness ($k_{n,je}$) is roughly determined as the ratio between the elastic modulus of mortar and the thickness of the mortar layer; this value is then divided by 10 to prevent potential convergence issues arising from

excessive stiffness (the values still remain considerably high if compared to the internal interfaces). The tangential stiffness ($k_{t,je}$) is then calculated through equation (8).

- Shear-tensile behaviour of internal mortar joints

  The results of triplet shear tests, outlined in Table 9, allow to determine cohesion (c_{ji}) and friction coefficient ($\tan\varphi_{ji}$) of the mortar joints interfaces. Figure 79 reports the linear regression curves of both peak strength and residual strength registered in the tests as functions of vertical stress. Subsequently, cohesion is determined as the intercept of the peak regression, measured at 0.11 MPa. As for the friction coefficient, the average of the slopes from the two regressions is adopted, equal to 1.02. The tensile bond strength ($f_{t,ji}$) is estimated as the cohesion divided by 1.4, following the suggestion reported in (Lourenço and Gaetani, 2022). Moreover, the fracture energies of Mode I ($G_{I,ji}$) and Mode II ($G_{II,ji}$) failures are defined, respectively, as 0.016 N/mm and 0.16 N/mm, as specified in Chapter 3.3.1.

- Tensile behaviour of brick-brick joints

  The tensile strength ($f_{t,b}$) is calculated as a function of compressive strength of the units ($f_{c,b}$) through relation (15), provided by Lourenco and Gaetani (2022), while the fracture energy ($G_{I,b}$) is determined through relation (10).

$$f_{t,b} = 2.12\ \ln\left(1 + 0.075\, f_{c,b}\right) \tag{15}$$

- Compression response of internal interfaces

  Bed-joints ($f_{c,h}$) are characterised by the experimental compressive strength of masonry, while, to account for the orthotropic response of masonry, the vertical joints compressive strength ($f_{c,v}$) for both mortar and internal brick interfaces is estimated as the 50% of the experimental compressive strength. The fracture energies, both in vertical and horizontal directions, are consequently determined through the Model Code 90 formulation (equation (9)).

- External frame-infill interfaces strength parameters

  The mechanical characteristics of external frame-infill interfaces are typically weaker than the mortar interfaces internal to the infills and are not known with a good degree of confidence. In this context, these mechanical characteristics are set with low values - specifically, the bond strength at 0.01 MPa, cohesion at 0.014 MPa, and the friction coefficient at 0.35. The frame-infill interfaces are configured to simulate only opening and sliding mechanisms, as they are modelled with high compressive strength. This feature aims to represent the high compression strength of columns and beams perpendicular to the fibres and to hinder excessive interpenetration between the infill and the frame.

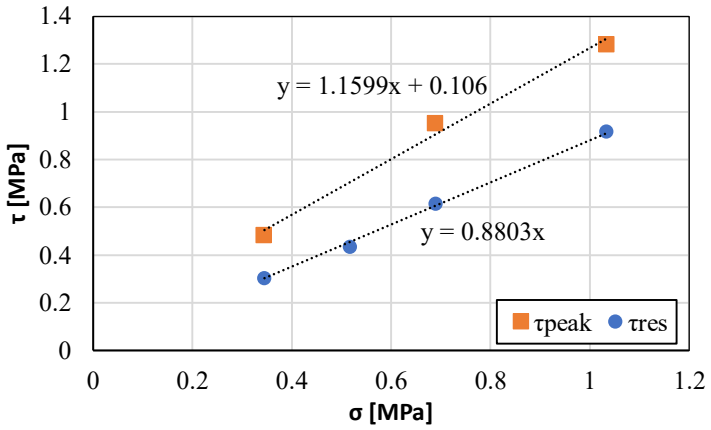

Figure 79: Evaluation of cohesion and coefficient of friction of mortar joints from triplet shear tests results

Table 19 Mechanical characterisation of the infill mesoscale model (subscript specification: n=normal; t=tangential or tensile; ji=internal joint; je=external joint; h=horizontal interface; v=vertical; b=brick; c=compression/crushing)

Parameter			Symbol	u.o.m.	
Units elastic parameters		Elastic modulus	E_b	N/mm^2	20000
		Poisson's coefficient	ν_b	-	0.2
Internal interfaces stiffness parameters	Mortar joints	Normal stiffness	$K_{n,ji}$	N/mm^3	491.9
		Tangential stiffness	$K_{t,ji}$	N/mm^3	196.8
	Bricks	Normal stiffness	$K_{n,b}$	N/mm^3	10^4
		Tangential stiffness	$K_{t,b}$	N/mm^3	10^4
External interfaces stiffness parameters		Normal stiffness	$K_{n,je}$	N/mm^3	2533
		Tangential stiffness	$K_{t,je}$	N/mm^3	1055
Internal interfaces strength parameters	Mortar joints (horizontal and vertical)	Cohesion	c_{ji}	N/mm^2	0.11
		Friction coefficient	$\tan\varphi_{ji}$	-	1.02
		Bond strength	$f_{t,ji}$	N/mm^2	0.08
	Bricks	Tensile strength	$f_{t,b}$	N/mm^2	1.61
	Horizontal interfaces (mortar bed joints)	Compressive strength	$f_{c,h}$	N/mm^2	15.10
	Vertical interfaces (mortar head-joints and bricks)		$f_{c,v}$	N/mm^2	7.55
Internal interfaces fracture energies	Mortar joints (horizontal and vertical)	Mode I	$G_{I,ji}$	N/mm	0.016
		Mode II	$G_{II,ji}$	N/mm	0.16
	Bricks	Mode I	$G_{I,b}$	N/mm	0.09
	Horizontal interfaces (mortar bed-joints)	Crushing	$G_{c,h}$	N/mm	20.67
	Vertical interfaces (mortar head-joints and bricks)		$G_{c,v}$	N/mm	18.02
External interfaces strength parameters		Cohesion	c_{je}	N/mm^2	0.014
		Friction coefficient	$\tan\varphi_{je}$	-	0.35
		Bond strength	$f_{t,je}$	N/mm^2	0.01
External interfaces fracture energies		Mode I	$G_{I,je}$	N/mm	0.01
		Mode II	$G_{II,je}$	N/mm	0.10

4.5.2 Analysis results

The shear-displacement response of the infilled-frame model is depicted in Figure 80, along with the bare-frame model response and the experimental results. The prediction of the capacity curve is satisfactory, showing good accuracy in estimating the initial stiffness and stiffness decay after the detachment of the infill. Although there is a slight overestimation of the maximum strength, it remains within 10%. The representation of the post-peak strength decay is well captured. Moreover, a significant

correspondence with the experiment is observed in the damage pattern, as illustrated in Figure 81. The primary diagonal crack evident in the experimental specimen is also present in the infill models, and the overall cracking damage reflects the experimental observations. Notably, the corner crushing responsible for reaching the ultimate resistance is reproduced. The damage to the frame is partially captured, including the damage at the top of the left-hand side column (which is also subjected to shear damage at large displacements) and at the bottom of the right-hand side column. However, the cracking observed at the centre of the top beam, possibly induced by a concentrated load exerted after a potential shift of the diagonal strut, is not reproduced in the model. In contrast, in the model, this effect manifests after the infill cracking resulting in damage at the middle of the left column.

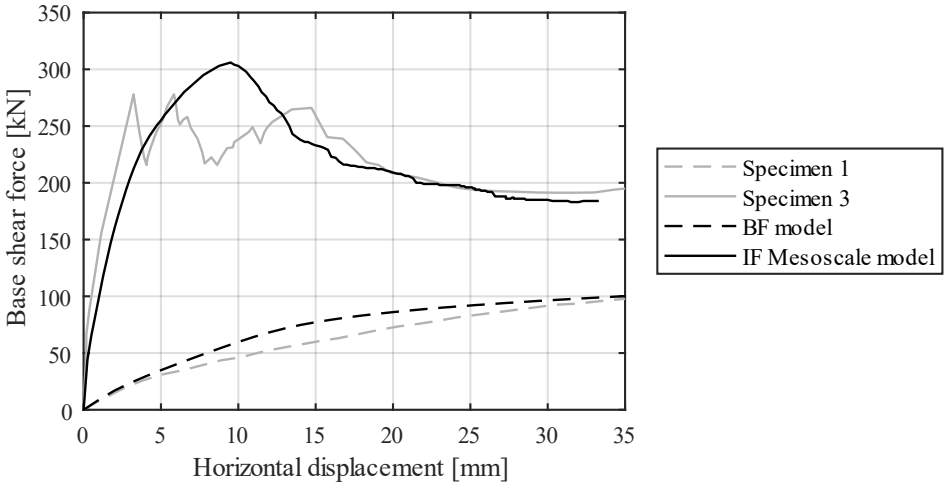

Figure 80 Shear-displacement response of bare-frame and mesoscale infilled-frame: comparison between experimental and numerical results

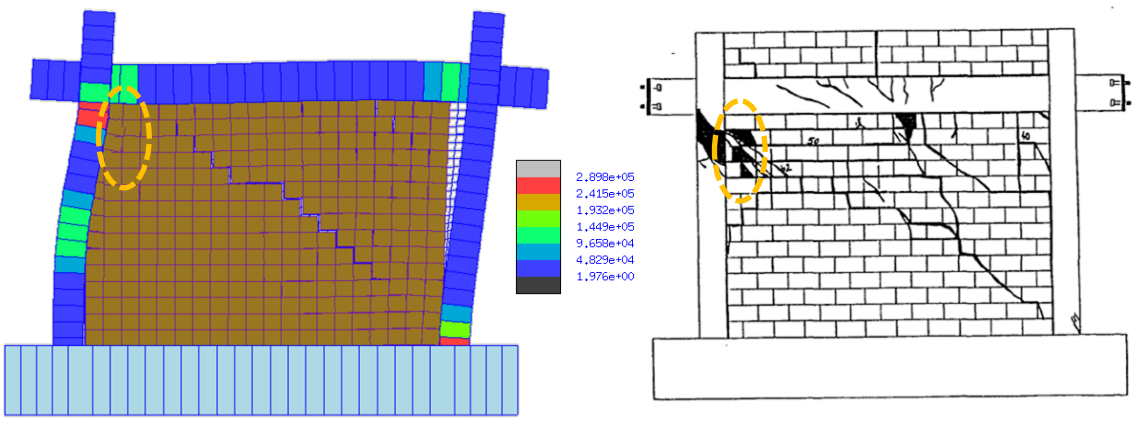

(a) (b)

Figure 81 (a) Deformed shape (5x amplification) at the last step reached with the contour on the frame indicating strain energy (values in legend expressed in N mm); (b) experimental damage pattern (Mehrabi, 1994)

Distinct phases are recognised as the imposed displacement increases. Initially, the infilled-frame behaves "monolithically", immediately followed by the detachment of the infill from the frame at the non-loaded corners (top-right and bottom-left corners) and by the onset of diagonal cracking within the infill. The cracks propagate throughout the infill, leading to a gradual decrease in stiffness. The applied force increases until reaching the maximum capacity, determined by crushing of the infill at the corner. Beyond this point, the strength of the infilled frame decreases, and the action is progressively transferred from the infill to the frame.

The different phases are depicted in various moments throughout the analysis through different representations: Figure 82 illustrates the principal stresses in the brick units of the infill, while Figure 83 and Figure 84 show the tensile and crushing damage of the interfaces, respectively.

Following the application of the vertical loads on the columns, the stress state is primarily concentrated on the sides of the infill (Figure 82a). This is accompanied by damage to interfaces at the middle-top of the infill (Figure 83a). As the displacement increases, the detachment of the infill from the frame occurs, and at around 1.5mm, the initiation of diagonal cracking begins. By this moment, the diagonal compressive strut is already developed (Figure 82b), slightly shifted downward and partially divided due to the presence of the crack. The latter is clearly observable by the damage state of the interfaces (Figure 83b). As the cracking state spreads, the diversification of the strut into two branches becomes more evident (Figure 82c), with the larger one continuing to translate downward as the interfaces above the diagonal become more damaged (Figure 83c). The reaching of the peak strength is marked by the onset of crushing damage at the corner (Figure 84a), which starts from a single vertical interface element and then involves more and more vertical ones (Figure 84b). As the crushing occurs, the inclination of the strut decreases, leading to a concentration of stresses not only at the corner but also in the middle of the left-hand side column (Figure 83d), responsible for its damage (as observed in Figure 81a).

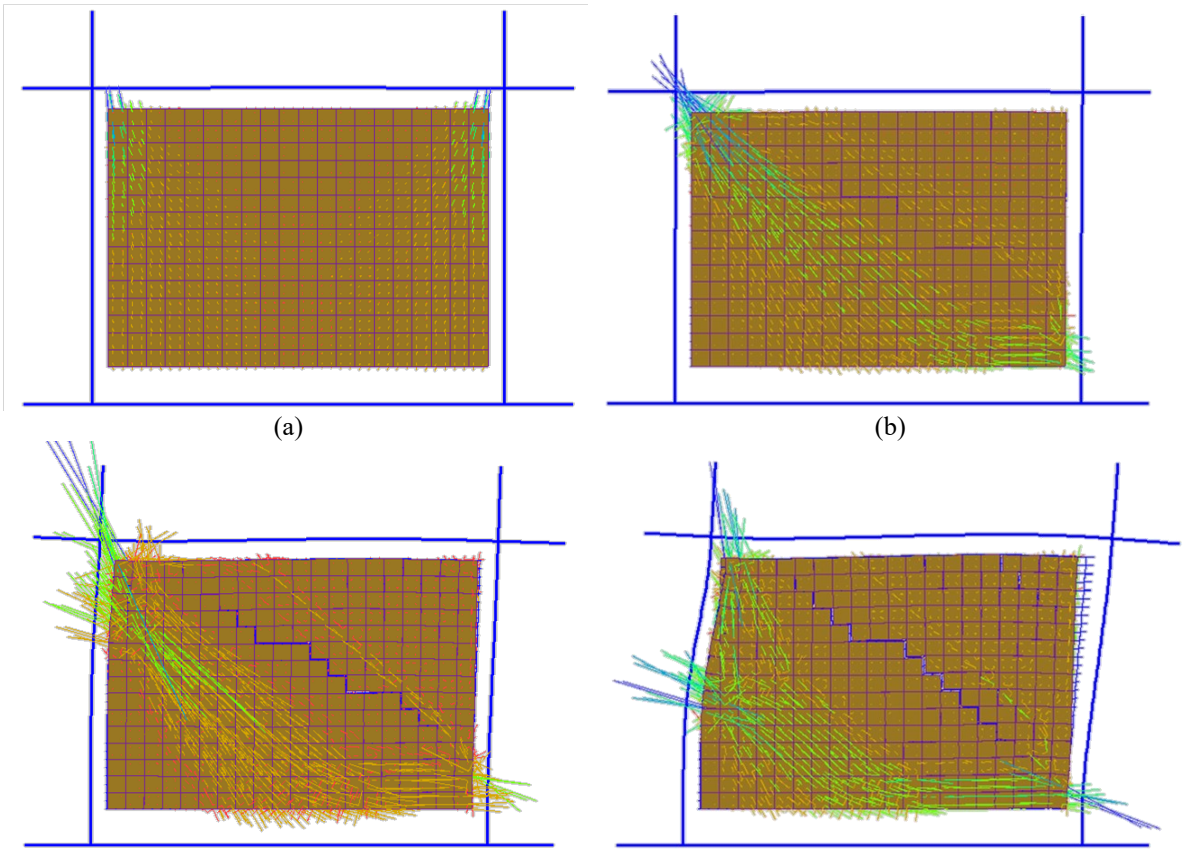

Figure 82 Representation of principal stresses throughout the analysis - (a) after the vertical load application, (b) at a horizontal displacement of 1.5mm, (c) at the peak-strength, and (d) at the last step (deformed shapes with 5x amplification)

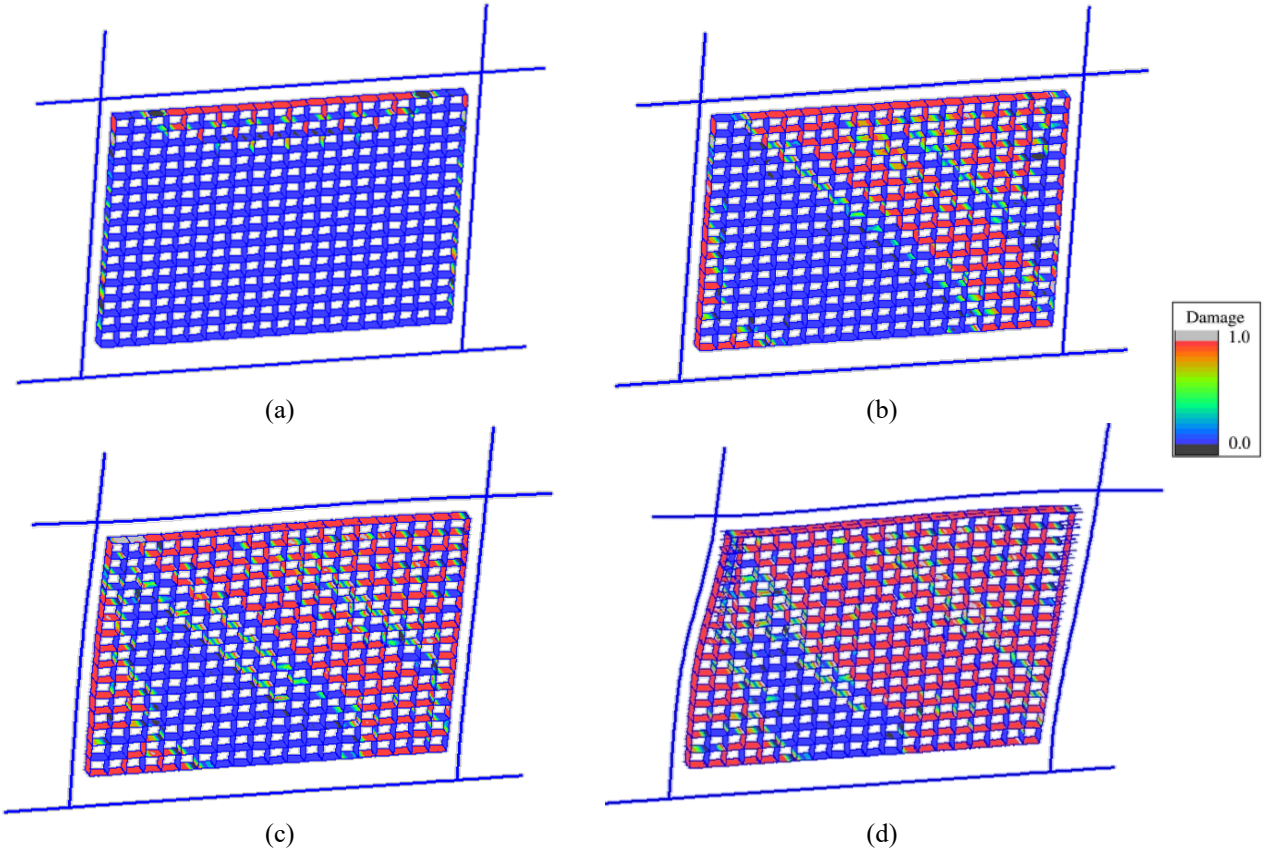

Figure 83 Representation of interfaces tensile damage throughout the analysis - (a) after the vertical load application, (b) at a horizontal displacement of 1.5mm, (c) at the peak-strength, and (d) at the last step (deformed shapes with 5x amplification)

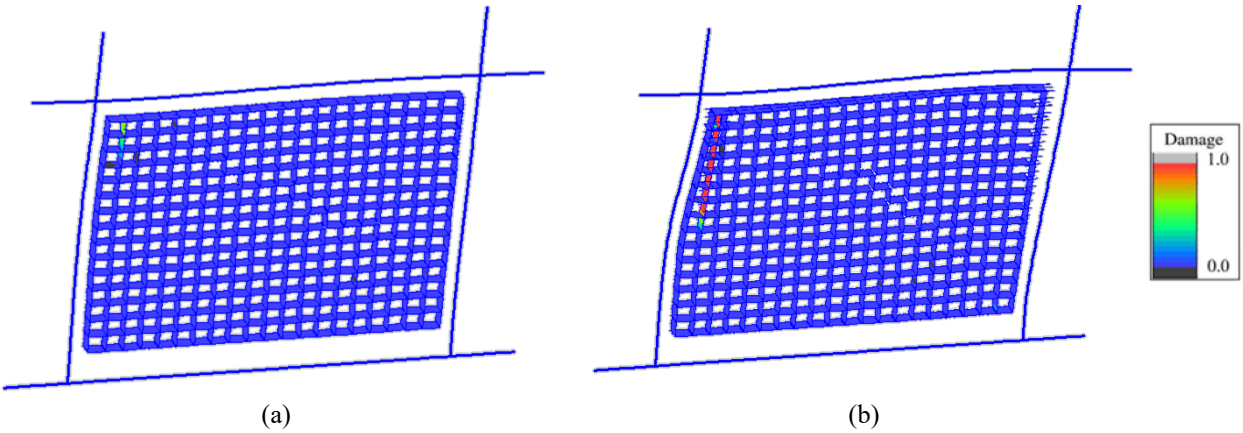

Figure 84 Representation of interfaces crushing damage (a) at the peak-strength, and (b) at the last step (deformed shapes with 5x amplification)

4.5.3 Sensitivity analysis

Within the calibration of the mechanical properties, several parameters were selected without complete confidence, as is common, by considering suggested values or analytical relations from literature. Assuming no awareness of the experimental outcome, sensitivity analyses are conducted to evaluate how the response may vary based on the analyst's choices. In particular, the situations assessed are listed below, while all the characterisations evaluated are reported in Table 20**.**

- Variant 1: Strength parameters of the external frame-infill interfaces
  Previously assessed with weak mechanical characteristics, they are also examined by adopting the same values as the internal mortar interfaces (defining the variant denoted as "Var 1.1") and by considering the average of the two scenarios ("Var 1.2").
- Variant 2: Stiffnesses of the external interfaces
  Further assessed considering one-tenth (resulting in stiffness values lower than the stiffnesses of the mortar interfaces internal to the infill; “Var 2.1”) or ten times (“Var 2.2”) the reference values.
- Variant 3: Horizontal strength of masonry
  One alternative evaluation involves the estimation of a diagonal-like compressive strength (denoted as $f_{c,diag}$) within the variant “Var 3.1”, using equation (16). This strength is determined by the slope (α) of the diagonal of the infill (equal to 35°), assuming a linear variation between the horizontal and the vertical values. The other alternative considers the vertical strength itself (“Var 3.2”). In both the situations, the crushing energies are determined through the Model Code 90 relation (9), coherently with the reference model.

$$f_{c,diag} = f_{c,h} + \frac{f_{c,v} - f_{c,h}}{90}\alpha \tag{16}$$

- Variant 4: Crushing fracture energies
  Contrarily, while maintaining the same compression strengths, the assessment of crushing energies, both horizontal and vertical, considers two alternatives. One (“Var 4.1”) is based on the relation (17), recommended by Lourenco and Gaetani (2022), while the other (“Var 4.2”) is provided by the analytical expressions (18) and (19), which distinguish between horizontal and vertical interfaces. These expressions are derived from linear regressions from experimental test results reported in (Jafari et al., 2022).

$$G_c = 32\, f_c/(10 + f_c) \tag{17}$$
$$G_{c,h} = 0.57\, f_{c,h} + 14.7 \tag{18}$$

$$G_{c,v} = 2.99\, f_{c,v} \tag{19}$$

- Variant 5: Internal joint fracture energies

  The variants, "Var 5.1" and "Var 5.2", are defined through the range provided for $G_{I,ji}$ and $G_{II,ji}$ in Table 8.

Table 20 Variants material characterisation for mesoscale infill model.

Variant 1 - External interfaces strength parameters					
Parameter	Symbol	u.o.m.	Ref.	Var 1.1	Var 1.2
Cohesion	c_{je}	N/mm^2	0.014	0.11	0.07
Friction coefficient	$\tan\varphi_{je}$	-	0.35	1.02	0.86
Bond strength	$f_{t,je}$	N/mm^2	0.010	0.08	0.05
Variant 2 - External interfaces elastic parameters					
Parameter	Symbol	u.o.m.	Ref.	Var 2.1	Var 2.2
Normal stiffness	$K_{n,je}$	N/mm^3	2533	253.3	25330
Tangential stiffness	$K_{t,je}$	N/mm^3	1055	105.5	10550
Variant 3 - Horizontal compressive strength (crushing energy accordingly)					
Parameter	Symbol	u.o.m.	Ref.	Var 3.1	Var 3.2
Vertical interfaces compressive strength	$f_{c,v}$	N/mm^2	7.55	10.50	15.10
Vertical interfaces crushing energy	$G_{c,v}$	N/mm	18.02	19.11	20.67
Variant 4 - Crushing fracture energies					
Parameter	Symbol	u.o.m.	Ref.	Var 4.1	Var 4.2
Horizontal interfaces crushing energy	$G_{c,h}$	N/mm	20.67	19.25	23.31
Vertical interfaces crushing energy	$G_{c,v}$	N/mm	18.04	13.77	22.57
Variant 5 - Internal joints fracture energies					
Parameter	Symbol	u.o.m.	Ref.	Var 5.1	Var 5.2
Mode I fracture energy	$G_{I,ji}$	N/mm	0.016	0.005	0.035
Mode II fracture energy	$G_{II,ji}$	N/mm	0.16	0.014	0.25

The numerical responses for all the situations assessed are given in Figure 85. The impact of the strength parameters of the external interfaces is significant. Specifically, if no distinction is made between internal and external interfaces, the predicted maximum strength results 35% higher. On the other hand, the assessment of stiffnesses of the external interfaces, shows no significant influence. A strong influence is also noticed, as expected, for the horizontal compression strength, particularly important in the context of infilled frame. If the experimental compression strength is used for the vertical interfaces as well, the maximum force reached is almost 30% higher. The evaluation of the crushing fracture energy has a minor impact on the capacity curve, although still significant, with variations within plus or minus 5% of the maximum strength and translations of the displacements corresponding to the peak strength. Finally, no variations are noticed with the variants related to the fracture energies of the internal joints.

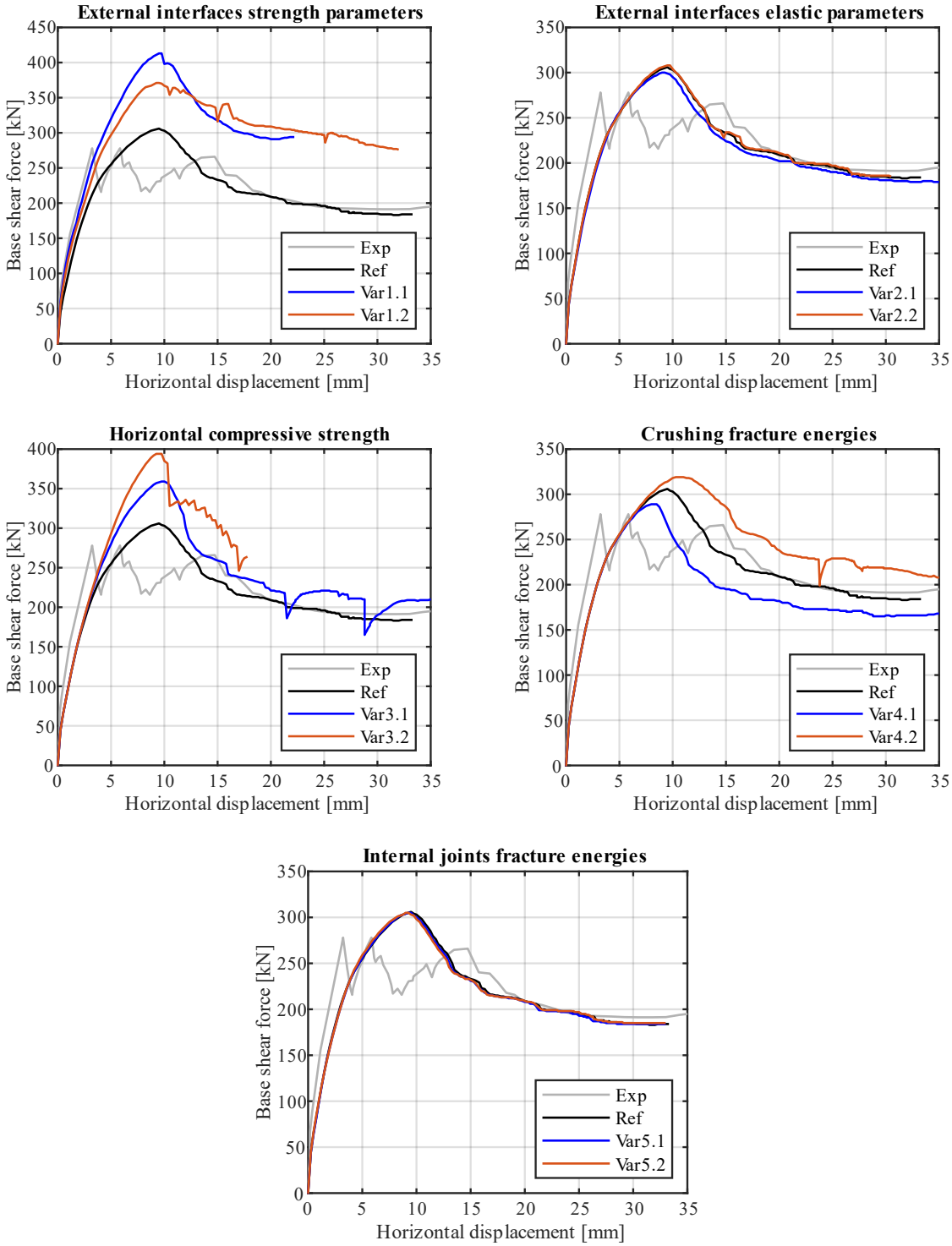

Figure 85 Shear-displacement curves from the variant mesoscale models.

4.6 Continuum macroscale modelling

In this section, the infilled-frame model is implemented using a continuum macroscale approach to represent the masonry infill. Second-order brick elements, characterised by the concrete damage plasticity law (CDP), are employed within the adoption of a 15x10 elements mesh discretisation. The frame-infill interfaces are represented also here using the element proposed in (Minga et al., 2018). The validated bare-frame model from Section 4.3 is adopted to represent the RC frame. Overall, the developed model includes 150 solid elements, 50 interface elements, and 92 beam elements, with a total of 1578 3-DoF nodes and 89 6-DoF nodes. Moreover, given the lower computational burden with respect to the mesoscale model, a monolithic partitioning approach is employed, by considering a single rank-0 element representing the infill. Figure 86 illustrates the infilled-frame model.

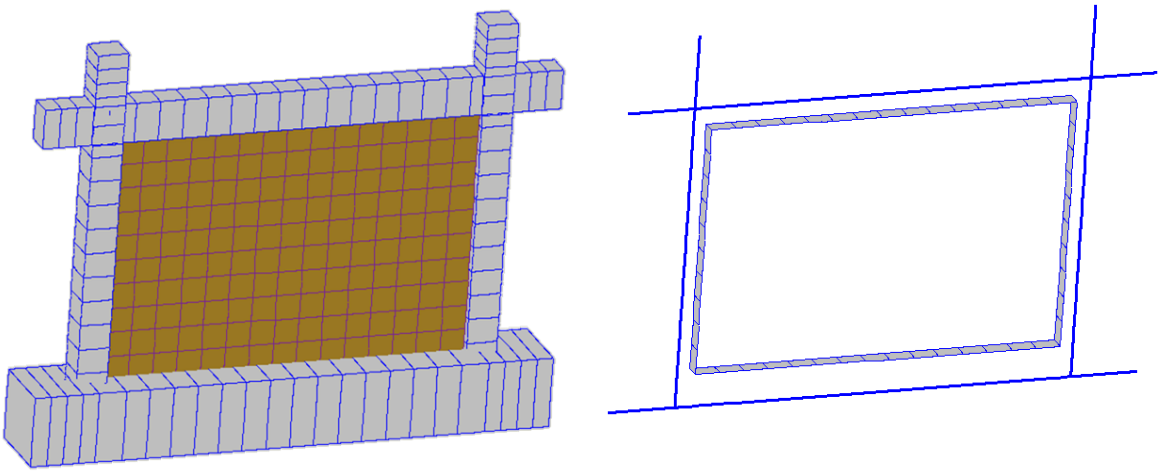

(a) (b)

Figure 86 Views of the infilled-frame continuum macroscale model - (a) Extruded frame and infill brick elements, and (b) external infill interfaces

4.6.1 Material characterisation

As previously done for the mesoscale model, an objective calibration of the mechanical characteristics of the infill and frame-infill boundary interfaces is carried out. The parameters adopted for the analysis are presented in Table 21. The main considerations are as follows:

- External frame-infill interfaces

  The strength and stiffness parameters align with those employed in the mesoscale model (Table 19).

- Masonry elastic modulus

  Estimated as a diagonal-like value (denoted as E_{diag}) through relation (20), considering a linear interpolation between the vertical elastic modulus (E_v, assumed as the initial tangent modulus derived from the compression test on the wallet, estimated at 14300 MPa) and the horizontal modulus (E_h, assessed as 0.7 times the vertical one, as suggested by Jafari et al., 2022).

$$E_{diag} = E_h + \frac{E_v - E_h}{90}\alpha \tag{20}$$

- Masonry compressive strength

  Since the material is isotropic, it is assessed as 50% of the vertical one to account for possible compressive failure in the horizontal direction, as previously done.

- Masonry tensile strength

  Estimated by considering two mechanisms of diagonal cracking:

  - Stepped-crack mechanism: Links the tensile strength to the cohesion of the mortar joint, the height of the unit, and the overlapping length through equation (11), resulting in a tensile strength of 0.12 MPa.
  - Straight-crack mechanism: Involves the failure of units and head joints, with the suggested masonry tensile strength being 50% of the tensile strength of the unit, as suggested by (Lourenco and Gaetani (2022) (the tensile strength of the unit is taken from
  - Table 15), resulting in a masonry tensile strength of 0.82 MPa.

  In this context, the tensile strength is estimated as the average of these two values.

- Dilatancy angle

  Set at a low value of 10°, given the high confining stress level provided by the surrounding frame.

- Other values are derived from Chapter 3.4.1.

Table 21. Reference characterisation and variant case studies for the panels analyses the variable parameters are reported in shaded cells.

Parameter		Symbol	U.o.m.	Reference values
Infill - Concrete Damage Plasticity				
Young's modulus		E	[MPa]	11660
Poisson's coefficient		ν	[-]	0.2
Dilatancy angle		ψ	[°]	10
Ratio between biaxial and uniaxial compressive strength		f_{b0}	-	1.16
Flow potential eccentricity		ε	-	0.1
Ratio of the second stress invariant on the tensile meridian to that on the compressive meridian at initial yield		K_c	-	0.66
Tensile strength		f_t	[MPa]	0.47
Tensile fracture energy		G_t	[N/mm]	0.02
Stiffness degradation		μ	[-]	0.2
Maximum compression strength		f_c	[MPa]	7.55
Ratio between uniaxial yielding stress and maximum strength in compression		f_{yr}	[-]	0.3
Plastic strain in compression		$k_{c,fmax}$	[-]	0.002
Tensile stiffness recovery		w_t	[-]	0
Compressive stiffness recovery		w_c	[-]	1
Frame-infill interfaces				
External interfaces strength parameters	Cohesion	c_{je}	N/mm^2	0.014
	Friction coefficient	$\tan\varphi_{je}$	-	0.35
	Bond strength	$f_{t,je}$	N/mm^2	0.01
External interfaces fracture energies	Mode I	$G_{I,je}$	N/mm	0.01
	Mode II	$G_{II,je}$	N/mm	0.10

4.6.2 Analysis results

The response obtained with the macroscale model is accurate and comparable to the prediction of the more refined mesoscale model, showing good predictions for stiffness, maximum strength, and post-peak behaviour (Figure 87). However, some discrepancies are observed: a slight overestimation of the stiffness decay after the detachment of the infill, a minimal overestimation of the maximum strength (within 10%), and a more noticeable underestimation of the residual strength, amounting to 22% at 35 mm of displacement. The observed damage pattern aligns with both experimental findings and the mesoscale model response (Figure 88), with similarities regarding the tensile damage, assimilable to the experimental diagonal cracking damage, and the crushing of the masonry at the corner, responsible for the reaching of the peak strength. Moreover, a similar damage state is observed in the reinforced concrete frame.

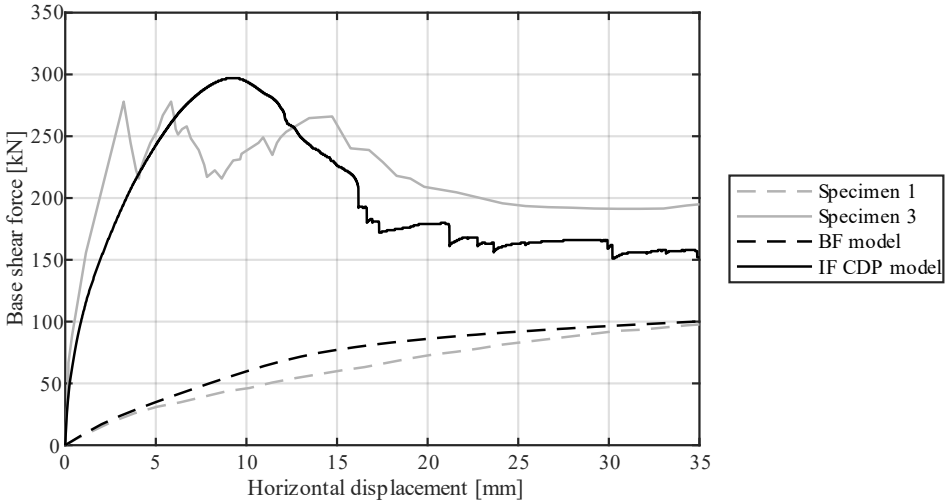

Figure 87 Shear-displacement response of bare-frame and continuum macroscale infilled-frame: comparison between experimental and numerical results.

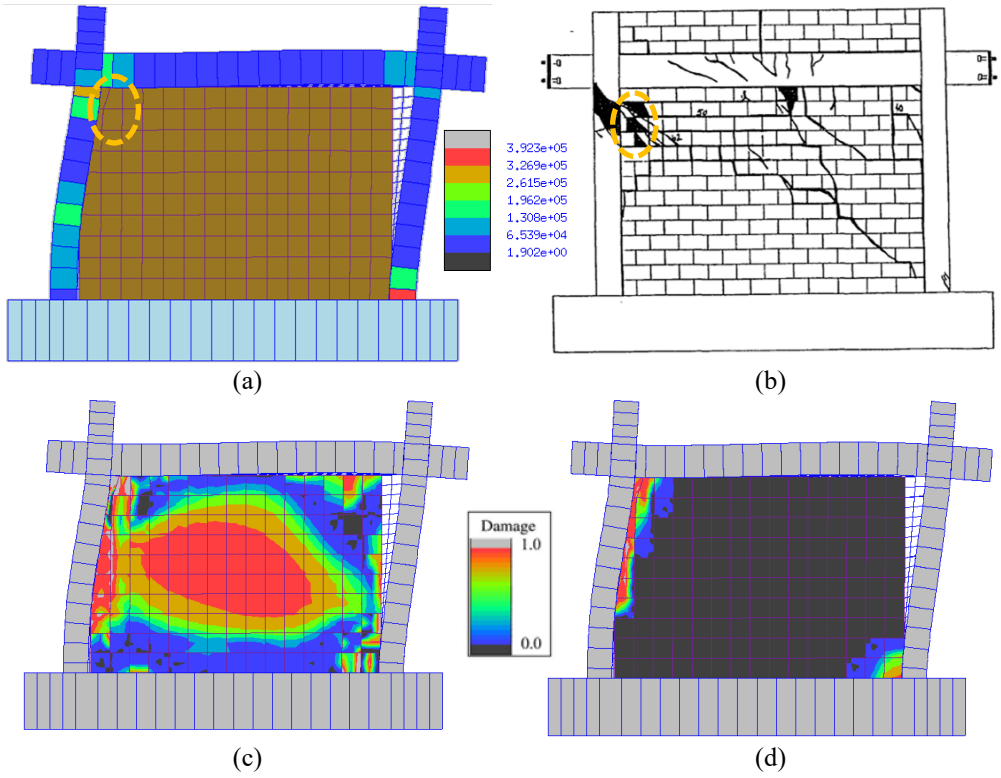

Figure 88 (a) Deformed shape (5x amplification) at the last step (35mm) with contours on the frame indicating strain energy (values in legend expressed in N mm); (b) experimental damage pattern (Mehrabi, 1994); (c) tensile and (d) compressive damage of the infill at the last step

The same characteristic phases identified in the mesoscale modelling are also observed within the macroscale modelling. Figure 89 illustrates the progression of the stress state, depicting the diagonal strut following a similar development pattern, although with a different distribution and more

concentrated stresses on the corners. After reaching the peak-strength, the diagonal strut deviates downward, resulting in stress concentration in the middle of the left-hand side column. Figure 90 presents the progression of infill tensile damage, revealing that diagonal cracking initiates right from the beginning of the analysis, occurring at 1.5 mm of horizontal displacement. The reaching of the peak strength is given by the onset of crushing damage, as observed in Figure 91, which depicts the compression damage progression. Notably, crushing damage is also observed at the bottom corner of the right-hand side column. Figure 92 illustrates the progression of external interfaces damage, showing a response similar to what was previously observed in the mesoscale analysis. The damage initiates at the top interfaces upon vertical load application, followed by the damaging of the interfaces at the top-right and bottom-left corners, ultimately resulting in damage across all interfaces.

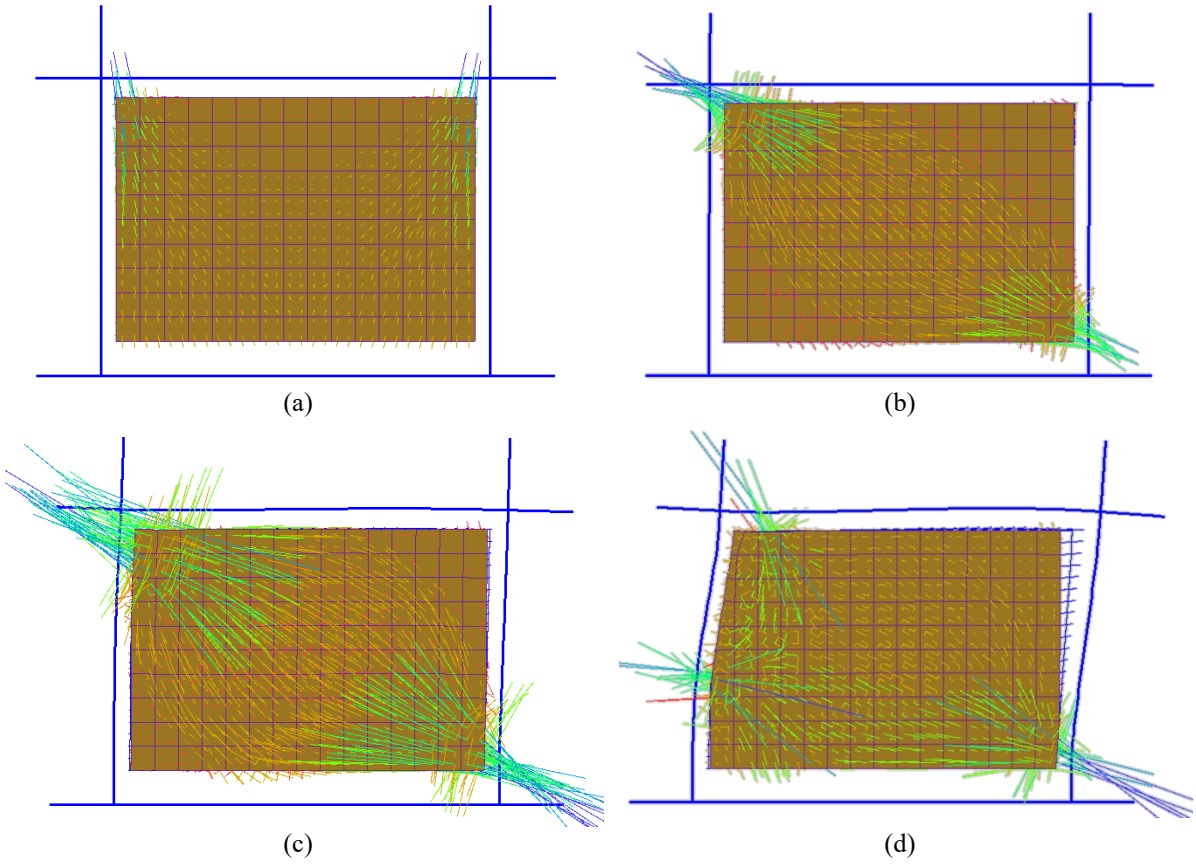

Figure 89 Representation of principal stresses throughout the analysis of the continuum macroscale model: (a) after the vertical load application, (b) at a horizontal displacement of 1.5mm, (c) at the peak-strength, and (d) at the last step (deformed shapes with 5x amplification)

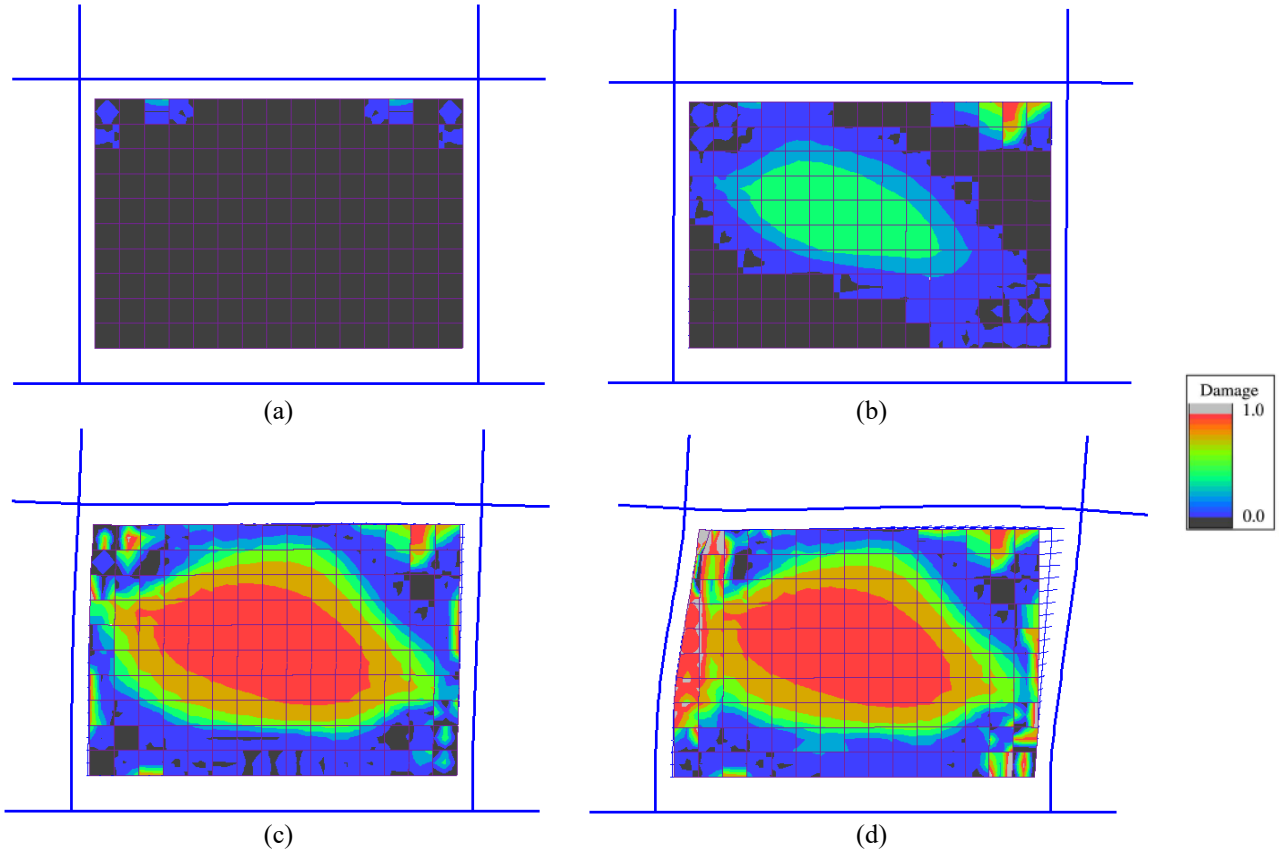

Figure 90 Representation of CDP tensile damage throughout the analysis - (a) after the vertical load application, (b) at a horizontal displacement of 1.5mm, (c) at the peak-strength, and (d) at the last step (deformed shapes with 5x amplification)

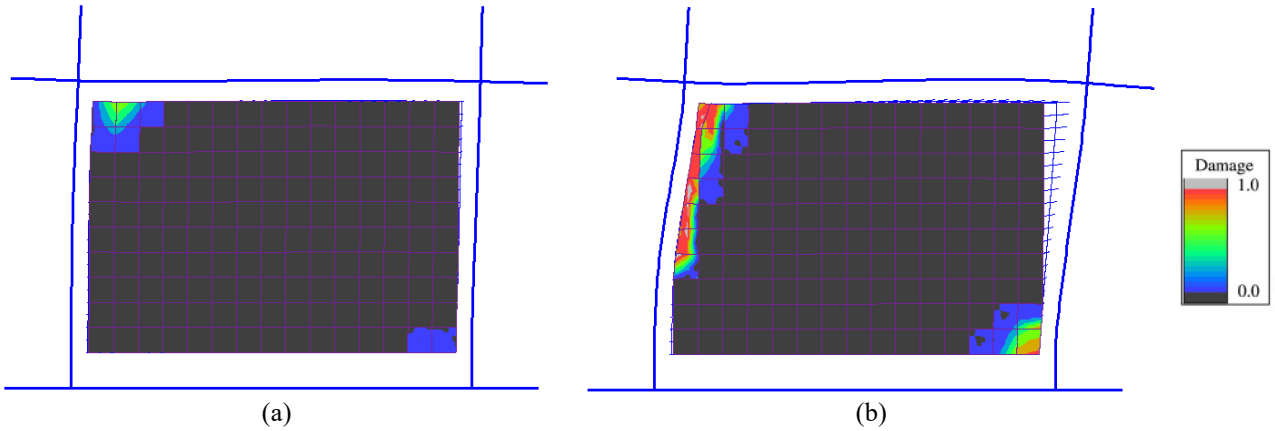

Figure 91 Representation of CDP compressive damage (a) at the peak-strength, and (b) at the last step (deformed shapes with 5x amplification).

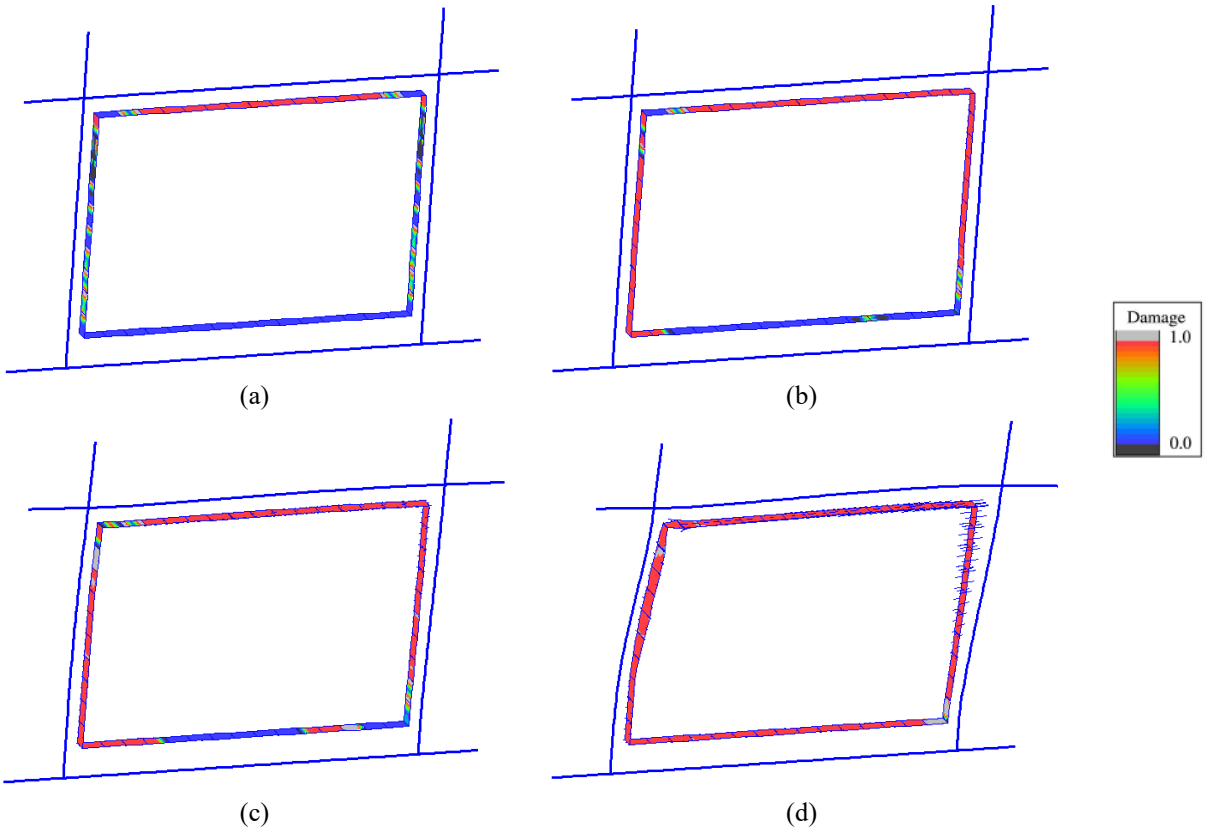

Figure 92 Representation of external interfaces tensile damage throughout the analysis - (a) after the vertical load application, (b) at a horizontal displacement of 1.5mm, (c) at the peak-strength, and (d) at the last step (deformed shapes with 5x amplification)

4.6.3 Sensitivity analysis

Sensitivity analyses are carried out to assess how the numerical response may vary based on the analyst's choices, as done within the mesoscale modelling. The specific scenarios considered are listed below, while all the characterisations evaluated are reported in Table 22**.**

- Variant 1: Strength parameters of the external frame-infill interfaces
  Evaluated considering the same scenarios employed in the mesoscale models.
- Variant 2: Stiffness parameters of the external frame-infill interfaces
  Evaluated with the same scenarios, along with an additional case analysed with stiffness one order of magnitude lower.
- Variant 3: Masonry elastic modulus
  Assessed by considering both horizontal and vertical moduli (as defined in Chapter 4.6.1).
- Variant 4: Compressive strength of masonry

Varies considering both the estimated diagonal strength (calculated as in relation (**20**), considering compression strength instead of elastic modulus) and the vertical strength.

- Variant 5: Plastic strain at the peak

  Linked to the crushing fracture energy, it is assessed within the range of 0.1% to 0.3%.

- Variant 6: Tensile strength of masonry

  Assessed by considering strengths from both mechanisms of diagonal cracking: stepped-crack and straight-crack.

- Variant 7: Fracture energy of masonry

  Evaluated by considering the range of variation reported in Table 10.

Table 22 Variants material characterisation for continuum macroscale infill model.

Variant 1 – Frame-infill interfaces strength parameters						
Parameter	Symbol	u.o.m.	Ref.	Var 1.1	Var 1.2	
Cohesion	c_{je}	N/mm^2	0.014	0.11	0.07	
Friction coefficient	$\tan\varphi_{je}$	-	0.35	1.02	0.86	
Bond strength	$f_{t,je}$	N/mm^2	0.010	0.08	0.05	
Variant 2 - Frame-infill interfaces elastic parameters						
Parameter	Symbol	u.o.m.	Ref.	Var 2.1	Var 2.2	Var 2.3
Normal stiffness	$K_{n,je}$	N/mm^3	2533	25.33	253.3	2533
Tangential stiffness	$K_{t,je}$	N/mm^3	1055	10.55	105.5	1055
Variant 3 – Infill elastic modulus						
Parameter	Symbol	u.o.m.	Ref.	Var 3.1	Var 3.2	
Young's modulus	E	N/mm^2	11660	9996	14280	
Variant 4 – Infill compressive strength						
Parameter	Symbol	u.o.m.	Ref.	Var 4.1	Var 4.2	
Maximum compression strength	f_c	N/mm^2	7.55	10.50	15.10	
Variant 5 – Infill strain at the peak						
Parameter	Symbol	u.o.m.	Ref.	Var 5.1	Var 5.2	
Plastic strain in compression	$k_{c,fmax}$	-	0.002	0.001	0.003	
Variant 6 – Infill tensile strength						
Parameter	Symbol	u.o.m.	Ref.	Var 6.1	Var 6.2	
Tensile strength	f_t	N/mm^2	0.47	0.12	0.82	
Variant 7 – Infill tensile fracture energy						
Parameter	Symbol	u.o.m.	Ref.	Var 7.1	Var 7.2	
Tensile fracture energy	G_t	N/mm	0.02	0.005	0.035	

The results, reported in Figure 93, mirror what was already seen in the mesoscale analysis. Notably, the important influence of the strength of the external interfaces is observed even here, although with a lower percentage of increase of strength (+24%), while no significant variations are observed by varying the specification of the stiffnesses. Remarkably, there is no influence detected from the elastic modulus, while, once again, a significant influence is evident from the choice of compressive strength, leading to +41% increase of the peak-strength. The effect of the strain at the peak also proves to be significant. Concerning tensile strength, no variations are noticed when adopting the higher value, while

considering the lower value leads to a significant change of shear-displacement curve, becoming more stepped and characterised by a higher stiffness decay. However, the maximum strength, primarily governed by the compressive behaviour of the infill, remains unaffected. Finally, there is no significant influence attributed to the tensile fracture energy.

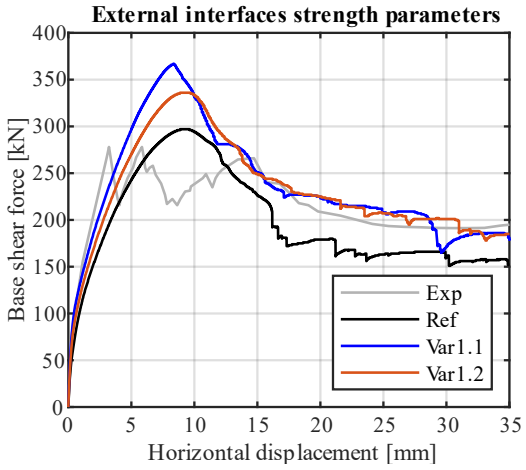

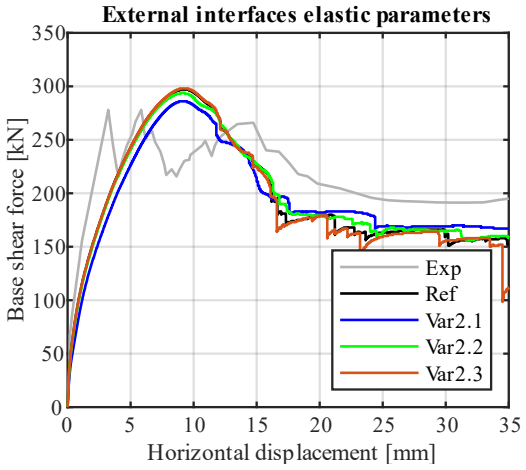

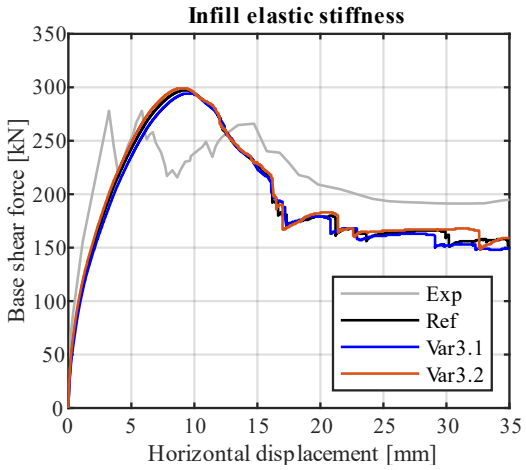

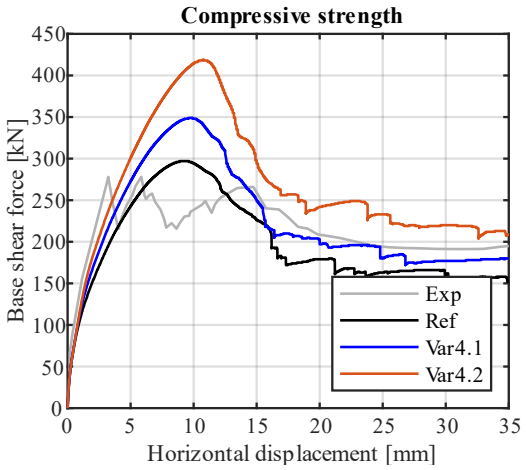

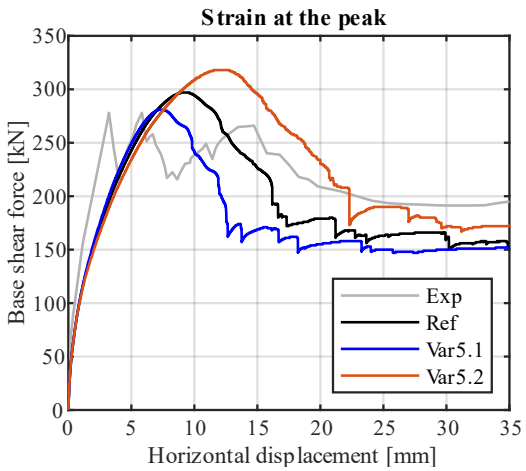

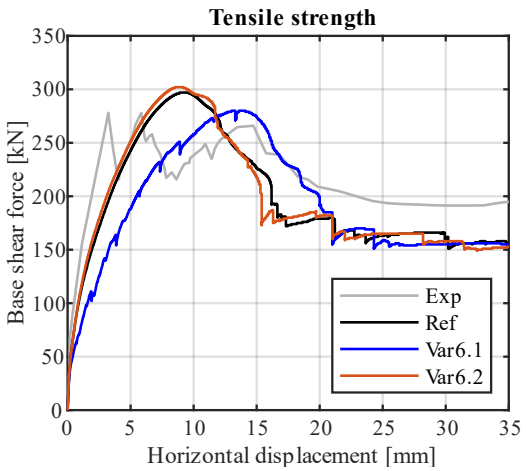

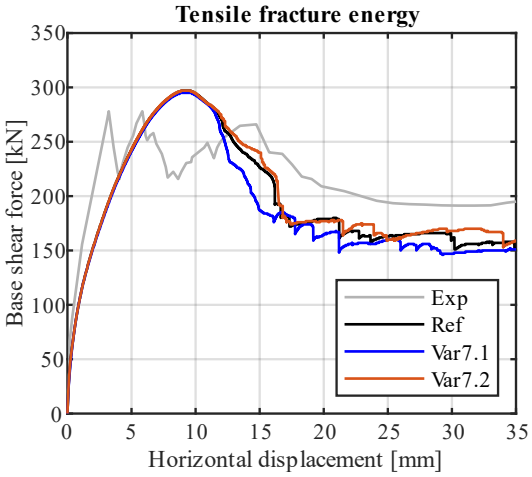

Figure 93 Shear-displacement curves from the variant continuum macroscale models.

4.7 Effects of openings in masonry-infills

As outlined in Chapter 2.4.4 and 2.5.3, the presence of openings can significantly impact the response of infilled frame structures, constituting a potential source of structural irregularity and consequently having a detrimental influence on their behaviour. In this section, the impact of the presence of openings within the infilled frame is examined. The continuum macroscale model, which has been evaluated in the previous chapter and demonstrated its accuracy in representing the experimental response while maintaining consistency with the more refined mesoscale model, is here adopted. Therefore, the same geometry and configuration of external action are considered herein. Six central openings are specified, differentiated into door and window openings. Standard dimensions are taken into account, considering typical dimensional ratios (ratios between the area, length, and height of the openings with those of the solid infill dimensions). The geometric characteristics of the analysed case are detailed in Table 23 and the views of the models are provided in Figure 94.

Table 23 Geometric characteristics of the infilled frames with openings examined (opening-solid infill ratios, α_b: length ratio; α_h: height ratio; α_a: area ratio)

Cases	b [mm]	h [mm]	α_b	α_h	α_a
W_1	419	284	20%	20%	4%
W_2	699	569	33%	40%	13%
W_3	978	853	47%	60%	28%
D_1	419	996	20%	70%	14%
D_2	699	996	33%	70%	23%
D_3	978	996	47%	70%	33%

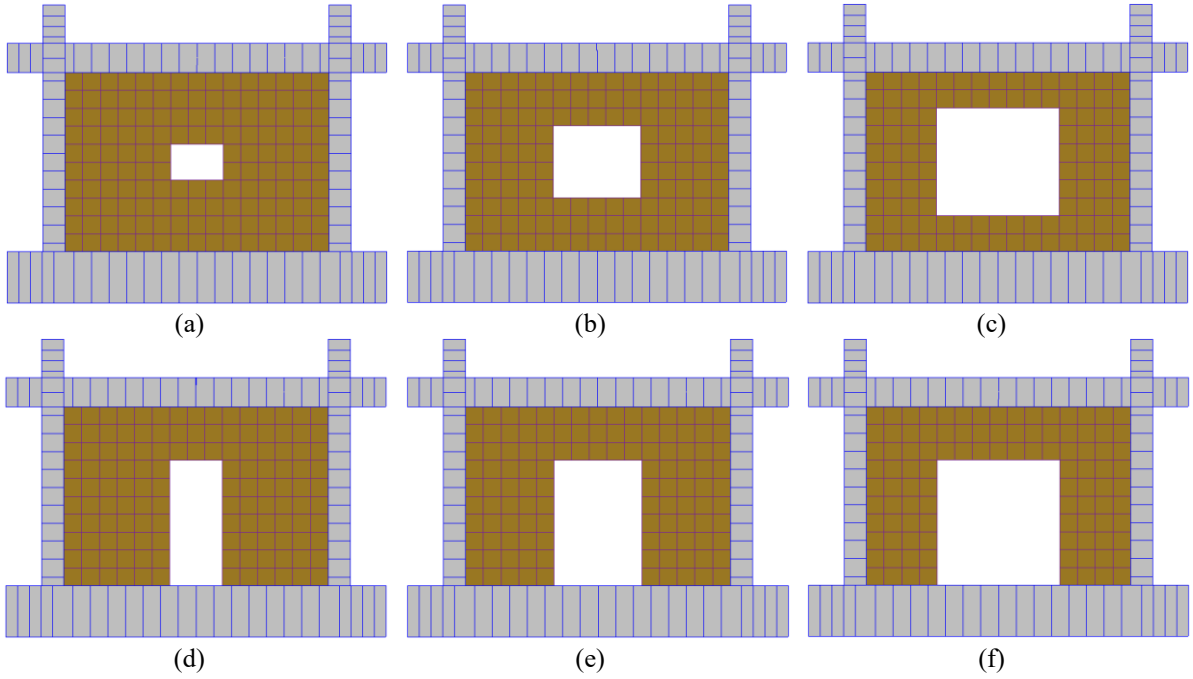

Figure 94 Models of infilled frames with openings: (a) W1, (b) W2, (c) W3, (d) D1, (e) D2, (f) D3

The base shear vs. horizontal displacement curves for window infills and door infills are presented in Figure 95 and Figure 96, respectively. The impact of the openings is significant, greatly influencing both the strength and stiffness of the infilled frame. As regards the windowed infilled frames, it is observed how they are notably affected by the opening dimensions. With a small opening (W1), the peak strength is nearly the same as that of the solid infilled frame, only leading to a reduction in stiffness and causing a slight shift in the peak point to a larger displacement. As the opening dimensions increase, the response shows a progressive decay in both strength and stiffness. The response of the model with the largest window (W3) is characterised by maximum strength close to the residual strength of the solid infilled frame. Conversely, concerning door infills, no remarkable variations are observed as the opening dimensions increase, with maximum strength of each model aligning with the residual strength of the solid infilled frame.

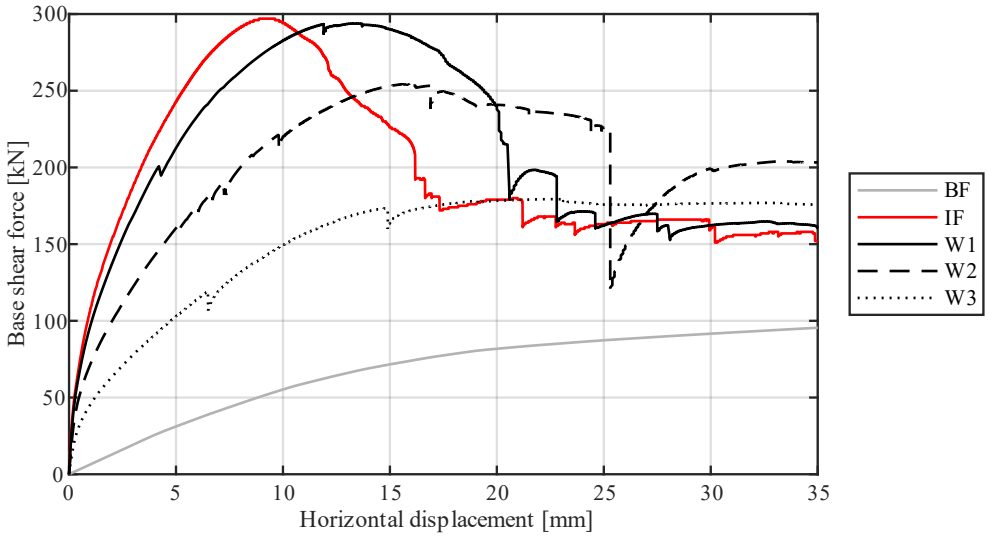

Figure 95 Shear-displacement curves for window-infills

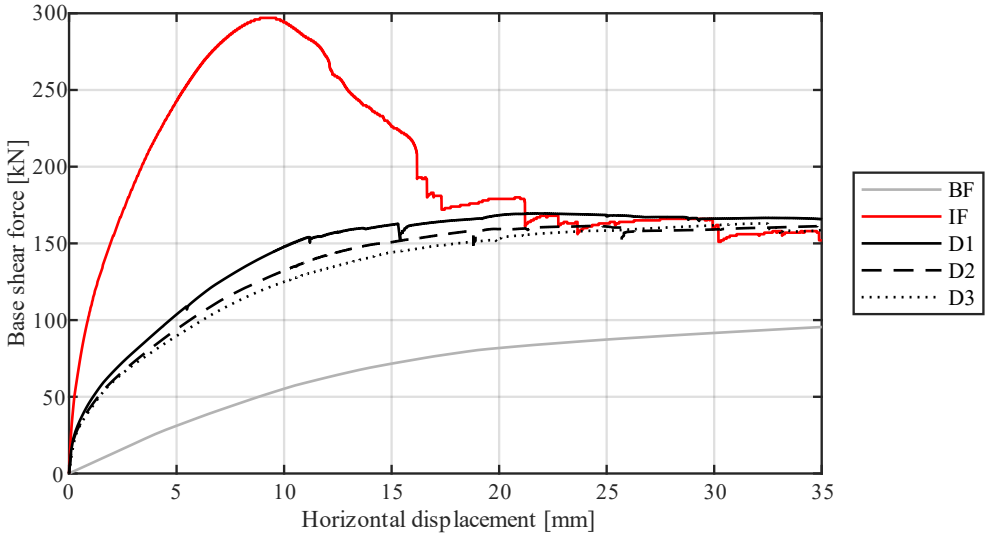

Figure 96 Shear-displacement curves for door-infills

The differences in the responses are evident also when analysing the infill stress distribution and the damage pattern. The progression of the stress state throughout the analysis for the window-infilled frame and door-infilled frame is illustrated Figure 97 and Figure 98, respectively. Additionally, Figure 98 and Figure 100 depict the compressive and tensile damage states of the infill, along with the damage on the RC frame, at the end of the analysis.

The influence of different window dimensions on the capacity of the infilled frame is clearly recognisable when examining the progression of the stress state (Figure 97). In the case of the small window (W1), a diagonal compressive strut still develops, leading to a response similar to that of the

solid-infilled frame. Conversely, the medium-sized window (W2) leads to the development of a double-strut, while the largest window (W3) is characterised by an even more complex stress state. Notably, as the opening increases the infill tends to remain adherent to the frame, given its higher deformability. The different behaviour is also evident in the damage pattern, shown in Figure 98. In the case of the small opening, the compressive damage is mainly present at the corners of the infills, while with larger windows it tends to extend to other areas, particularly the corners of the openings. Regarding tensile damage of the infill, a similar pattern is observed among the models, with damage spread throughout the infill.

Conversely, the response for the door infills remains consistent across the different dimensions. Specifically, it is characterised by a rocking mechanism of the right hand-side pier, which is accompanied by the development of an internal diagonal strut (Figure 99). Additionally, stress concentrations are observed at both the top-right corner of the opening and the loaded corner of the infill, leading to the crushing of masonry (Figure 100). Minimal damage is observed on the left-hand side pier, which presents a sliding mechanism at the external interface with the bottom beam.

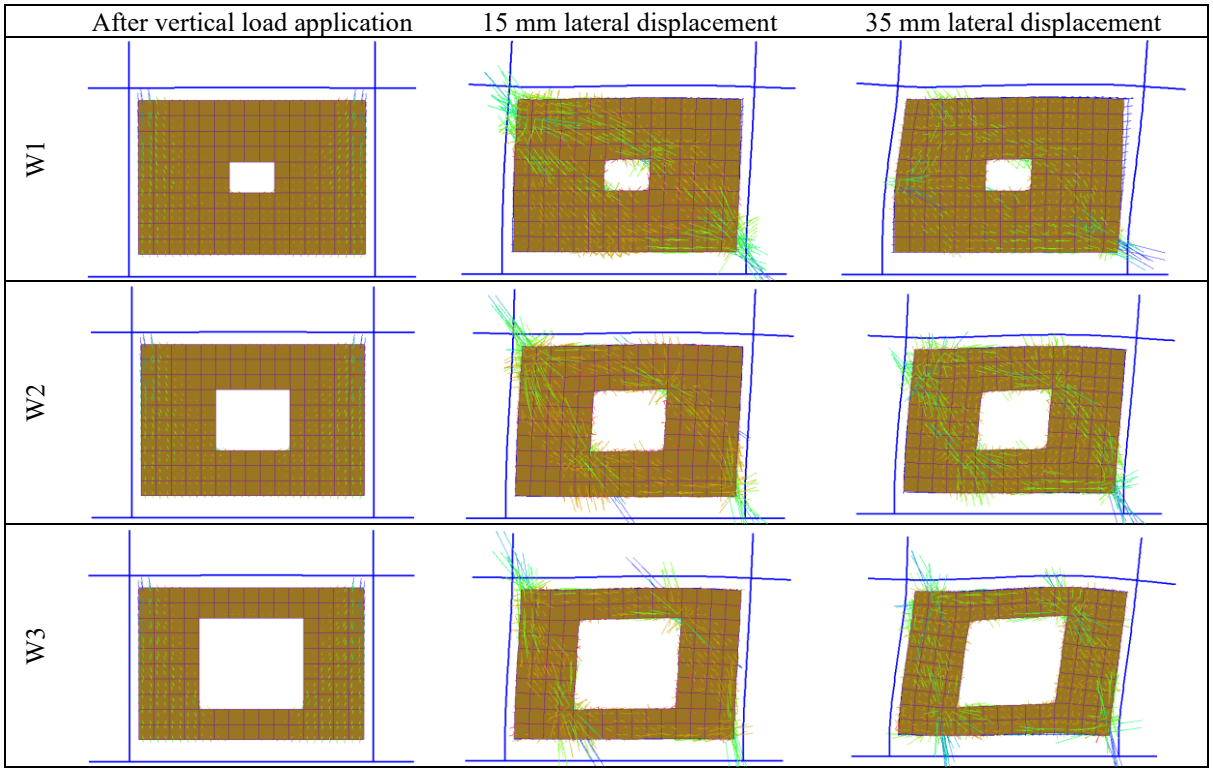

Figure 97 Principal stresses in the windowed infilled-frame models at different analysis phases (deformed shapes with 5x amplification)

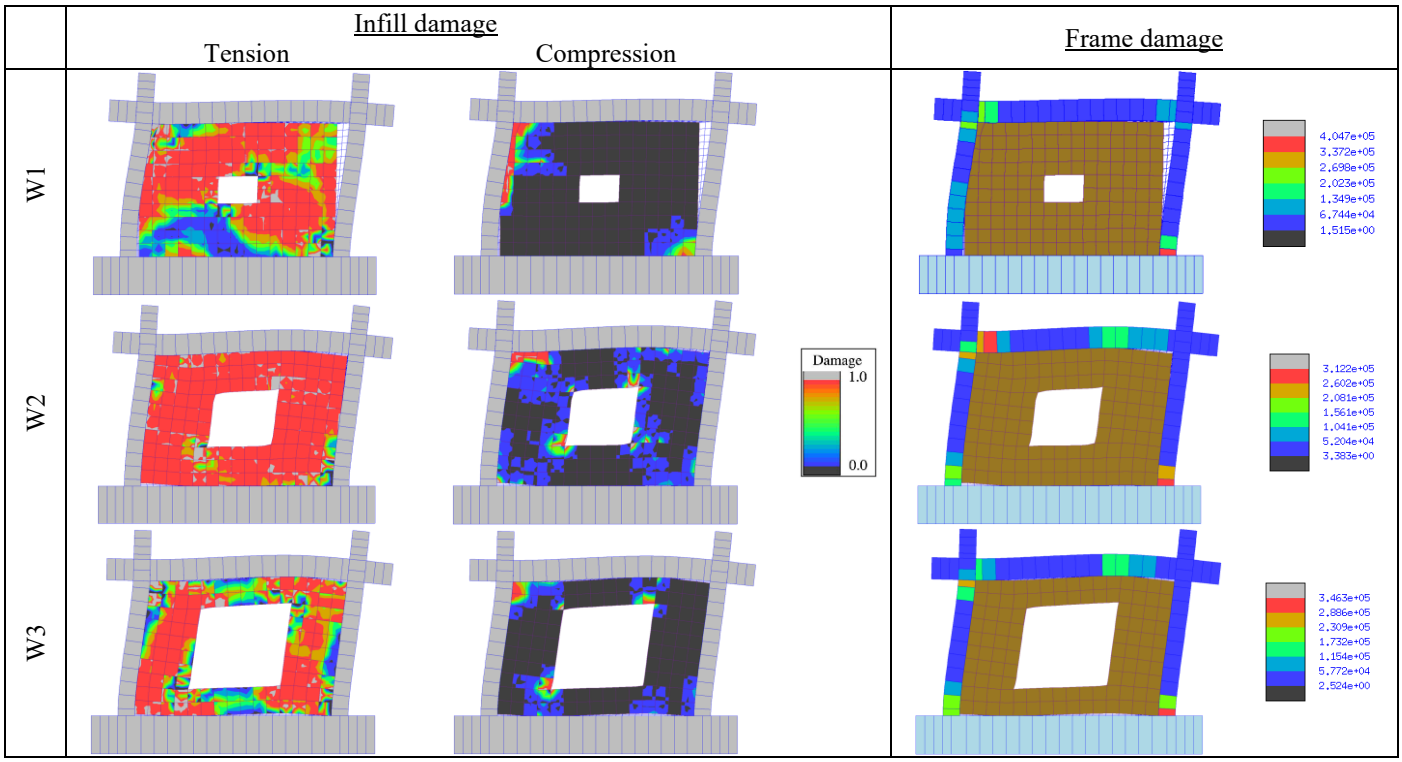

Figure 98 Tensile and compressive damage in the infill, along with strain energy in the frame at the conclusion of the analysis of the windowed infilled-frame models (deformed shapes with 5x amplification)

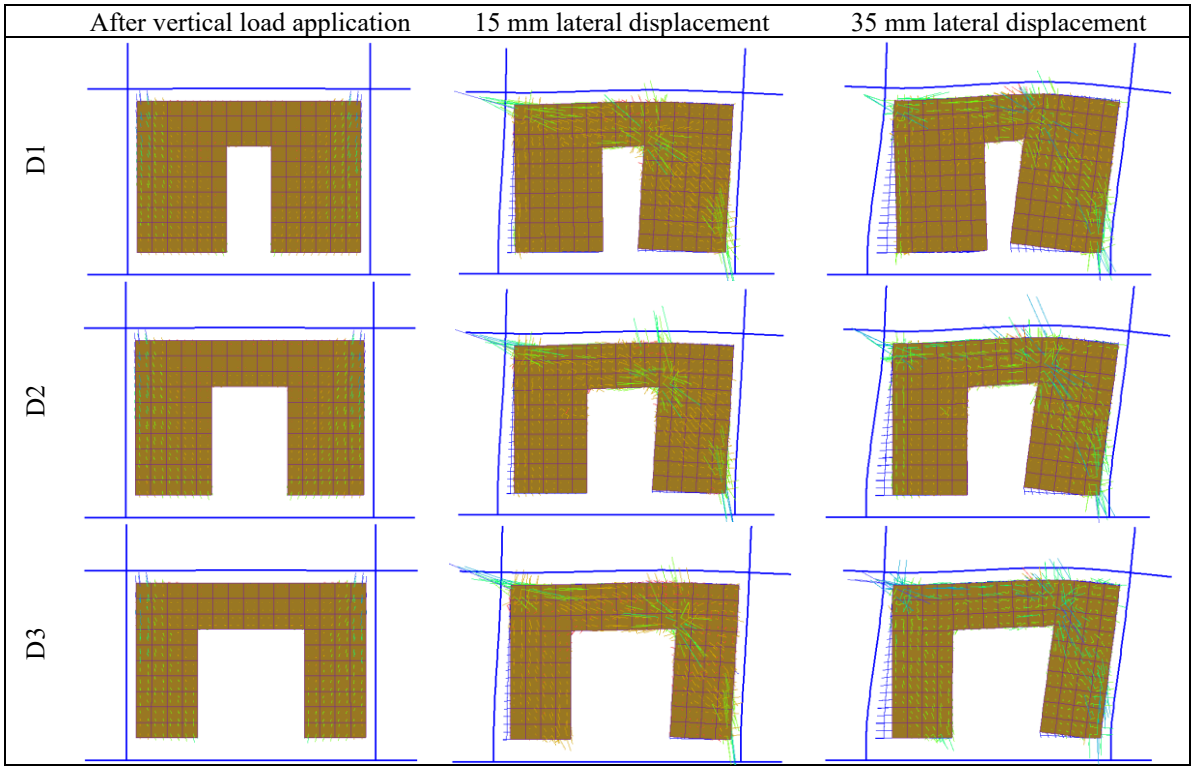

Figure 99 Principal stresses in the door infilled-frame models at different analysis phases (deformed shapes with 5x amplification)

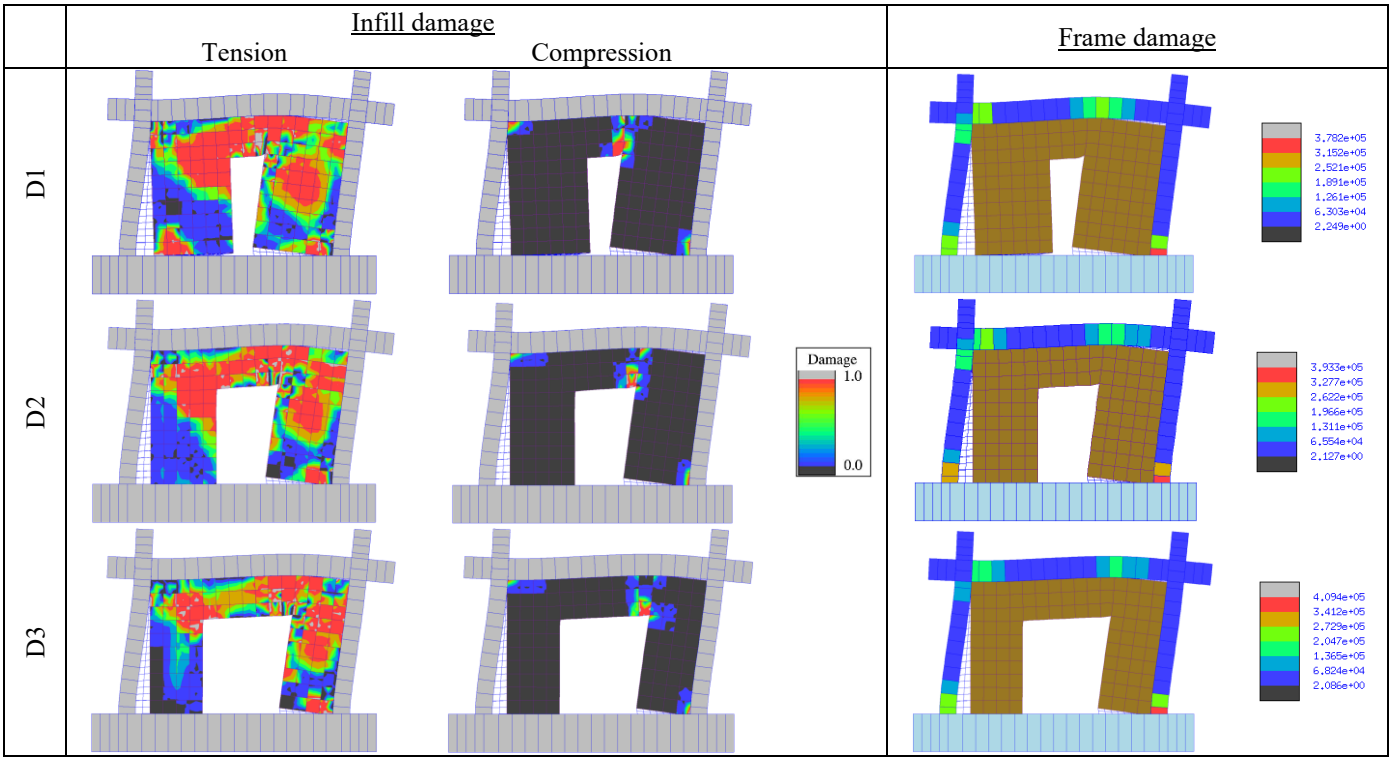

Figure 100 Tensile and compressive damage in the infill, along with strain energy in the frame at the conclusion of the analysis of the door infilled-frame models (deformed shapes with 5x amplification)

Finally, an analytical evaluation is conducted to assess the decrease of maximum strength and pre-peak stiffness resulting from the presence of openings. As discussed in Section 2.5.3, many authors consider reduction coefficients to account for openings, within the equivalent strut modelling approach. These coefficients are applied to reduce the section of the equivalent strut. Some authors propose a single value for both stiffness and strength reduction, while others evaluate them separately. Table 24 presents the peak strength reached (V_{max}) along with two secant stiffness values (K_{sec}), considering either 60% or 100% of the strength. Strength and stiffness reductions are then calculated as percentages of decreases from the solid-infilled frame response.

Table 24 Evaluation of the effects of openings presence

		Infilled Frame	W1	W2	W3	D1	D2	D3
V_{max}	[kN]	297.1	293.8	254.2	179.3	169.5	160.6	163.3
K_{sec}(0.6Vmax)	[kN/mm]	65.4	53.4	33.2	19.9	21.0	18.4	16.4
K_{sec}(Vmax)	[kN/mm]	30.3	22.0	16.3	8.0	8.5	7.3	7.4
ΔV		-	-1.1%	-14.4%	-39.6%	-42.9%	-46.0%	-45.1%
$\Delta K_{60\%}$		-	-27.4%	-46.1%	-73.6%	-72.1%	-75.9%	-75.5%
$\Delta K_{100\%}$		-	-18.3%	-49.3%	-69.7%	-67.9%	-71.9%	-75.0%

In Figure 101, the reduction values are depicted as functions of α_a, the ratio between the opening and infill areas. Interestingly, the variation of the reduction values is approximately linear for both strength and stiffness, whether for window-infill or door-infill. Notably, the reduction of strength and stiffness is not equal, with a higher impact on the reduction of stiffness. Moreover, the two reductions vary in parallel with each other. No significant differences are noticed when considering the stiffness at 60% of the peak or at 100% of the peak. For the door infills, the reductions, which remain almost constant due to the low variability of the response, are around -50% for peak strength and -75% for stiffness. On the other hand, the large variability of the window infills is reflected by the slope of the linear regression: the stiffness reduction varies between -30% and -75%, while strength reduction ranges from -5% to -40%.

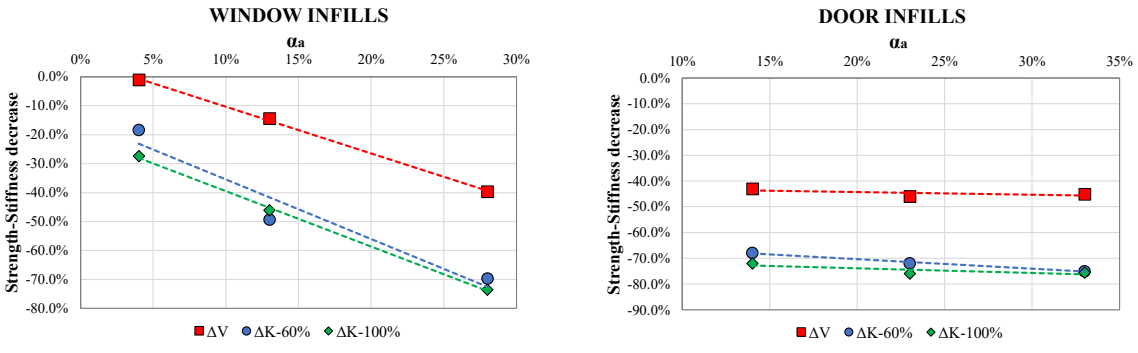

(a) (b)

Figure 101 Decrease of strength and stiffnesses due to openings presence: (a) window infills; (b) door infills

4.8 Summary and conclusions

In this chapter, the performance of masonry-infilled frames has been examined using advanced finite element modelling strategies. The reinforced concrete frame has been represented through beam elements formulated based on a fibre-plasticity approach, while the masonry infill has been modelled using both a mesoscale strategy and a continuum macroscale strategy (employing the concrete damage plasticity material law). To ensure effective coupling between the 3D masonry representation and the 1D beam/column elements, a multi-dimensional partitioned strategy has been employed.

Experimental tests from the literature have been simulated, involving the initial calibration of the reinforced concrete frame through the simulation of a bare-frame experimental test. Subsequently, the masonry infill has been modelled using both mesoscale and macroscale strategies, with an accurate objective calibration of the material. The results have demonstrated a good level of accuracy, providing a representation that effectively captures both the global response, namely the capacity curve, and the local behaviour, including the failure mechanisms of the infill, frame, and frame-infill interfaces. Additionally, sensitivity analyses have been conducted to identify the parameters that significantly impact the response. Notably, the response of the infilled frame has been found to be particularly influenced by the strength of the external frame-infill interfaces and the compressive response of the masonry infill.

Finally, the study has examined the influence of the presence of openings within the infills. The continuum macroscale infilled-frame model has been adopted as the solid reference model. Six cases with openings have been evaluated, considering either door or window openings. The influence on the response of either windows or doors has been found different, considering the capacity curve (specifically, maximum strength and pre-peak stiffness reduction), the progression of the stress state, and the damage development. Remarkably, the responses of door infilled-frames have not shown significant variation with changing opening dimensions, while the window infilled-frame response has been notably affected by window dimensions.

CHAPTER 5

A NOVEL ENHANCED 3D MACROELEMENT FOR URM AND INFILLED FRAME STRUCTURES MODELLING

5.1 Introduction

Despite their reliability, the computational demand of mesoscale models generally restricts their application to small-scale structures. Additionally, even in finite element macroscale modelling, simulating large-scale URM and infilled-frame structures under realistic dynamic loading conditions often requires extensive numerical analyses, leading to significant computational requirements.

This chapter introduces an enhanced macro-element model to overcome these limitations, building upon the groundwork established by the element introduced in (Minga et al. 2020). The model has already shown high potential, providing accurate results with reduced computational cost. The advances introduced in the present work address certain limitations of the original implementation, leading to improved response predictions.

A comprehensive exposition of the macroelement formulations is provided, encompassing kinematic characteristics, connectivity properties, and a description of the behaviour of cohesive boundaries and in-plane and out-of-plane nonlinear springs. The main drawbacks of the original implementation are highlighted, for which refinements and innovations are introduced in the enhanced macroelement and presented in the chapter.

5.2 Macroelement formulation

The 3D macroelement approach proposed by E. Minga et al. (2020) was developed to analyse unreinforced masonry structures subjected to in-plane and out-of-plane actions, used to represent significant portions of masonry walls. The macroelement, illustrated in Figure 21a, is formulated based on an inner deformable block equipped with in-plane and out-of-plane nonlinear springs (Figure 21b and c) and surrounded by four external edges, connected through zero-thickness cohesive-frictional interfaces. The element can interact along those edges with adjacent elements, allowing a realistic representation of any plane geometry. The model is able to represent all the typical failure modes of masonry buildings, including both in-plane (as illustrated in Figure 5) and out-of-plane modes (Figure 7), while maintaining a high level of computational efficiency. Moreover, distinct from previous macroelement strategies (e.g., Caliò et al., 2012; Pantò et al., 2016, 2017), this approach was developed within a FEM framework, enabling flexible connectivity with adjacent elements through its four boundary edges. This feature allows the combination of the macroelement with different types of finite elements, such as quadratic beams and shells.

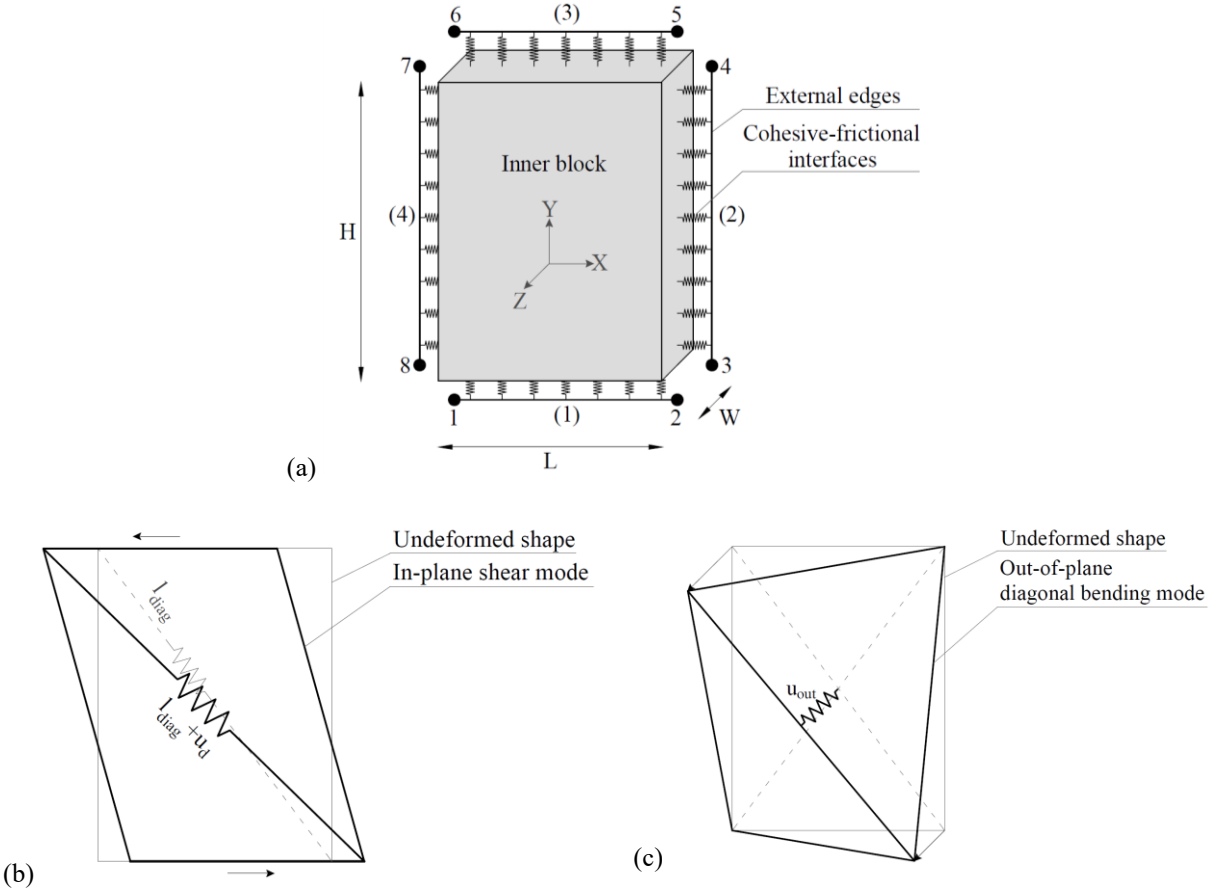

Figure 102 (a) URM macroelement; (b) in-plane shear and (c) out-of-plane diagonal bending deformation modes of the inner block

Kinematics

The macroelement is, in general, defined by 8 nodes, where pairs of nodes at the corners share identical coordinates (though sketched separately for the sake of clarity). Each node generally has 3 translational and 3 rotational degrees of freedom (DOFs). In the local element coordinate system XYZ, translational DOFs are represented as u_X, u_Y, u_Z, and rotational DOFs are denoted as θ_X, θ_Y, θ_Z, as illustrated in Figure 103. The DOFs required at the edge nodes vary depending on whether the external edge connects a macroelement with a steel or reinforced concrete surrounding frame or links two macroelements. In the first case, the external edge is defined as a 'full-DOF' edge, where all the 6 DOFs of the nodes must be considered to represent a deformation mode compatible with the elastic deformation of the beam element. Conversely, when an external edge connects two adjacent macroelements, the interacting faces remain plane since the interpolation of displacements within the inner block is linear. In this case, edges are defined by 4-DOF nodes and are referred to as 'reduced-DOF' edges (only twisting rotations are necessary to represent the out-of-plane displacements). Moreover, in the case of a macroelement adjacent to a frame element, the nodes corresponding to beam-column joints are merged (as further shown in Figure 105). Therefore, every single macroelement is generally defined through n distinct nodes, where $4 \leq n \leq 8$; the vector of size 6n containing all the nodal DOFs (degrees of freedom) of the macroelement in the element reference system XYZ can be expressed as:

$$U_s = \left[u_{X,1}\ u_{Y,1}\ u_{Z,1}\ \theta_{X,1}\ \theta_{Y,1}\ \theta_{Z,1}\ \cdots\ u_{X,n}\ u_{Y,n}\ u_{Z,n}\ \theta_{X,n}\ \theta_{Y,n}\ \theta_{Z,n}\right]^T \tag{21}$$

The displacement field within the external edges U_{ed} is determined by employing either linear shape functions in the case of reduced degrees of freedom (DOF) edges, or cubic shape functions for edges with full degrees of freedom (DOF) (refer to Figure 103 for an example of deformed shapes).

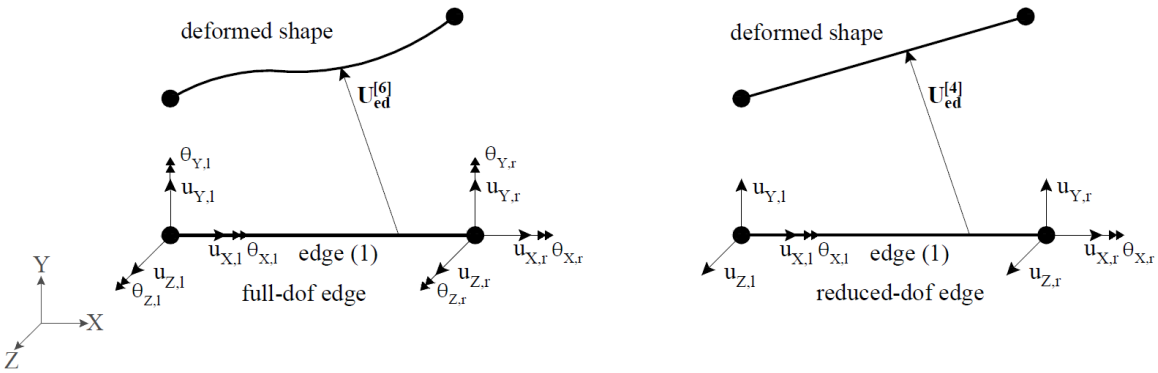

Figure 103 Basic DOFs of external edges in the local element coordinate system and example of deformed shapes

In addition to the nodal DOFs, each macroelement is defined by eight additional DOFs that govern the deformation modes of the inner block, as depicted in Figure 104: DOFs from d_1 to d_4 are associated to the in-plane response, while DOFs from d_5 to d_8 to the out-of-plane response. The vector representing these additional DOFs of the macroelement is denoted as:

$$U_a = [d_1 \ d_2 \ d_3 \ d_4 \ d_5 \ d_6 \ d_7 \ d_8]^T \tag{22}$$

while the vector containing all the basic and additional degrees of freedom (DOFs) of the element is given by:

$$U = [U_s \ U_a]^T \tag{23}$$

The displacement field of the inner block, denoted as U_{bl}, is determined through a linear interpolation of the displacements related to the additional DOFs. To achieve this, a linear distribution of the translations of vector U_a is assumed along the mid-surface of the block. Additionally, it is assumed that the mid-surface rotates around axes X and Y due to differential out-of-plane translations; within the block, a linear distribution of rotations is also assumed. An example of mixed-mode deformation of the inner block is provided in Figure 104.

For more information on the interpolation of the displacement fields of external edges and inner block refer to Minga (2017).

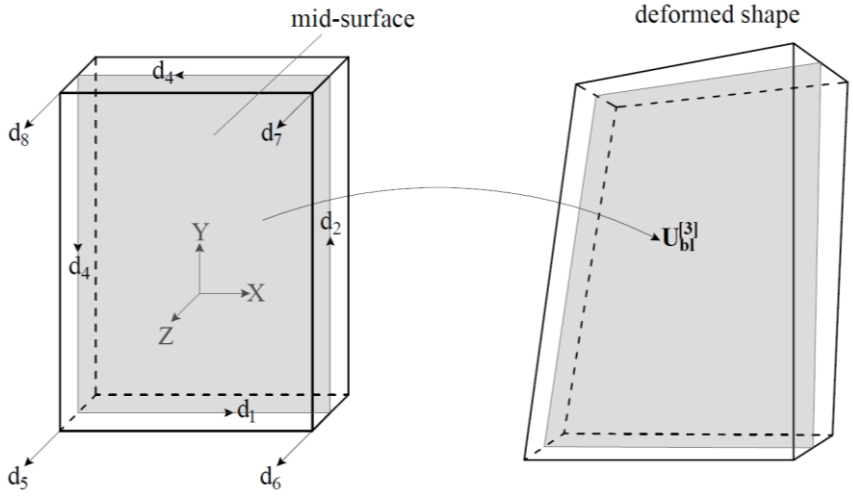

Figure 104 Inner block additional DOFs and example of deformed shape

Connectivity

The element connectivity is determined based on the specific structure being modelled. Specifically, the pairs of nodes situated at the corners can be considered separately or merged into a single node; this feature depends on whether the external edge connects two adjacent masonry blocks or links a masonry portion with a steel or reinforced concrete frame (see Figure 105). In the case of bare URM structures (Figure 105a) the external edges serve as fictional boundaries between masonry portions, not transferring moments and allowing for a linear relative displacement field in the normal and transversal directions. In this scenario, two distinct nodes are considered for each corner. On the other hand, in the case of masonry-infilled frames (Figure 105b), the connectivity of the macroelement to the frame elements requires the transfer of forces and moments between the edges in contact with the frame. In this case, the corner corresponding to the beam-column joint consists of a single node, and all the nodes shared with frame elements are merged.

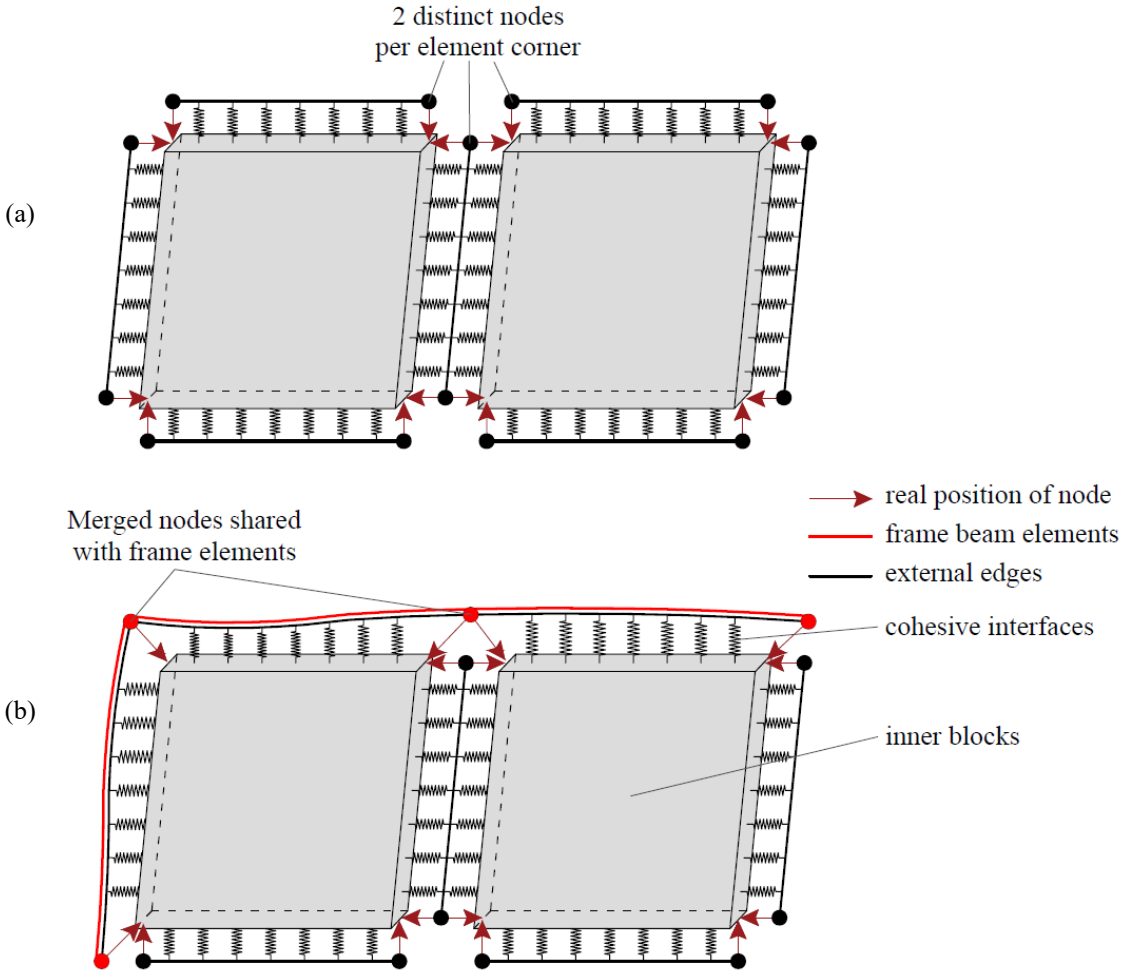

Figure 105 Types of nodal connectivity: (a) adjacent URM blocks; (b) URM blocks surrounded by a frame

Cohesive interfaces

The boundary interfaces are characterised by cohesive-frictional behaviour governed by a 3D plasticity-damage constitutive law. This law establishes the relationship between the relative displacements ε_i and the interface tractions σ_i at each Gauss Point within the 2D domain of the zero-thickness interface, as illustrated in Figure 106a. Relative displacements and interface tractions are expressed in (4) and (5), respectively, as defined in the local reference system xyz of boundary (i) (refer to Figure 106), where y represents the direction normal to the zero-thickness interface mid-surface. In contrast, x and z represent the tangential directions.

$$\varepsilon_i = \left[\varepsilon_{x,i}\ \varepsilon_{y,i}\ \varepsilon_{z,i}\right]^T \tag{24}$$

$$\sigma_i = \left[\sigma_{x,i}\ \sigma_{y,i}\ \sigma_{z,i}\right]^T \tag{25}$$

The relative displacements are determined (as expressed by equation (24)) as the difference between the internal displacement field along the face of the block constituting the internal side of the zero-thickness interface (i), denoted as $u_{int,i}$, which depends on the additional DOFs U_a of the inner block, and the external displacement field along the 2D surface defined by the two-noded edges, denoted as $u_{ext,i}$, which depends on the basic nodal DOFs U_s (see Figure 106b). The interpolation of the displacement fields $u_{int,i}$ and $u_{ext,i}$ is performed by considering appropriate matrices $N_{a,i}$ and $N_{s,i}$ which depend on U_a and U_s respectively.

$$\varepsilon_i = u_{int,i} - u_{ext,i} = N_{a,i}U_a - N_{s,i}U_s \tag{26}$$

For the interpolation of internal and external displacement fields refer to Minga (2017) and Minga et al. (2020). The relationship between the relative displacement and the traction is governed by the sophisticated 3D plasticity-damage constitutive law developed for the representation of joint interfaces under cyclic loading, as proposed in (Minga et al., 2018). This model was previously employed within the mesoscale approach described in Chapter 2.3.1, for the modelling of mortar joints and internal brick-to-brick interface. Hence, instead of considering uncoupled springs as in previous implementations (e.g., Caliò et al., 2012; Pantò et al., 2016, 2017), the integration of this model interface directly couples normal and tangential behaviour, therefore acting as triaxial springs located at the Gauss points.

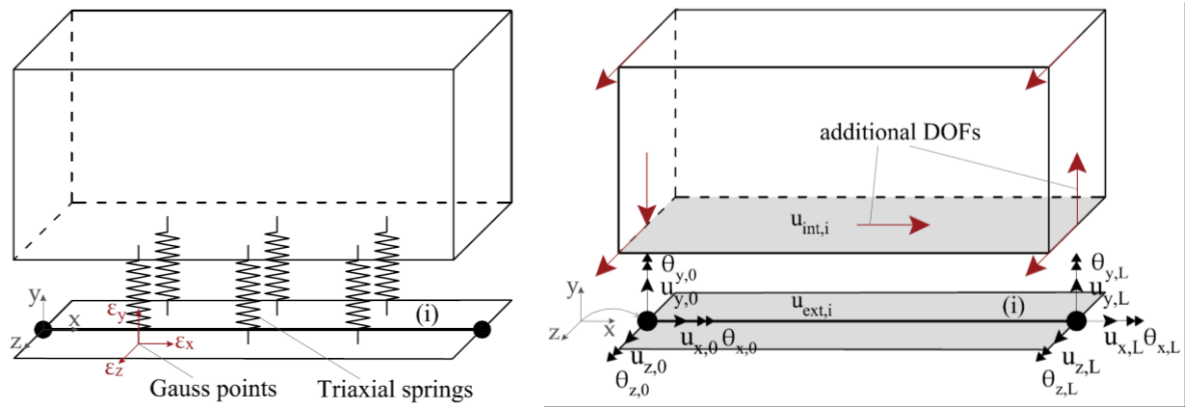

(a) (b)

Figure 106 (a) Internal and external displacement fields on the two sides of the i-th interface; (b) local reference system and Gauss points along the i-th macroelement cohesive-frictional boundary

The damage along the macroelement interfaces enables the representation of various typical masonry collapse mechanisms, including shear-sliding (both in-plane, as depicted in Figure 5c, and out-of-plane, as in Figure 7b), flexural cracking (both in-plane, as illustrated in Figure 5d, and out-of-plane, as in Figure 7a) and toe crushing (Figure 5e). The elastic stiffnesses of the interfaces are assumed so as all normal elastic in-plane deformation within the masonry block is concentrated along these interfaces, based on the influence areas related to the corresponding volumes (as illustrated in Figure 107). Consequently, the normal stiffness $K_{n,i}$ of each edge is determined by the ratio of the normal elastic modulus (denoted as E_x or E_y, depending on the direction) over half of the element's height (denoted as H) or length (denoted as L), respectively, as in equations (27) and (28) (where the number subscript refer to the external edge as specified in Figure 21). On the contrary, the shear stiffness is assumed to be infinitely high, as the element shear deformability is entirely attributed to the deformability of the inner block.

$$K_{n,1} = K_{n,3} = \frac{2E_y}{H} \tag{27}$$

$$K_{n,2} = K_{n,4} = \frac{2E_x}{L} \tag{28}$$

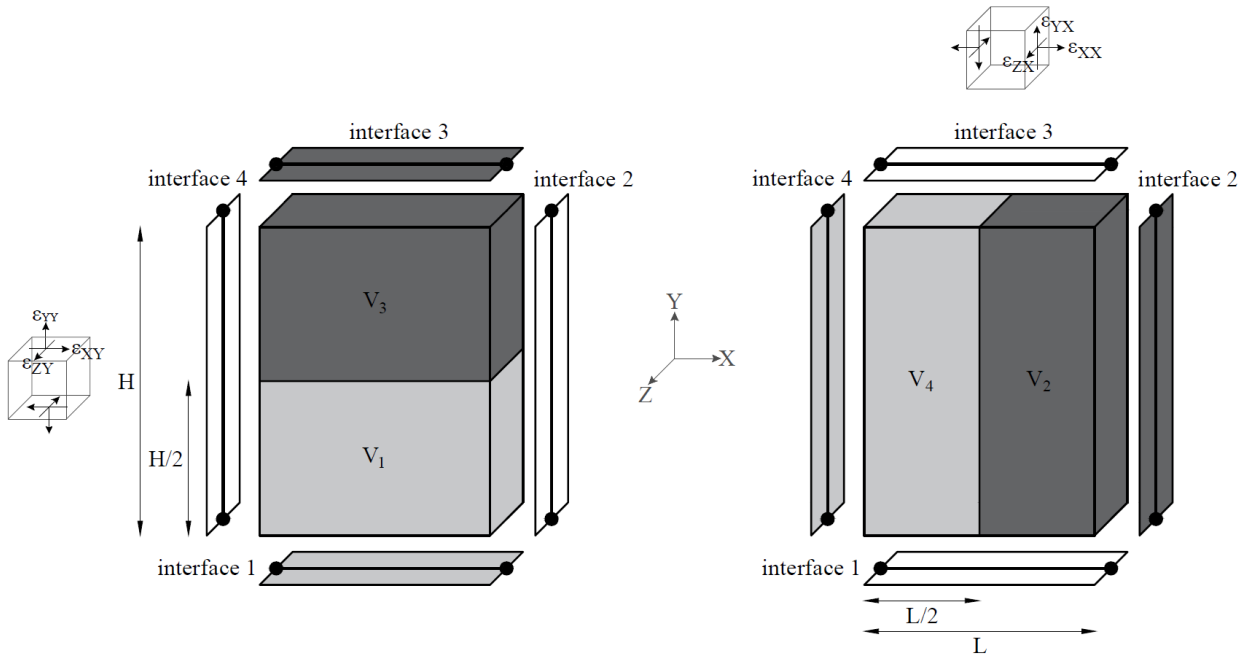

Figure 107 Areas of influence of the interfaces between the inner block and the external edges

In-plane and out-of-plane springs

The mechanisms of in-plane diagonal cracking of masonry (illustrated in Figure 5a and Figure 5b) and out-of-plane two-way flexural bending (Figure 7c) cannot be described by damage in the surrounding interfaces. Therefore, these modes are represented in the macroelement in a phenomenological way through specific deformation modes of the inner block, represented by nonlinear springs (as illustrated in Figure 108) and depending on the additional DOFs. In particular, the in-plane shear deformation (an example of which is provided in Figure 108a) is defined by a single lagrangian parameter, denoted as u_d, conveniently controlled by an individual nonlinear spring. This parameter is associated to the in-plane additional DOFs of the element (d_1, d_2, d_3 and d_4, as depicted in Figure 104). Considering α as the angle between the diagonal spring and the top edge of the macroelement, as shown in Figure 108a, the calculation of u_d is as follows:

$$u_d = N_d \, U_a \tag{29}$$

where:

$$N_d = [\cos\alpha \;\; -\sin\alpha \;\; \cos\alpha \;\; -\sin\alpha \;\; 0 \;\; 0 \;\; 0 \;\; 0] \tag{30}$$

Similarly, the out-of-plane two-way flexural bending (an example of which is shown in Figure 108b) is governed by the out-of-plane additional DOFs (d_5, d_6, d_7 and d_8, as depicted in Figure 104) and is

associated with a single nonlinear spring governed by a lagrangian parameter, u_{out}. The deformation of the out-of-plane spring is determined by the lateral distance between the central points of the two diagonals of the inner block mid-surface, which is zero in the undeformed configuration. The parameter u_{out} is calculated as follows:

$$u_{out} = N_{out}\, U_a \tag{31}$$

where:

$$N_{out} = \frac{1}{2}[0\ \ 0\ \ 0\ \ 0\ \ -1\ \ 1\ \ \ -1\ \ 1] \tag{32}$$

It is noteworthy that the incorporation of the out-of-plane deformation mode allows the description of two-way out-of-plane bending deformation with the use of coarser meshes, while in the macroelement proposed by Pantò et al. (2016, 2017) this mechanism could be simulated with a larger number of elements.

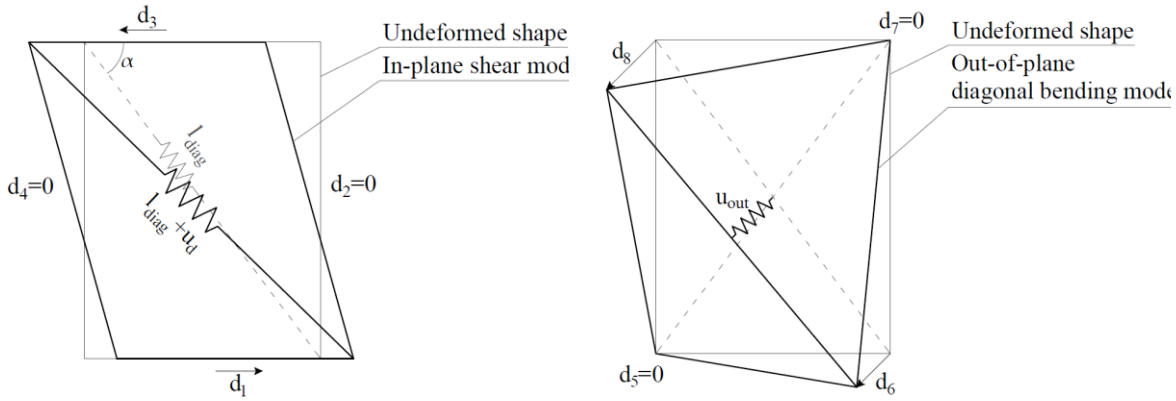

Figure 108 Inner block mid-surface deformations: (a) In-plane shear mode; (b) Out-of-plane diagonal bending mode

The force-displacement relationship, adopted for both in-plane (denoted as F_d-u_d) and out-of-plane (denoted as F_{out}-u_{out}) springs, is based on a simplified piecewise-linear law, illustrated in Figure 109, featuring a bilinear backbone curve with a softening post-peak branch, followed by a final residual branch. The cyclic response is characterised by unloading branches with no stiffness degradation, while the reloading occurs by pointing towards the last maximum displacement reached in the considered direction. Consequently, damage accumulates independently in positive and negative displacements.

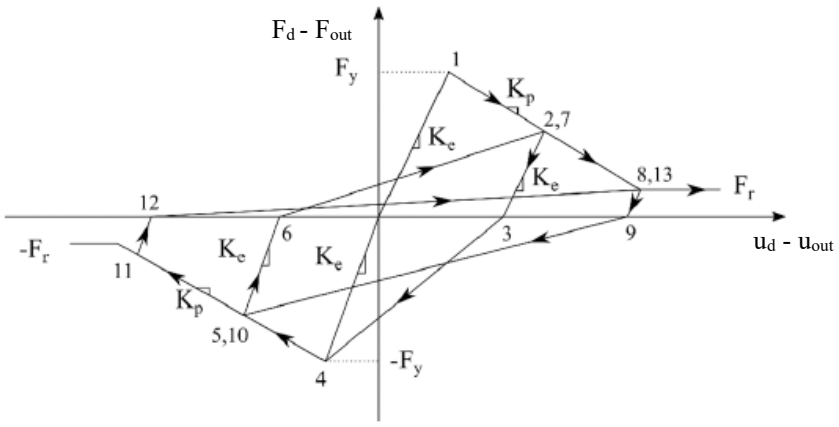

Figure 109 Simplified piecewise-linear constitutive law employed for the macroelement in-plane and out-of-plane springs (image taken from Minga et al., 2020)

As regards specifically the in-plane spring, the model parameters defining the spring force-displacement law include the initial stiffness $K_{d,e}$, the post-peak stiffness $K_{d,p}$, the maximum strength $F_{d,y}$ and the residual strength $F_{d,r}$. The stiffnesses values can be determined through an equivalence between the macroelement inner block and a homogeneous masonry plate under pure shear, as illustrated in Figure 110 and following equations (33) and (34), where L, H and W represent length, height and thickness of the homogeneous plate, α is the angle between the horizontal and the diagonal spring and G_e and G_p are the masonry elastic and post-peak shear modulus.

$$K_{d,e} = G_e \frac{LW}{Hcos^2\alpha} \tag{33}$$

$$K_{d,p} = G_p \frac{LW}{Hcos^2\alpha} \tag{34}$$

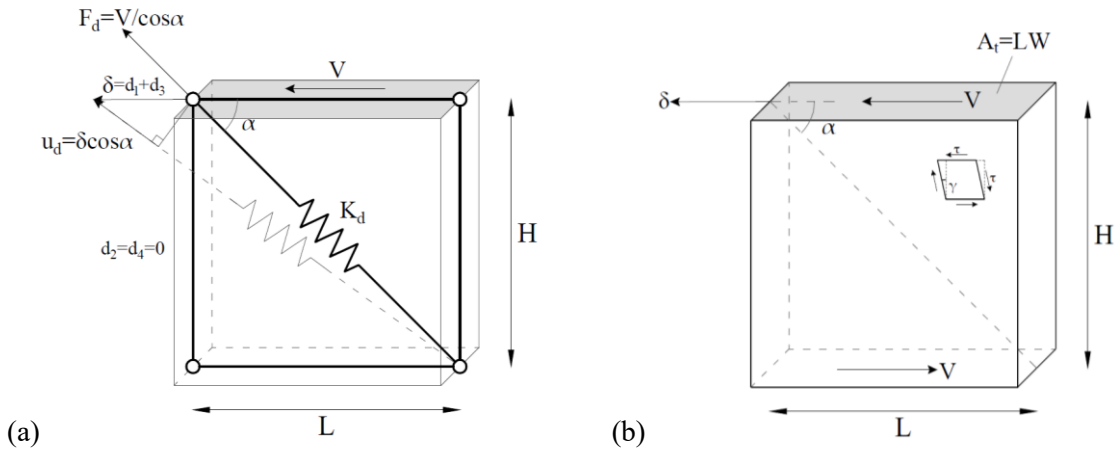

Figure 110 Equivalence of (a) the macroelement inner block to a (b) homogeneous masonry plate under pure shear

The maximum strength of diagonal spring $F_{d,y}$ is determined by applying the criterion proposed by Mann and Müller (1980). The calculation of the horizontal shear strength for diagonal cracking, denoted as V_{res}, is calculated according to relations (35), (36) and (37), which depend on the characteristics of the single masonry constituents, specifically the unit interlocking and cohesive and frictional characteristics of the mortar joints. Additionally, it is also influenced by the level of confinement σ_n, calculated as the average normal stress in the boundary interfaces at the previous converged step of the analysis. The shear diagonal strength is finally calculated through (38).

$$V_{res} = L\,W\,(\tilde{c} + \tilde{\mu} \cdot \sigma_n) \tag{35}$$

$$\tilde{c} = \frac{c}{1 + 2\mu\frac{\Delta H}{\Delta L}} \tag{36}$$

$$\tilde{\mu} = \frac{\mu}{1 + 2\mu\frac{\Delta H}{\Delta L}} \tag{37}$$

$$F_{d,y} = \frac{V_{res}}{\cos\alpha} \tag{38}$$

In the equations c and μ are cohesion and friction angle of the masonry joints, ΔH and ΔL are the length and height of the brick units, c̃ and μ̃ are the global equivalent values of cohesion and coefficient of friction.

The same simplified constitutive law was adopted for the out-of-plane spring, as previously mentioned. In contrast to the in-plane evaluation of diagonal cracking strength, there is currently no established mechanical criterion in the literature for assessing the out-of-plane two-way bending strength. Therefore, the authors (Minga et al., 2020) proposed a calibration of the model parameters by testing an equivalent detailed mesoscale model (with the same dimensions of a single macroelement), following the mesoscale strategy presented by Minga et al. (2018). The schematisation of the mesoscale model, regarded as a virtual numerical test, is illustrated in Figure 111a. The model is pinned along two edges, and an out-of-plane force F_z is applied to the free corner, inducing a deformation mode corresponding to the activation of the out-of-plane spring (Figure 111b). Simultaneously, a uniform vertical pressure σ_n is applied to the top edge. The model was tested under various levels of confinement. Figure 111c illustrates an exemplary response, depicting the out-of-plane force per unit surface (denoted as the pressure p, given by the ratio between the out-of-plane force F_z and the area HL) as a function of the out-of-plane displacement at the corner. The obtained responses can be approximated to piecewise-linear fitting curves, with a second branch of softening followed by a final residual phase. Consequently, the backbone curve of the spring constitutive law appears suitable for representing the out-of-plane

bending response. Moreover, the response is clearly influenced by the vertical stress. As depicted in Figure 111d, both maximum and residual pressure exhibit a nearly linear increase with the respect of confinement level; the linear regression curves of yield and residual pressures are plotted, each characterised by the respective slopes denoted as $\mu_{out,y}$ and $\mu_{out,r}$.

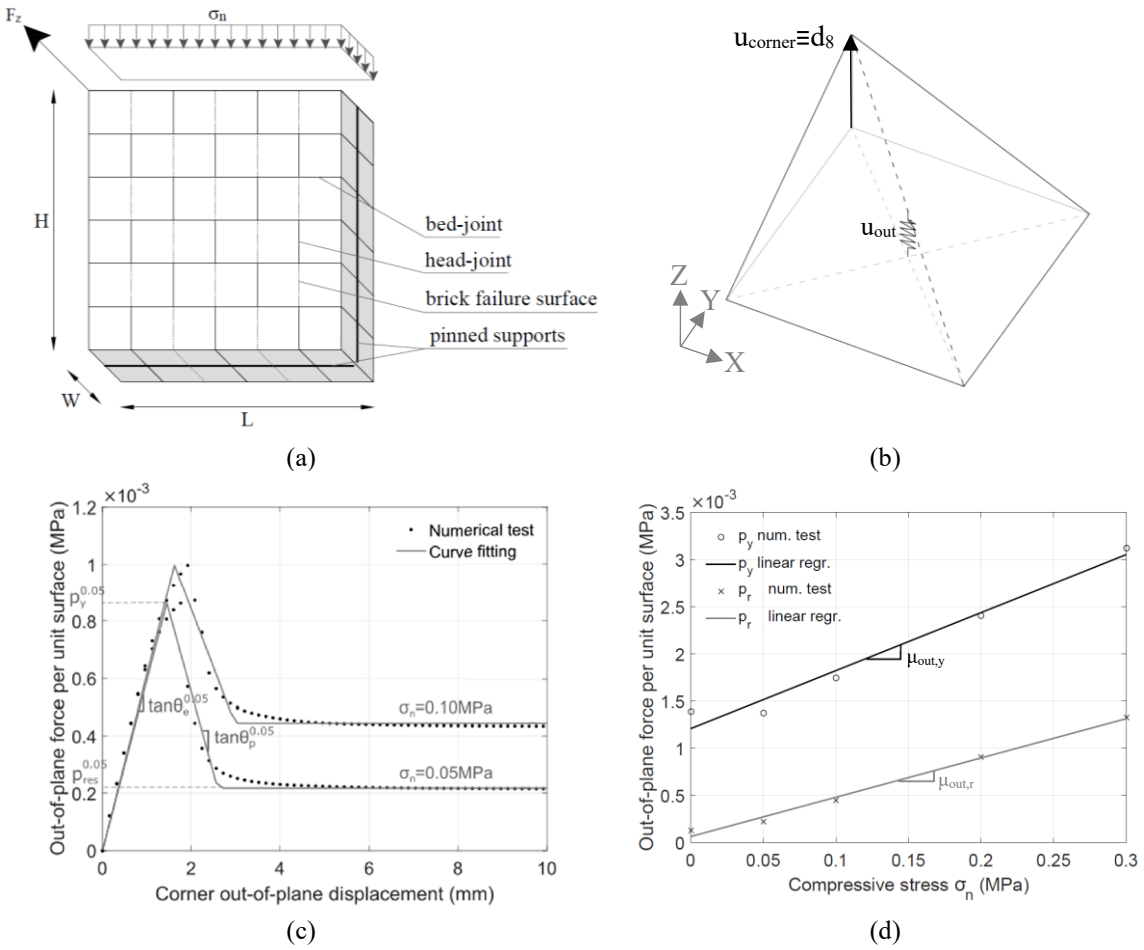

Figure 111 Calibration of the out-of-plane spring: (a) boundary and loading conditions of the meso-scale test and (b) corresponding out-of-plane deformation mode of the inner block; (c) curve fitting and mechanical parameter identification; (d) linear regression of yield and residual pressure with respect to the normal compressive stress (images taken from Minga et al., 2020, and Minga, 2017)

The fitting curves of displacement-pressure (Figure 111c) are determined by the slope of the elastic branch $\tan\theta_e$, the slope of the post-peak branch $\tan\theta_p$, the yield pressure p_y and the residual pressure p_r. The calibration of the initial and post-peak stiffness of the spring can be assessed as the average values for different confinement levels, following equations (40) and (43).

$$K_{out,e} = \frac{1}{n}\sum_{k=1}^{n} 4LH \tan\theta_{e,k} \quad (39)$$

$$K_{out,p} = \frac{1}{n}\sum_{k=1}^{n} 4LH \tan\theta_{p,k} \quad (40)$$

Regarding the forces, the yield and residual pressures ($p_{y,0}$ and $p_{r,0}$ respectively) under zero vertical stress are associated with the corresponding out-of-plane spring reactions $F_{out,y,0}$ and $F_{out,r,0}$ as determined by the following relations:

$$F_{out,y,0} = 2LHp_{y,0} \quad (41)$$

$$F_{out,r,0} = 2LHp_{r,0} \quad (42)$$

Ultimately, the spring forces are derived from relations (43) and (44), considering the contribution of vertical stress, through the yield and residual coefficients obtained from linear regressions.

$$F_{out,y}(\sigma_n) = F_{out,y,0} + \mu_{out,y}\sigma_n \quad (43)$$

$$F_{out,r}(\sigma_n) = F_{out,r,0} + \mu_{out,r}\sigma_n \quad (44)$$

Drawbacks and advances

The accuracy of the proposed macroelement strategy underwent validation through numerical simulations of experimental tests, providing reliable predictions while maintaining high computational efficiency. Nevertheless, mechanical enhancements and further in-depth evaluation of its ability to simulate the actual response of masonry and masonry-infilled frame should be undertaken.

In particular, the constitutive law governing in-plane and out-of-plane springs (Figure 109) is overly simplified, not considering stiffness and strength degradation, as well as the actual dependency on the response between positive and negative displacements, as also highlighted by the authors (Minga et al., 2020). Indeed, this representation separates the response in the different directions, thus strength degradation progresses independently in the positive and negative quadrants. Consequently, any softening behaviour observed in one direction does not influence the response in the opposite direction. This means that, upon reaching a specific displacement in the positive direction, the unloading branch points towards the maximum negative displacement previously attained, independently from the specific positive value attained, leading to possible inaccuracies in the response prediction. An illustrative example of this is provided in Figure 112, which pertains to the simulation of an

experimental test conducted by Griffith et al. (2007). The experiment involved subjecting a wall to two-way bending under an out-of-plane pressure. The specimen comprised a long wall exposed to cyclic uniform pressure from both sides, along with two short return walls serving to stabilise the main walls and provide fixed restraints at both ends (as depicted in Figure 112a and b). In Figure 112c, the experimental-numerical comparison is presented, showcasing the macroelement response obtained using a macroelement model. Notably, while the numerical response in the first quadrant substantially aligns with the experimental envelope, there is a significant reduction in strength upon load reversal, resulting in an overall cycle that deviates considerably from the experimental findings. As highlighted by the authors, this discrepancy can be attributed to the characteristics of the constitutive law, wherein strength degradation occurs independently in the positive and negative quadrants. To address this issue, the enhanced macro-element presented in this chapter integrates a more advanced constitutive law for both in-plane (Chapter 5.3) and out-of-plane (Chapter 5.4) springs, sourced from the literature (Tomaževič and Lutman, 1996). This updated model enables the appropriate consideration of actual strength and stiffness degradation.

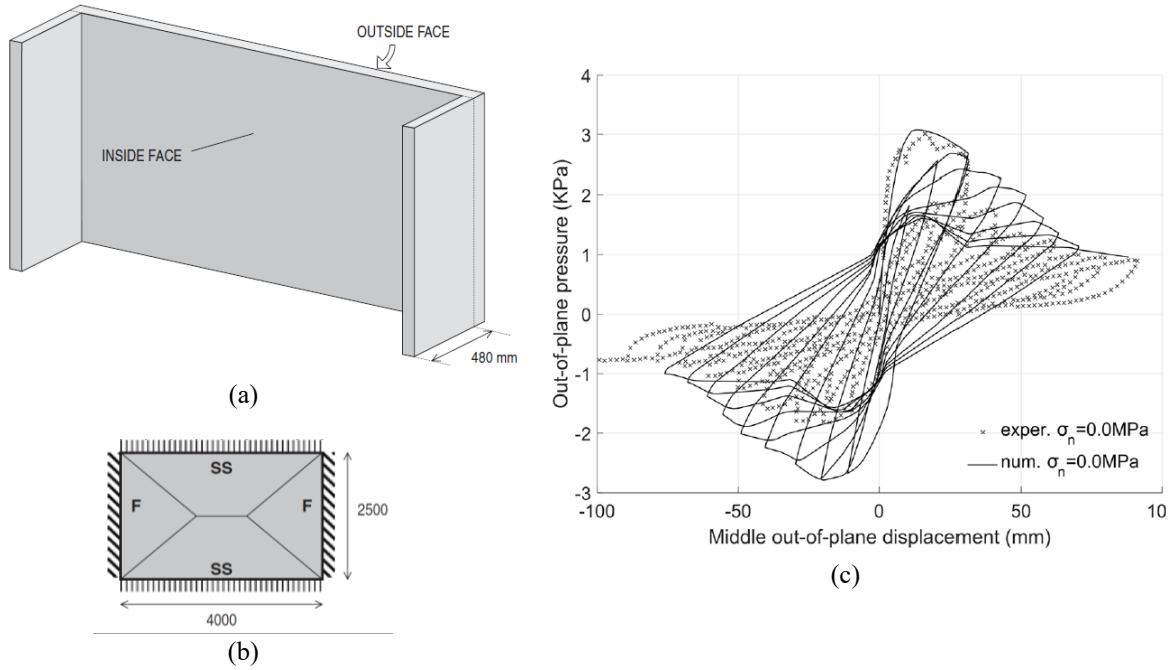

Figure 112 Two-way bending of URM walls subjected to out-of-plane pressure: (a), (b) geometry and boundary conditions (F: fixed support; SS: simple support; Griffith et al., 2007); (c) Numerical-experimental comparison (Minga et al., 2020)

Moreover, an essential modification concerns the definition of the post-peak branch characteristics in the skeleton curve, aimed at ensuring mesh objectivity. This adjustment is crucial as the original specification fails to guarantee it, as will be demonstrated and discussed in Chapter 5.3.1. Furthermore,

an additional parameter controlling the extent of the stiffness degradation is also introduced (Chapter 5.5).

Another drawback of the original model was the impossibility to mechanically differentiate the material characteristics of all the boundary interfaces, which is particularly important for modelling infilled-frames. It is emphasised that an accurate prediction of the infilled-frame structure response strongly depends on the characteristics of the complex and ever-changing contact between frame and infill. This is particularly important, considering the typically poor mechanical properties of the external interfaces and their crucial role in influencing the responses of infilled-frame structures. In the infilled-frame specimen assessed in (Minga et al. 2020), the same material characteristics were adopted for both external frame-to-infill interfaces and internal infill interfaces. As a consequence, the novel enhanced macroelement introduces the capability for this specific differentiation. This aspect, along with the material calibration of infilled-frame models, is presented in Chapter 5.6.

Finally, the macroelement strategy was not assessed within the following important scenarios:

- Analysis of the cyclic response of masonry infilled-frame structures: The macroelement capability to simulate the response of MIF structures was assessed only under monotonic action and was not evaluated under cyclic actions.
- Nonlinear dynamic response: The macroelement was not tested under earthquake loading, neither for URM nor infilled-frame structures.
- Testing on real-sized structures: The macroelement has yet to be tested for the analysis of real-sized structures, highlighting the need to evaluate its applicability and accuracy in practical scenarios.

The application of the enhanced macroelement will be thoroughly examined in Chapter 6 and Chapter 7, where these scenarios will be investigated.

5.3 Modelling of in-plane spring response

The constitutive law for the diagonal in-plane is derived from the model described in (Tomaževič and Lutman, 1996). This model is a cyclic constitutive law for masonry walls, developed based on several experimental tests on masonry piers subjected to in-plane cyclic lateral loading. This constitutive law has been previously utilised in (Rinaldin et al., 2016) for the nonlinear shear springs of a monodimensional macro-model within an equivalent frame description for masonry wall structures.

The amended macro-element subroutine is written in Fortran and implemented into the finite element software ADAPTIC of Imperial College London (Izzuddin, 1991). The pre-processing and post-processing MATLAB scripts (MathWorks, 2022), firstly developed by Minga (2017), were extended and improved to allow damage and deformed shape visualisation of the enhanced macroelement.

5.3.1 Backbone curve

The skeleton curve proposed by Tomazevic-Lutman consists of a lateral load vs. lateral displacement tri-linear curve symmetric with respect to the origin, comprising an elastic and two plastic branches, where the first is characterised by hardening and the second represents softening. The curve is applied on the diagonal spring by considering the direction of the diagonal with respect to the horizontal, as in equation (38). The complete definition of the axial force vs. axial displacement of the diagonal spring requires three points, as illustrated in Figure 113: the elastic limit ($u_{d,y}$, $F_{d,y}$), the point of maximum strength (u_{Fmax}, $F_{d,max}$) and the point of ultimate displacement ($u_{d,u}$, $F_{d,u}$). The curve is dependent on the level of confinement σ_n for the calculation of the maximum strength; thus, the curve is recalculated at each step by considering the average normal stress in the boundary interfaces from the previous converged step of the analysis. This dependency also influences the hysteretic response, which is assessed by allowing for potential step-by-step changes in the vertical stress. Such variations may strongly influence the performance of masonry structures, particularly when subjected to significative ground motion vertical components, as highlighted by Chieffo et al. (2021) and Rinaldin et al. (2019).

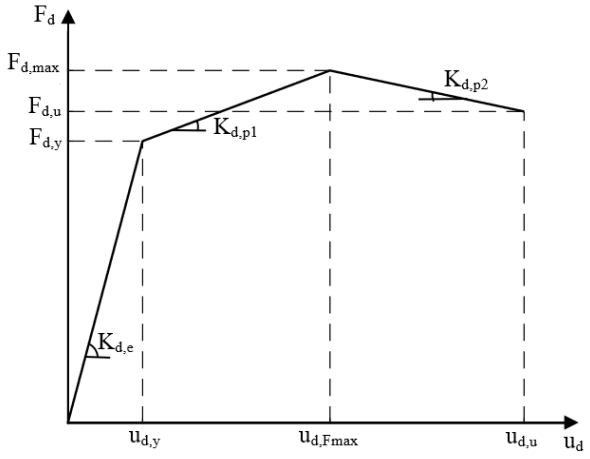

Figure 113. Backbone curve of in-plane spring with the model proposed by Tomazevic-Lutman

The elastic and the first plastic branches of the in-plane spring are uniquely determined by the strengths $F_{d,y}$ and $F_{d,max}$, and the stiffnesses $K_{d,e}$ and $K_{d,p1}$, the latter representing the elastic stiffness and the stiffness of the first plastic branch, respectively.

For the evaluation of the maximum force, two strength criteria are incorporated into the model for evaluating the shear diagonal cracking strength V_{res}, which can be calculated employing either the anisotropic criterion of Mann and Müller (1980), described by equations (35), (36) and (37), or the isotropic criterion of Turnsek and Cacovic (1971) and Turnsek and Sheppard (1980), incorporated in the enhanced formulation and described by the following relation (MIT, 2019):

$$V_{res} = \frac{W \cdot L \cdot f_t}{\xi} \sqrt{\frac{\sigma_n}{f_t} + 1} \tag{45}$$

where f_t is the masonry tensile strength along the diagonal direction of the panel and ξ is a correction coefficient associated with the stress distribution on the section, dependent on the slenderness ratio H/L of the panel (ξ is equal to 1 if H/L is lower than 1, to 1. 5 if H/L is higher than 1.5, and H/L otherwise), while the other parameters are known. $F_{d,max}$ is then calculated though (38). The yielding force $F_{d,y}$ is user-specified as a percentage of the maximum force (a value of 0.7 was assumed by Rinaldin et al., 2016).

The initial axial elastic stiffness of a single diagonal spring, denoted as $K_{d,e}$, depends on the masonry shear modulus G_e and the macro-element geometry, as in (33). The first plastic branch stiffness $K_{d,p1}$ is subsequently defined as a fraction of the initial elastic stiffness, denoted as $K_{d,p1}/K_{d,e}$ (suitable values can be in the range 0.1÷0.2).

In the original formulation, the post-peak stiffness $K_{d,p2}$ was determined by defining a post-peak shear modulus G_p, as outlined in relation (34). Noteworthy, according to this approach, the dimensions of the analysed element are not taken into account, potentially leading to mesh-sensitivity issues. To prove this, a wall subjected to horizontal in-plane monotonic loading is analysed using masonry macroelements with four different mesh refinements: a basic discretisation with a single macroelement and three increasingly refined models with 2x2, 3x3 and 6x6 elements (geometry, load conditions and mesh adopted are illustrated in Figure 114). The wall is fixed at the nodes along the base edges (or the single base edge for the single-element mesh) and restrained against rotations at the nodes on the top edges (or the single top edge for the single-element mesh), where the horizontal displacement δ is applied. A total vertical load F_v of 150kN is distributed among the nodes along the top edges (the vertical load on each node depends on the mesh discretisation). The strength parameters and stiffnesses of the external interfaces are assumed to be infinitely high to exclude their contributions to the overall response. The maximum strength for the diagonal spring of each element in the adopted meshes is

determined using the isotropic criterion of Turnsek-Cacovic. Mechanical and geometric characteristics are provided in Table 25, including the post-peak elastic modulus G_p.

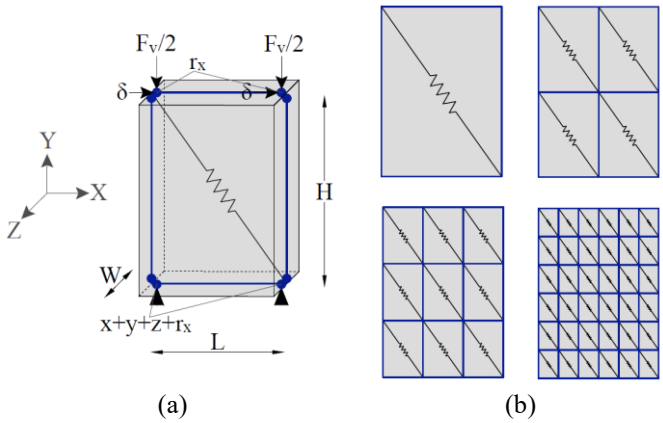

Figure 114. Mesh sensitivity analysis: (a) Geometry and load conditions (case of mesh with a single element); (b) mesh discretisations adopted

Table 25. Geometric and mechanical characteristics of the differently mesh-refined models

Parameter	Symbol	Unit	Value
Height	H	[m]	1.35
Width	L	[m]	1.00
Thickness	W	[m]	0.25
Elastic modulus	G_e	[MPa]	580
Post-peak modulus	G_p	[MPa]	-25
Tensile strength	f_t	[MPa]	0.2
Yielding force ratio	F_y/F_{max}	[-]	0.8
1st plastic branch ratio	K_{p1}/K_e	[-]	0.1
Vertical force	F_v	[kN]	150

The resulting capacity curves for each adopted mesh are shown in Figure 115, illustrating that, despite the accordance on initial stiffness, first post-elastic stiffness and maximum strength, the overall post-peak branch becomes steeper as the mesh becomes more refined. Hence, mesh objectivity is not guaranteed. This fact would also affect the cyclic behaviour, where a minor dissipative capacity would be noticed with increasing mesh refinement.

This issue is resolved by introducing a common fictitious ultimate axial displacement, denoted as $u^*_{d,u}$. This parameter defines the post-peak slope and remains invariant with the mesh discretisation. Notably, the actual ultimate displacement $u_{d,u}$ is either less or equal to $u^*_{d,u}$. Upon revisiting the previous numerical example, a fictitious ultimate lateral displacement δ^*_u equal to 18 mm is considered, which corresponds to a displacement $u^*_{d,u}$ equal to 10.7 mm. As a result, this new definition leads to a post-peak stiffness for the diagonal spring that varies with mesh refinement, becoming steeper as the mesh

becomes coarser, as illustrated in Figure 116a. This results in consistent responses for the entire walls, as the shear vs. lateral displacement curves are now in agreement, as depicted in Figure 116b, thereby ensuring mesh objectivity.

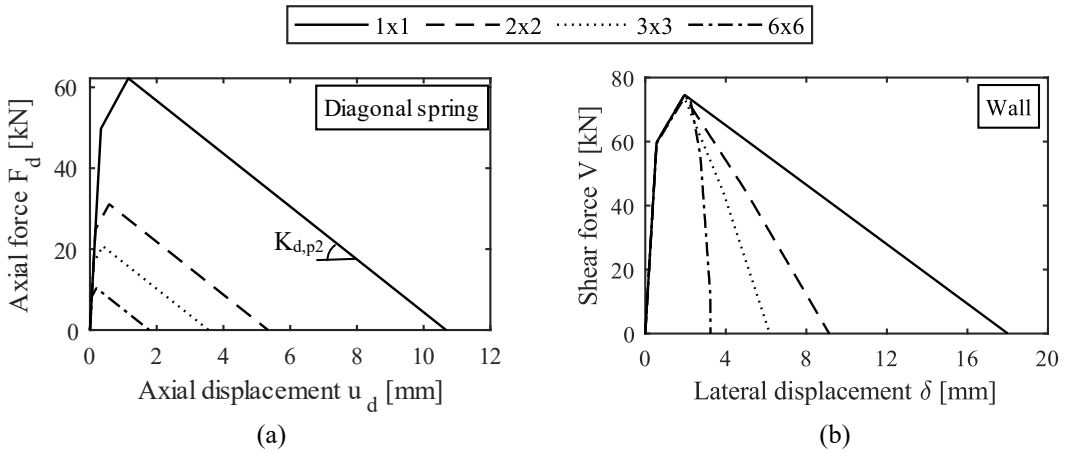

Figure 115. Mesh-sensitivity analysis with former post-peak stiffness definition: (a) axial force versus axial displacement diagonal spring curves; (b) horizontal base shear versus horizontal displacement wall curves

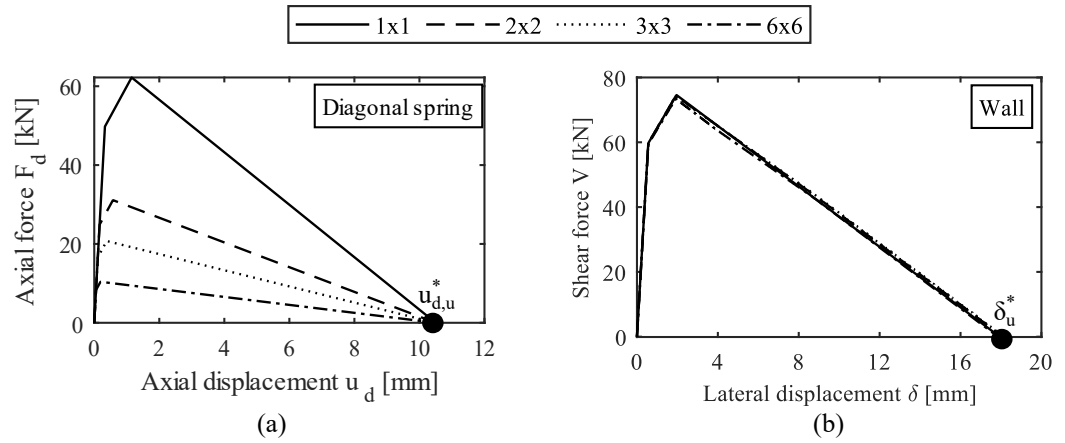

Figure 116. Mesh-sensitivity analysis with new post-peak stiffness definition: (a) axial force versus axial displacement diagonal spring curves; (b) horizontal base shear versus horizontal displacement wall curves

The ultimate point of the backbone curve ($u_{d,u}$, $F_{d,u}$) can be determined by specifying a percentage value of the maximum force $F_{d,max}$. In the present work, the 100% of maximum force decay is considered, thus assuming the fictitious ultimate displacement as the actual one. It should be considered that, in general, a macroelement portion does not coincide with a structural member, namely piers or spandrels. As a result, the typical maximum limit drifts used for such members (MIT, 2008) are not applicable in this context. This feature will be re-examined in future research.

5.3.2 Hysteretic behaviour

The hysteresis cycle proposed by Tomaževič and Lutman (1996) is characterised by a sequence of unloading and reloading branches, as depicted in Figure 117, accounting for strength and stiffness degradation. A representative cycle is reported, starting from the origin O and terminating at the final point H. Initially, the element resides within the elastic field along branch OA, after which it enters the first plastic branch. At point B, a change in the direction of the applied load occurs. Subsequently, within branch BC, the force gradually decreases until it reaches a predetermined percentage (denoted as C_F) of the previously attained maximum load at point C. In particular, branch CD is characterised by an unloading stiffness, denoted as K_d', defined as a certain percentage of the initial elastic stiffness and dependent on the maximum displacement reached $u_{d,1}$; generally, the unloading stiffness decreases as the maximum displacement reached increases, as further shown (Figure 118a). Subsequently, branch CD exhibits a pinching effect, ending at a point symmetric with respect to the origin, at a displacement equal to $-u_{d,1}$. The curve then follows the backbone until another change in the load direction occurs at point F. Here, once again, the force decreases until it reaches a predetermined percentage of the maximum load attained (now corresponding to the maximum strength), with the unloading stiffness dependent on the displacement $u_{d,2}$ (the corresponding unloading stiffness of branch GF is lower than that of branch BC). Finally, in branch GH, the curve is characterised by a reloading branch ending at a point further from the symmetric point with respect to the origin, owing to an additional increase in target displacement Δu due to strength degradation. This additional increase is accounted for during reloading from the third softening branch after overcoming the maximum strength.

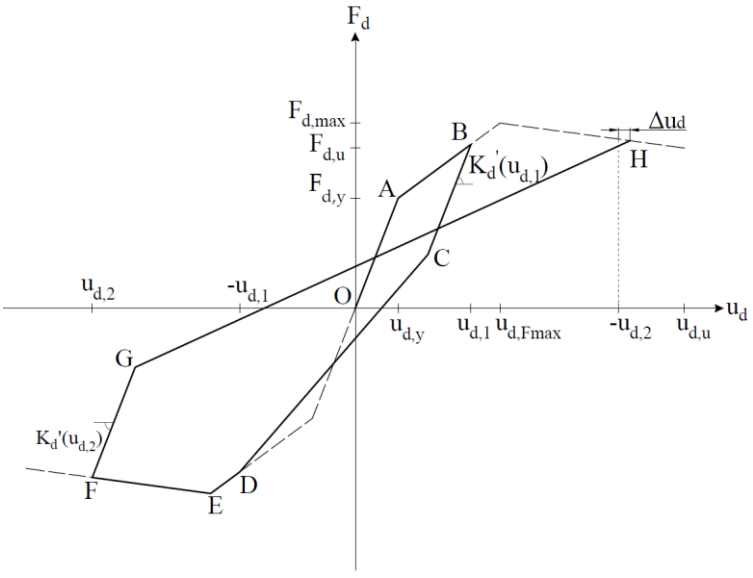

Figure 117. Hysteretic law proposed by Tomazevic-Lutman.

The unloading stiffness $K_d^{'}$ of the unloading branches is described by a linear relationship, as illustrated in Figure 118a, linking it with the maximum displacement reached. This relationship is linear between the initial elastic stiffness $K_{d,e}$ and the ultimate stiffness $K_{d,u}^{'}$, the latter corresponding to the ultimate displacement $u_{d,u}$. In particular, $K_{d,u}^{'}$ is determined as a percentage α of the initial elastic stiffness (46) while a stiffness degradation parameter C_k (47) defines the slope of the unloading stiffness linear decay. The unloading stiffness is finally calculated through equation (48).

$$K'_{d,u} = \alpha\, K_{d,e} \tag{46}$$

$$C_k = \left[\left(K'_{d,u}/K_{d,e}\right) - 1\right]/\left[\left(u_{d,u}/u_{d,y}\right) - 1\right] \tag{47}$$

$$K'_d(u_d) = K_{d,e}\left[1 + C_k\left(\left(u_d/u_{d,y}\right) - 1\right)\right] \tag{48}$$

The strength degradation is based on the estimation of the energy dissipated throughout an entire plastic cycle. As depicted in Figure 118b, an additional displacement is added during the reloading phase, resulting in a lower strength value for a given target displacement. The increase in target displacements Δu is given through the equations (49) and (50), for loading in positive and in negative direction, respectively. Here, β represents a strength degradation parameter (a value of 0.06 is suggested in Tomaževič and Lutman, 1996), dW is the energy dissipated in a cycle and $F_{d,max}$ is the maximum force attained.

$$\Delta u_d^+ = \beta\left(dW^+/F_{d,max}\right) \tag{49}$$

$$\Delta u_d^- = \beta\left(dW^-/F_{d,max}\right) \tag{50}$$

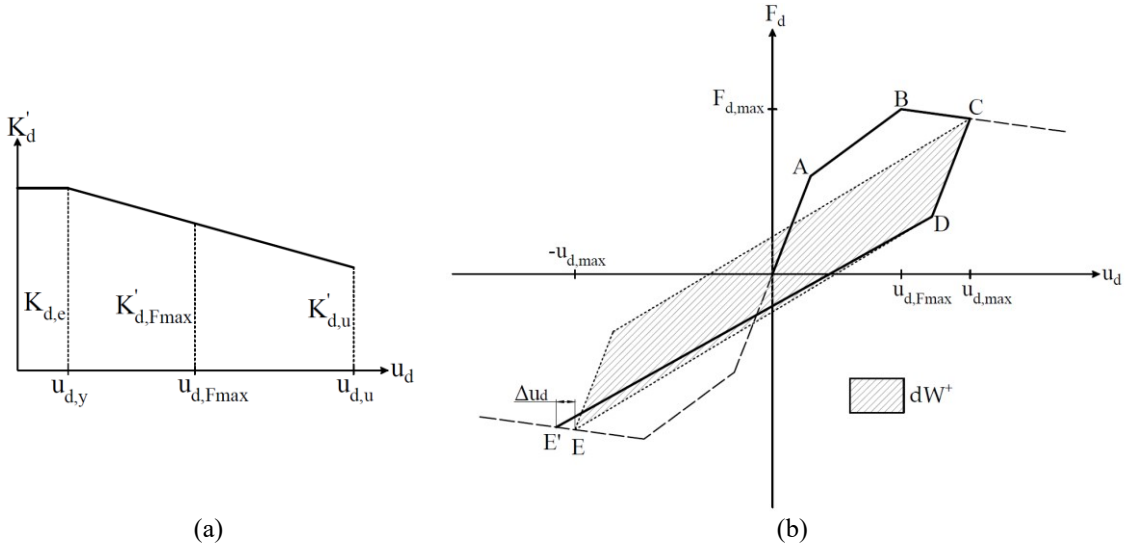

(a) (b)

Figure 118. (a) Definition of the stiffness degradation parameter Ck; (b) Definition of the strength degradation parameter β (after Park et al., 1987)

The deformed shape and in-plane spring damage condition of the macroelement models are represented using a MATLAB post-processing script. A damage parameter, denoted as DAM_{IP}, is evaluated through equation (51), where u_d is the maximum displacement attained. DAM_{IP} linearly varies between 0 and 1, corresponding respectively to the yielding point condition and the ultimate point condition. In the post-processing program $u_{d,y}$ and $u_{d,u}$ are determined by evaluating the backbone curve once the yielding limit is surpassed (note that the backbone curve may vary due to changes in the confinement level).

$$DAM_{IP} = \begin{cases} 0 \;\; u_d < u_{d,y} \\ \dfrac{u_d - u_{d,y}}{u_{d,u} - u_{d,y}} \;\; u_{d,y} \le u_d \le u_{d,u} \\ 1 \;\; u_d > u_{d,u} \end{cases} \tag{51}$$

Illustrative shear base vs. lateral displacement cycles are reported in Figure 119a, representing the responses of a 1x1 model under in-plane cyclic loading, for which both the old and new implementations of the constitutive law for the diagonal spring are utilised to qualitatively show the different responses. The panel analysed is the same as in Chapter 5.3.1, as illustrated in Figure 114, with geometric and mechanical characterisation provided in Table 25. The post-peak branch is evaluated within the new constitutive model by fixing a horizontal ultimate displacement of 18mm. The additional hysteretic parameters for the Tomazevic-Lutman constitutive relationship are derived from (Rinaldin et al., 2016); in particular, the force percentage for the evaluation of the first unloading branch C_F is set equal to 0.4, the stiffness degradation parameter α is 0.8 and the strength degradation β is 0.06. The imposed displacements for the short panel considered in Chapter 3 (Figure 39a) are horizontally applied at the top of the specimen. The deformed shape corresponding to the maximum displacement is illustrated in Figure 119b. Additionally, the damage plot for the in-plane diagonal spring is reported in Figure 119c, with different damage levels specified in the colormap on its side.

In Chapter 6.2, the capability of the enhanced macroelement, defined with the new constitutive law for the spring, to accurately simulate the in-plane response of masonry structures will be extensively examined by simulating several experimental tests.

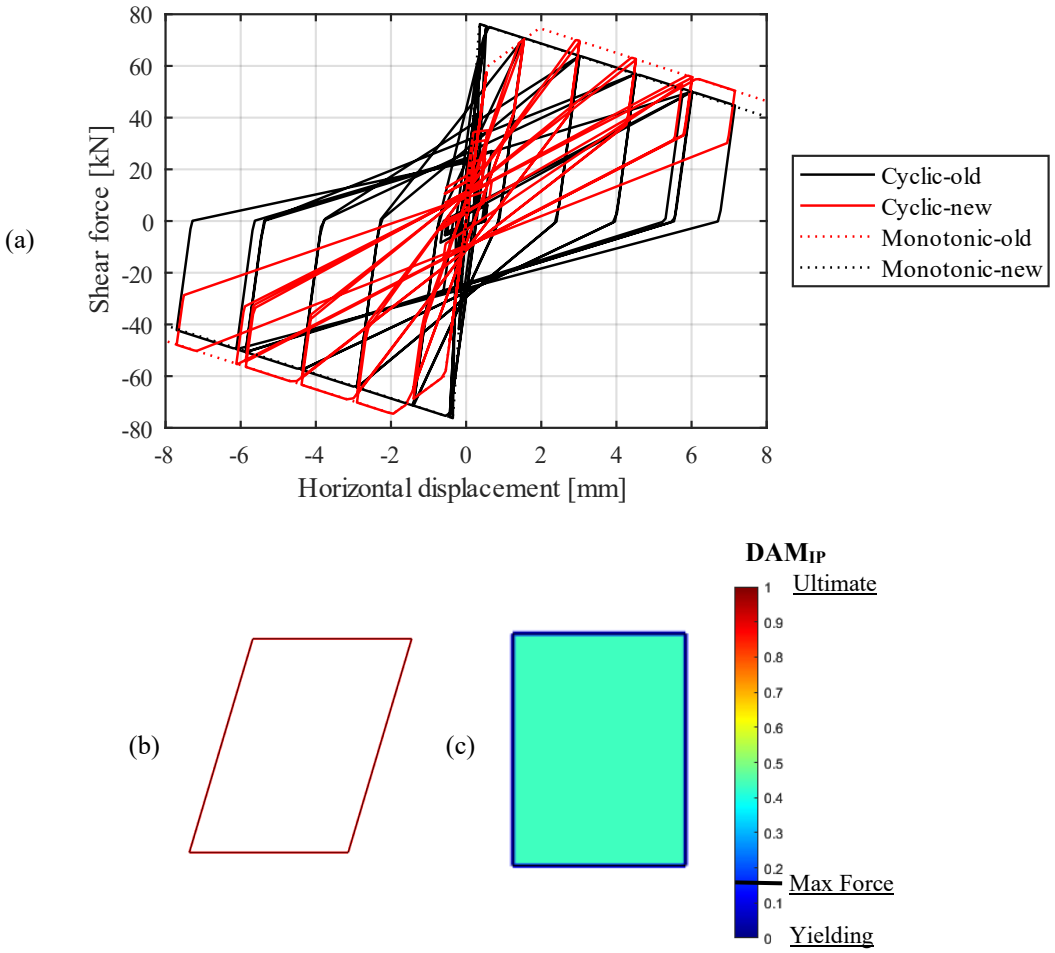

Figure 119. (a) Comparison of shear base vs. lateral displacement cycles between the original and the new models for the in-plane diagonal spring; (b) Deformed shape at maximum displacement (amplification factor of 20); (c) Damage state at the last step of the analysis

5.4 Modelling of out-of-plane spring response

The Tomazevic-Lutman law is applied also to the out-of-plane diagonal spring introducing a distinct model description. As outlined in Chapter 5.2 the monotonic force-displacement response of a wall subjected to out-of-plane loading can be described by a trilinear relationship (Figure 111c), featuring an initial linear-elastic behaviour, a second branch with softening and a third horizontal plateau representing the actual residual strength. Therefore, for the out-of-plane spring, the Tomazevic-Lutman model is applied by considering a backbone curve with a different configuration of the plastic branches to maintain consistency with the previous implementation. Hence, the spring modification only pertains

to the definition of the hysteretic response, for which the model described in Chapter 5.3.2 is utilised, following the same rules for defining the F_{out}-u_{out} cyclic response.

The characterisation of the backbone curve involves the definition of the elastic stiffness $K_{out,e}$, the post-peak stiffness $K_{out,p}$, the maximum strength $F_{out,y}$ (which coincides with the yielding strength) and the residual strength $F_{out,r}$. These parameters can be derived from the masonry Young's modulus E_e, the post-peak modulus E_p, the yield pressure with zero compression $p_{y,0}$, the residual pressure with zero compression $p_{r,0}$, the peak friction-angle $\mu_{o,p}$ and the residual friction angle $\mu_{o,r}$, using equations from (39) to (44). Detailed mesoscale models, as suggested in (Minga et al., 2020), offer a reliable tool for the evaluation of the required mechanical parameters.

In-plane spring and out-of-plane spring act independently one to each other, thus their damage states are represented separately. For the out-of-plane spring, a damage parameter denoted as DAM_{OOP} is defined and evaluated through equation (52), depending on the maximum force reached on the spring. DAM_{OOP} linearly varies between 0 and 1, corresponding respectively to the yielding point condition, which for the out-of-plane spring coincides with the maximum strength, and the residual strength. As for the in-plane spring, in the post-processing program, $F_{out,y}$ and $F_{out,r}$ are determined by evaluating the backbone curve once the yielding limit is surpassed.

$$DAM_{OOP} = \begin{cases} 0 \;\; F_{out} < F_{out,y} \\ \dfrac{F_{out,y} - F_{out}}{F_{out,y} - F_{out,r}} \quad F_{out,y} \le F_{out} \le F_{out,r} \\ 1 \;\; F_{out} > F_{out,r} \end{cases} \tag{52}$$

Illustrative out-of-plane corner force vs out-of-plane corner displacement cycles are reported in Figure 19a, representing the responses of a basic 1x1 model macroelement subjected to out-of-plane loading, for both the old and new implementations for the out-of-plane spring constitutive law. The model features free rotations at the nodes and is pinned in the Z-direction at 3 out of 4 corners while an out-of-plane force is applied to the free corner node (Figure 120b). Geometric and mechanical properties and the applied load are provided in Table 26. The out-of-plane deformed shape at the maximum displacement is depicted in Figure 120c. In contrast, the damage of the out-of-plane spring is represented in Figure 120d, corresponding to full damage given that the residual branch has been reached.

In Chapter 6.3, the capability of the enhanced macroelement to accurately simulate the out-of-plane response of masonry structures will be extensively examined through the simulation of experimental

tests regarding the out-of-plane loading of a wall subjected to two-way bending under different configurations of vertical loads and the presence of openings. The notable pinching effects, which characterise the physical response of panels subjected to out-of-plane loading (Griffith et al., 2007) and were not fully represented by the original implementation in (Minga et al., 2020), as also reported in Figure 112, can be accurately predicted by the enhanced material model, as will be further shown.

Table 26 Geometric and mechanical characteristics of the 1x1 model subjected to out-of-plane loading.

Parameter	Symbol	Unit	Value
Height	H	[m]	1.25
Width	B	[m]	2.00
Thickness	W	[m]	0.11
Elastic modulus	E_e	[MPa]	1000
Post-peak modulus	E_p	[MPa]	-50
Yield pressure with zero compression	$p_{y,0}$	[KPa]	1
Residual pressure with zero compression	$p_{r,0}$	[KPa]	0.05
Yield out-of-plane friction-angle	$\mu_{o,y}$	[-]	0.004
Residual out-of-plane friction-angle	$\mu_{o,r}$	[-]	0.004
Total vertical load	F_v	[kN]	44.0

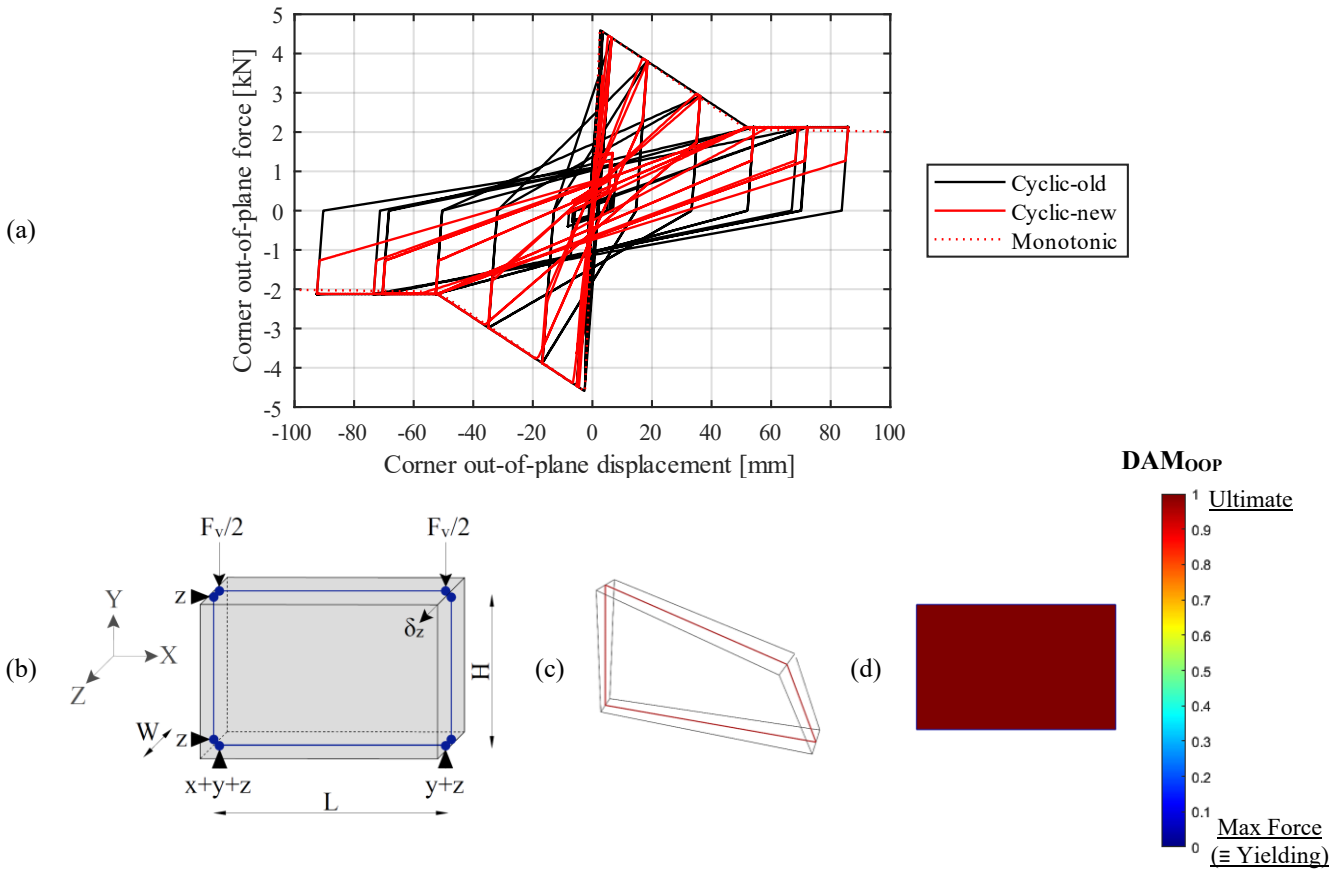

Figure 120. (a) Comparison of out-of-plane force vs. out-of-plane displacement cycles between the original and the new models for the in-plane diagonal spring; (b) Geometry of URM block; (c) Deformed shape at maximum displacement (amplification factor of 20) and (d) Damage state at the last step of the analysis

5.5 Stiffness recovery

Introducing the new spring law, designed to simulate both in-plane and out-of-plane cyclic behaviour, results in a mutual dependence of damage propagation in opposite directions. Specifically, when the spring unloads after reaching a displacement +u within the plastic region (defined by either the plastic pre- or post-peak branch), it follows a linear branch towards the displacement -u, which is equal and opposite to +u. Hence, this characteristic differs from the previous implementation (illustrated in Figure 109), where the cycles evolved independently in the first and third quadrants.

To allow for achieving an intermediate behaviour, the enhanced implementation offers users the ability to specify a parameter, denoted as k_{rec}, that governs a certain stiffness recovery during cyclic actions. This parameter represents the percentage by which the unloading stiffness increases. The recovery is applied to the reloading branches after reaching the maximum strength. However, it is limited by the slope that would lead to the already attained peak strength. This parameter can be applied to both in-plane and out-of-plane springs.

The modification leads to wider cycles as k_{rec} increases, resulting in higher dissipation capacity. This effect can be observed in Figure 121, where the macroelement model analysed in Section 5.3.2 (Figure 114; Table 25) is re-examined with the inclusion of the stiffness recovery, specifically considering recovery of 10% and 20%. The stiffness recovery factor significantly affects the shear displacement cycle (Figure 121a) and the amount of total energy (Figure 121b). This additional feature may improve the prediction of experimental responses, as shown further in the simulations of Chapter 6.

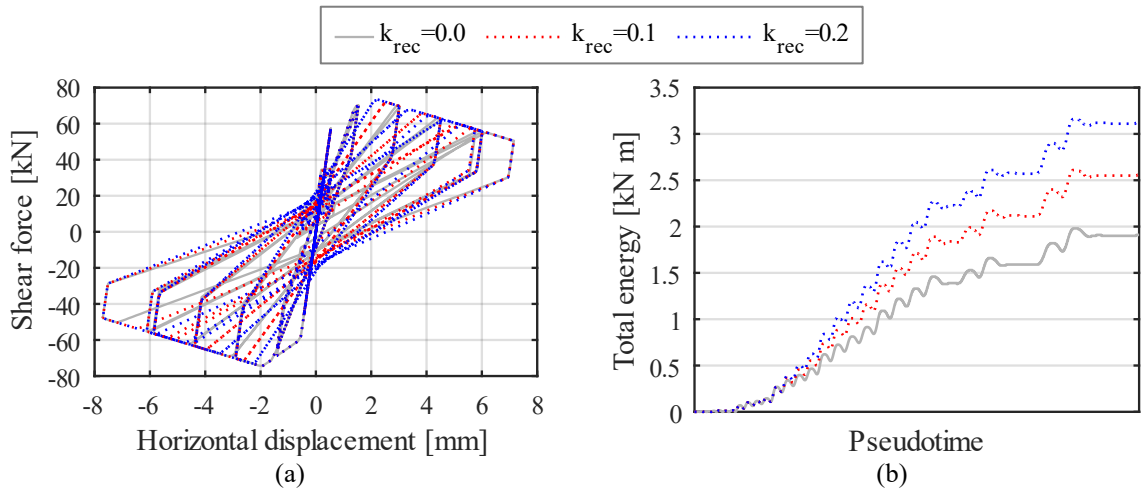

Figure 121. Application of different stiffness recovery parameters: (a) shear-displacement cycles; (b) dissipation energies

5.6 Enhanced macroelement for infilled-frame structures modelling

This chapter focuses on modelling masonry infilled frames using the novel enhanced macroelement. It discusses the advancements made within the macroelement and the calibration characteristics of infilled-frame models, which enable the representation of all the typical in-plane resistance mechanisms of this structural typology.

In the original implementation, the mechanical characterisation of the macroelement cohesive interfaces could not be distinctly specified for each edge since the two horizontal interfaces (top and bottom edges) share a single set of material properties, as for the vertical interfaces (left and right edges). Consequently, introducing separate properties for internal and external frame-infill interfaces of macroelements at the boundaries of a masonry infill panel was impossible.

As emphasised in Chapter 4, the external frame-infill mortar layers play a crucial role in the overall response of infilled-frame structures, typically weaker than the internal mortar joints. Consequently, the enhanced macroelement model allows for the distinct specification of materials for all cohesive interfaces, addressing this limitation. In particular, the proposed refinement enables considering the different characteristics of external frame-infill interfaces, permitting more accurate predictions of the overall response.

Figure 122 shows an illustrative infilled-frame model featuring a 3x3 mesh representing the masonry infill and highlighting the components characterising the infilled-frame macroelement model. It is noted that the external cohesive interfaces at the border between the frame and infill may have different characteristics from the internal ones. Additionally, the representation of external edges varies depending on whether they are full dof edges (considered when adjacent to frame elements) or reduced dof edges (considered between two adjacent masonry macroelements), as mentioned in Chapter 5.2 (see Figure 105).

The complete characterisation of the model necessitates the specification of:

- External cohesive interfaces, characterised by low strength properties for both shear and tensile responses, but high compression strength, as discussed in Chapter 4. These interfaces are crucial during the initial phases of analysis, influencing the detachment of the infill from the frame.
- In-plane diagonal spring, modelled using the Tomazevic-Lutman constitutive law, as presented for in-plane springs in Chapter 5.3, for both backbone and hysteretic responses. In this context,

since diagonal cracking typically does not represent an ultimate collapse mechanism, following the guidelines of (Comité Euro-International du Béton, 1996) and supported by the results of Chapter 4 analysis with more refined models, the maximum strength ($F_{d,max}$) is assumed to represent the corner crushing mechanism, while the yielding strength ($F_{d,y}$) represents the actual diagonal cracking mechanism.

- Internal interfaces, defined utilising the properties of mortar joints and bricks. These interfaces play a crucial role in representing the ultimate mechanism of sliding; moreover, the compressive and tensile responses of these interfaces may have a significant impact in presence of openings and more generally in the post-plastic phase.

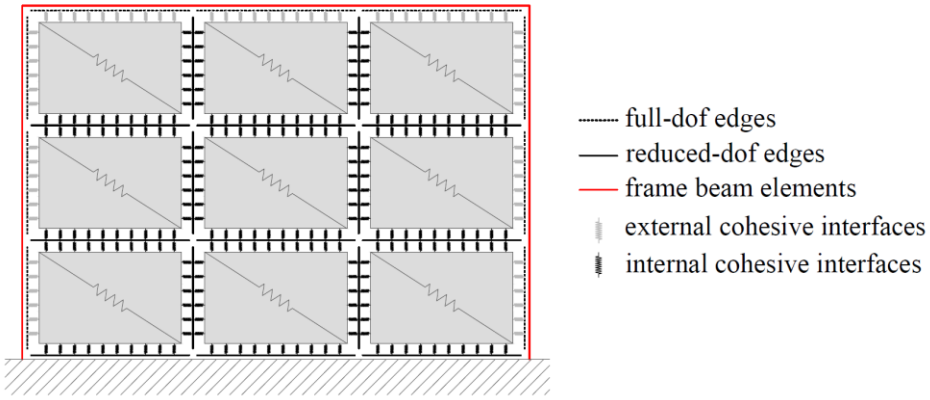

Figure 122 Macrolement infilled-frame modelling

Figure 123 provides a qualitative representation of the typical in-plane resistant mechanisms in infilled frames along with their corresponding macroelement representations. In particular, diagonal cracking (Figure 123-a1 and a2) can occur due to the yielding of the in-plane springs along the infill diagonal or in its proximity. The corner crushing (Figure 123-b1 and b2), generally occurring after diagonal cracking, may result from the collapse of the springs at the corners. The sliding mechanism is represented in Figure 123-c1 and c2 by the Mode II failure of a row of internal cohesive interfaces. These representations are simplifications, and the mechanisms that occur are generally more complex, often involving a combination of failure modes. For instance, part of the crushing may also be attributed to the failure of internal cohesive interfaces, and diagonal cracking may occur outside the infill diagonal elements.

Possible out-of-plane mechanisms are not considered herein. Indeed, it is deemed necessary to implement a corotational approach within the macroelement formulation to adequately consider the geometric nonlinearity, which can be significant in slender panels used for infills. This aspect will be

re-examined in the future. Finally, frame failure can be captured through the adopted fibre-plasticity approach proposed by Izzuddin and Elnashai, (1993b), as described in Chapter 4.3 and employed for the modelling of the frame.

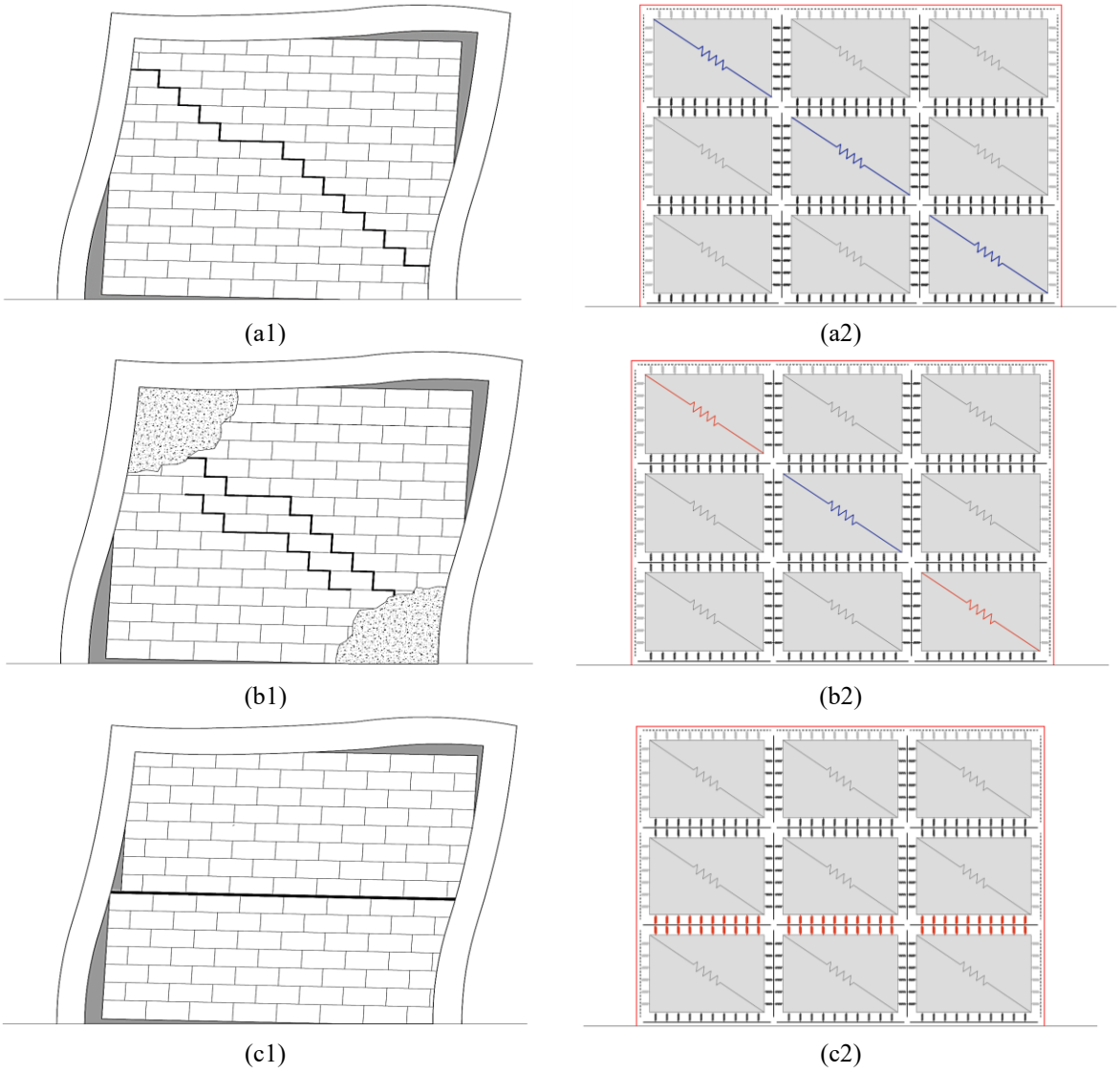

Figure 123 Qualitative representation of typical in-plane infilled-frame resistant mechanisms and their macroelement representations: (a) diagonal cracking; (b) corner crushing (considered occurring after diagonal cracking); (c) sliding

To highlight the influence of external interfaces on the overall response of a macroelement model and to present the calibration characteristics, the infilled frame model discussed in Chapter 4 is revisited (experimental test taken from Mehrabi et al., 1996). Two scenarios are analysed, involving external interfaces that are either equivalent to or weaker than the internal ones.

The geometry and mechanical characteristics of the infilled frame have been presented in Chapter 4. Specifically, the experimental mechanical properties of the concrete for specimen 1 (bare-frame) and specimen 3 (infilled rame) are presented in Table 14. Additionally, the properties of the masonry infill are detailed in Table 15, while the experimental mechanical properties of steel can be found in Table 16. Figure 124 depicts the modelling of the bare RC frame, which is discretised with a coarser mesh compared to those employed for mesoscale and continuum macroscale infills. The bare-frame mesh is chosen to enable the insertion of up to 6x6 infill macroelements (which represent the finest mesh evaluated in Chapter 6). As mentioned, the bare-frame model is discretised with elements considering the fibre-plasticity approach proposed by Izzuddin and Elnashai (1993b) while rigid elements are adopted for the modelling of beam-column joints and for the bottom ends of the columns. The mechanical properties employed are reported in Table 18.

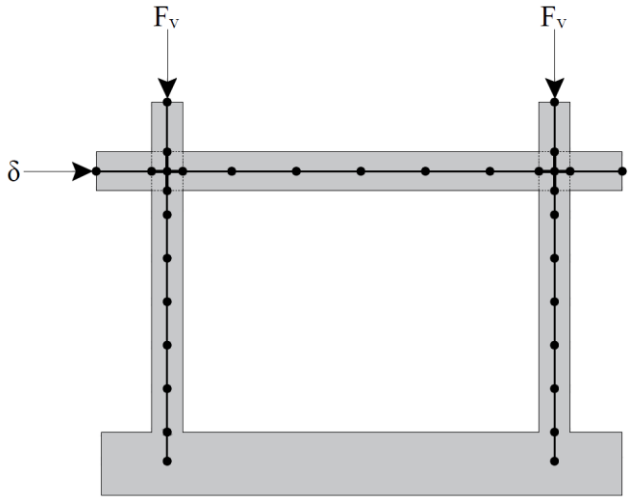

Figure 124 Bareframe modelling

The macroelement infill model is discretised with a 3x3 mesh, with an additional row of infinitely stiff and strong elements at the base, replicating the behaviour of the RC bottom beam. Table 27, Table 28 and Table 29 provide the mechanical characteristics of internal interfaces, external interfaces, and diagonal springs, respectively.

Concerning the stiffness values, the same elastic moduli are applied for internal (Table 27) and external interfaces (Table 28). This choice is made because each edge contributes to the elastic deformability of a specific portion of an element, depending on its area of influence. The normal modulus E_n of the horizontal interfaces is taken as the tangent of the experimental elastic modulus (derived from the experimental stress-strain curves reported by Mehrabi, 1994), while for the vertical ones 70% of its

value is assumed. The tangential elastic modulus of interfaces is assumed to be infinitely high, as the shear elastic deformability is considered concentrated along the diagonal springs. The shear modulus of the diagonal spring G_e (Table 29) is determined to be 40% of the normal Young's modulus of the interfaces.

The strength parameters (bond strength, cohesion and friction angle) of the horizontal internal interfaces are derived from the results of triplet shear tests (Table 17 and Figure 79), consistent with the mesoscale modelling. For vertical interfaces, average values between mortar interfaces and internal brick interfaces are employed for cohesion and bond strength (where the cohesion of brick-brick interfaces is assumed to be equal to the tensile strength), while the same coefficient of friction as the horizontal interfaces is considered. The compressive strength of the horizontal interfaces is defined as the experimental compressive vertical strength. At the same time, 50% of its value is adopted for the vertical interfaces coherently with mesoscale and macroscale modelling.

The weak shear strength parameters for the external interfaces are determined based on the reference configurations of both mesoscale and continuum macroscale approaches aiming to capture the mechanisms of opening and sliding that occur between the infill and frame. On the other hand, the external interfaces are modelled using a high compressive strength. As mentioned, this feature is intended to represent the high compression strength of the column and beam perpendicular to the fibres and to prevent excessive interpenetration between the infill and the frame.

The estimation of the diagonal spring strength is undertaken by applying a criterion that assesses the lateral strength of an infilled frame concerning the corner crushing failure mechanism, as presented in Chapter 5.6.1. This involves evaluating an equivalent tensile strength f_t, to be applied within the Turnsek-Cacovic criterion. The actual diagonal cracking mechanism corresponds to the yielding point, being assessed by determining an appropriate $F_{d,y}/F_{d,max}$ ratio. Furthermore, the ultimate displacement δ_u^* is chosen to fit the post-peak branch of the experimental response.

Figure 125 provides a comprehensive representation of the model, wherein each macroelement is distinctly identified based on edge characteristics, including materials, the number of degrees of freedom considered, and specific features related to the diagonal springs. This representation also differentiates the nodes belonging to the macroelements from those exclusively associated with the RC frame. Details regarding the characteristics of the edges and the diagonal springs for each element are outlined in Table 30.

Table 27 Internal infill interfaces material parameters for infilled frame specimen 3.

		E_n [MPa]	f_t [MPa]	c [MPa]	tanϕ [-]	f_c [MPa]	$G_{f,I}$ [N/mm]	$G_{f,II}$ [N/mm]	$G_{f,c}$ [N/mm]
Horizontal	Int-h	14300	0.075	0.11	1.02	15.10	0.05	0.10	20.7
Vertical	Int-v	10010	0.86	0.88	1.02	7.50	0.05	0.10	18.0

Table 28 External frame-infill interfaces material parameters for infilled frame specimen 3.

		E_n [MPa]	f_t [MPa]	c [MPa]	tanϕ [-]	$G_{f,I}$ [N/mm]	$G_{f,II}$ [N/mm]
Horizontal	Ext-h	14300	0.01	0.014	0.35	0.05	0.10
Vertical	Ext-v	10010	0.01	0.014	0.35	0.05	0.10

Table 29. Diagonal springs characterisation for infilled frame specimen 3.

Identification	G_e [MPa]	f_t [MPa]	δ_u^* [mm]	k_{pl1}	F_y/F_{max}	C_F	α	β
Diag	5720	1.2	15	0.1	0.53	0.4	0.8	0.06

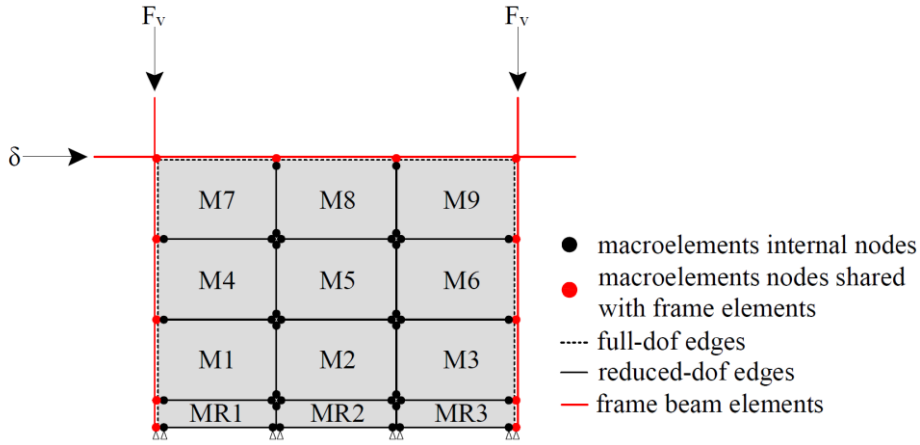

Figure 125 Macroelement infilled-frame modelling

Table 30 Characteristics of the macroelements in the 3x3 infilled frame model. "Rig" and "Diag-rig" denote infinitely strong and stiff interface and diagonal spring; "R" and "F" indicate reduced-DOF edge and full-DOF edge, respectively.

Macroelement identification	Edge 1		Edge 2		Edge 3		Edge 4		Diagonal spring
	Material	DOF	Material	DOF	Material	DOF	Material	DOF	
MR1	Rig	R	Rig	R	Rig	R	Rig	F	Diag-rig
MR2	Rig	R	Rig	R	Rig	R	Rig	R	Diag-rig
MR3	Rig	R	Rig	F	Rig	R	Rig	R	Diag-rig
M1	Ext-h	R	Int-v	R	Int-h	R	Ext-v	F	Diag
M2	Ext-h	R	Int-v	R	Int-h	R	Int-v	R	Diag
M3	Ext-h	R	Ext-v	F	Int-h	R	Int-v	R	Diag
M4	Int-h	R	Int-v	R	Int-h	R	Ext-v	F	Diag
M5	Int-h	R	Int-v	R	Int-h	R	Int-v	R	Diag
M6	Int-h	R	Ext-v	F	Int-h	R	Int-v	R	Diag
M7	Int-h	R	Int-v	R	Ext-h	F	Ext-v	F	Diag
M8	Int-h	R	Int-v	R	Ext-v	F	Int-v	R	Diag
M9	Int-h	R	Ext-v	F	Ext-h	F	Int-v	R	Diag

5.6.1 Diagonal spring strength assessment

The assessment of the in-plane spring strength involves the consideration of a corner crushing mechanism, corresponding to the experimental failure mode also observed by mesoscale and macroscale modelling. The criterion proposed by (Decanini et al., 2004) within a single-strut modelling approach is taken into account. This criterion is implemented in the macroelement model by considering a proper equivalent tensile strength through the application of the Turnsek-Cacovic criterion. While not simulating ultimate failure, the diagonal cracking mechanism is treated as a reduction in stiffness of the second branch of the backbone curve (see Figure 113). As a result, the in-plane spring accounts in a phenomenological manner for both the diagonal cracking and corner crushing mechanisms.

(Decanini et al., 2004) introduced analytical relationships for the different mechanisms characterising the infill frame response. Specifically, the strength associated with corner crushing in contact with the frame, denoted as σ_{cc}, is given by the following relationship:

$$\sigma_{cc} = \frac{(1.12\ \sin\theta\cos\theta)}{K_1(\lambda_h)^{-0.12} + K_2(\lambda_h)^{0.88}} f_c \tag{53}$$

where f_c is the masonry compressive strength, θ is the slope of the strut with respect to the horizontal axis, λ_h is a non-dimensional parameter depending on the geometric and mechanical characteristics of the frame-infill system, K_1 and K_2 are coefficients functions of λ_h and calibrated based on experimental tests. The λ_h parameter is determined through the relation (Smith, 1967, 1966; Smith and Carter, 1969):

$$\lambda_h = h\sqrt[4]{\frac{E_m t_{inf} \sin 2\theta}{4E_c I_c h_{inf}}} \tag{54}$$

where E_m is the equivalent elastic modulus corresponding to the complete cracking stage of the infill, E_c is the elastic modulus of concrete, t_{inf} is the thickness of the infill masonry panel, h is the story height, h_{inf} is the height of the masonry infill panel, I_c is the second moment of area of the column cross section. The width of the strut ω is introduced by means of the relative stiffness parameter λ_h, the two constants K_1 and K_2, and length d of the equivalent strut, as in the following relation:

$$\omega = \left(\frac{K_1}{\lambda_h} + K_2\right) d \tag{55}$$

Finally, the lateral strength of the equivalent strut associated with corner crushing $V_{res,CC}$ is given by the following relation:

$$V_{res,CC} = \sigma_{cc}\, t_{inf}\, \omega\, \cos\theta \tag{56}$$

The calculation of the lateral strength for the analysed case is reported in Table 31.

Table 31 Calculation of lateral strength for corner compression failure.

Frame			Infill			Lateral strength Corner compression failure		
h	1536.5	mm	f_c	15.1	MPa	λh	4.55	
b	2337	mm	t_{inf}	92	mm	K_1	0.707	
b_c	178	mm	l_{inf}	2337	mm	K_2	0.01	
h_c	178	mm	h_{inf}	1422	mm	ω	462.33	mm
I_c	$8.366 \cdot 10^7$	mm4	E_M	9520	MPa	σ_{cc}	12.37	MPa
E_c	21930	MPa	d	2796.9	mm	$V_{res,CC}$	439.79	kN
			θ	33.3	°			

The equivalent tensile strength $f_{t,eq}$, can be then determined by inverting the Turnsek-Cacovic criterion (equation (45)):

$$f_{t,eq} = \frac{-\sigma + \sqrt{\sigma^2 + 4\left(V_{res,CC}\,\xi / t_{inf} l_{inf}\right)^2}}{2} \tag{57}$$

In this way, it is possible to evaluate the equivalent tensile strength as a function of the vertical stress σ_n. The vertical stress of the infill varies throughout the analysis, progressively increasing with the lateral displacement. In an initial estimation, assuming a uniform distribution of the total applied load to the infill leads to a vertical stress of 1.37 MPa, corresponding to a tensile strength of 1.47 MPa. To gain insight into the potential variation of the equivalent tensile strength with vertical stress, the parabolic relation σ_n - $f_{t,eq}$ is depicted in Figure 126, for vertical stresses between 0 and 3 MPa. A sensitivity evaluation within this range enables a simple estimation of the final value adopted for the analysis, which was set as 1.2 MPa.

The diagonal spring represents the diagonal cracking mechanism by adopting an appropriate $F_{d,y}/F_{d,max}$ ratio. This is evaluated by calculating the shear strength V_{res} using the Turnšek-Cacovič criterion, as described by relation (45), and considering a tensile strength value f_t corresponding to either the corner crushing mechanism or the diagonal cracking mechanism. The confinement level is assumed to be equal to 1.37 MPa, approximating the initial vertical stress. First, the equivalent tensile strength determined for the corner crushing mechanism (assumed to be equal to 1.2MPa) is applied, resulting in a shear strength of 377.6 kN. Then, the tensile strength corresponding to the diagonal cracking mechanism

assumed to be equal to 0.47 MPa and derived from the continuum macroscale model analysed in Chapter 4 (Table 21), is applied, resulting in a shear strength of 199.9 kN. Finally, the $F_{d,y}/F_{d,max}$ ratio for the diagonal spring is taken as the ratio of the two shear strength values, resulting in a value of 0.53.

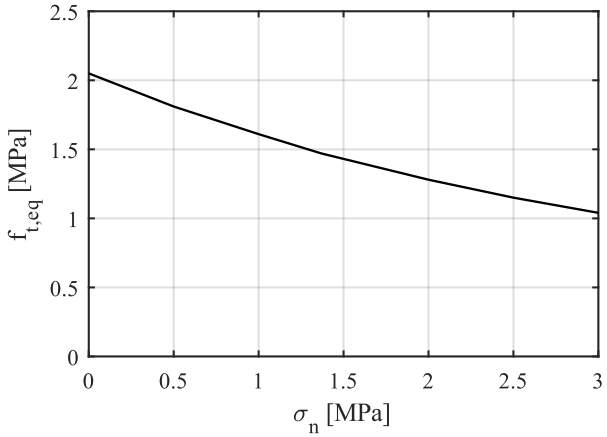

Figure 126 Equivalent tensile strength as a function of vertical stress.

5.6.2 Macroelement infilled-frame response

Figure 127 presents the shear-displacement responses for two infilled-frame models: one with weak external interfaces (referred to as “Model A”) and another with external interfaces equal to the internal ones (referred to as "Model B"). The experimental curve is also included for comparison.

The main distinction lies in the model ability to capture the initial decrease in stiffness, attributed to the detachment of the infill from the frame. The differentiation of external interfaces in Model A allows a more accurate representation of this initial stiffness decrease, contrasting with Model B, where it is overestimated. The difference is evident in the progression of the deformed shape and damage of diagonal springs, as depicted in Figure 128 for model A and Figure 129 for model B.

In model A, right from the beginning of the analysis (at a displacement of 0.5 mm), the weakened characteristics of the external interfaces result in an early detachment at the top-right corner, followed by detachment at the bottom-left corner (visible with a displacement equal to 2 mm). After the complete detachment of the infill frame, the diagonal strut begins to develop as the diagonal spring yields, surpassing the diagonal cracking strength. By a displacement of 4 mm, recognisable diagonal cracking damage is evident, with the diagonal spring along the infill diagonal within the first plastic phase. The peak strength is reached when some diagonal springs reach their maximum strength, corresponding to

a displacement of around 6.5 mm. Therefore, the damage progression of the model aligns with the experimental observations.

The progressive frame-infill detachment also takes place in Model B, with external interfaces equal to the internal ones but with a certain delay, not allowing for a correct prediction of the stiffness in the elastic phase (Figure 129). This would decrease the fundamental period of vibration and, consequently, a higher magnitude of the seismic actions. Moreover, the greater resistance against tensile debonding and sliding provided by the external interfaces, results in a more stepped curve, in contrast to the smoother curve observed in the case of weak interfaces (Figure 127). Nevertheless, comparisons with the experimental response reveal that both models accurately predict the maximum force. Concerning the post-peak behaviour, both models accurately capture the rate of strength decay. However, an extended stepped plateau of maximum strength is observed in the model without interfaces distinction after the peak.

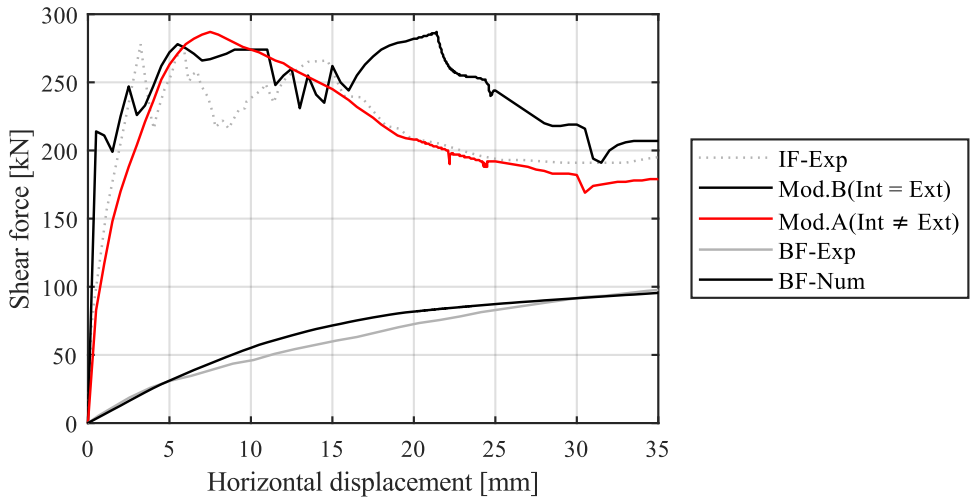

Figure 127 Infilled-frame shear-displacement responses (Int: internal interfaces, Ext: external interfaces, Exp: experimental response; Num: numerical response; IF: Infilled Frame; BF: Bare Frame)

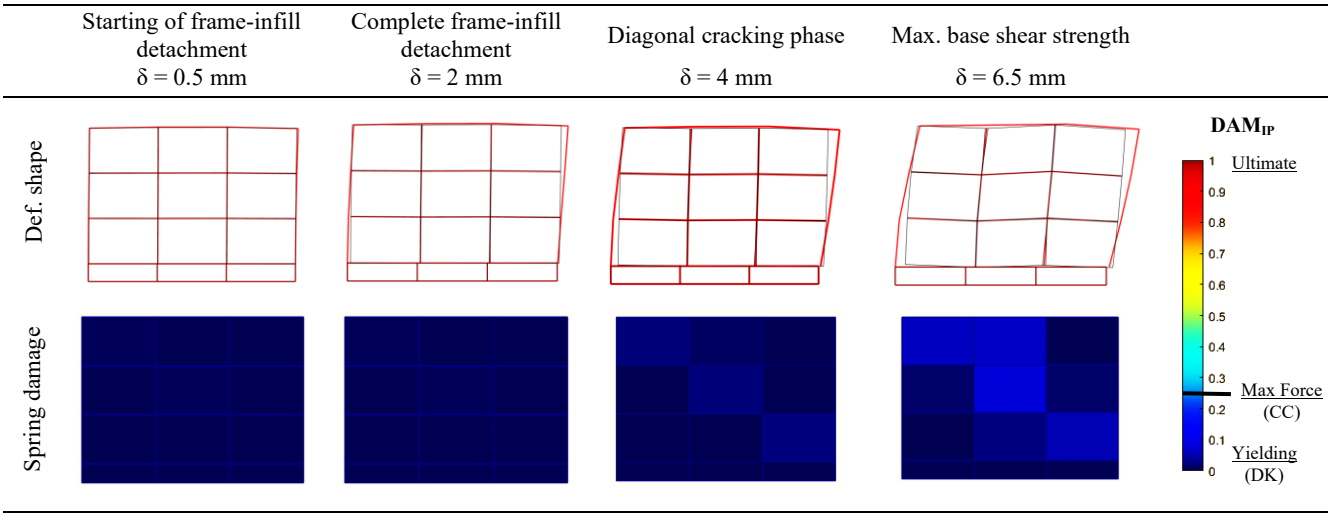

Figure 128 Model A: deformed shape (amplification factor of 50) and in-plane diagonal spring damage progressions at three steps in the first phase of the analysis (DK: diagonal cracking; CC: corner crushing)

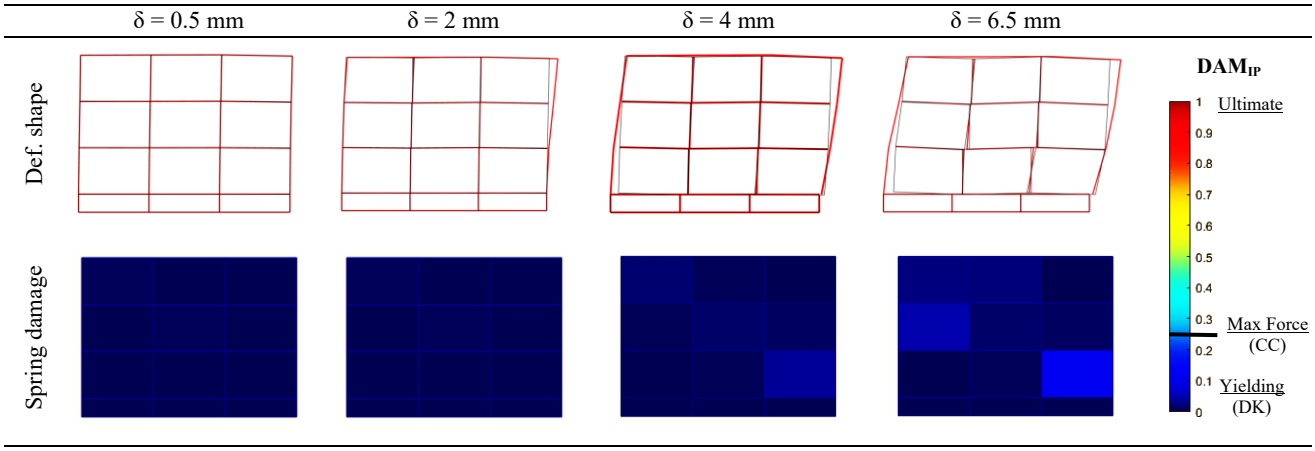

Figure 129 Model B: deformed shape (amplification factor of 50) and in-plane diagonal spring damage progressions at three steps in the first phase of the analysis (DK: diagonal cracking; CC: corner crushing)

In Figure 130, infill deformed shapes and in-plane spring damages at the last step are presented for both models, revealing some differences between them.

In the first model (Figure 130a), four elements at the top-left corner have exceeded the corner crushing conditions, indicating that the diagonal springs have surpassed their maximum strength. While the element at the corner still retains some residual capacity (the damage indicator is around 0.65), the other three have reached the collapse limit, as evidenced by the attainment of the ultimate displacement. This damage state resembles the experimental observations, wherein crushing mechanisms are observed not only at the top-left corner but also in the top-middle of the panel, possibly after the splitting of the diagonal strut where one branch pointed towards the centre of the top beam (suggestion given also by the cracking of the top beam). Additionally, spring damage is accompanied by crushing and tensile

debonding of internal cohesive interfaces at the bottom-right corner, which develops towards the end of the analysis and is not observed in the experimental observations. Therefore, given the simplified nature of the macroelement approach, the enhanced macroelement model provides a reasonably accurate prediction of the damage state progression, not only in the pre-peak phase but also in the post-peak phase.

Not considering the differentiation of frame-infill cohesive interfaces leads to a different response in terms of damage progression within the post-peak phase, as shown in Figure 130b. The spring element at the bottom right corner is fully damaged, and sliding mechanisms are also visible, neither of which were observed in the experimental observations.

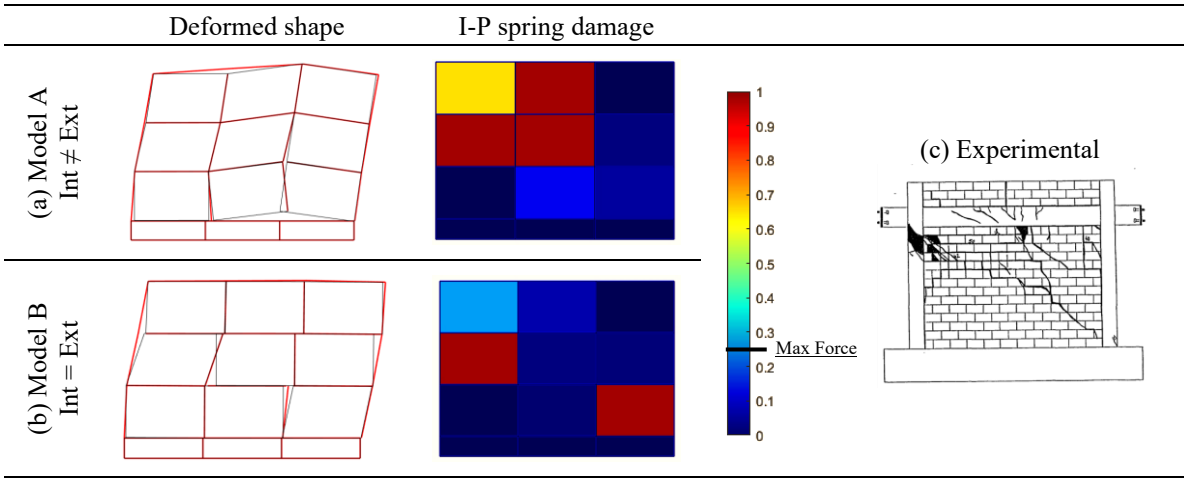

Figure 130 Post-peak phase: deformed shape (amplification factor of 5) and in-plane diagonal spring at the last step of analysis, for models with frame-infill external interfaces either (a) differentiated from or (b) equal to the internal infill interfaces, and (c) experimental damage at the end of the experimental test (Mehrabi et al., 1996)

Figure 131 illustrates the deformed shape and damage of the RC frame at the final step, providing a comparison between the results obtained from the macroelement modelling (specifically considering model A) and those obtained from the more refined mesoscale and continuum macroscale modelling employed in Chapter 4. The damage pattern of the RC frame within the macroelement modelling agrees well with the experimental observations and is consistent with the results obtained from mesoscale and continuum macroscale models. In particular, the damages observed at the top of the left column and the centre-left of the top beam in the macroelement model, resulting from the failure of the macroelements at the top-left corner, align with experimental evidence. Nevertheless, the severe damage observed at the bottom of the right column was less pronounced in the experimental observations; this, however, aligns with findings from mesoscale and macroscale models. Similarly, the damage observed in the

middle of the left column was not evident in the experiments but was observed in both mesoscale and continuum macroscale models.

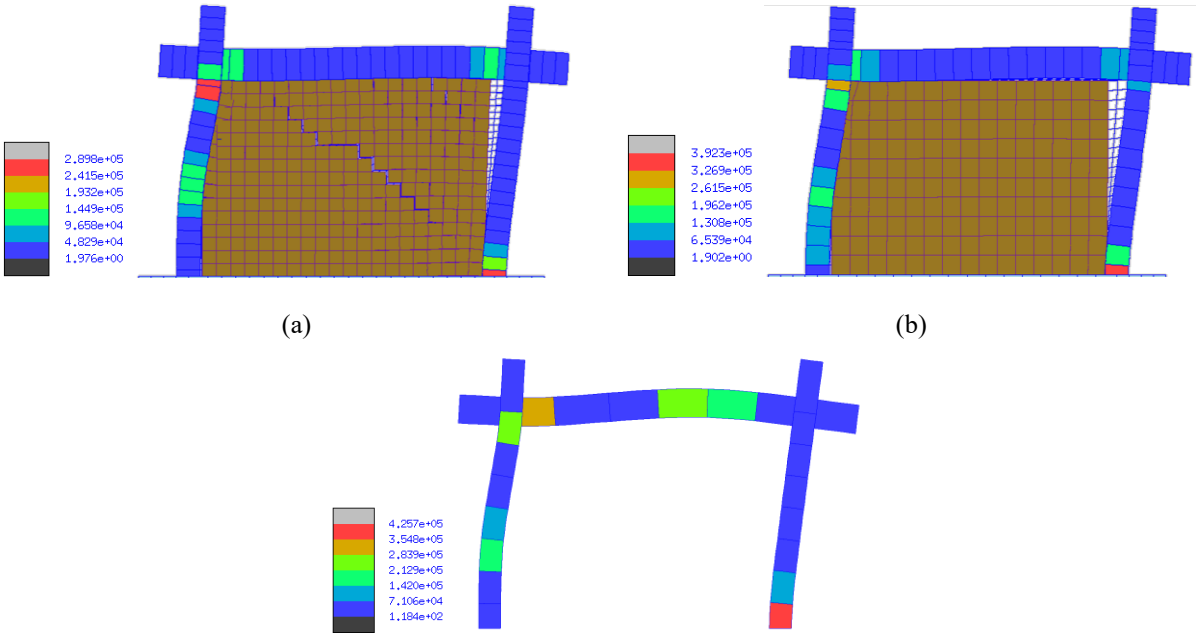

Figure 131 Deformed shape (5x amplification) at the last step with the contour on the frame indicating strain energy (values in legend expressed in N mm), for, (a) mesoscale model, (b) continuum macroscale model and (c) macroelement (Model A)

5.7 Summary and conclusions

The present chapter presents developments introduced to enhance an existing macroelement model. An improved constitutive law governing the phenomenological evaluation of both in-plane and out-of-plane response was implemented. The updated relationship is characterised by realistic strength and stiffness degradation. An important refinement also concerned the post-peak branch definition in the skeleton curve. To assure mesh objectivity, the post-peak branch is defined by specifying an ultimate displacement independent from the adopted mesh. Users can also specify an intermediate cyclic response by introducing a stiffness recovery factor, which determines the characteristics of the unloading and reloading branches.

Finally, a separate definition of the mechanical properties of the external frame-infill interfaces and the internal masonry interfaces has been introduced to predict the actual response of infill frames. This allows for considering frame-infill interfaces characterised by weaker mechanical characteristics as found in actual structures. This feature enables an improved prediction of the actual behaviour at the

first loading stages by capturing the actual stiffness degradation after the initial detachment of the infill from the frame. Additionally, an objective calibration of the various components of the infill macroelement was presented. As a result, the enhanced macroelement can represent all typical in-plane mechanisms of infilled-frame structures. Finally, the macroelement has been tested against experimental outcomes, demonstrating its significant potential in assessing this particular structural typology.

The enhanced macroelement will be deeply validated in the next chapter by simulating experimental tests on both URM and masonry-infilled frame structures.

CHAPTER 6

MACROELEMENT SIMULATIONS OF URM AND MASONRY-INFILLED FRAME STRUCTURES

6.1 Introduction

In this chapter, an exhaustive evaluation of the enhanced macroelement approach is undertaken, focusing on applications for both URM and masonry-infilled frame structures.

The structural components under investigation include the masonry elements subjected to in-plane loadings previously studied in Chapter 3. This examination encompasses a short wall, characterised by a shear failure mode with diagonal cracking, a tall panel exhibiting a typical flexural response, and the entire façade with openings. Furthermore, the analysis extends to the crucial out-of-plane response, essential for comprehensively assessing the seismic performance of existing masonry buildings. This is achieved through the simulation of four experimental cyclic tests conducted on unreinforced masonry walls subjected to two-way bending. Additionally, the enhanced macroelement potential is evaluated through the simulation of an experimental test on a 3D masonry structure subjected to earthquake loading.

In relation to infilled frame structures, the solid masonry-infilled frame specimen investigated in Chapter 4, employing advanced mesoscale and continuum macroscale modelling techniques for the masonry infills, is revisited herein with the utilisation of macroelements for the modelling of the infill. Subsequently, the simulation of a cyclic experimental test is conducted to evaluate the capability of the enhanced macroelement model in predicting the hysteretic response of masonry-infilled frames. Finally, the macroelement is assessed for its capability to consider the presence of openings within the masonry infills in infilled frames by comparing its outcomes with those derived from the continuum macroscale

models implemented in Chapter 4 (models derived from a solid infilled frame model calibrated based on experimental tests).

6.2 URM structures under in-plane actions

6.2.1 Single panels

The URM wall structures examined in Chapter 3 are here evaluated to determine the accuracy provided by the enhanced macroelement in representing the response under in-plane horizontal loading up to collapse. The experimental mechanical parameters are reported in Table 5, while the geometry of the analysed specimens is given in Table 6.

Concerning the stiffness parameters, the normal elastic modulus (E_n) of the horizontal interfaces is set as the experimental tangent modulus, which has been derived from the experimental stress-strain curves reported in (Binda et al., 1995) in Chapter 3. The normal elastic modulus of the vertical interfaces is evaluated as 70% of the horizontal one, as suggested by Jafari et al. (2022). The elastic shear modulus (G_e) for the diagonal spring is determined using the secant experimental elastic modulus, calculated through interpolation within the range values specified by the Italian code for assessing existing masonry structures (MIT, 2019), by considering the typology of masonry with solid brick and lime mortar (Table 9).

The strength parameters of the horizontal interfaces, namely tensile bond strength (f_t), cohesion (c), and friction angle (tanφ), are determined from the experimental values. For the vertical interfaces, cohesion and tensile bond strength are considered as average values between the characteristics of bricks and mortar (where the cohesion of brick-brick interfaces is assumed equal to its tensile strength), while the friction angle is set to the horizontal value. The compressive strength (f_c) of the horizontal interfaces corresponds to the experimental masonry compressive strength, while for the vertical interfaces the 50% of the same value is assumed. The mode I and mode II fracture energies are set to 0.05 and 0.1 MPa (as in Minga et al., 2020), respectively, while crushing fracture energies are computed through the relation proposed by Model Code 90 (Comité Euro-International du Béton, 1993). Finally, the shear strength of the diagonal spring is evaluated using the anisotropic criterion of Mann-Müller (as described by relations (38), (36) and (37)); this criterion represents one of the two alternatives available for determining the shear strength of the diagonal spring, alongside the isotropic criterion of Turnsek-Cacovic described in equation (45). The global equivalent values of cohesion and friction angle, denoted as $\tilde{c}$ and $\tilde{\mu}$, are determined based on the experimental characteristics of mortar joints and the

arrangement of the masonry texture. The diagonal spring ultimate displacement (δ_u^*) has been evaluated to fit the experimental cyclic strength degradation. Finally, the additional parameters (α, β and C_F) are those employed in the models evaluated in Chapter 5, derived from (Rinaldin et al., 2016).

Table 32 Material parameters of the interfaces for the single panels simulations

Interface	E_n [MPa]	f_t [MPa]	c [MPa]	tanϕ [-]	f_c [MPa]	$G_{f,I}$ [N/mm]	$G_{f,II}$ [N/mm]	$G_{f,c}$ [N/mm]
Horizontal	1980	0.04	0.23	0.58	6.2	0.05	0.1	17.5
Vertical	1386	0.63	0.73	0.58	3.1	0.05	0.1	16.3

Table 33. Material parameters of the diagonal springs for the single panels simulations

G_e [MPa]	$\tilde{c}$ [MPa]	$\tilde{\mu}$ [-]	δ_u^* [mm]	K_{pl}/K_{el}	F_y/F_{max}	C_F	α	β
580	0.17	0.42	10.5	0.1	0.8	0.4	0.8	0.06

The experimental set-up is reproduced through the explicit modelling of the rigid base and the upper beam; these are modelled through macroelements characterised by infinitely stiff and strong interfaces and diagonal springs. The base is fully fixed while the upper beam is allowed only to translational motion, maintaining a horizontal orientation.

The short panel has been examined through four distinct mesh discretisations, and the corresponding responses are given from Figure 132 to Figure 135. These encompass shear force vs. horizontal displacement diagrams, deformed shapes and damage patterns for the diagonal springs for both monotonic and cyclic simulations. Regarding the damage representation, it is important to note that DAM_{IP} values (defined in relation (51)) range from 0 to 1, representing the transition from the yielding point and elastic phase to the ultimate displacement. For the monotonic analysis, spring damage and deformed shape are given at the midpoint and at the end of the analysis, as well as for the spring damage snapshots in the cyclic analysis. Besides, cyclic analysis deformed shapes are reported at the maximum and the minimum displacements.

The shear-displacement curves are in close agreement with the experimental response, with a satisfactory alignment starting from the coarse 2x2 mesh. Improved accuracy is observed with the more refined 3x3 and 6x6 meshes. Initial stiffness, maximum strength and force at the onset of damage are correctly reproduced for the monotonic and cyclic responses. The wide hysteretic shear-displacements cycles, due to diagonal-cracking, are close to the experimental response. Indeed, when the wall is subjected to reversal cyclic actions, strength and stiffness degradations are reasonably well simulated.

As far the shear damage pattern is concerned, the monotonic response is characterised by the propagation of damage (shear springs failures) in the elements along the compression diagonal. This is accompanied by the occurrence of horizontal crack openings at both the bottom and the top of the wall. As for the cyclic analysis, the numerical responses exhibit a first phase wherein the diagonal damage displays a somewhat mirrored pattern, resulting in the characteristic X-shaped damage. In the final phase, the collapse of the elements in a single row is observed.

Only the basic 1x1 model fails to capture the actual response, exhibiting a flexural behaviour characterized by an S-shaped cycle. This response is marked by openings at the top and bottom interfaces, accompanied by only marginal damage in the diagonal springs.

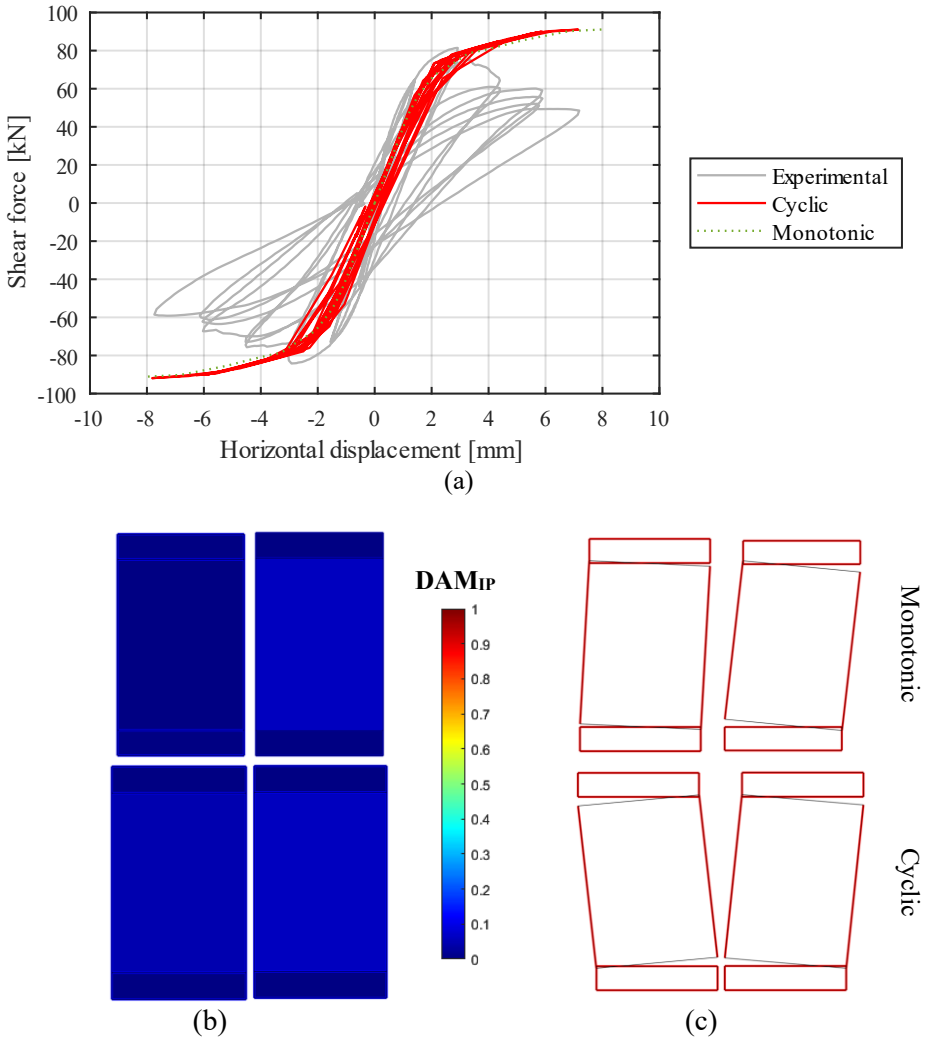

Figure 132 Short panel responses with 1x1 discretisation: a) experimental-numerical shear-displacement curves; b) in-plane diagonal spring damage for monotonic and cyclic analysis (at half and at the end of the analysis); c) deformed shape for monotonic (at half and at the end of the analysis) and cyclic analysis (at the maximum positive and minimum negative displacements; amplification factor 20)

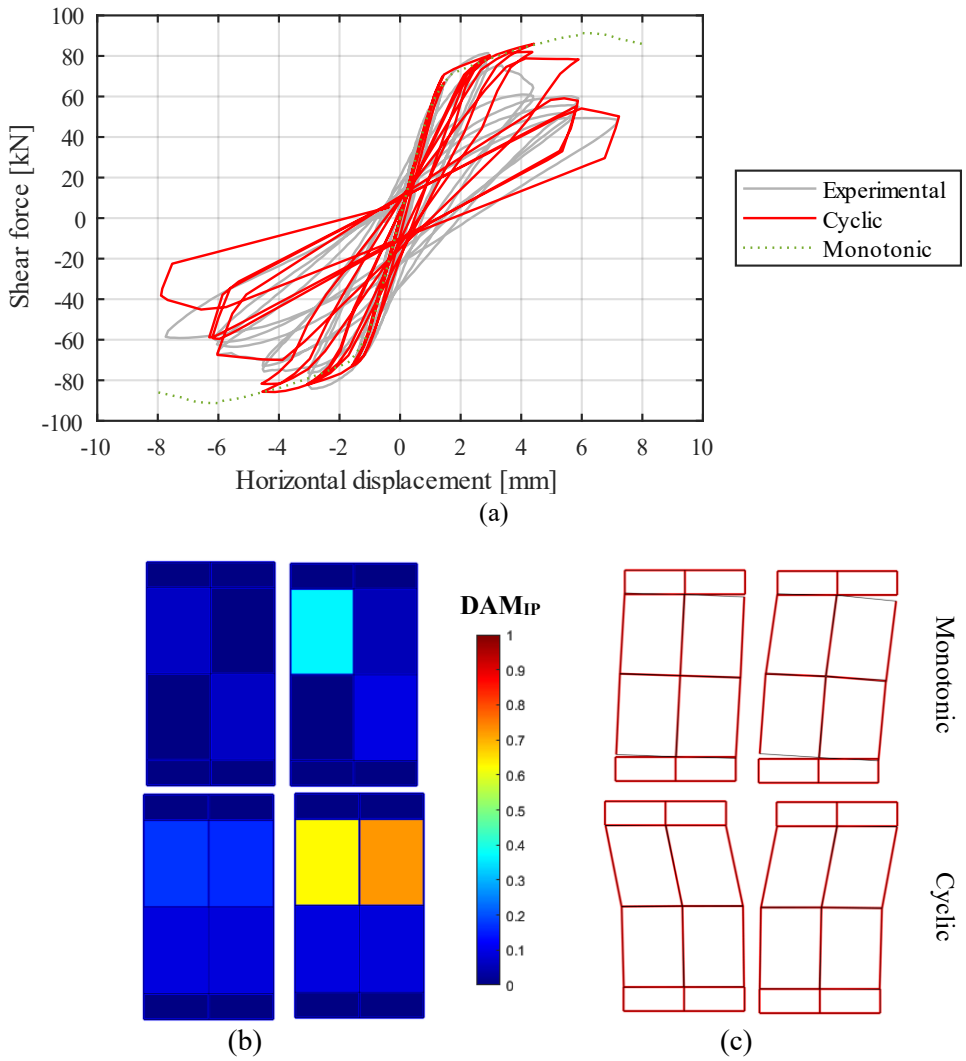

Figure 133 Short panel responses with 2x2 discretisation: a) experimental-numerical shear-displacement curves; b) in-plane diagonal spring damage for monotonic and cyclic analysis (at half and at the end of the analysis); c) deformed shape for monotonic (at half and at the end of the analysis) and cyclic analysis (at the maximum positive and minimum negative displacements; amplification factor 20)

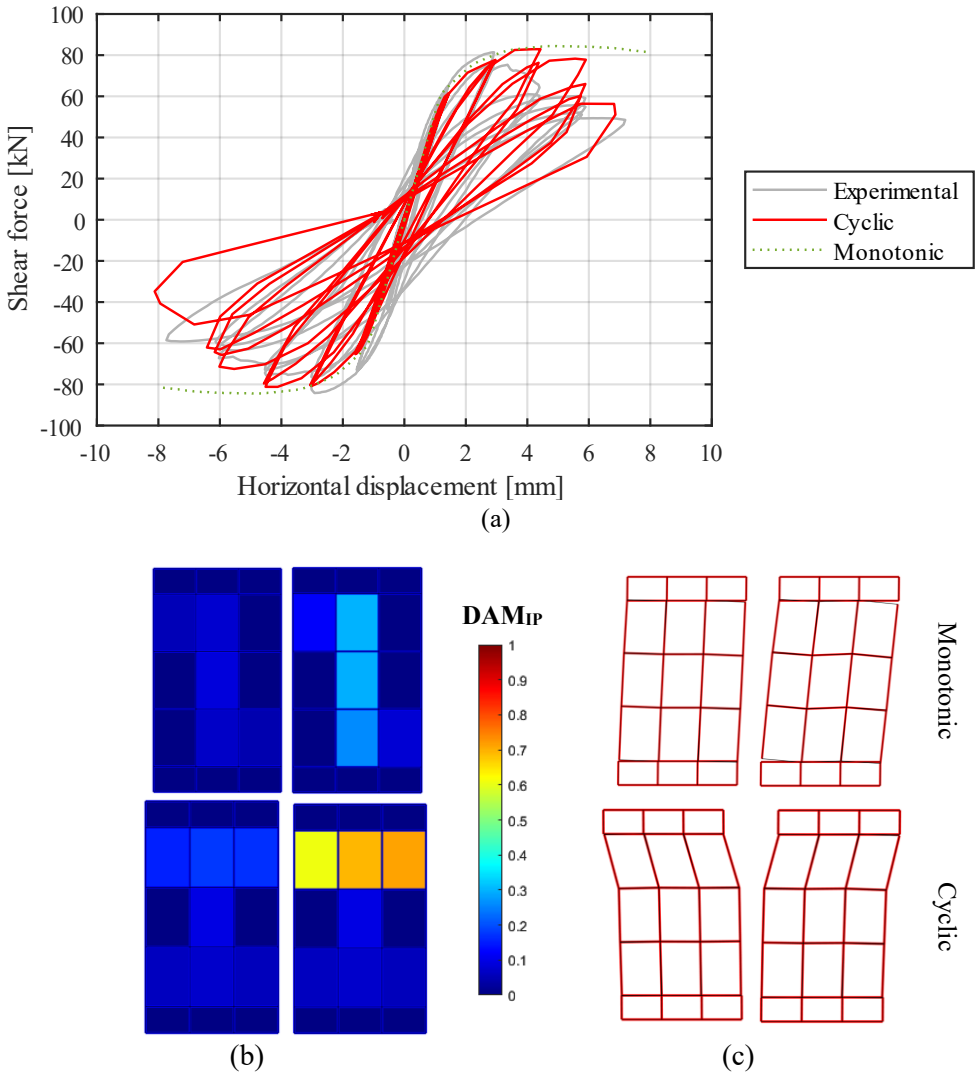

Figure 134 Short panel responses with 3x3 discretisation: a) experimental-numerical shear-displacement curves; b) in-plane diagonal spring damage for monotonic and cyclic analysis (at half and at the end of the analysis); c) deformed shape for monotonic (at half and at the end of the analysis) and cyclic analysis (at the maximum positive and minimum negative displacements; amplification factor 20)

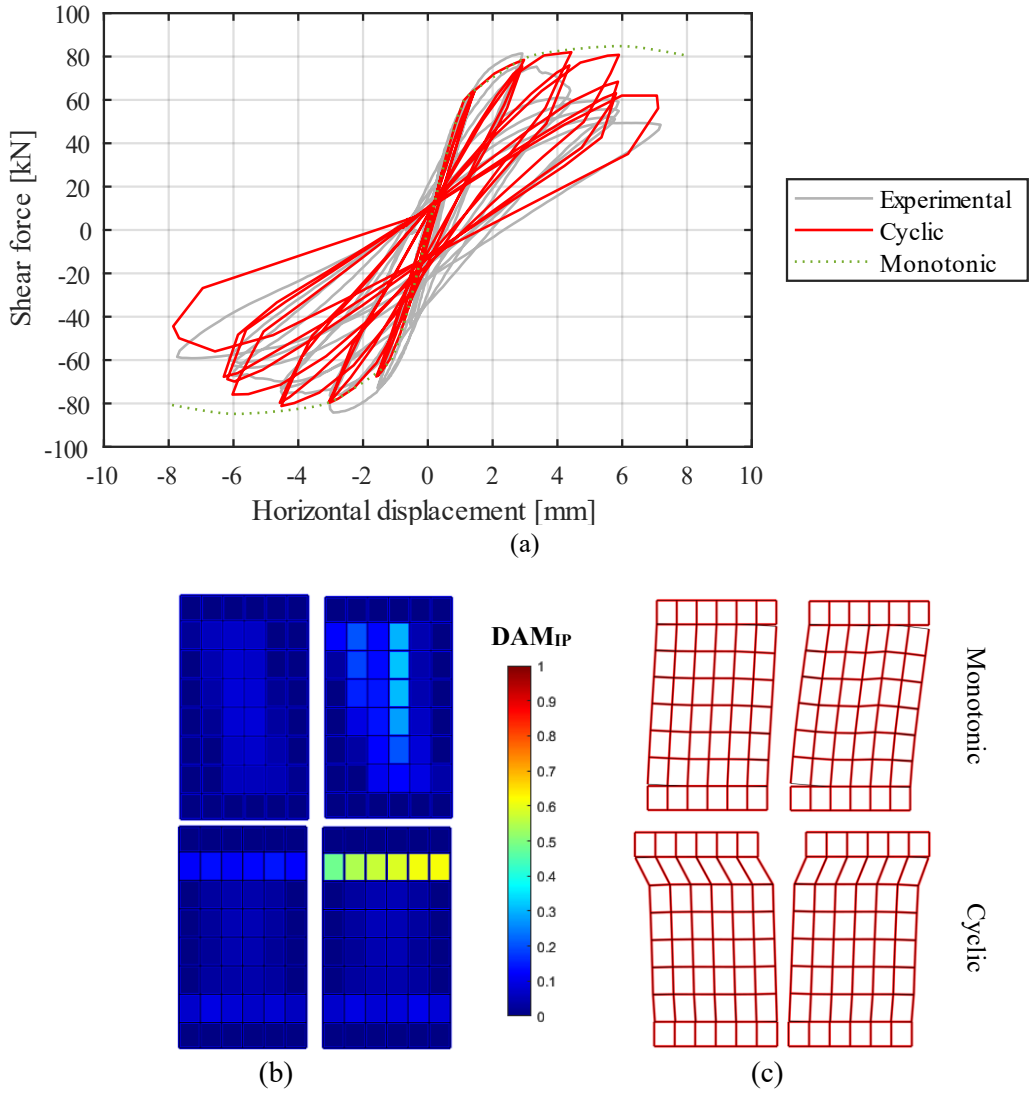

Figure 135 Short panel responses with 6x6 discretisation: a) experimental-numerical shear-displacement curves; b) in-plane diagonal spring damage for monotonic and cyclic analysis (at half and at the end of the analysis); c) deformed shape for monotonic(at half and at the end of the analysis) and cyclic analysis (at the maximum positive and minimum negative displacements; amplification factor 20)

Due to the similarities of the numerical and experimental cyclic load-displacement curves, the numerically predicted amount of total energy closely matches the experimental result. This is illustrated in Figure 136a, where the energy progression of the 3x3 model is shown alongside the experimental response. The numerical final amount of energy is observed to be slightly lower than the experimental result.

Further numerical simulations have been conducted using the model with 3x3 macroelements allowing for a certain stiffness recovery. Specifically, the model is tested with stiffness recovery parameters (k_{rec})

set to 0.1 and 0.2, resulting in broader shear-displacement cycles (Figure 136b) and consequently higher energy dissipated. In particular, when considering a 10% recovery of unloading stiffness, the final amount of energy closely aligns with the experimental value (Figure 136a). The stiffness recovery can also have a slight impact on the damage response. In Figure 136c, it can be observed that, in the last step, the damage pattern is characterised by the collapse of different elements among the three analysed variants, occurring even at different row levels. Meanwhile, the first loading phase retains the typical X-shaped damage pattern.

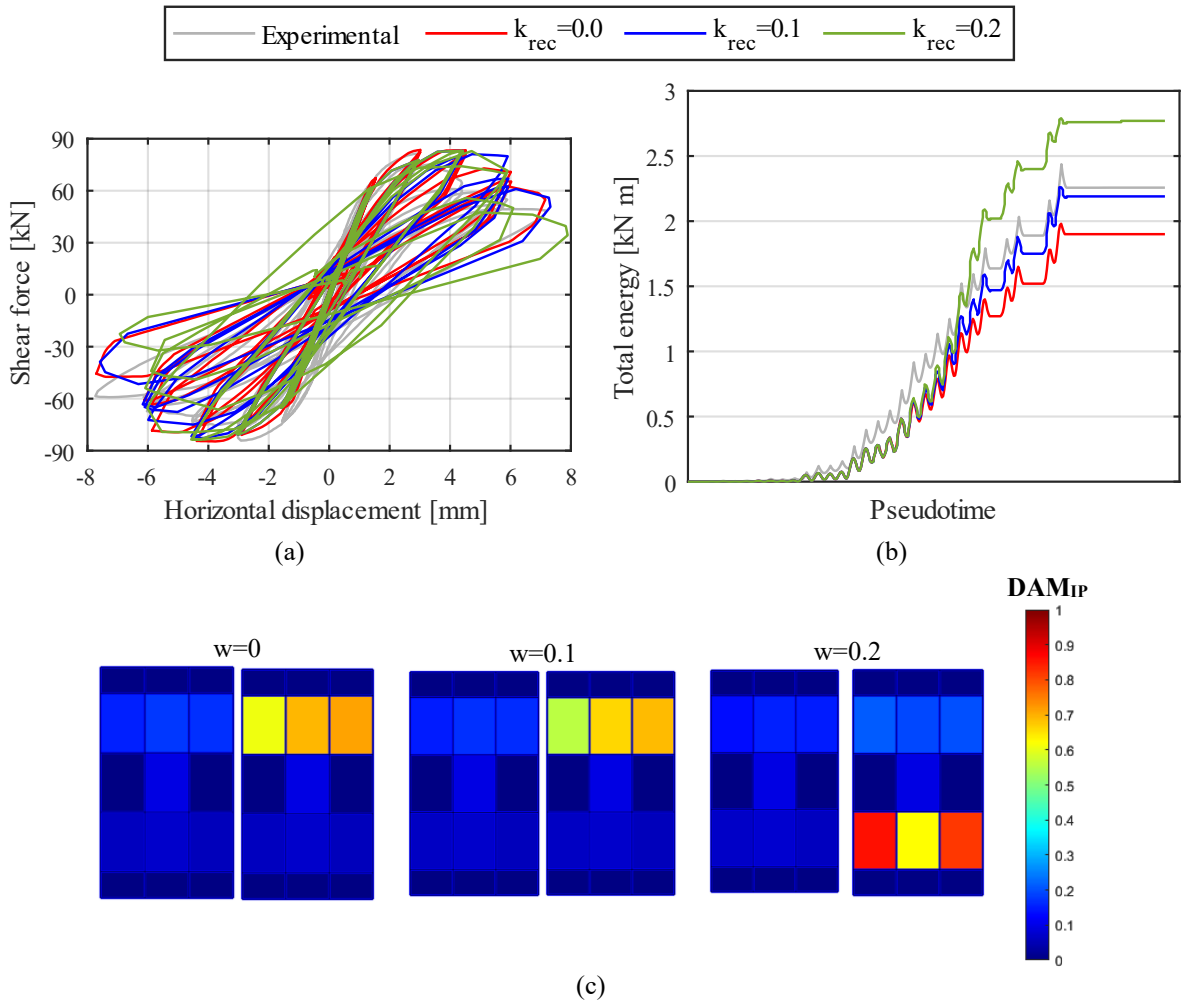

Figure 136 Comparison among 3x3 discretised short panel model with different stiffness recoveries: a) shear-displacement diagrams, b) energy dissipation comparison and c) in-plane diagonal spring damage for monotonic and cyclic analysis (at half and at the end of the analysis)

Finally, the slender panel with a higher height-to-width ratio is investigated using a 3x3 model. The material characteristics are the same as the short panel, reported in Table 32 and Table 33. The responses of the model are depicted in Figure 137. The shear-displacement curves show an accurate prediction of

the initial stuffiness, yielding strength and hardening branch. Indeed, the typical flexural S-shaped cycles are satisfactorily reproduced. However, the experimentally observed stiffness degradation is not captured. The same outcome was observed for the mesoscale model in Figure 47. This could be attributed to the assumption of simplified elastic unloading–reloading in the constitutive model of Minga et al. (2018), which, in reality, involves a certain level of hysteresis. The deformed shape is characterised, in both monotonic and cyclic response, by cracks opening in the bed joints at the two extremities of the wall specimen, along with partial damage in the shear springs of the macroelements at the corners.

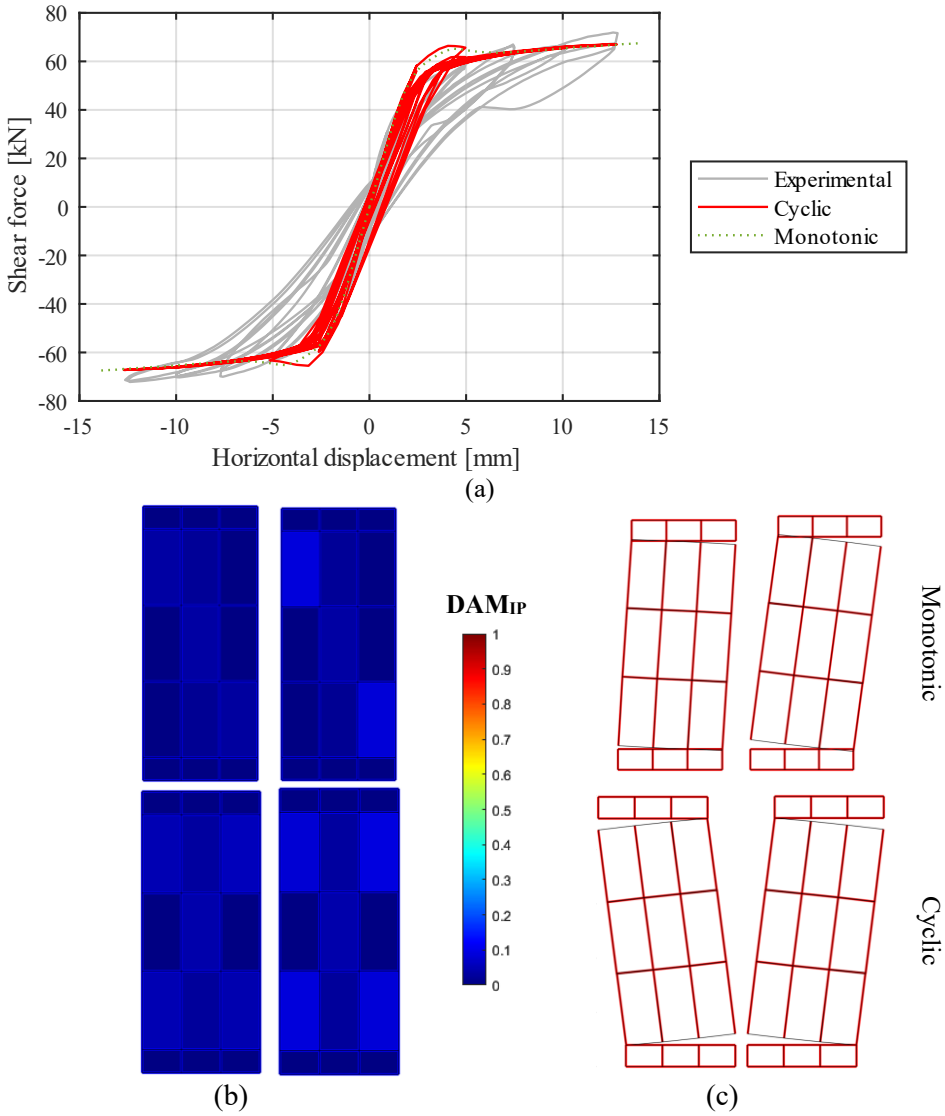

Figure 137 Tall panel responses with 3x3 model: a) experimental-numerical shear-displacement diagrams comparison; b) in-plane diagonal spring damage for monotonic and cyclic analysis (at half and at the end of the analysis); c) deformed shape for monotonic(at half and at the end of the analysis) and cyclic analysis (at the maximum positive and minimum negative displacements with amplification factor of 20)

6.2.2 Two-storey façade

The ability of the enhanced macroelement to accurately simulate the in-plane response of masonry wall elements has been further examined considering a larger façade with openings. The cyclic behaviour of the Wall-D, previously examined in Chapter 3 through mesoscale and continuum macroscale approaches, is here simulated considering various macroelement models, each featuring different mechanical characterisation variants.

As done for the mesoscale and continuum macroscale approaches in Chapter 3, the macroelement model is implemented by applying the external action through a spreader system (Figure 49).

The material characteristics for the single panels analysed before, as provided in Table 32 and Table 33, serve as initial reference. From this first "solution 1", two additional characterisations are then evaluated, with the aim of progressively improving the prediction of the cyclic response and better fitting the experimental curve through reasonable and plausible variations. The three material characterisations are outlined in Table 34: "solution 2" involves higher ultimate displacement (δ_u^*) and unloading factor (C_F) for the diagonal springs, while "solution 3" additionally considers increased tensile bond strength and cohesion for the horizontal interfaces, which are assumed as two times the reference values for "solution 1".

Table 34 Variant parameters for the material characterisations of Wall-D

	diagonal springs		horizontal interfaces	
	δ_u^* [mm]	C_F [-]	f_t [MPa]	c [MPa]
Solution 1	10.5	0.4	0.04	0.23
Solution 2	15	0.8	0.04	0.23
Solution 3	15	0.8	0.08	0.46

The capacity curve of "solution 1" (depicted in Figure 138) aligns well with the envelope of the experimental cycle response, accurately capturing initial stiffness, maximum strength and strength decay. Nevertheless, the cyclic response displays pronounced pinching and low dissipation capacity. This is mainly attributed to the low ductility of the diagonal springs, resulting in a rapid failure of the first-floor spandrels reaching the ultimate displacement. In addition to this, the behaviour of the facade is governed by the rocking of the three piers, from the bottom bed-joint openings (cracks also observed in the experimental response, see Figure 42) to the top of the windows at the first floor. Further interface openings are observed at the second-floor level, between the 7th and the 8th rows of macroelements (also counting the rigid elements at the base). This corresponds to the crack openings observed in the

experimental test between the second-floor windows and the second-floor level in the lateral piers. No damage at all is observed on the diagonal springs of the lateral piers, which were, however, experimentally observed. Furthermore, regarding the central pier at the bottom, the maximum capacity of the in-plane springs (specifically in the lower half elements of the pier) is reached, consistent with experimental observations (where the pier collapsed due to shear diagonal cracking), but still with residual post-peak capacity. The increase in ductility and hysteretic capacity of the diagonal spring, as provided by "solution 2", results in an improved response characterised by wider cycles (see Figure 42). Qualitatively, the response remains similar, with the same crack propagation.

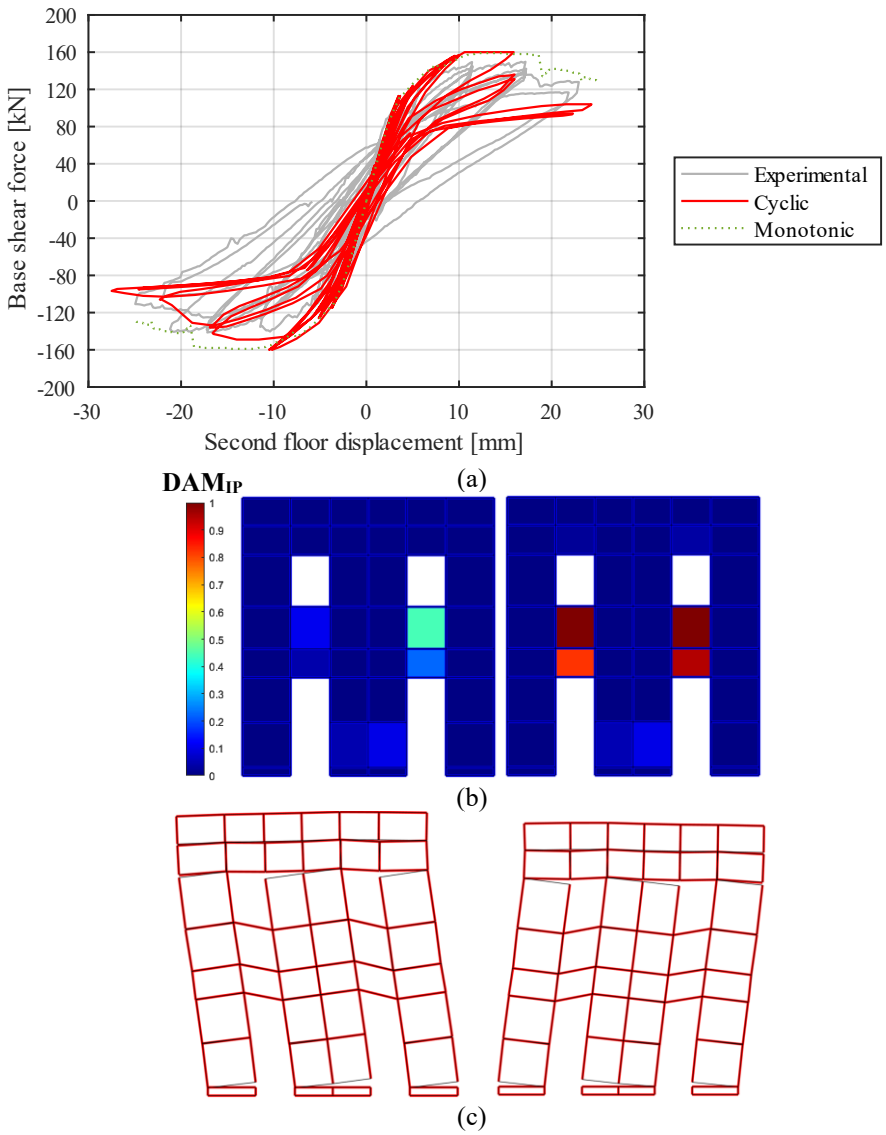

Figure 138 Wall D responses with solution 1: a) experimental-numerical shear-displacement diagrams comparison; b) in-plane diagonal spring damage under cyclic analysis (at half and at the end of the analysis); c) deformed shape under cyclic analysis (at the maximum positive and minimum negative displacements with amplification factor of 30)

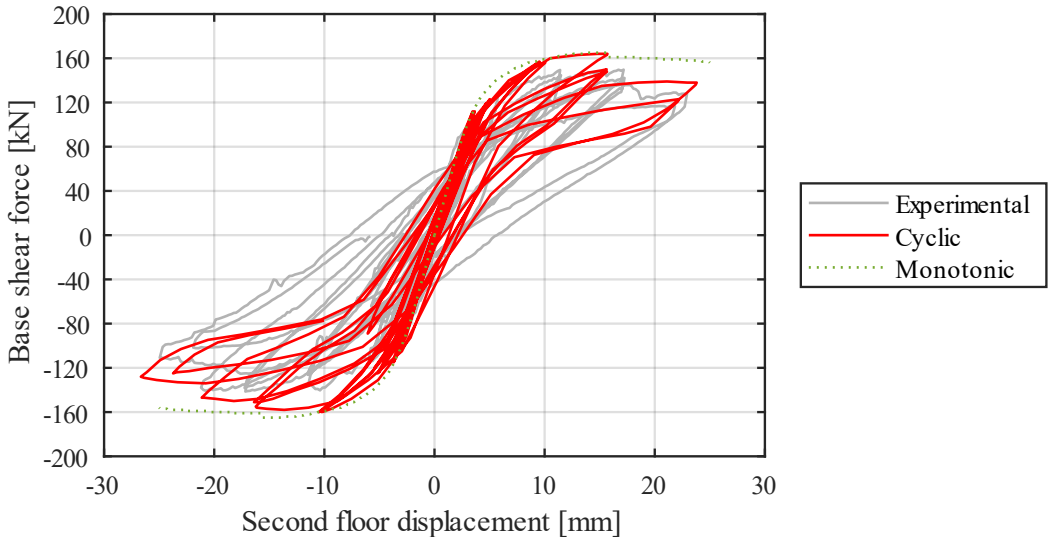

(a)

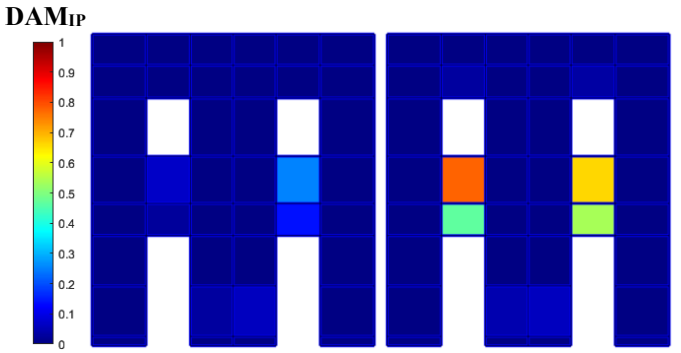

(b)

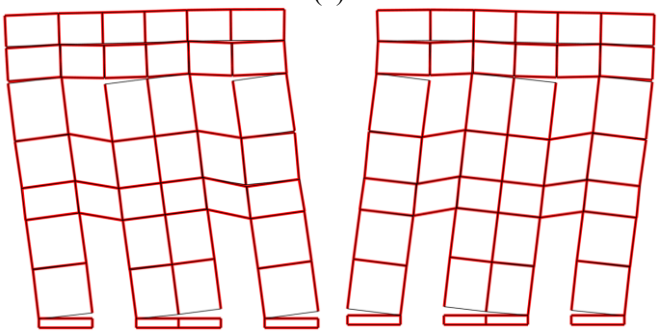

(c)

Figure 139 Wall D responses with solution 2: a) experimental-numerical shear-displacement diagrams comparison; b) in-plane diagonal spring damage under cyclic analysis (at half and at the end of the analysis); c) deformed shape under cyclic analysis (at the maximum positive and minimum negative displacements with amplification factor of 30)

It is important to note that, according to the proposed macroelement modelling approach, flexural damage is attributed to the opening of individual interfaces that may represent multiple mortar bed joints. Therefore, the assessment of strength parameters for frictional-cohesive interfaces should be

conducted by taking into account the mesh discretisation. In “solution 3”, characterised by horizontal interfaces with higher cohesion and bond strength, the resultant shear-displacement cyclic response, as depicted in Figure 140, aligns more closely to the experimental curve, even if pinching is still slightly overestimated. The crack openings at the top of the first-floor windows, which appeared in solutions 1 and 2, do not take place in this third solution. This may result in damage to the springs of the second-floor spandrels, leading to a wider overall shear-displacement cycle, and accompanied by the formation of a full span crack opening at the second-floor level. Furthermore, a similar damage pattern to the previous cases is observed for the diagonal springs of the central pier at the ground floor.

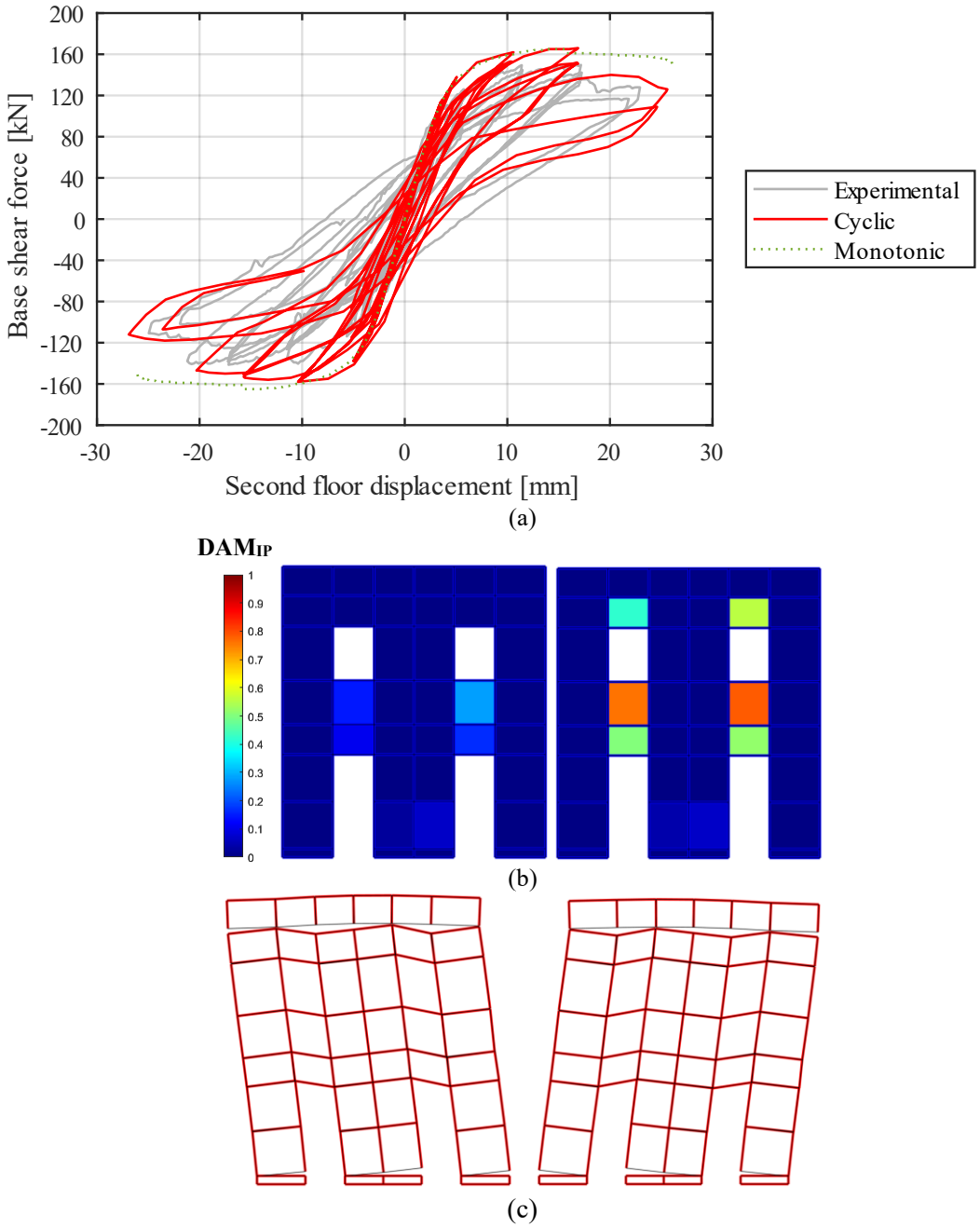

Figure 140 Wall D responses with solution 3: a) experimental-numerical shear-displacement diagrams comparison; b) in-plane diagonal spring damage under cyclic analysis (at half and at the end of the analysis); c) Deformed shape under cyclic analysis (at the maximum positive and minimum negative displacements with amplification factor of 30)

The evolution of the dissipation energy provided by the solution 3 model is closer to the experimental one, as shown in Figure 141 alongside the responses of the other solutions. Furthermore, an additional simulation with the solution 3 model allowing for a 20% stiffness recovery for the unloading branches

gives an improved approximation of the experimental data, despite the ultimate dissipation magnitude remains equivalent to that of the original solution 3 model without stiffness recovery.

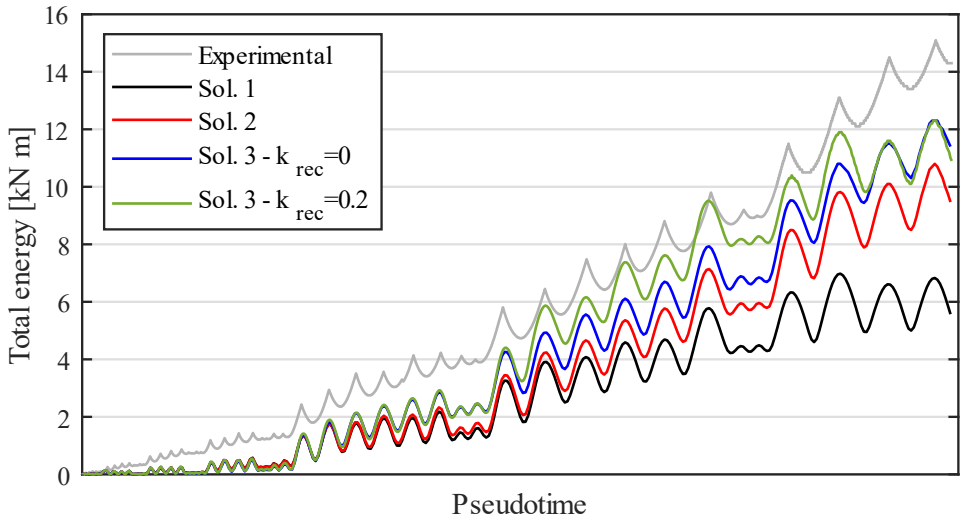

Figure 141 Wall D energy dissipation comparison among different material characterisations

In conclusion, considering the inherent simplifications associated with the macroelement modelling approach and the coarse mesh utilised, the outcomes derived from an objective material characterisation are satisfactory, closely simulating the experimental response in terms of monotonic and cyclic load-displacement response and failure mode. However, further studies should be conducted to improve the calibration for the ultimate displacement of the diagonal springs and the specification of the mechanical characteristics of the nonlinear interfaces in relation to the mesh discretisation.

6.3 Out-of-plane two-way bending

URM buildings subjected to earthquakes loading often experience damage associated with the out-of-plane response of URM walls. Thus, an accurate prediction of the seismic performance of URM building structures necessitates a rigorous consideration of the out-of-plane failure mechanism of the walls. The typical out-of-plane response involves the development of diagonal cracks eventually leading to the wall collapse. In this section, the response of URM walls subjected to out-of-plane loading is analysed, with a focus on wall components supported along both horizontal and vertical edges.

The macroelement formulation described in Chapter 5.2 includes the representation of the out-of-plane response, which is primarily governed by the out-of-plane spring but also influenced by the cohesive-

frictional interfaces, as the effects of tensile opening and sliding significantly impact the dissipation capacity of elements subjected to out-of-plane loadings, as shown later on.

To evaluate the model ability of predicting this failure mode, the experimental tests conducted by (Griffith et al., 2007) are simulated. The experiments considered URM walls laterally supported along all four edges, including various configurations obtained by varying vertical loads and the presence of openings.

These tests had already been examined in (Minga et al., 2020). However, the former out-of-plane spring showed limitations in accurately capturing the actual response of masonry walls subjected to out-of-plane loading (as reported in Figure 112). Indeed, as highlighted by the authors, the model did not adequately capture the strong pinching effects and the strength degradation following the loading reversal, as observed in the physical tests. Besides, the amount of dissipation energy appeared to be overestimated in comparison to the experimental one.

One of the reasons of this inadequate response prediction was the overly simplified law implemented for the out-of-plane spring, where strength degradation develops separately in the positive and negative quadrants. Consequently, the softening behaviour in one direction does not influence the response in the other direction. The novel constitutive law implemented for out-of-plane spring (described in Chapter 5.4) has been developed to address these issues.

6.3.1 The experimental tests

The experimental tests conducted by Griffith et al. (2007) focused on evaluating several single-wythe running bond URM walls under out-of-plane two-way bending conditions, made with cored clay masonry units measuring 230 x 110 x 76 mm and mortar joints of 10 mm thickness. The specimens considered in the present study consisted of a main wall 4000 × 2500 mm, flanked by return walls on both sides, each extending 480 mm. The thickness of the walls is 110 mm. The top and the bottom edge of the main wall were simply supported in the direction of the loading, while the vertical edges of the return walls were restrained to obtain a full-moment connection. Four different test configurations are examined in a numerical study, taking into account the presence or absence of an eccentric opening, as well as the inclusion or exclusion of a uniform vertical loading. Details of these configurations are provided in Table 35, where specifications for vertical stress, loading history and geometry are given. Figure 142 presents a 3D view of a generic specimen.

The out-of-plane load was applied through an airbags system. The airbags were gradually inflated on alternate sides to provide a uniform pressure on the face of the wall. The specimens were first subjected to a static monotonic action, until a certain damage level was reached. Subsequently, from the residual displacements, they were subjected to a cyclic history of imposed displacement (Figure 143a). Two type of displacement history were considered: the type A was applied to the solid specimens and the loaded-windowed one, while the window specimen with no initial vertical loading was subjected to type B displacement history (Figure 143b).

Table 35 Wall geometry and loading conditions

Specimen	Vertical stress	Loading history	Geometry (dimensions in mm)
Solid loaded	0.10 MPa	Type A	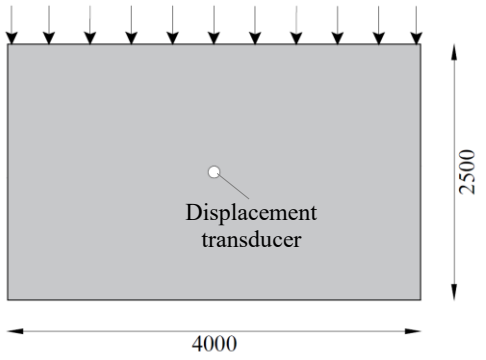
Solid not-loaded	0 MPa	Type A	
Windowed loaded	0.10 MPa	Type A	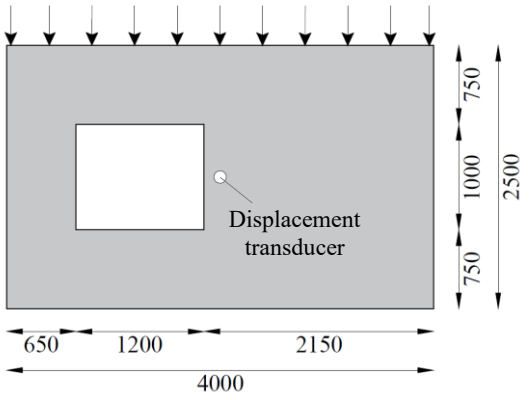
Windowed not-loaded	0 MPa	Type B	

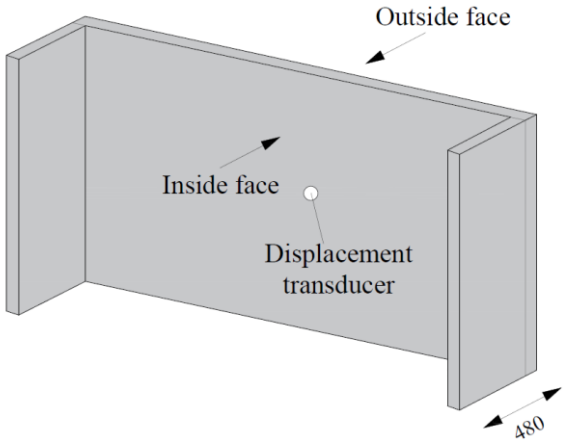

Figure 142 3D view of the specimen

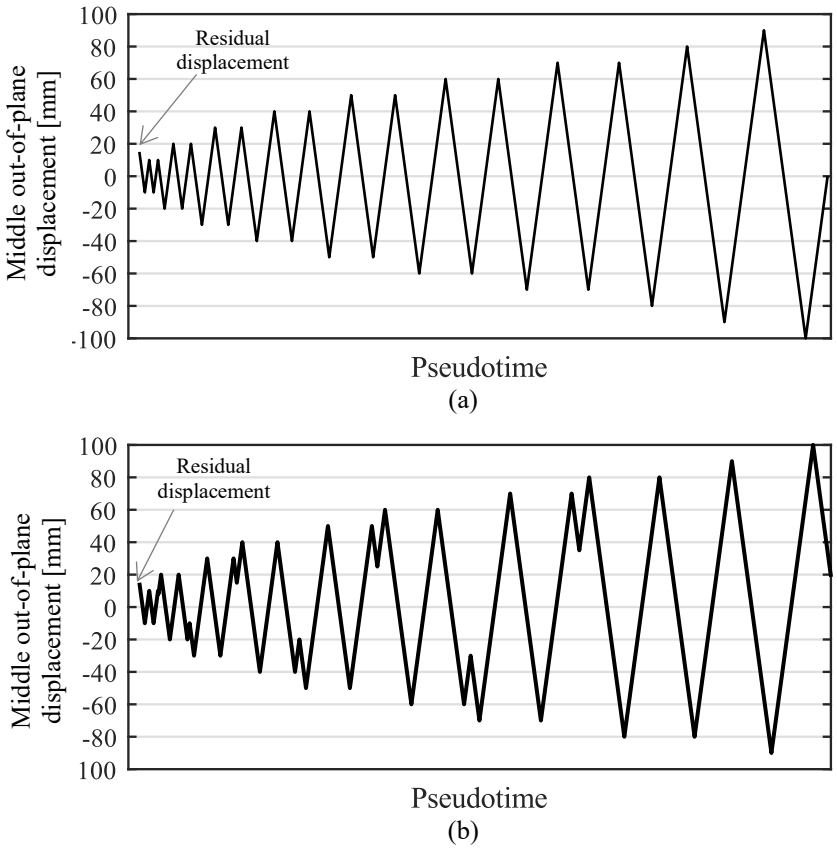

Figure 143 Cycling loading histories: (a) type A and (b) type B

6.3.2 Numerical modelling

In the solid specimens, the main wall is represented by 6x4 macroelements of equal size, and each lateral wall is modelled by 1x4 elements (see Figure 144a). To account for the presence of the openings,

a more refined mesh is adopted for the window wall specimens, featuring 7 columns and six rows for the main walls, while each lateral wall is modelled considering a mesh of 1x6 elements (Figure 144b).

The bottom edges of the walls are fully restrained, while the top edges are restrained only in the out-of-plane direction, providing a pinned support. The external edges of the return walls are restrained through a moment restraint and also preventing the horizontal translations. Vertical loads are applied at the top nodes of both the main and return walls. The out-of-plane action is imposed to the main wall face using nodal forces corresponding to the area of influence of each node. This is achieved through a spreader system controlled by an external master non-structural node. Cyclic displacement histories are applied at this node.

The material properties reported in Table 36 and in Table 37 have been derived from (Minga, 2017). In particular, the interface properties were obtained from a mesoscale modelling of the experimental test. Besides, the out-of-plane spring characteristics (described in Chapter 5.2 and 5.4) were assessed through the calibration procedure presented in Chapter 5.2. This involved the testing of an equivalent detailed mesoscale model, with dimensions comparable to those of a single element within a macroelement model. Table 38 contains the material parameters for the in-plane springs. The shear modulus (G_e) is derived from interpolation within the range of values suggested in the Italian code (MIT, 2019), considering the experimental elastic modulus and a masonry class of masonry in semi-solid bricks with cement mortar. The global cohesion ($\tilde{c}$) and global coefficient of friction ($\tilde{\mu}$) are determined by considering the characteristics of the horizontal interfaces and the dimensions of the units, and are derived from equations (36) and (37). The other parameters are taken from Table 33.

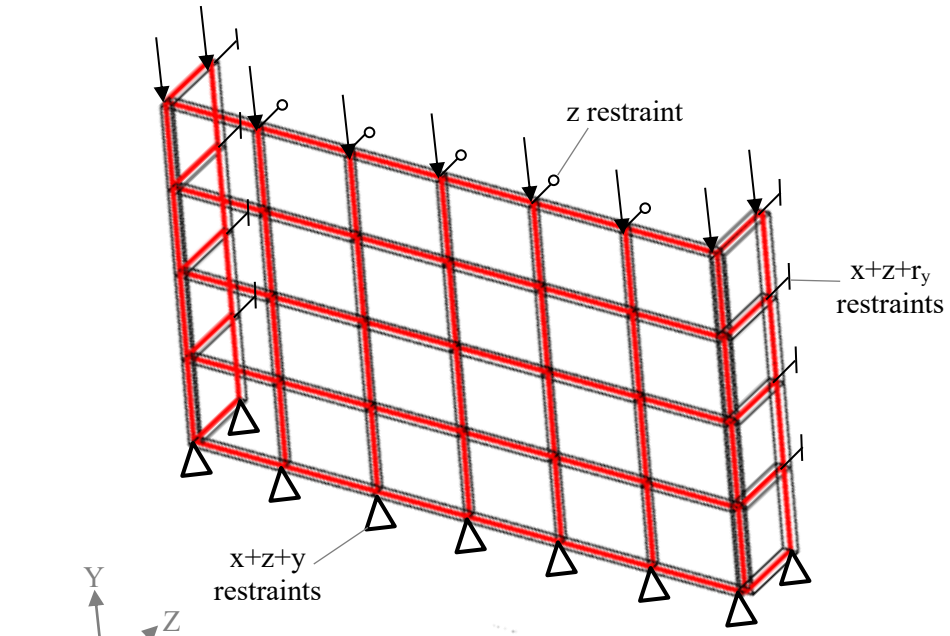

(a)

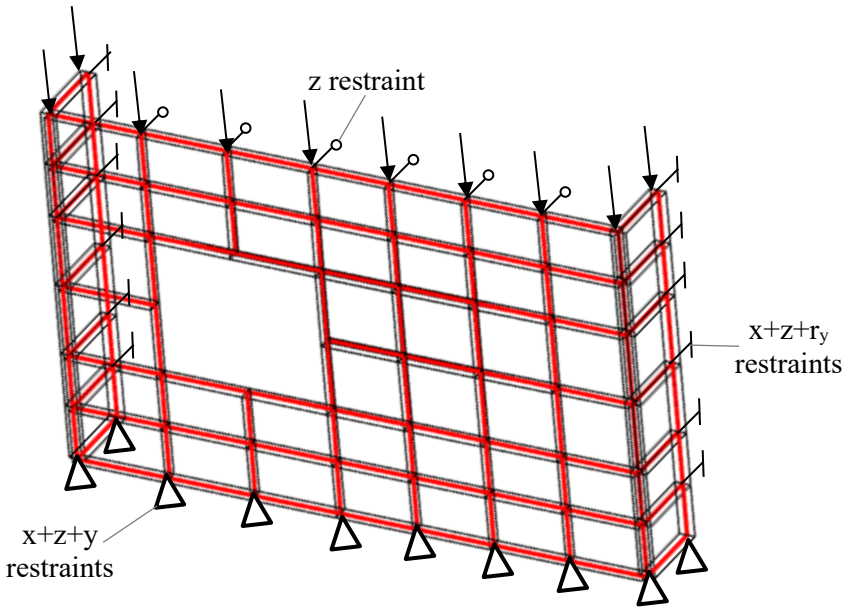

(b)

Figure 144 Macroelement models for the out-of-plane loaded specimens: (a) solid walls, (b) window walls

Table 36 Material parameters for interfaces of specimens subjected to out-of-plane loading

Interface	E_n [MPa]	f_t [MPa]	c [MPa]	tanϕ [-]	f_c [MPa]	$G_{f,I}$ [N/mm]	$G_{f,II}$ [N/mm]	$G_{f,c}$ [N/mm]
Horizontal	3540	0.16	0.75	0.24	17.6	0.05	0.1	17.5
Vertical	2124	1.08	2.43	0.56	8.80	0.05	0.1	10

Table 37. Material parameters for out-of-plane springs of specimens subjected to out-of-plane loading

Specimens	E_e [MPa]	E_p [MPa]	$p_{y,0}$ [kPa]	$p_{r,0}$ [kPa]	$\mu_{o,y}$ [-]	$\mu_{o,r}$ [-]	C_F	α	β
Solid walls	1815	-74	2.4	0.22	0.0143	0.0148	0.8	0.8	0.06
Window walls	1593	-90	4.9	0.23	0.0279	0.0279			

Table 38. Material parameters for in-plane diagonal springs of specimens subjected to out-of-plane loading

G_e [MPa]	$\tilde{c}$ [MPa]	$\tilde{\mu}$ [-]	δ_u^* [mm]	K_{pl}/K_{el}	F_y/F_{max}	C_F	α	β
885	0.64	0.20	10.5	0.1	0.8	0.4	0.8	0.06

The numerical results are presented in the following paragraphs, focusing on numerical-experimental comparisons of the load-displacement response, damage pattern in the out-of-plane springs (only the out-of-plane damage is depicted, as DAM_{OOP}, defined in (52); no damage is observed for the in-plane springs).

6.3.3 Solid wall specimen

Figure 145 illustrates the out-of-plane response for the solid loaded specimen, presenting the displacements at the monitoring point against the applied pressure. The latter is determined by the ratio between the total force applied at the monitoring point and the area of the main wall. The numerical curve is shown together with the experimental results. The first monotonic loading phase is accurately predicted since initial stiffness and maximum strength are well captured. Moreover, the cyclic response is well-replicated, exhibiting strength decay and an overall dissipation capacity that closely align with the experimental response. Therefore, the improved spring formulation, which considers damage accumulation during the reversal of action direction, enables an accurate prediction of strength degradation and pinching effect. This represents a significant improvement compared to the former formulation.

The overall numerical response is governed by both the out-of-plane spring and the nonlinear interfaces. In Figure 146a, the damage of the out-of-plane springs is displayed, showing that the elements at the corners are fully damaged, having reached the residual branch of the capacity curve (indicated by brown colour in Figure 146a). This damage pattern is consistent with the experimental observations presented in Figure 146e and Figure 146f for the inside and outside faces, respectively. The localisation of damage coincides with the areas where the diagonal cracks appeared during the experimental test.

The evident pinching effect of the cyclic curve is significantly influenced by the contribution of the nonlinear interfaces. As evident in the deformed shapes presented in Figure 146b, Figure 146c and

Figure 146d (depicting 3D and plan-view deformed shapes), marked areas indicate interfaces that experience significant damage. The flexural damage along the two damaged vertical interfaces can be associated with the experimental cracking pattern, although located more externally. Similarly, the cracked horizontal interfaces can be correlated with the single horizontal crack along bed joints observed at the centre of the experimental specimen, characterised by different lengths from the inside to the outside face.

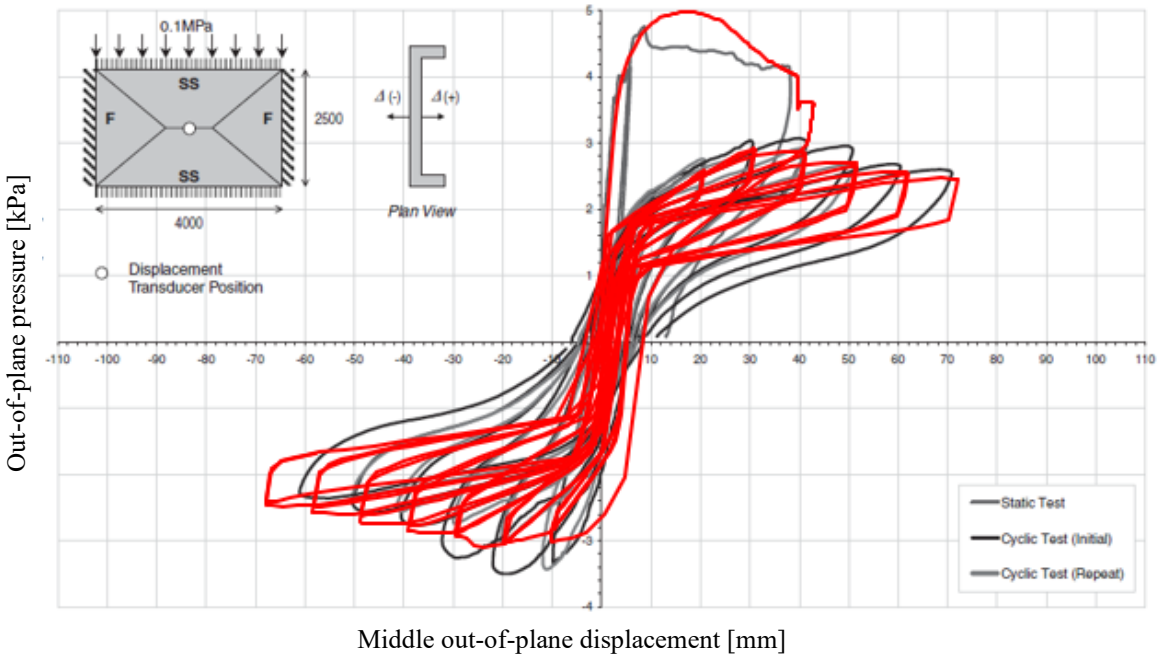

Figure 145 Solid wall specimen with vertical load: experimental-numerical shear-displacement diagrams (numerical response in red; the background is taken from Griffith et al., 2007)

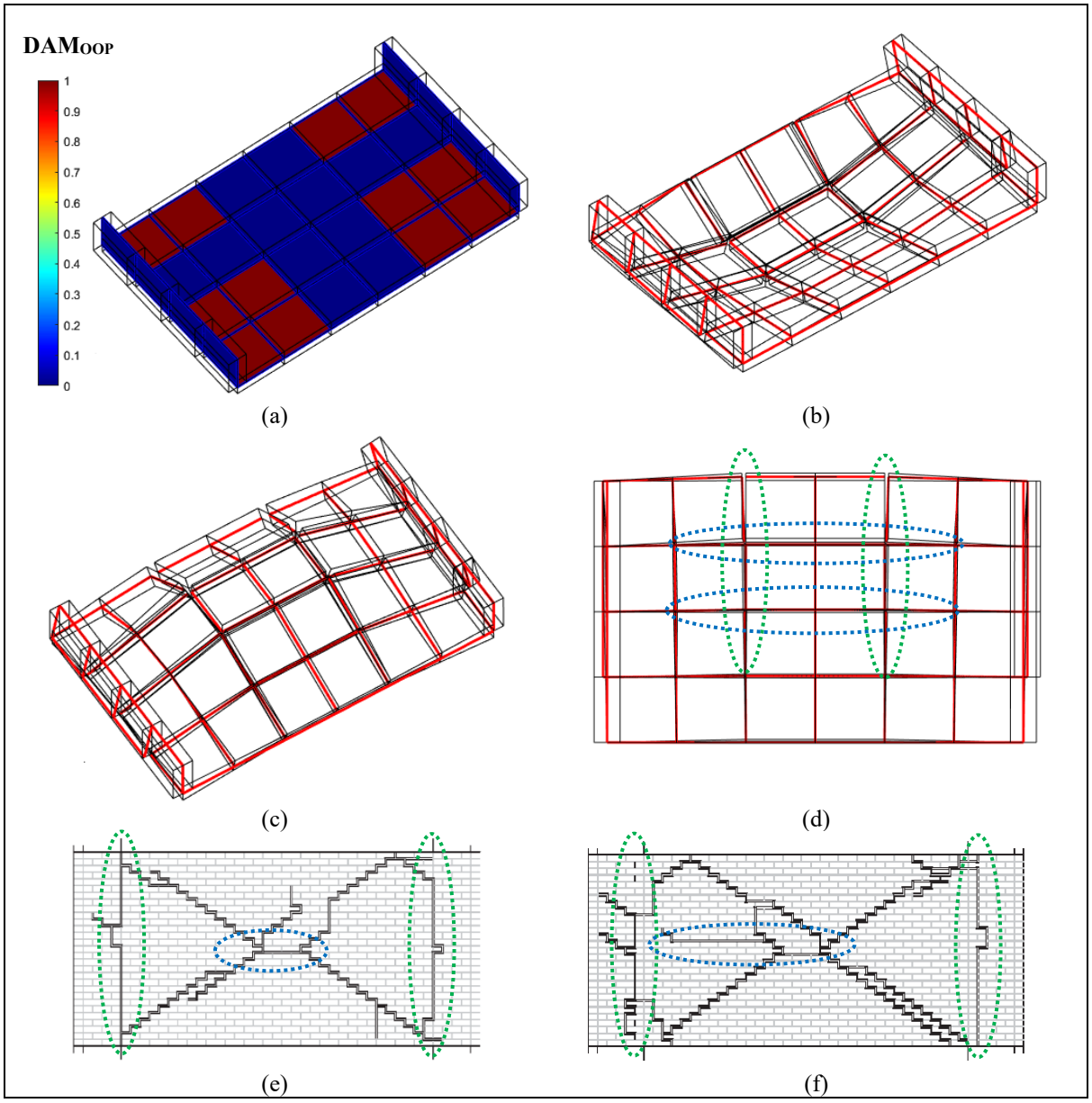

Figure 146 Solid wall specimen with vertical load: (a) out-of-plane spring damage at the last step of analysis; (b) 3-D view of deformed shape at minimum displacement and (c) maximum displacement (amplification factor of 5); (d) plan-view of maximum displacement (amplification factor of 2); experimental cracking pattern in the (e) inside face and (f) outside face

The cyclic pressure-displacement response for the case with zero compressive stress is illustrated in Figure 147. The numerical model accurately reproduces the experimental response, for both the monotonic and cyclic phases. Notably, it correctly captures the decrease in the maximum strength and the increase in the rate of strength degradation due to the reduction of the confinement offered by the vertical loading.

The damage in the diagonal springs is depicted in (Figure 148a). The absence of vertical load results in a symmetric damage pattern, where two columns of elements on each side are fully damaged. This pattern aligns with the actual wall areas where cracking occurs, as represented in the experimental pattern given in Figure 148e and Figure 148f.

The broadness of cycles becomes progressively narrower as the displacements increase, which is due to the increasing flexural damage of the interfaces (Figure 148b, c and d). The more pronounced damage of the interfaces, in comparison to the model with vertical load, results in a lower dissipation capacity. The localisation of the damaged interfaces is consistent with the experimental observations, allowing for the same considerations made for the loaded model.

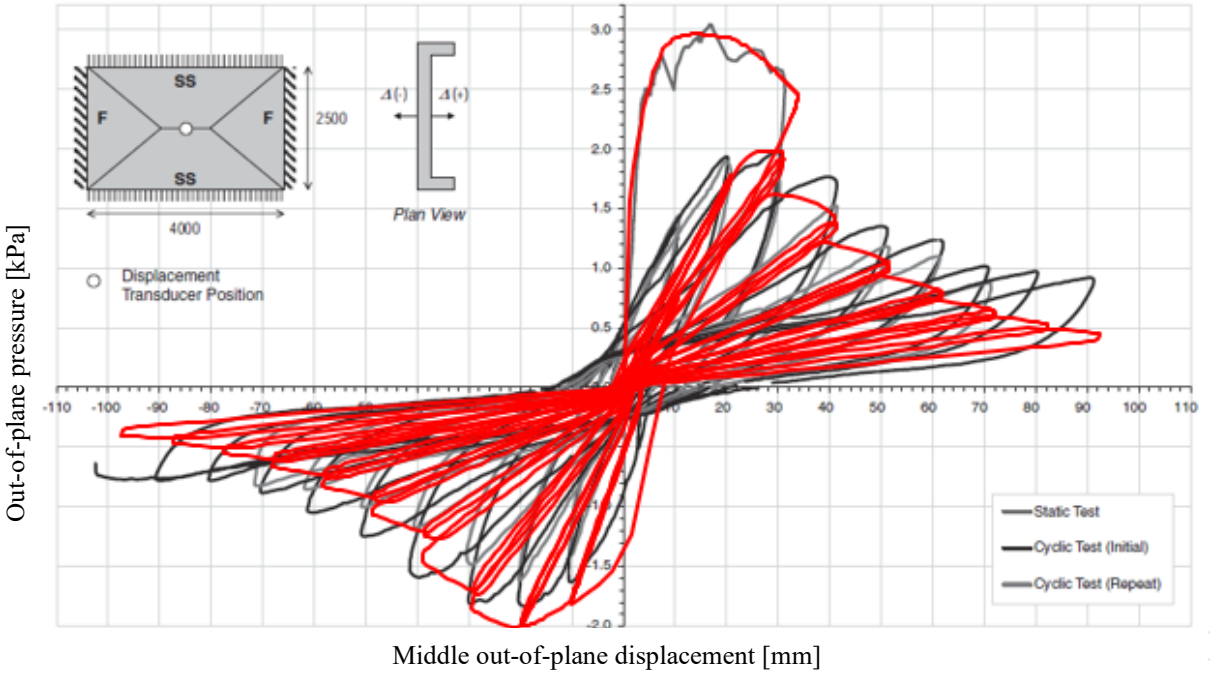

Figure 147 Solid wall specimen without vertical load: experimental-numerical load-displacement curves (numerical response in red; the background is taken from Griffith et al., 2007)

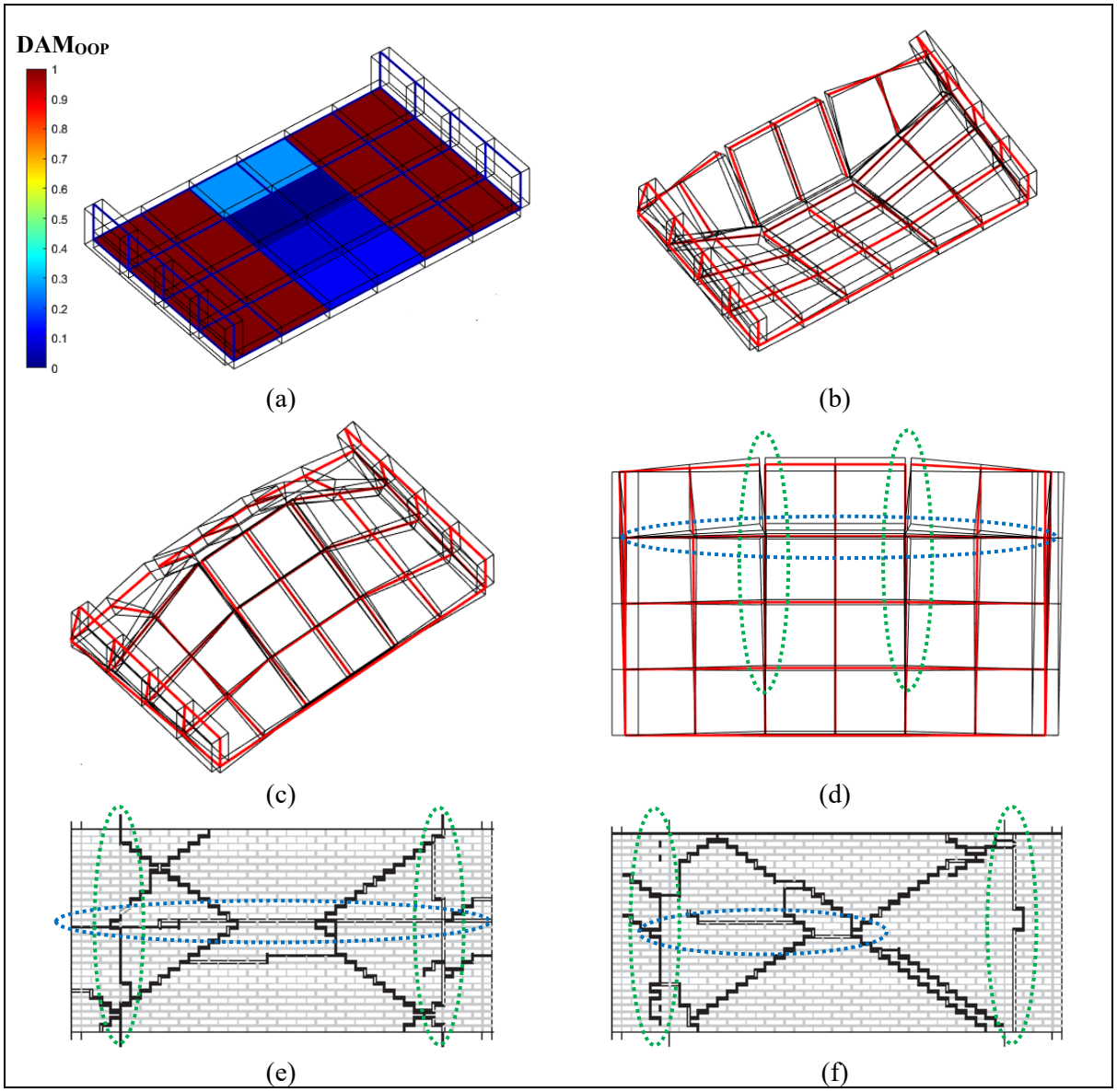

Figure 148 Solid wall specimen without vertical load: (a) out-of-plane spring damage at the last step of analysis; (b) 3D view of deformed shape at minimum displacement and (c) maximum displacement (amplification factor of 5); (d) plan-view of maximum displacement (amplification factor of 2); experimental cracking pattern in the (e) inside face and (f) outside face

6.3.4 Window wall specimen

The cyclic out-of-plane response for the window walls specimens, both with and without vertical pressure, is also examined. Numerical-experimental comparisons are presented in Figure 149 and Figure 151. In both the models, the monotonic phase closely matches the experimental results, with initial stiffnesses and maximum strengths aligning closely with the experimental values. For the not-loaded specimen, the influence of the vertical loads is accurately considered, observing a lower

maximum pressure compared to the loaded specimen, although slightly higher than the experimental one. Moreover, also the cyclic responses are in good agreement with the experimental curves, accurately predicting strength degradation, although with slightly higher strengths at the first load reversal.

The experimental cracking patterns, given in Figure 150e, Figure 150f and Figure 152e, are similar to the ones of the solid wall specimen. However, there is a more extensive cracking pattern both below and above the eccentric opening. The damage in the out-of-plane springs, as illustrated in Figure 150a and Figure 152a, reflects this extensive damage, with nearly all macroelements exhibiting full damage.

Furthermore, the observed damage in the nonlinear interfaces is consistent with the experimental patterns. Horizontal bed-joint cracks can be related to the large horizontal interfaces openings (Figure 150c and Figure 152c). Vertical cracks are also well predicted, even if, in the loaded model, the crack starts from the opposite corner of the opening (Figure 150c). In the experimental pattern, flexural damage appears quite widespread, while in the model, it is concentrated along some main cracks.

Nevertheless, the amount of dissipated energy is generally underestimated compared to the experimental amount. Besides, the numerical cycles are generally narrower than those of the solid specimen. This difference can be attributed to a higher damage of the interfaces with respect to the solid specimen, resulting in a predominantly flexural response characterised by low dissipation of energy. Nonetheless, the response is overall consistent with the experimental evidence, considering the still coarse mesh adopted and the simplified nature of the modelling strategy.

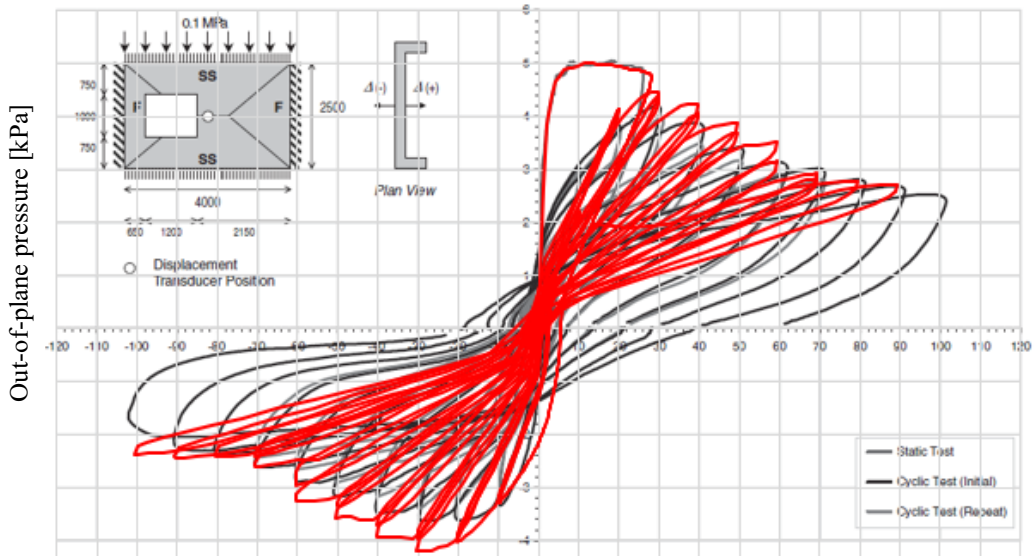

Figure 149 Window wall specimen with vertical load: experimental-numerical shear-displacement diagrams (numerical response in red; the background is taken from Griffith et al., 2007).

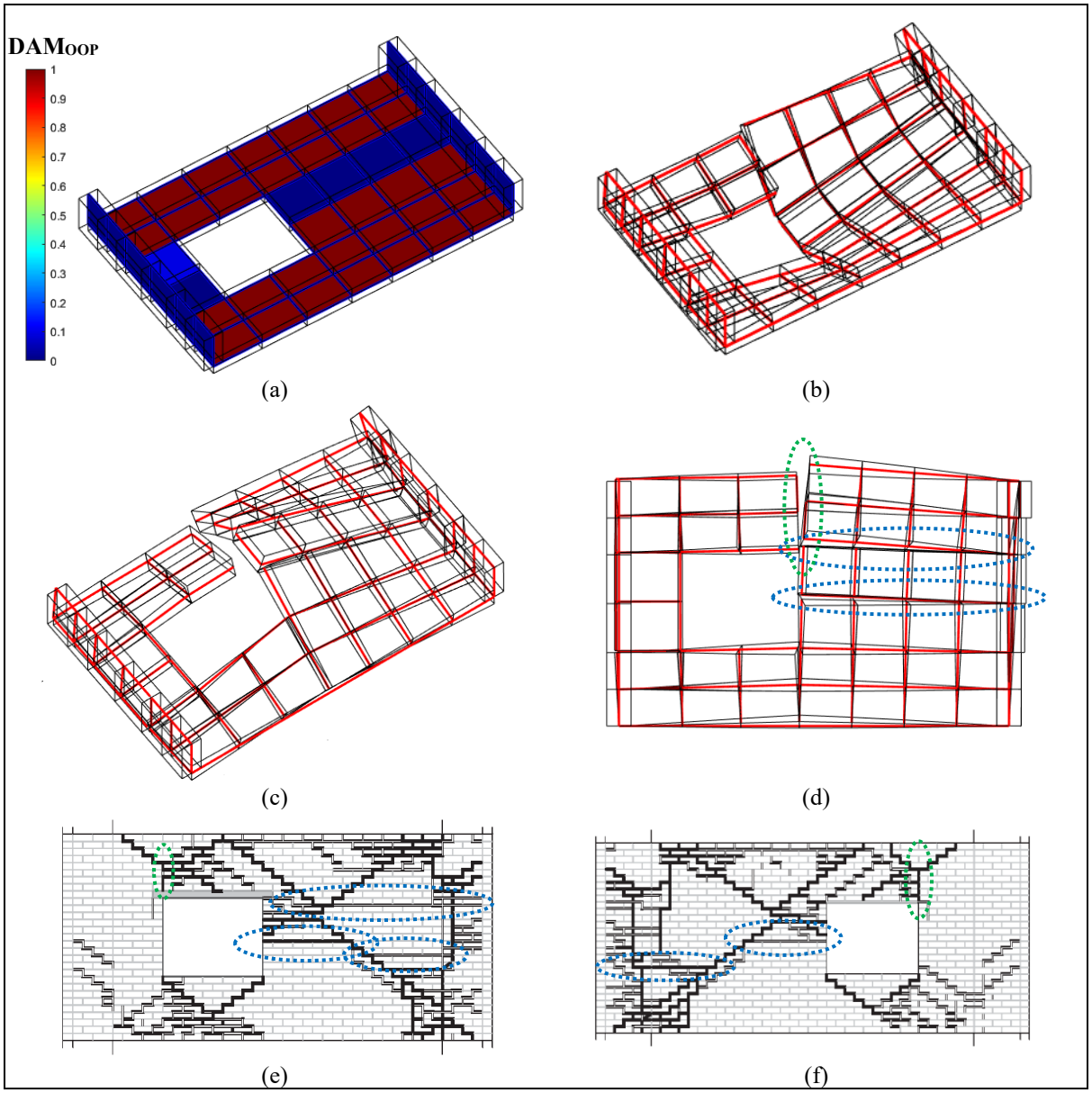

Figure 150 Window wall specimen with vertical load: (a) out-of-plane spring damage at the last step of analysis; (b) 3D view of deformed shape at minimum displacement and (c) maximum displacement; (d) plan-view of maximum displacement (amplification factor of 2) ; experimental cracking pattern in the (e) inside face and (f) outside face

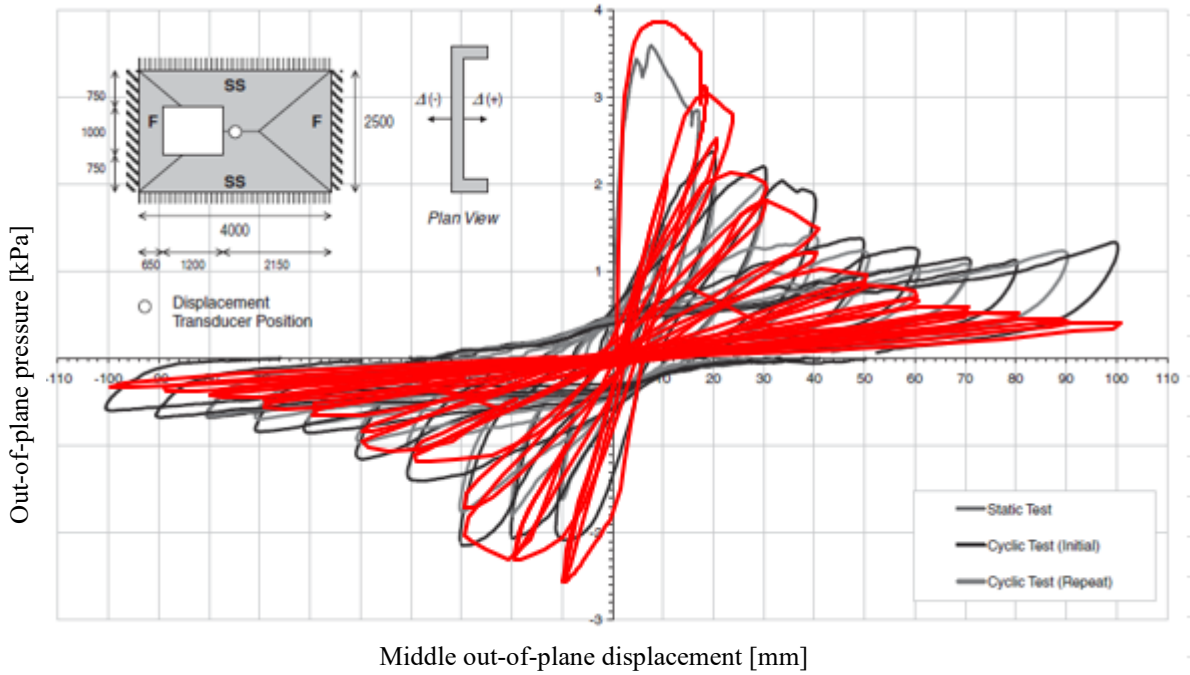

Figure 151 Window wall specimen without vertical load: experimental-numerical shear-displacement diagrams (numerical response in red; the background is taken from Griffith et al., 2007).

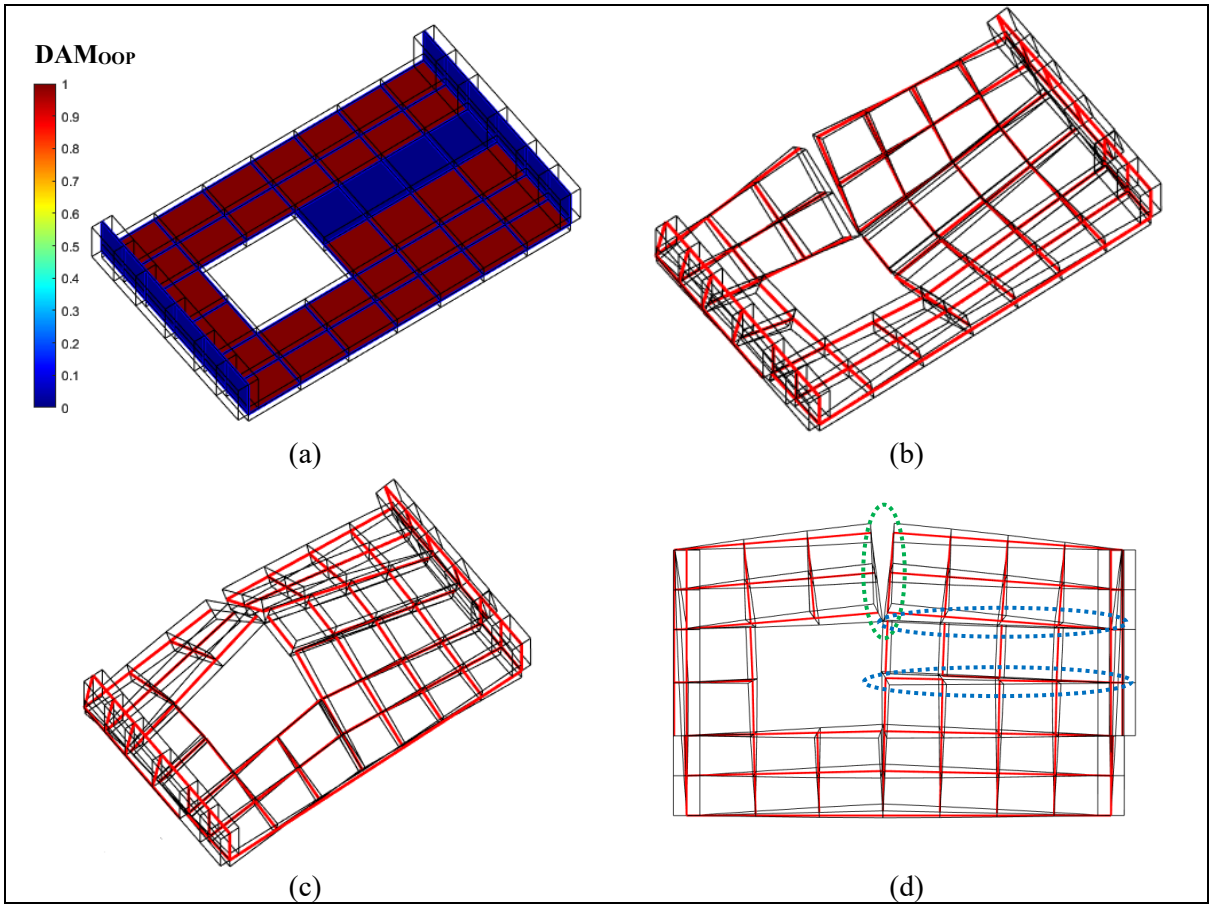

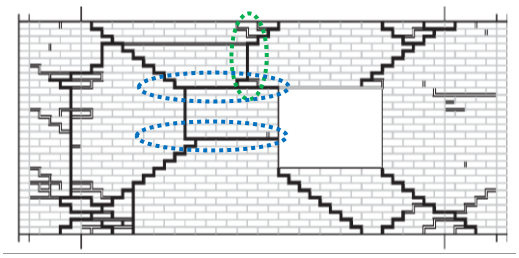

(e)

Figure 152 Window wall specimen without vertical load: (a) out-of-plane spring damage at the last step of analysis; (b) 3D view of deformed shape at minimum displacement and (c) maximum displacement; (d) plan-view of maximum displacement (amplification factor of 2); (e) experimental cracking pattern in the outside face

6.4 3D URM structure subjected to earthquake loading

6.4.1 Experimental test

In a final simulation focusing on the analysis of URM structures, an experimental test was simulated verifying the earthquake performance of a 2-story terraced house with a rigid base and two RC floor slabs. The seismic testing of the full-scale prototype was conducted at the European Laboratory for Structural Assessment (ELSA) Reaction-wall Laboratory of the Joint Research Centre (JRC), utilising pseudodynamic testing techniques (Anthoine and Capéran, 2008). The specimen, representing one symmetric half of a house, had overall dimensions of 5.30 × 4.75 m and a height of 5.40 m (see Figure 153). Each shear wall was connected to the perpendicular long walls through a continuous vertical mortar joint with masonry connectors (e.g., metal strips) inserted in the mortar bed joints. The concrete slabs were directly poured onto the units at the levels of the two floors without any mortar joint.

The walls consisted of calcium silicate units measuring 250 × 175 × 250 mm, arranged though thin mortar bed-joints and unfilled head-joints. The out-of-plane connection was established by matching vertical grooves. Compression and tensile tests were conducted on individual units and small assemblages, providing the mechanical properties listed in Table 39.

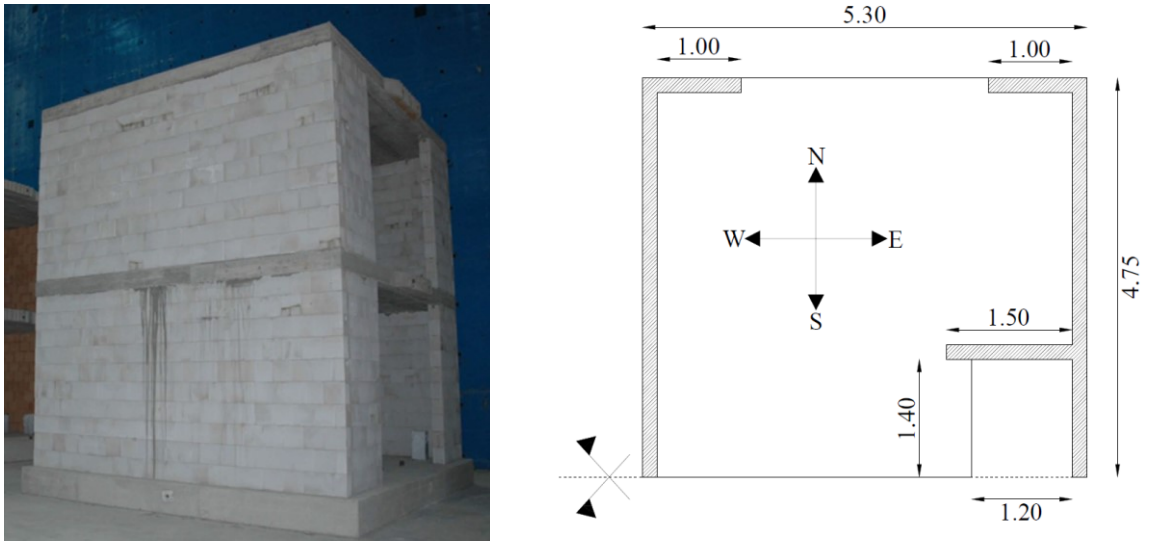

(a) (b)

Figure 153 Pseudodynamic test: (a) view of the structure (adapted from Michel et al., 2011); and (b) plan view

Table 39 Mechanical properties of units and joints

Material	Property	Value
Unit	Young's modulus	13620 MPa
	Poisson's ratio	0.253
	Compressive strength	23.6 MPa
	Tensile strength	1.49 MPa
Mortar joint	Young's modulus	2849 MPa
	Poisson's ratio	0.028
	Tangent of friction angle	0.55
	Cohesion	0.28 MPa

The pseudodynamic tests were conducted under the vertical loading conditions prescribed by the seismic design standards, as outlined in Eurocode 8, which include the application of dead loads and 30% of the live loads. To achieve the necessary loads, a distribution of water tanks was arranged on each floor, also taking into account the testing setup. The placement of the tanks was designed to exert gravity loads on the masonry walls consistent with the expected values in the original terraced house, while also minimising the eccentricity between the centre of mass and the centre of stiffness. The total added mass on the first floor amounted to 4.52 t, while on the second floor, it was 7.39 t.

The pseudodynamic tests were unidirectional, conducted in the east-west direction (as indicated in Figure 153b). Consequently, in the pseudodynamic algorithm, the tested structure had only 2 degrees of freedom, with one translation at each floor level. The equations of motion were iteratively solved online using experimentally observed stiffness to determine the corresponding relative displacements. These displacements were then applied to the structure using hydraulic actuators fixed on both sides at

the two floor levels (Figure 154). Each floor slab movement was controlled by these actuators, imposing identical horizontal displacements to prevent any rotation around the vertical axis.

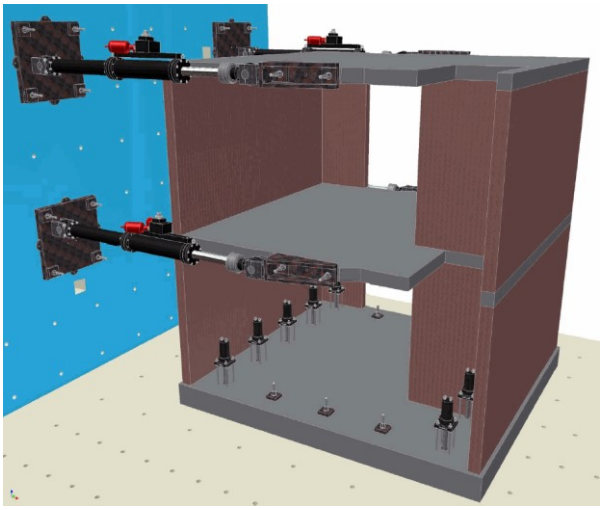

Figure 154 Experimental testing setup

An artificial accelerogram was utilized as reference ground motion. It was generated to align with the Eurocode 8 (EN 1998-1-1, 2005) design spectrum, considering an elastic response Spectrum type I, a peak ground acceleration (PGA) of 0.04g, and Soil type B. The duration of the accelerogram is 10.23 seconds. A series of scaled ground motions with increasing intensity (0.02g, 0.04g, 0.06g, ..., 0.20g) was applied to the specimen. Since significant damages were first reported with the application the 0.12g test, this accelerogram (reported in Figure 155) is utilised for the subsequent numerical simulations involving the macroelement strategy. Refer to (Anthoine and Capéran, 2008) for a detailed description of the experimental setup and outcomes.

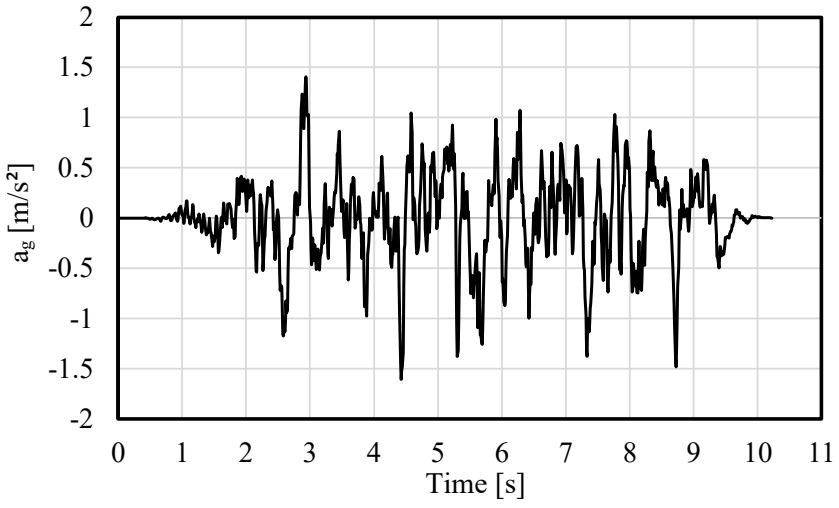

Figure 155 0.12g scaled accelerogram for the pseudodynamic test

6.4.2 Macroelement model

The two-floor macroelement model (illustrated in Figure 156) utilises a mesh discretisation approach for the URM walls, comprising 152 elements with a thickness of 175 mm, fully restrained at the bottom nodes. For the reinforced concrete slab floors, elastic shell elements with a thickness of 22 cm and with a Young's modulus of 30000 MPa are employed. The wall-to-floor connections are established by considering full-DOF edges for the macroelements boundaries shared with the slabs, as detailed in Chapter 5.2 regarding frame-macroelement connectivity (refer to Figure 107). The slabs are discretised to align with the macroelement borders and allow for the exact application of the added loads derived from water tanks, as in the experiment.

Regarding the loading conditions, a dynamic pseudo-static analysis is conducted, following the approach used in (Chisari et al., 2020). The experimental displacements are transformed into equivalent floor accelerations by fitting them with spline curves and subsequently differentiated twice. These accelerations are applied to the nodes corresponding to the actuators (see Figure 105b) by performing dynamic nonlinear analysis.

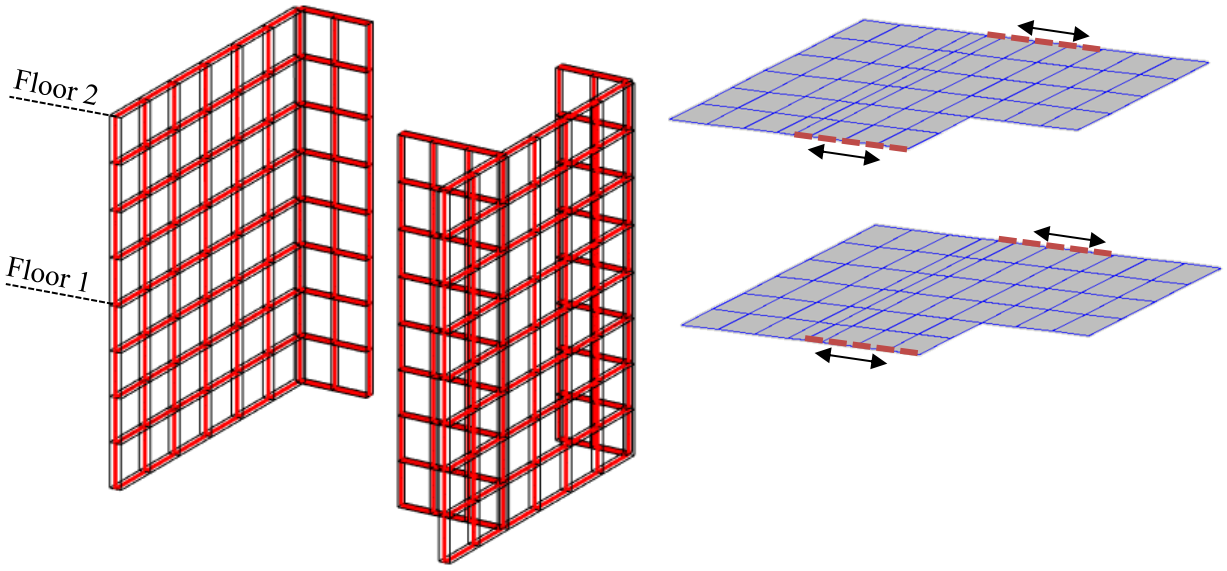

Figure 156 Macroelement model: (a) macroelement for the modelling of the wall elements (Matlab post-processing) and (b) shell elements for the floors (Adaptic post-processing)

The material characteristics of the macro-elements are determined following the procedure described in the previous paragraphs and taking into account the results of material tests reported in Table 39. Interface characteristics are provided in Table 40, while diagonal in-plane spring characteristics are

outlined in Table 41. Specifically, for the horizontal interfaces, the tensile strength is derived by dividing cohesion by 1.4, as suggested by Lourenço and Gaetani (2022). For the vertical interfaces, the elastic modulus is taken as 0.7 times that of the horizontal interfaces, and the tensile strength and cohesion are calculated as the averages between values obtained from mortar joints and units (with the cohesion of units assumed to be the tensile strength). Regarding the diagonal spring, the shear modulus is set at 0.4 times the Young's modulus, and the strength parameters are determined using the Mann-Muller criterion, through relations (35), (36) and (37).

Table 40 Material parameters for interfaces of the 3D structure macroelement model

Interface	E_n [MPa]	f_t [MPa]	c [MPa]	tanϕ [-]	f_c [MPa]	$G_{f,I}$ [N/mm]	$G_{f,II}$ [N/mm]	$G_{f,c}$ [N/mm]
Horizontal	2849	0.20	0.28	0.55	18.4	0.05	0.1	21.7
Vertical	1994	0.85	0.89	0.55	9.20	0.05	0.1	18.7

Table 41. Material parameters for in-plane diagonal springs of the 3D structure macroelement model

G_e [MPa]	$\tilde{c}$ [MPa]	$\tilde{\mu}$ [-]	δ_u^* [mm]	K_{pl}/K_{el}	F_y/F_{max}	C_F	α	β
1140	0.13	0.26	15	0.1	0.7	0.4	0.8	0.06

The characteristics of the out-of-plane spring are determined employing a mesoscale model representing a portion of the masonry specimen, following the approach outlined in (Minga et al., 2020) and detailed in Chapter 5.2. The dimensions of the model are 750x750x175 mm, reflecting the dimensions of the macroelements utilised in the model (which slightly vary across the walls). The mesoscale model is pinned along two sides, subjected to a certain level of confinement, and to an out-of-plane force applied to the free corner. Figure 157a illustrates the boundary and loading conditions of the mesoscale virtual test, while Figure 157b depicts a typical deformed shape.

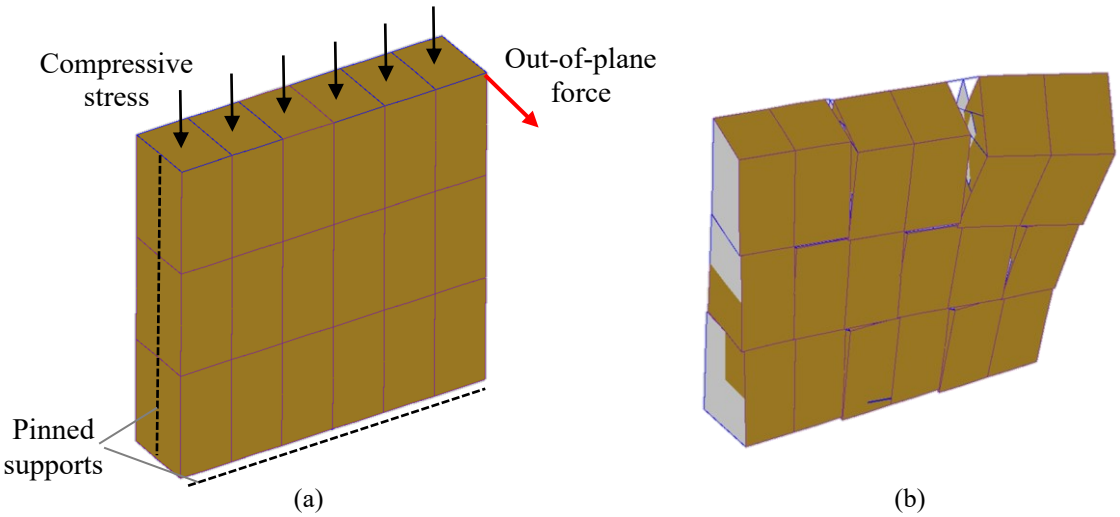

Figure 157 Mesoscale virtual test model: (a) boundary and loading conditions and (b) deformed shape

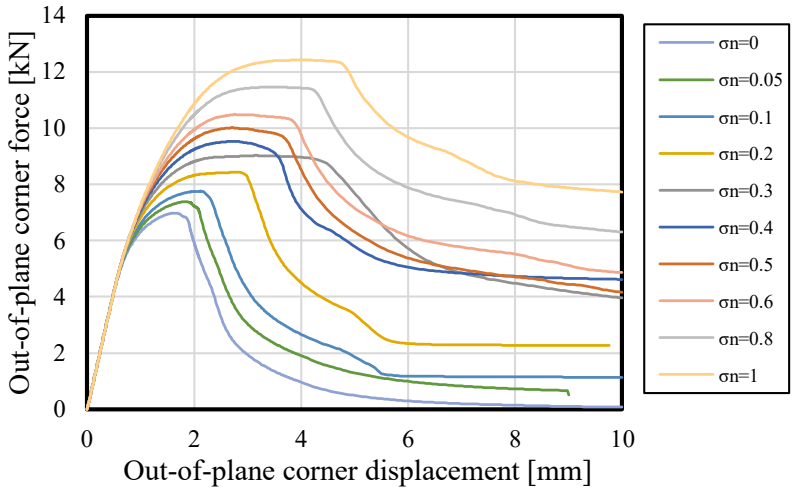

Figure 158 Out-of-plane corner displacement vs. force of the mesoscale model under various level of compressive stress σ_n

The force-displacement curves are then transformed into equivalent trilinear pressure-displacement curves (out-of-plane force per unit surface against out-of-plane corner displacement), as illustrated in Figure 113b. Maximum pressure (p_y) and residual pressure (p_r) from each analysis, along with the pre-peak slope ($\tan\theta_e$) and the post-peak slope ($\tan\theta_p$), are reported in Table 11. Elastic pre-peak modulus (E_e) and post-peak modulus (E_p) are then derived by multiplying $\tan\theta_e$ and $\tan\theta_p$ by the surface of the mesoscale model. The average values of the modulus E_e and E_p are adopted within the spring specification, as shown in Table 12.

Table 42 Calibration of out-of-plane springs: values obtained by idealisation of numerical curves

σ	p_y	p_r	$\tan\theta_e$	$\tan\theta_p$	E_e	E_p
N/mm^2	N/mm^2	N/mm^2	N/mm^3	N/mm^3	N/mm	N/mm
0	0.012	0.001	0.0100	-0.0041	5631	-2326
0.05	0.013	0.002	0.0095	-0.0044	5350	-2490
0.1	0.014	0.003	0.0092	-0.0032	5172	-1777
0.2	0.015	0.004	0.0088	-0.0022	4961	-1247
0.3	0.016	0.008	0.0087	-0.0010	4905	-555
0.4	0.017	0.009	0.0087	-0.0015	4913	-851
0.5	0.018	0.009	0.0088	-0.0017	4961	-943
0.6	0.019	0.010	0.0088	-0.0014	4956	-803
0.8	0.020	0.012	0.0086	-0.0011	4835	-645
1	0.022	0.016	0.0083	-0.0009	4689	-527
					5037	**-1216**

Maximum pressure (p_y) and residual pressure (p_r) from each analysis are depicted as functions of compressive stress (σ_n) in Figure 159, alongside the corresponding linear regressions, which exhibit a good fit. The resulting y-intercepts, $p_{y,0}$ and $p_{r,0}$, and the slopes $\mu_{o,y}$ and $\mu_{o,r}$, are included in the spring definition (Table 43). The remaining parameters are assumed to be the same as those listed in Table 37.

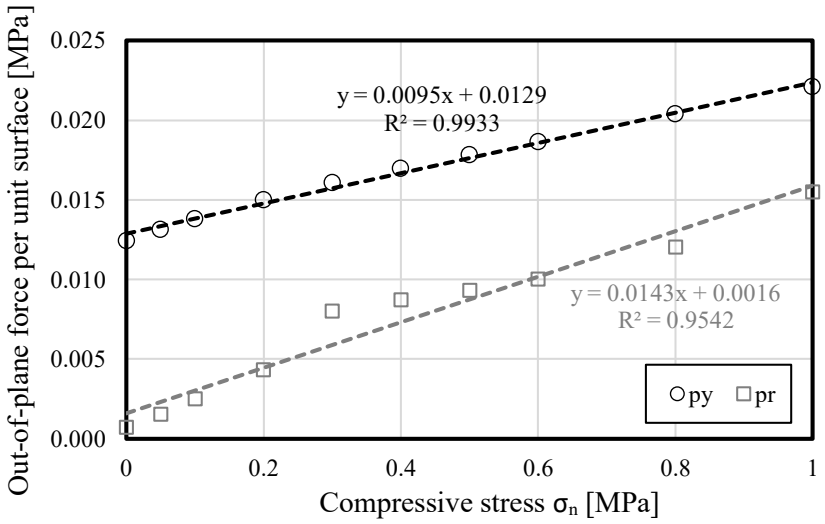

Figure 159 Linear regression of yield and residual pressure with respect to the normal compressive stress

Table 43. Material parameters for out-of-plane springs of the 3D structure macroelement model

E_e [MPa]	E_p [MPa]	$p_{y,0}$ [kPa]	$p_{r,0}$ [kPa]	$\mu_{o,y}$ [-]	$\mu_{o,r}$ [-]	C_F	α	β
5037	-1216	0.0129	0.0016	0.0095	0.0016	0.8	0.8	0.06

6.4.3 Numerical simulations

The experimental test has already been simulated using both the mesoscale approach, as described in (Chisari et al., 2021) and the continuum macroscale approach, as detailed in (Chisari et al., 2020), modelling strategies employed throughout the present research. In the mesoscale model, the accelerogram was applied within a dynamic analysis with ground motion at the base. In the macroscale model, both loading conditions were considered: dynamic analysis with ground motion at the base and dynamic pseudo-static analysis with experimental displacements applied at the floors on the two floors. The results obtained, in terms of horizontal displacements (of both the first and the second floor) versus base shear force, from the three approaches are presented in Figure 160 (for the macroscale model, the results obtained from dynamic pseudo-static analysis are reported). It can be observed that the response obtained with the macroelement (Figure 160a and b) closely matches the experimental outcomes in terms of initial stiffness, maximum strength attained, stiffness degradation, and overall hysteretic cycle.

Remarkably, the curves even exhibit a closer fit to the experimental responses compared to the continuum macroscale curves (Figure 160c and d) and the mesoscale model (Figure 160e and f).

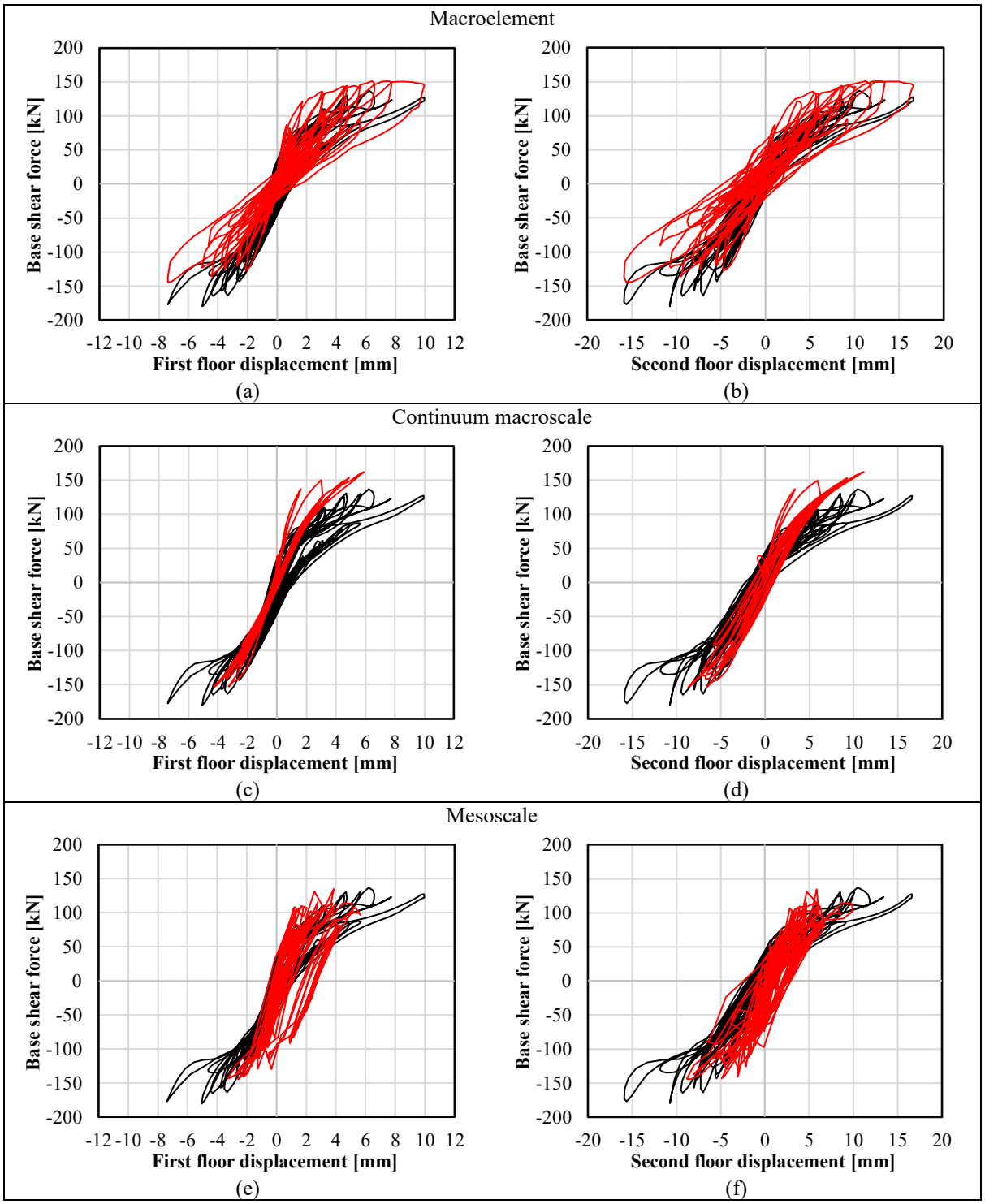

Figure 160 Experimental-numerical comparison of base shear force vs. horizontal displacement, including both first and second floors, for (a-b) macroelement model, (c-d) continuum macroscale model, and (e-f) mesoscale model; experimental curves in black, numerical curves in red

To compare the computational efficiency among the three approaches, the analysis for the macroelement model is conducted under the same conditions as the other two models. The calculation is performed within the high-performance computing facilities at Imperial College London. The differences in the problem dimensions and computational time are illustrated in Table 44. Essentially, the difference in terms of degrees of freedom is one order of magnitude higher when passing from the macroelement to the continuum macroscale to the mesoscale. In terms of computational time, the macroelement and macroscale approaches are similar, but it is important to note that a single partition is used for the macroelement, while 14 partitions were employed for the continuum macroscale model, which tackled the computational burden. On the other hand, for the mesoscale model, which involved 105 partitions, the analysis time was approximately six times longer. Hence, the macroelement strategy provides high reliability while offering a lower computational cost compared to the other more refined strategies.

Table 44 Comparison of the computational efficiency of the modelling strategies

Strategy	Mesoscale	Continuum macroscale	Macroelement
Number of partitions	105 partitions	14 partitions	1 partition
Number of DoFs	161748	20256	4470
Analysis time	69h,6min (not completed)	11h,33min (completed)	10h,59min (completed)

The damage pattern observed in the macroelement model resembles the experimental observations. Specifically, the damage exhibited by the diagonal in-plane springs (illustrated in Figure 161) closely aligns with the actual damage observed along the walls in the direction of the applied actions. Many elements exceed the maximum strength of the diagonal springs (indicated by a DAM_{IP} indicator of around 0.2, which may vary depending on the dimensions of the elements), mirroring the experimental findings where shear diagonal cracking damage is observed. Out-of-plane flexural damage on interfaces is observed, as highlighted in Figure 162a, showing views of the deformed shape at the final step reached. This type of damage was also observed during the experimental test, as shown in Figure 162b. In contrast, no damage is observed on the out-of-plane springs, despite experimental evidence showing some out-of-plane diagonal cracking.

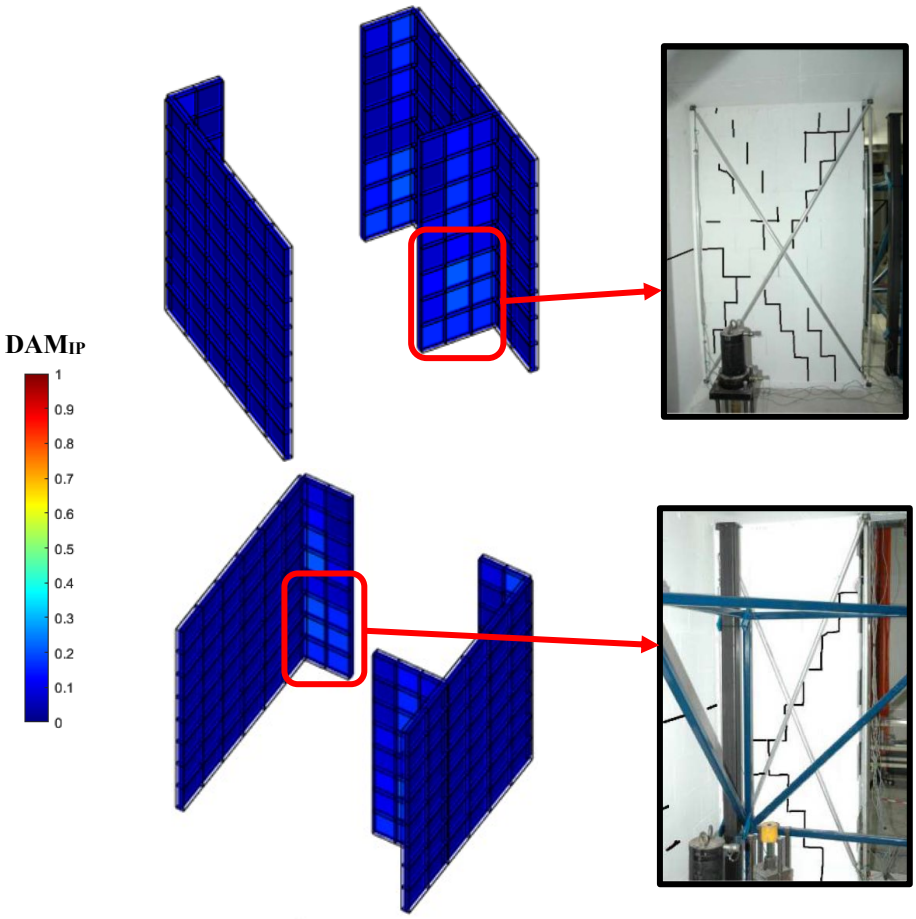

Figure 161 3D views of the damage pattern of the in-plane diagonal spring aligning with experimental observations

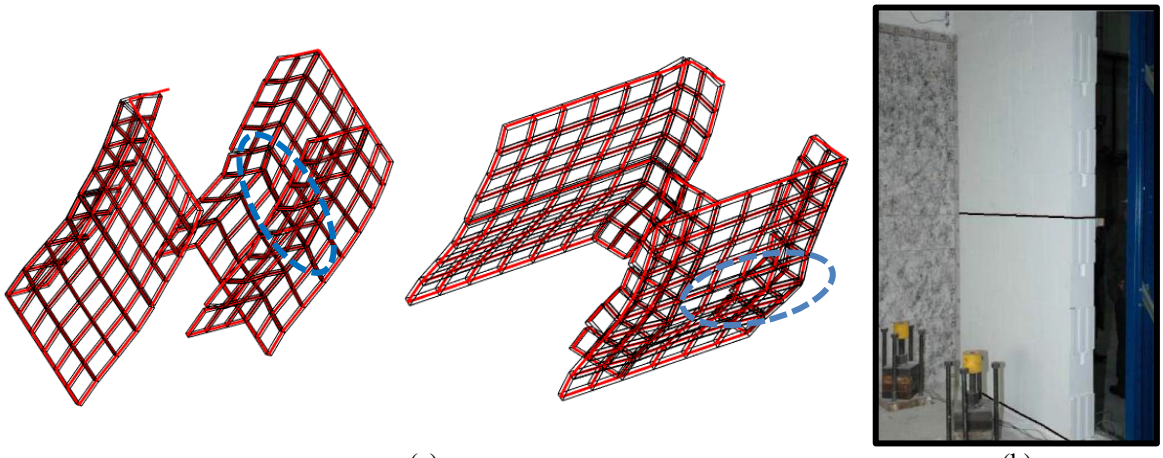

(a) (b)

Figure 162 (a) 3D views of the deformed shape at the maximum displacement reached (amplification factor x50) highlighting the out-of-plane flexural damage; (b) experimental out-of-plane flexural damage

6.5 Infilled frames

The field of applications of the macroelement include the assessment of the behaviour of masonry-infilled frames. As previously mentioned, the proposed macroelement strategy is developed within a FEA framework, ensuring its compatibility with different types of finite elements. Thus, the model is suitable for modelling masonry infills. Additionally, the amendment allowing for a distinct material characterisation for each interface, described in Section 5.6, enables an accurate representation of the ever-changing interaction between the infill and the external frame. This chapter evaluates the macroelement ability to reproduce the behaviour of this structural typology by simulating existing experimental tests, under both monotonic and cyclic loading conditions. The influence of openings is also examined by comparing the results obtained with the more refined continuum macroscale model.

6.5.1 Response of solid masonry-infilled frames

The analysis of the "Specimen 3", which was experimentally tested in (Mehrabi et al., 1996) and simulated using mesoscale and macroscale modelling strategies in Chapter 4, has been conducted within the framework of macroelement modelling strategy in Section 5.6. It has been emphasised there how distinct material characterisation for the external interfaces enables a more accurate representation of the actual experimental response. The numerical-experimental comparison depicted in Figure 127 demonstrates the correctness of the prediction in terms of initial stiffness, maximum strength, and post-peak softening. Moreover, the macroelement model response prediction is consistent with the results provided by the two alternative more sophisticated and computationally expensive modelling approaches, as illustrated in Figure 163.

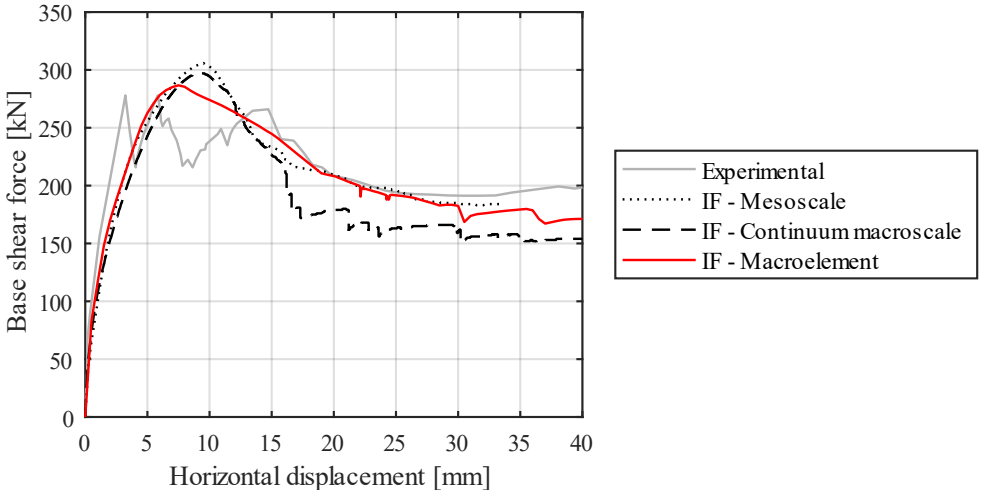

Figure 163 Comparison among the different masonry modelling approaches adopted for the modelling of infilled frames.

To investigate the influence of the mesh characteristics, the infilled-frame specimen is analysed with different meshes with 1x1, 2x2 and 6x6 macroelements. The results are illustrated in Figure 164.

The outcomes from the coarser 1x1 and 2x2 meshes deviate significantly from the experimental response in terms of maximum strength and post-peak behaviour. In particular, the behaviour of the basic 1x1 mesh with only one macroelement is solely determined by the single spring positioned along the compression diagonal. Lacking internal interfaces for the redistribution of internal forces, the response results in a steep post-peak branch. The 2x2 model, still excessively coarse, exhibits a comparable initial phase of the capacity curve, with higher strength and stiffness. However, the post-peak behaviour is notably different, characterised by a lower strength decay. This difference can be attributed to the redistribution of internal forces facilitated by the presence of internal interfaces.

The further refinement of the mesh discretisation enables a differentiation of the internal forces path, allowing for a more scattered damaging of the diagonal springs. The overall response, previously dominated by the in-plane springs, is now determined by the interaction among all the components, including the in-plane springs, the internal and external nonlinear interfaces. The response prediction provided by more refined 6x6 mesh closely resembles that of the 3x3 model, exhibiting a similar path and aligning with experimental findings. Similar to the 3x3 model, the initial phase is characterized by damage of the diagonal springs, followed by the ultimate failure of a horizontal row of elements.

As a result, the response generally decreases from coarser to finer models, though not in a strictly gradual manner (the 6x6 model exhibits a slightly more resistant response than the 3x3 model, in line with the coarser meshes 2x2 and 1x1). Reasonably, this nonlinear variation may be expected considering the discrete nature of the modelling approach and the complex interactions among the three components of the infill - diagonal springs, internal interfaces, and external interfaces - and the surrounding frame components.

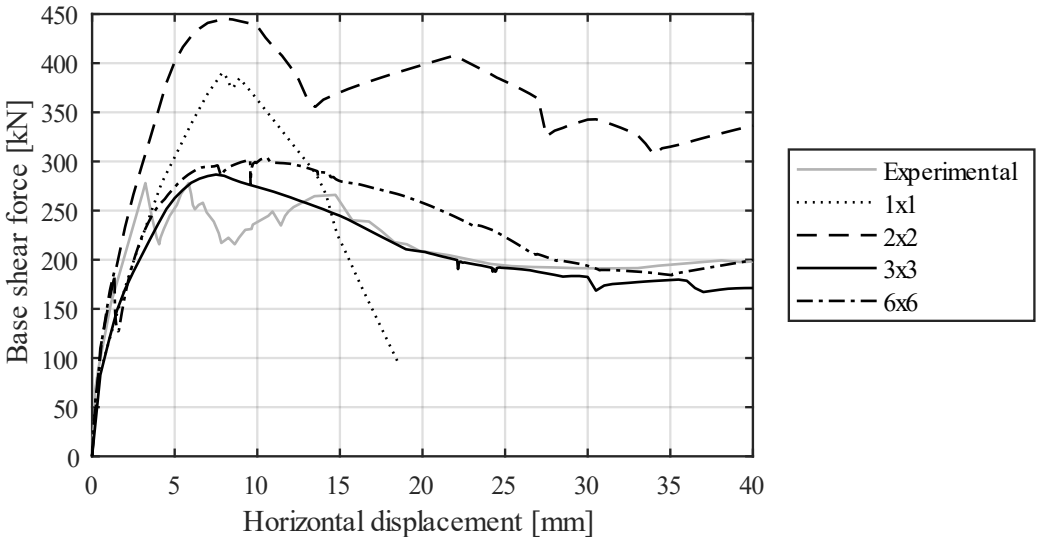

Figure 164 Comparison among different mesh refinements for masonry-infilled frame specimen 3.

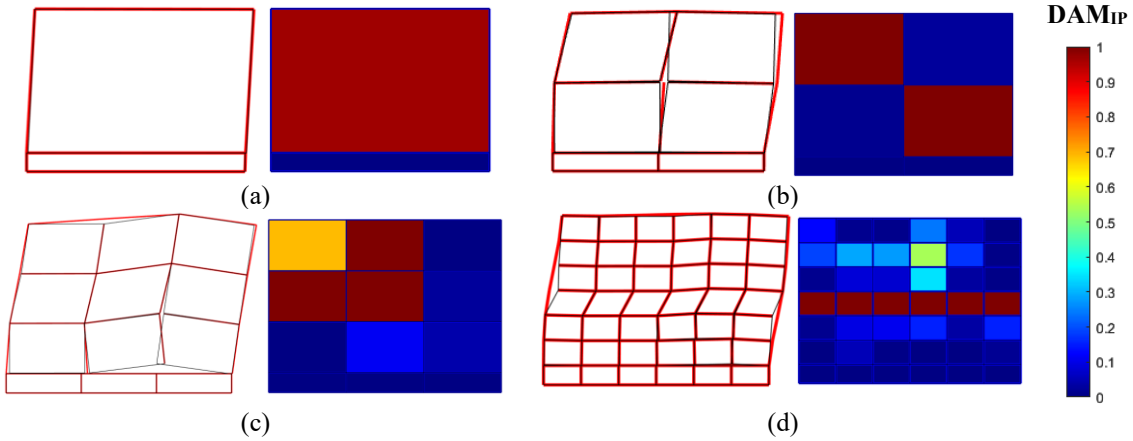

Figure 165 Deformed shape and damage in the diagonal springs at the last step of the nonlinear simulation for different mesh discretisations: (a) 1x1, (b) 2x2, (c) 3x3, (d) 6x6

Finally, two additional experimental tests (Mehrabi, et al. 1996) are simulated. In order to assess the ability of the adopted modelling strategy with macroelements to effectively consider the influence of vertical loading, 'Specimen 9' is investigated. This specimen was subjected to a load distribution different from that of s 'Specimen 3,' involving a fraction of 1/3 of the total load subtracted from the columns and uniformly applied to the top beam. Additionally, the macroelement crucial ability to accurately reproduce the hysteretic cyclic response is examined by simulating 'Specimen 5,' which was subjected to cyclic horizontal displacement history.

The experimental material characteristics of concrete and masonry are presented in Table 45 and Table 46, highlighting differences among the specimens, particularly in terms of Young's modulus and

compressive strength for both masonry and concrete. These variations are appropriately taken into account in the model, and the same material characterisation procedure adopted in Section 5.6 is applied here.

Table 45 Mechanical properties of the concrete material of the tested specimens (Mehrabi et al., 1996)

Specimen	Secant modulus (*) [MPa]	Compressive strength [MPa]
3	21930	30.9
5	18070	20.9
9	17240	26.8

*At 45% of the compressive strength

Table 46 Mechanical properties of the masonry of the tested specimens (Mehrabi et al., 1996)

Specimen	Masonry secant modulus (*) [MPa]	Masonry compressive strength [MPa]	Masonry strain at peak stress [-]	Brick compressive strength [MPa]	Mortar compressive strength [MPa]
3	9520	15.10	0.0029	15.59	16.00
5	8950	13.86	0.0023	15.59	13.38
9	8240	14.21	0.0026	15.59	12.48

*At 45% of the compressive strength

The material characterisation of the macrolement infill for Specimen 9 is provided in Table 47, Table 48 and Table 49. The numerical response, as illustrated in Figure 166, closely approximates the experimental curve, providing an accurate prediction of the initial stiffness degradation and showing a slightly higher maximum strength. By the point of peak load, the diagonal springs have already reached their maximum strength (Figure 167a), and the second phase is characterised by the failure of the central elements band (Figure 167b). Hence, the model proves to be capable of accurately capturing the behaviour of a masonry infill frame under a different vertical load configuration.

Table 47 Internal infill interfaces material parameters for the macroelements of Specimen 9 model.

	E_n [MPa]	f_t [MPa]	c [MPa]	tanϕ [-]	f_c [MPa]	$G_{f,I}$ [N/mm]	$G_{f,II}$ [N/mm]	$G_{f,c}$ [N/mm]
Horizontal	12360	0.075	0.11	1.02	14.21	0.05	0.1	20.4
Vertical	8652	0.86	0.88	1.02	7.11	0.05	0.1	17.8

Table 48 External infill interfaces material parameters for the macroelements of Specimen 9 model.

Direction	E_n [MPa]	f_t [MPa]	c [MPa]	tanϕ [-]	$G_{f,I}$ [N/mm]	$G_{f,II}$ [N/mm]
Horizontal	12360	0.01	0.14	0.35	0.05	0.1
Vertical	8652					

Table 49. Diagonal springs characterisation for the macroelements of Specimen 9 model.

G_c [MPa]	f_t [MPa]	δ_u^* [mm]	K_{pl}/K_{el}	F_y/F_{max}	C_F	α	β
5700	1.1	30	0.1	0.7	0.4	0.8	0.06

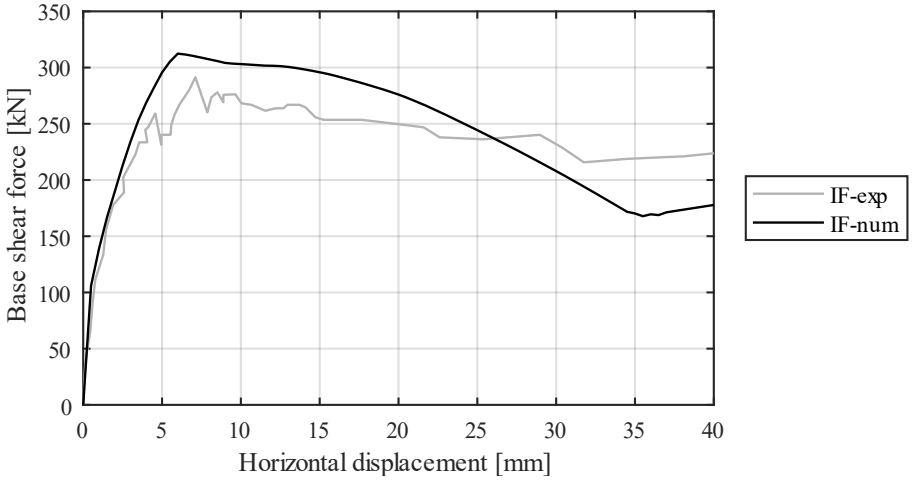

Figure 166 Experimental-numerical comparison for masonry-infilled frame Specimen 9.

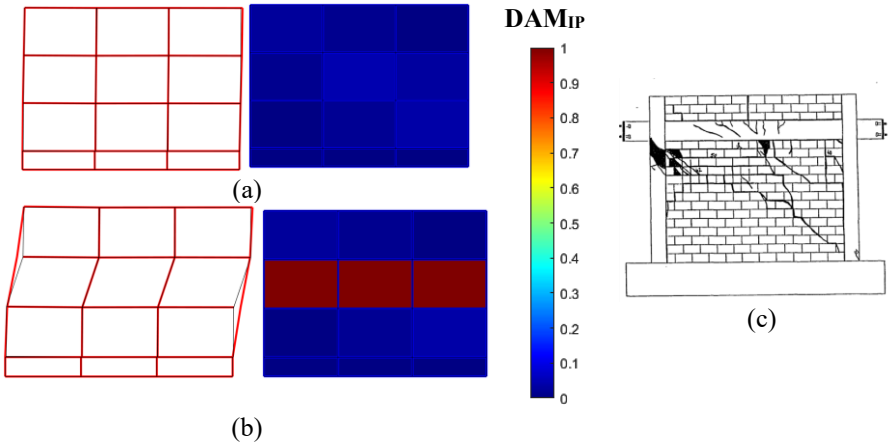

Figure 167 Infilled frame 3x3 model of specimen 9: deformed shape (amplification factor of 5) and damage of diagonal springs at two displacements: (a) 6mm and (b) 40mm; (c) Experimental damage pattern at the end of the analysis for the Specimen 9 (Mehrabi, 1994)

Finally, the cyclic response is assessed by simulating Specimen 5', which underwent cyclic testing. The geometry and load configuration mirror that of 'Specimen 9,' with an amount of the applied loads exerted onto the top beam. The macroelement characteristics are detailed Table 50, Table 51 and Table 52. The model undergoes an initial load cyclic history (Figure 168a), followed by a displacement-control phase (Figure 168b). The numerical-experimental comparison is depicted in Figure 169.

Notably, the numerical prediction closely aligns with the experimental cyclic curve, accurately capturing initial stiffness, maximum strength, and overall strength decay. Furthermore, the pinching effect is well-represented, albeit with a slight underestimation of the hysteretic capacity. The final damage pattern, as illustrated in Figure 170, is in good agreement with the experimental observations, with damage concentrated mostly on a horizontal central band. The obtained responses are remarkable, especially considering the simplified nature of the model and its very low computational burden.

Table 50 Internal infill interfaces material parameters for the macroelements of Specimen 5 model.

	E_n [MPa]	f_t [MPa]	c [MPa]	tanϕ [-]	f_c [MPa]	$G_{f,I}$ [N/mm]	$G_{f,II}$ [N/mm]	$G_{f,c}$ [N/mm]
Horizontal	11370	0.08	0.11	1.02	13.86	0.05	0.1	20.3
Vertical	7959	0.86	0.88	1.02	6.93	0.05	0.1	17.8

Table 51 External infill interfaces material parameters for the macroelements of Specimen 5 model.

Direction	E_n [MPa]	f_t [MPa]	c [MPa]	tanϕ [-]	$G_{f,I}$ [N/mm]	$G_{f,II}$ [N/mm]
Horizontal	11370	0.01	0.014	0.35	0.05	0.1
Vertical	7959					

Table 52. Diagonal springs characterisation for the macroelements of specimen 5 model.

G_e [MPa]	f_t [MPa]	δ_u^* [mm]	K_{p1}/K_{el}	F_y/F_{max}	C_F	α	β
4548	0.82	30	0.1	0.7	0.4	0.8	0.06

(a)

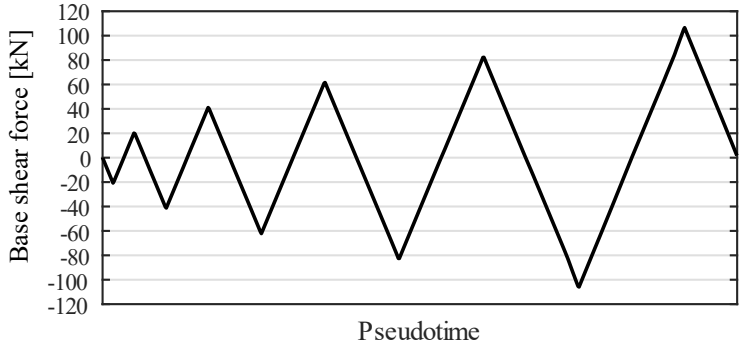

(b)

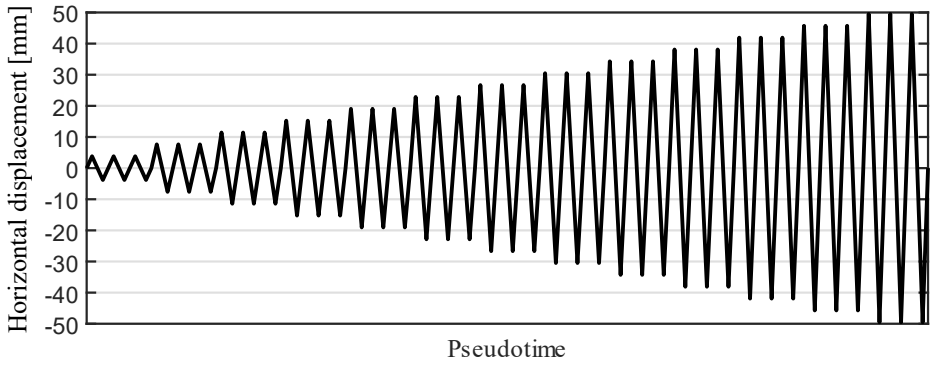

Figure 168 Cyclic analysis actions: (a) load-control phase, (b) displacement-control phase

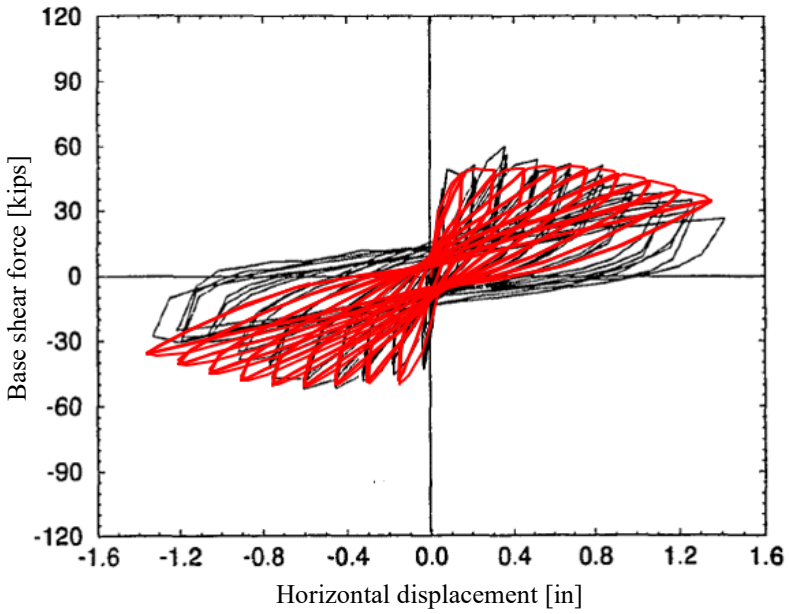

Figure 169 Cyclic response of the infilled-frame: experimental-numerical load-displacement curves (numerical response in red; the background is taken from Mehrabi, 1994)

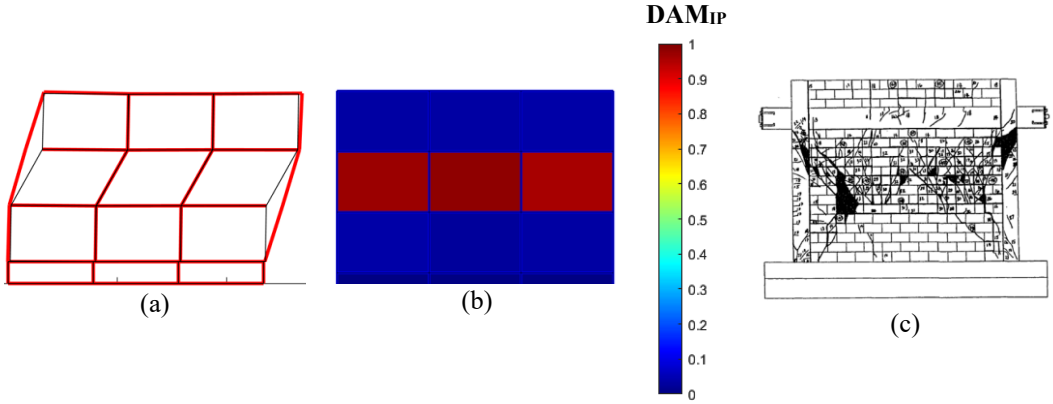

Figure 170 Infilled frame 3x3 model of specimen 5: (a) deformed shape (amplification factor of 5) at the maximum displacement, (b) damage of diagonal springs at the last step reached; (c) Experimental damage pattern (Mehrabi, 1994)

6.5.2 Response of masonry-infilled frames with openings

The presence of openings significantly influences the final response of infilled frames. In current engineering practice, openings are typically evaluated through the application of specific stiffness and strength reduction factors in association within a simplified equivalent-strut modelling. However, the determination of these factors could be not straightforward, and their application may lead to inaccuracies in the response prediction. On the contrary, the use of macroelements allows for the

representation of the actual geometry of the infill, incorporating any specific openings, without the necessity of defining any a priori equivalent coefficient.

The impact of openings in the infills is assessed by comparing the macroelement outcomes with those derived from continuum finite element modelling, as detailed in Section 4.7. Pushover analyses are conducted on identical geometries, covering both door-infills (models D1, D2 and D3) and window-infills (models W1, W2 and W3). Geometry and identification of the analysed models are specified in Table 23. In addition, BF and IF stand for bare and infilled frame, respectively. Two distinct mesh discretisations are employed, originating from 3x3 models ("Mesh 1") and 6x6 models ("Mesh 2") of 'Specimen 3', with element dimensions suitable for the insert of openings. The final models are subsequently obtained by removing the elements within the opening area. The material characteristics of the infilled-frame model are given in Table 18, Table 27, Table 28 and Table 29.

The results of the analyses on macroelement door infills are in accordance with the outcomes previously obtained using a 3D continuum mesh with the CDP material model for masonry, even with the coarse Mesh 1. The load-displacement responses presented in Figure 171 reveal that stiffness and strength reductions from the solid infilled frame model are accurately captured, closely aligning with continuum finite element results. The curves exhibit an approximately elasto-perfectly plastic behaviour, given the inability of the diagonal compression strut to develop due to the presence of the openings. Furthermore, the maximum force closely approximates the residual force of the solid-infilled frames.

The curves corresponding to different openings are close to each other, suggesting that in presence of door openings, extending from the bottom base, the opening dimensions do not exert a significant influence on the final response.

Furthermore, the progression of damage is consistent among the modelling strategies, as observed in Figure 172. Crushing damage occurs at the top right corner of the opening in each macroelement model, along with slight damage on the nearby diagonal springs. This damage pattern aligns with the one obtained using the continuum finite element model.

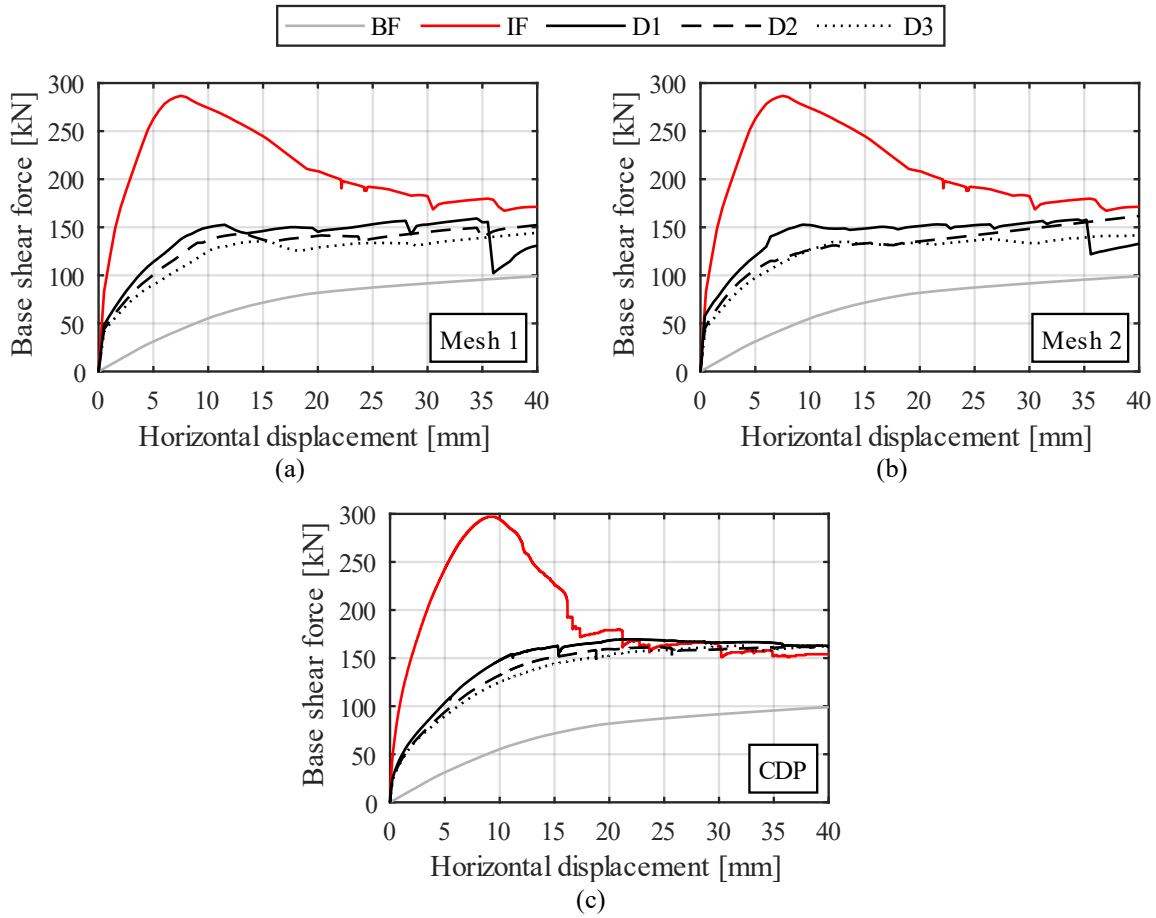

Figure 171 Load-displacement curves for door-infills: (a) macroelement Mesh 1, (b) macroelement Mesh 2 and (c) continuum finite element (CDP material model)

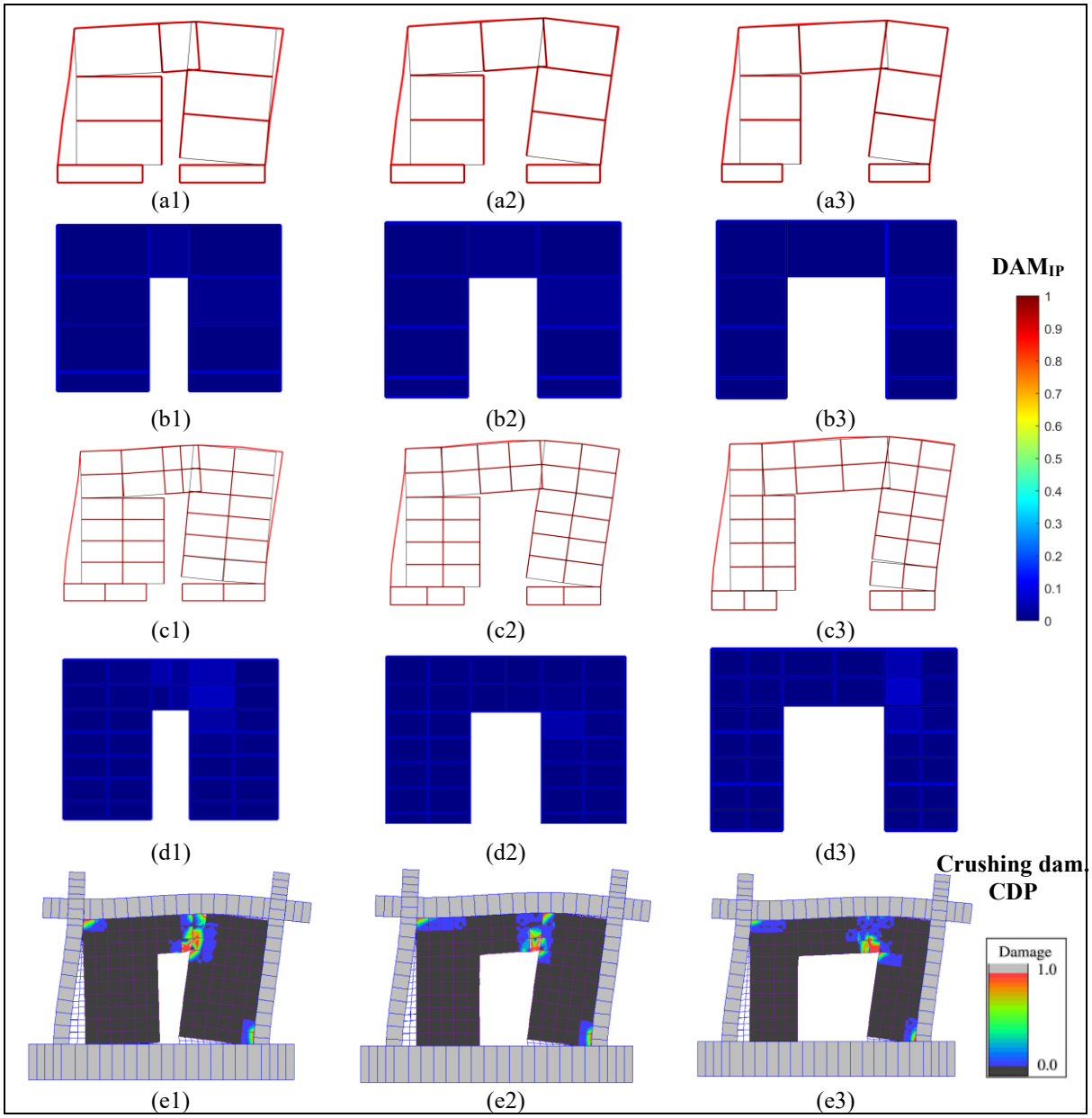

Figure 172 Door Infilled frames responses: (a-c) deformed shape (amplification factor of 5) and (b-d) damage in the diagonal springs at the end of the analysis for the macroelement models with mesh 1 and mesh 2; (c) Compressive damage at the end of the analysis for the macroscale CDP models (deformed shape with amplification factor of 5); (1) Infill D1; (2) Infill D2; (3) Infill D3

The results for window-infills models are also remarkable, demonstrating a comparable prediction of strength and stiffness decay given by macroelement models and finite element models (Figure 173). A notable agreement is observed in the case of W2 and W3 models, particularly concerning initial stiffness and maximum strength.

However, significant differences are noticed for the model with the small window (W1). In the finite element model, the small dimensions of the opening allow the development of the compression strut, enabling the model to attain the same shear strength as the solid-infilled frames. Conversely, the macroelement models exhibit the failure of springs around the opening, which is observed in both Mesh 1 and Mesh 2. Nevertheless, the prediction of initial stiffness is nearly identical, with the differences in maximum strength predictions being relatively small and around 10%.

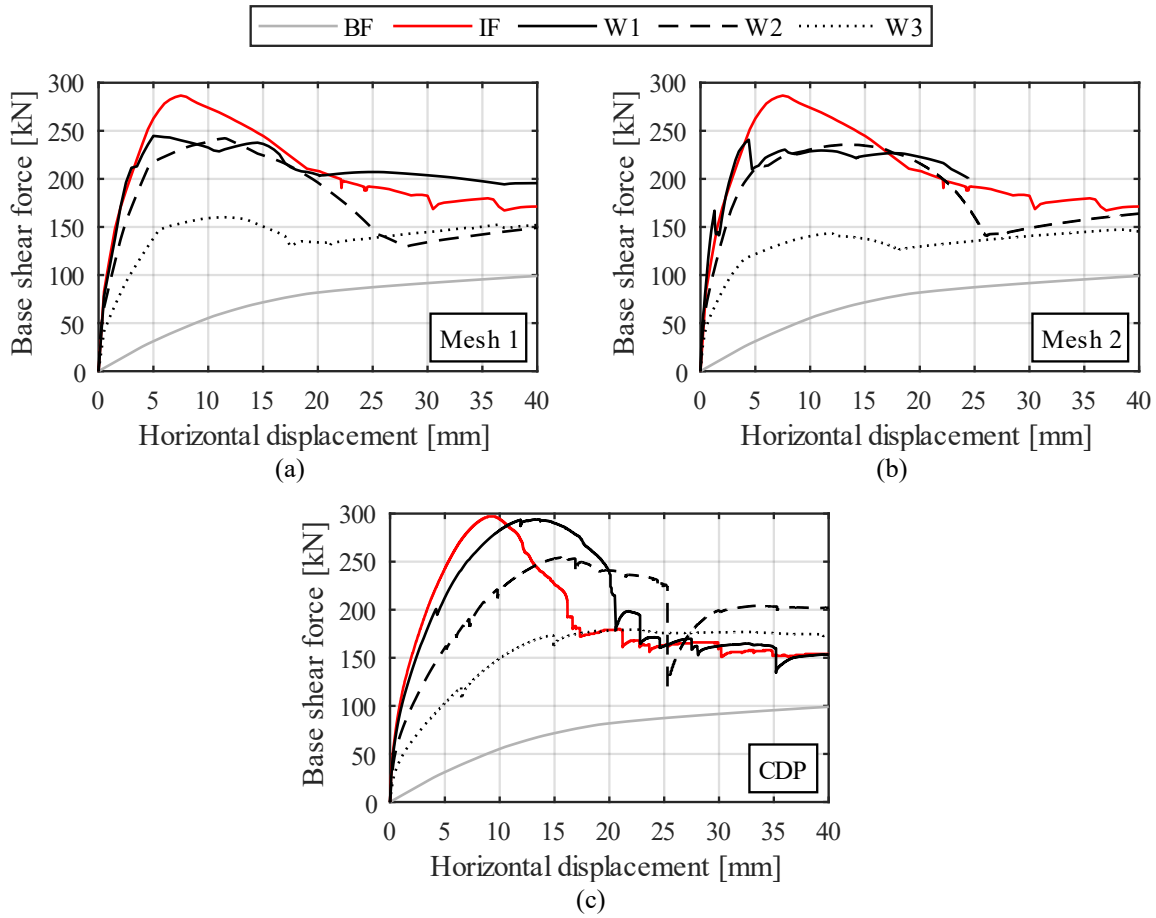

Figure 173 Load-displacement curves for window-infills: (a) macroelement Mesh 1, (b) macroelement Mesh 2 and (c) continuum finite element (CDP material model)

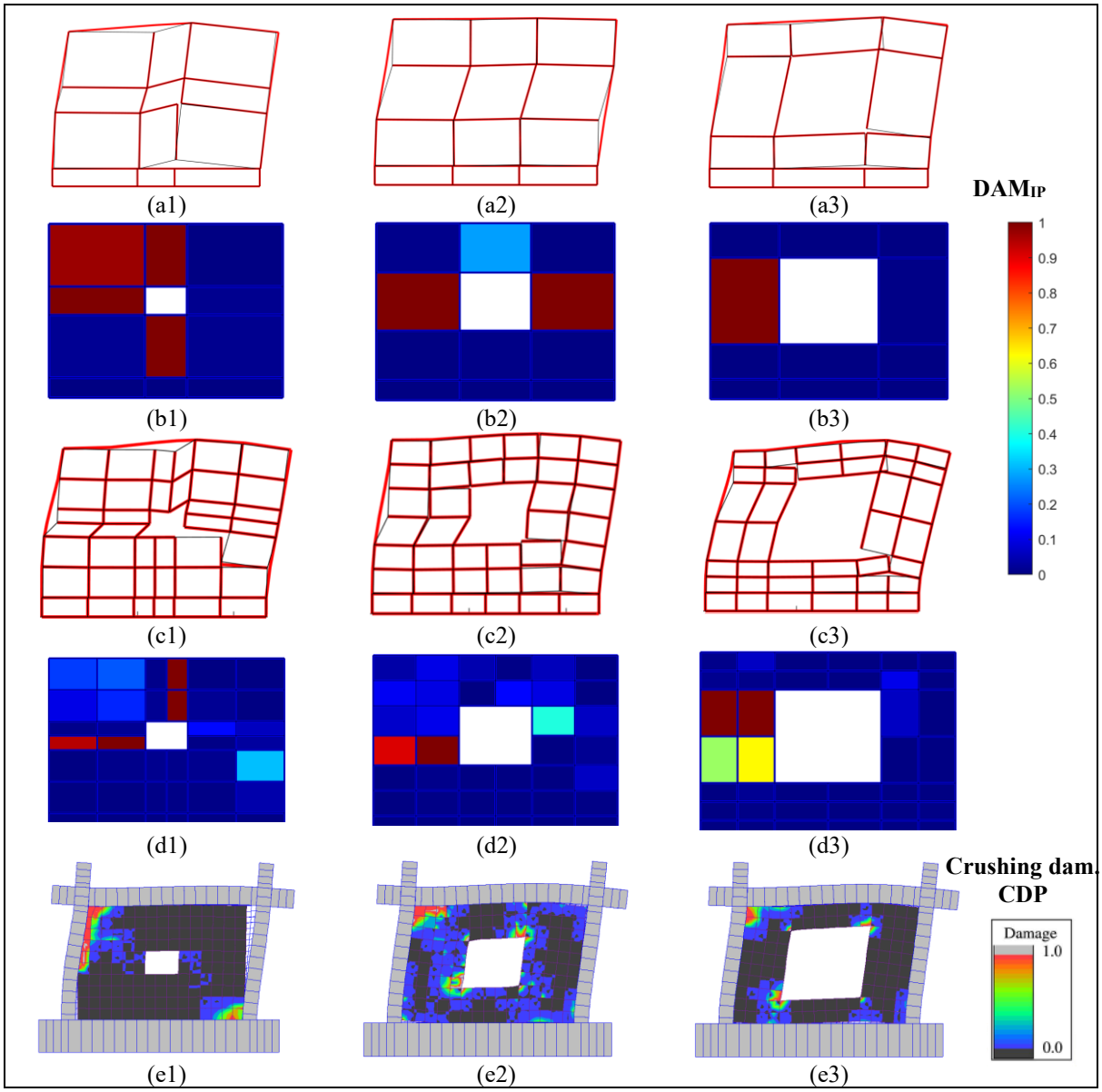

Figure 174 Window infilled frames responses: (a-c) deformed shape (amplification factor of 5) and (b-d) damage in the diagonal springs at the end of the analysis for the macroelement models with mesh 1 and mesh 2, (e) compressive damage at the end of the analysis for the macroscale CDP models (deformed shape with amplification factor of 5); (1) Infill W1; (2) Infill W2; (3) Infill W3

In conclusion, the developed macroelement modelling proves to be effective in accurately simulating the effects of opening, producing results closely aligned with the more refined continuum finite element models while maintaining high computational efficiency.

6.6 Summary and conclusions

In this chapter, the enhanced macroelement has been validated against experimental outcomes, encompassing both unreinforced masonry and infilled frame structures.

First, the macroelement was tested to simulate the cyclic response of individual masonry solid panels with varying height-to-width ratios, demonstrating its ability to accurately predict shear diagonal cracking and flexural responses. Moreover, a large perforated brick-masonry wall was modelled achieving an accurate response prediction under monotonic loading also using a coarse mesh of macroelements with a straightforward calibration of the material model parameters. An improved model calibration led to a very accurate prediction also under cyclic loading. Furthermore, the out-of-plane response of masonry walls was also assessed, for which certain drawbacks were highlighted within the original version. The new implementations facilitated the calibration of the experimental responses, achieving very good agreement with both monotonic and cyclic behaviour. The model was successfully tested against several masonry specimens both in the presence or absence of openings, and with or without vertical loading. Notably, it was found that the adopted improved macroelement model can adequately capture pinching effects and strength decay which develop in the physical test under cyclic loading conditions. The model also successfully reproduced the structural response of a 3D URM building experimentally tested under earthquake loading, with high accuracy and significantly lower computational demands compared to other, more sophisticated modelling approaches employed for replicating the same test.

The macroelement was also tested against experimental infilled frame tests. The model demonstrated its ability to accurately predict the response, accurately reproducing the actual failure mechanisms characterising the complex response of infilled frame structures. This includes initial stiffness degradation due to early frame-infill detachment and the development of a diagonal compression strut, through a proper damage development in in-plane diagonal springs. Monotonic pushover analyses, conducted using models with different confinement levels, exhibited very good agreement with the experimental outcomes. Moreover, the model proved highly effective in predicting the cyclic response. Finally, the presence of infill with openings was also evaluated. The results demonstrated a significant concordance with the outcomes previously obtained using more refined finite element models.

Thus, the enhanced macroelement strategy stands as a reliable tool, capable of accurately predicting the response of masonry wall structures, while maintaining high computational efficiency, making it approp for accurate analysis of real-sized buildings.

CHAPTER 7

SEISMIC ASSESSMENT OF A REAL RC MASONRY-INFILLED FRAME BUILDING

7.1 Introduction

The proposed macroelement strategy has demonstrated its ability to accurately represent the response of URM and infilled frame structures under both monotonic and cyclic loading, while maintaining a high computational efficiency. This makes it a valuable tool for analysing the structural response of real-size structures.

This concluding chapter focuses on applying the novel macroelement strategy to assess the seismic vulnerability of a real 4-story irregular RC existing building, originally not designed to withstand seismic actions. The assessment aims to evaluate the impact of masonry infills on the structural response. Nonlinear dynamic analyses are conducted using a set of natural spectrum-compatible accelerograms, considering both horizontal and vertical directions simultaneously. The assessment includes scenarios with and without masonry infill, featuring different configurations. The analysis highlights the significant impact of masonry infills on the final vulnerability assessment, emphasising the necessity of considering them for an accurate representation of the behaviour of existing RC structures.

7.2 Case study

The analysed structure represents a typical Italian school building from the 1960s, designed in accordance with strategies commonly employed in Italy before the implementation of seismic regulations. The structure, characterised by the typical scheme of weak columns and strong beams,

presents notable irregularities both in plane and in elevation, making the nonlinear dynamic analysis necessary to accurately predict the nonlinear response of the structure.

The building consists of the first two floors with an equal area of 1239 m², while the last two floors have a smaller area of 660 m² (Figure 182). Regarding loads, the dead load on the floors is 4.6 kN/m², the live load is 3.0 kN/m², and the variable load due to snow on the top floor is 0.8 kN/m². The infills weight is equal to 15 kN/m^3, considered as linearly applied on the perimeter beams. Comprehensive on-site and laboratory tests were carried out on various elements, encompassing steel bar tension tests and compression tests on concrete specimens. The mechanical characteristics adopted for the subsequent analyses, as detailed in Table 53, appropriately take into account the achieved knowledge level, specifically the KL2 level (as defined by the Italian code - MIT, 2018, and Eurocode 8 - EN 1998-1-1, 2005; please refer to Chapter 2.3.5). Floor plans and reinforcement details of some columns and beams are depicted from Figure 175 to Figure 180. The bare reinforced concrete frame structure has already been analysed in previous research (Izzuddin et al., 2013; Masjuki, 2017).

Table 53 Concrete and steel material properties

Concrete compressive strength	f_c	18.7	MPa
Beam steel reinforcements yield strength	$f_{y,beam}$	382.5	MPa
Column steel reinforcements yield strength	$f_{y,column}$	284.0	MPa
Concrete Modulus of elasticity	E_c	26544	MPa
Steel Modulus of elasticity	E_s	210000	MPa
Steel strain hardening factor	μ	0.1	

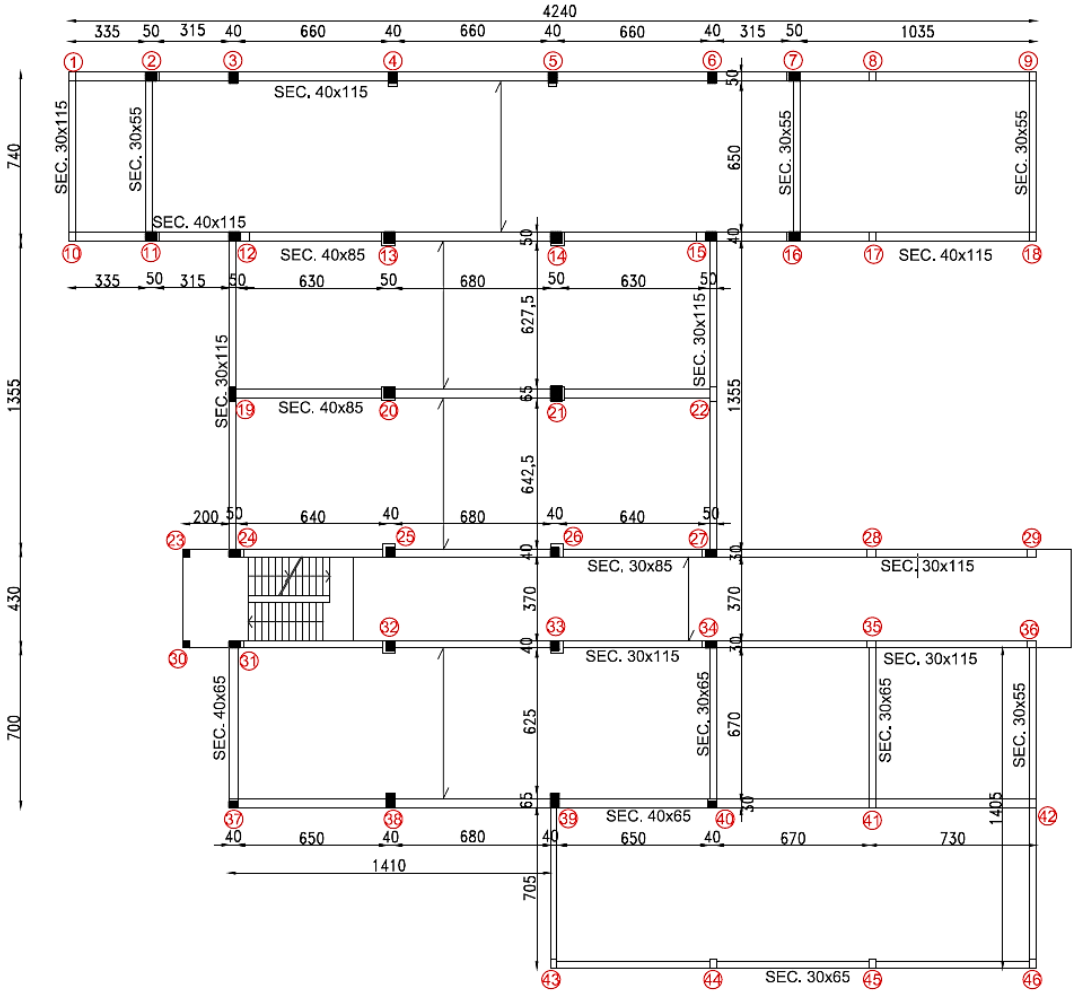

Figure 175 First and second floor plan

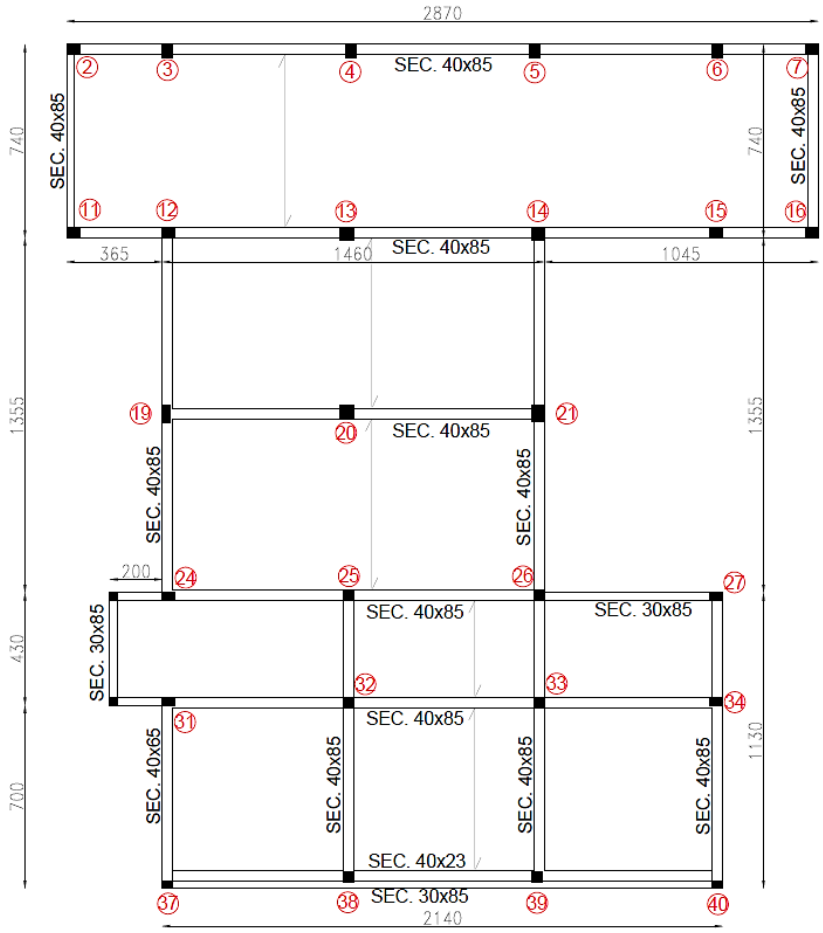

Figure 176 Third and fourth floor plan

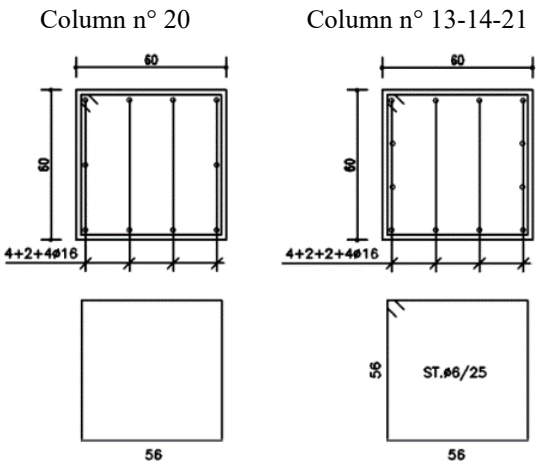

Figure 177 Reinforcements detailing on columns of the 1st and 2nd floors

First floor – Beam 19-20-21-22

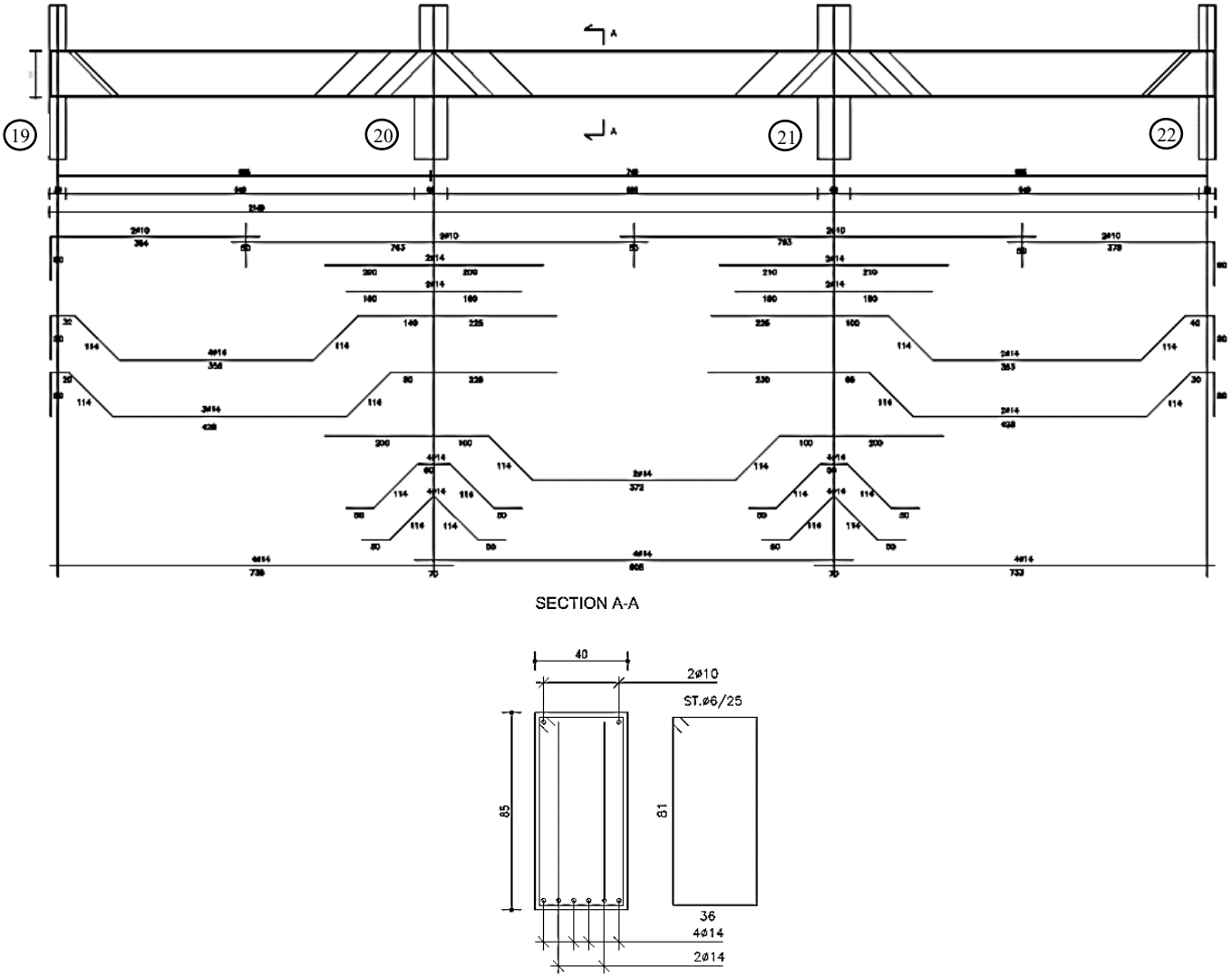

Figure 178 Reinforcements detailing on beams of the 1st and 2nd floors

Column n° 20 Column n° 13-14

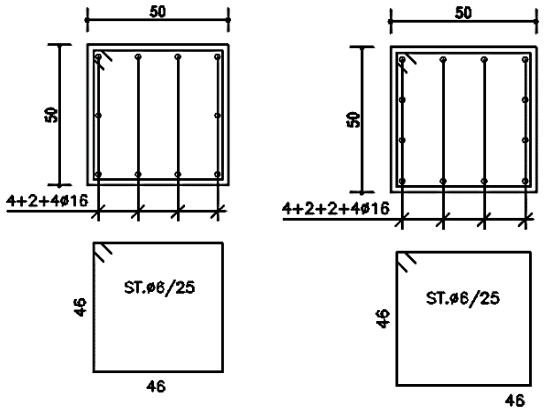

Figure 179 Reinforcements detailing on columns of the 3rd and 4th floors

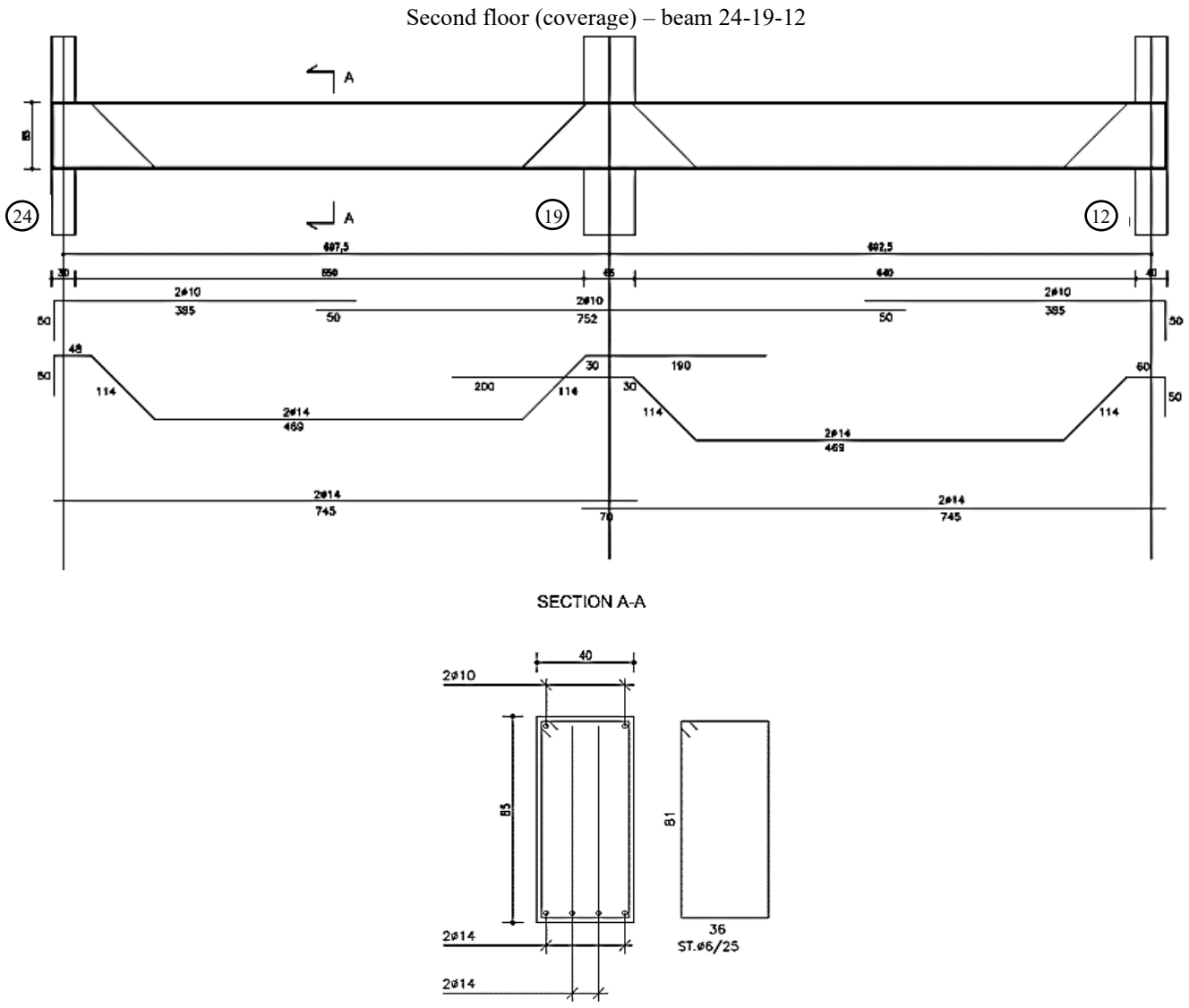

Figure 180 Reinforcements detailing on beams of the 3rd and 4th floors

7.3 Modelling of the structures

The modelling approach for the RC frame involves the use of 1D elastic-plastic frame elements proposed by Izzuddin and Elnashai (1993a, 1993b), already employed throughout the thesis and described in Chapter 4.3. Each RC member is modelled through different segments, to effectively capture the development and spread of plasticity along its various sections. Specifically, the columns are discretised into 6 elements, while the beams are divided into 10. The same beam elements are adopted for the modelling of stairs and landing platforms. Fully fixed restraints are considered at the bottom of the columns, where the seismic accelerations are applied. Figure 182 shows an axonometric view of the numerical model implemented in Adaptic.

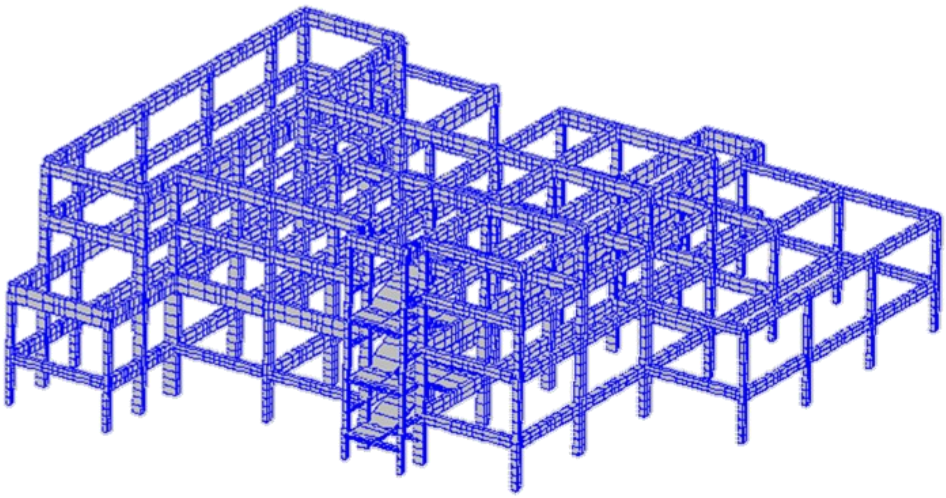

Figure 181 3D extruded view of the bare-frame model

Given the presence of holes within the floors, the modelling considers the actual deformability of the slabs in their plane. Specifically, the floor diaphragms are modelled using a system of elastic link elements, following the approach described by Yettram and Husain (1966). Each portion of the floor, assimilated as a solid slab with uniform thickness, is represented by a rectangular frame along the perimeter with an internal X-brace. The external perimetral elements are characterised by specific flexural stiffness ($EI_{y,f}$) and axial stiffness (EA_f), while X-brace elements are trusses defined through a certain axial stiffness (EA_d). These characteristics are evaluated through equations (58), (59) and (60):

$$EI_{y,f} = \frac{E_c\, h}{60} l_x^2 l_z \tag{58}$$

$$EA_f = \frac{E_c\, h\, l_z}{2}\left[1 - 0.2\left(\frac{l_x}{l_z}\right)^2\right] \tag{59}$$

$$EA_d = \frac{E_c\, h}{10}\left(\frac{l_x^2 + l_z^2}{l_x l_z}\right)^{3/2} \tag{60}$$

where E_c represents the concrete elastic modulus of the floor, h is the thickness of the equivalent solid slab (assumed equal to the concrete slab topping), and l_x and l_z denote the dimensions in the plane of the floor portion. Figure 182 depicts the schematic plans of the floors, indicating the locations of the floor link systems and column numbering adopted for the subsequent analysis. In Figure 183, an axonometric view of the model is presented, illustrating the representation of the slabs using link elements.

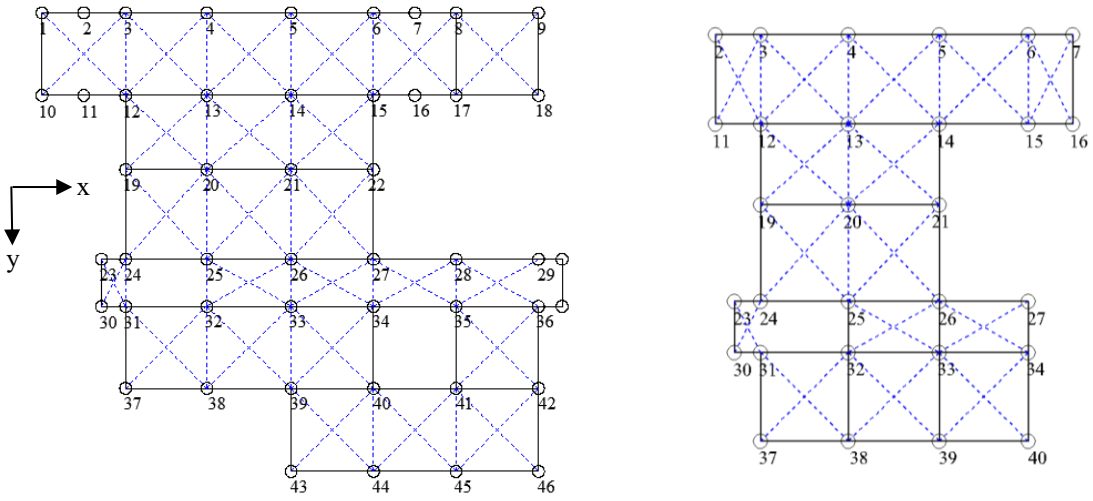

Figure 182 Schematic representation of (a) the first two floors and (b) the last two floors, indicating the column numbering adopted for modelling and verifications.

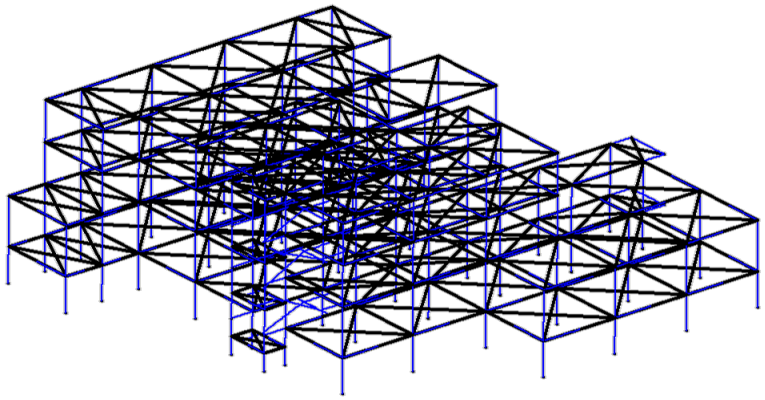

Figure 183 3D view of the bare-frame model with highlighted floor link-system

Two different configurations of infills are considered: the real infill configurations, characterised by an irregular distribution of infills, including empty zones (mainly on the ground floor) and various types of openings, and the limiting hypothesis in which the frame is fully infilled. The two configurations are visualised in Figure 184, represented through post-processing MATLAB scripts. The macroelements modelling is automatically performed through the implementation of pre-processing MATLAB scripts. The material properties for the masonry macro-elements, representing typical hollow clay brick masonry panels, are provided in Table 54, Table 55 and Table 56, considering a thickness of 120 mm.

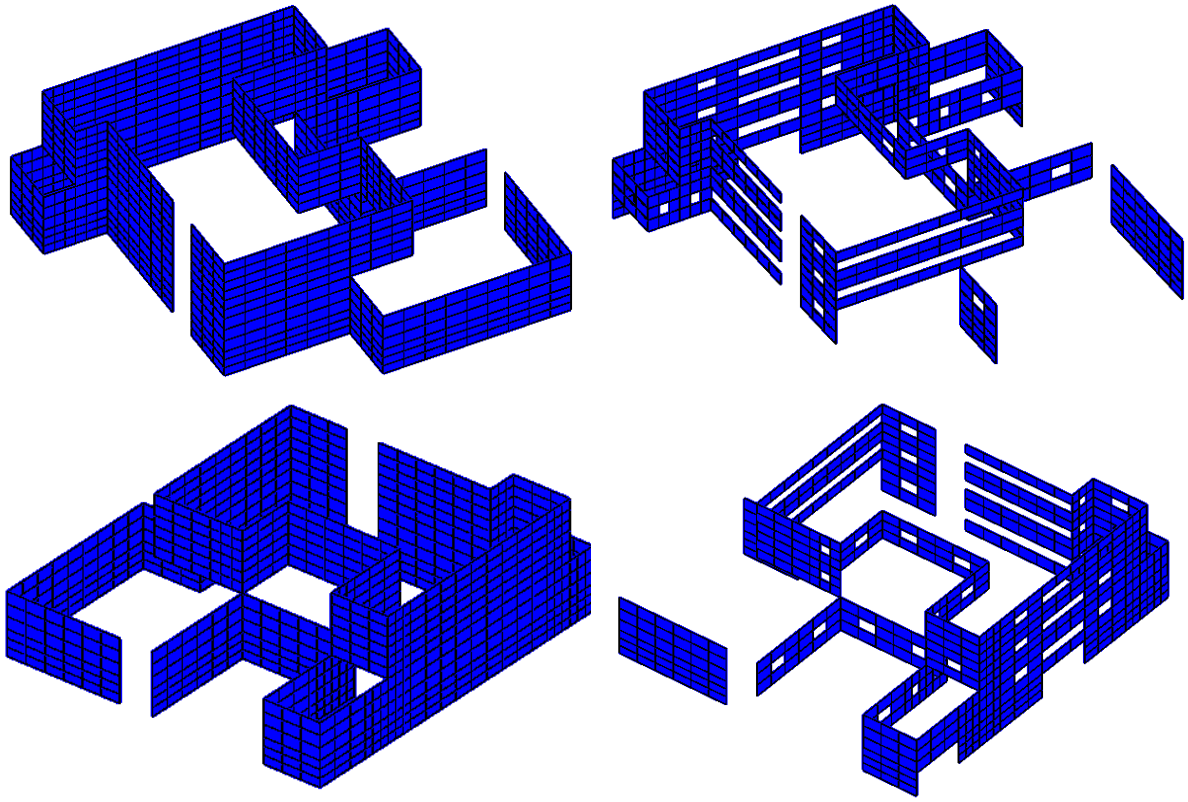

(a) (b)

Figure 184 3D views of masonry macroelements in (a) fully and (b) partially infilled frame models

Table 54 Internal infill interfaces material parameters

		E_n [MPa]	f_t [MPa]	c [MPa]	tanϕ [-]	f_c [MPa]	$G_{f,I}$ [N/mm]	$G_{f,II}$ [N/mm]	$G_{f,c}$ [N/mm]
Horizontal	Int-h	1400	0.1	0.14	0.7	3	0.05	0.10	16.3
Vertical	Int-v	840	1.5	1.5	1	1.5	0.05	0.10	15.2

Table 55 External frame-infill interfaces material parameters

		E_n [MPa]	f_t [MPa]	c [MPa]	tanϕ [-]	$G_{f,I}$ [N/mm]	$G_{f,II}$ [N/mm]
Horizontal	Ext-h	1400	0.01	0.014	0.35	0.05	0.10
Vertical	Ext-v	840	0.01	0.014	0.35	0.05	0.10

Table 56. Diagonal springs characterisation

Identification	G_e [MPa]	f_t [MPa]	δ_u^* [mm]	K_{p1}/K_{el}	F_y/F_{max}	C_F	α	β
Diag	560	0.2	20	0.1	0.7	0.4	0.8	0.06

7.3.1 Partitioning approach

The computational demands required for performing nonlinear dynamic analysis can become significant due to the size of the model. To address the potentially high computational cost associated

with a monolithic model, the partitioned modelling approach introduced by Jokhio (2012), already employed throughout this thesis, is adopted herein. The model is divided into four partitions (see Figure 185 and Figure 186, for bare frame and infilled frames, respectively), each corresponding to a single storey. The parent element is defined by the nodes at the ends of the columns situated between two consecutive storeys, enabling the communication between them. Additionally, in the presence of infills, nodes on beams that are common to two consecutive storeys must also be included.

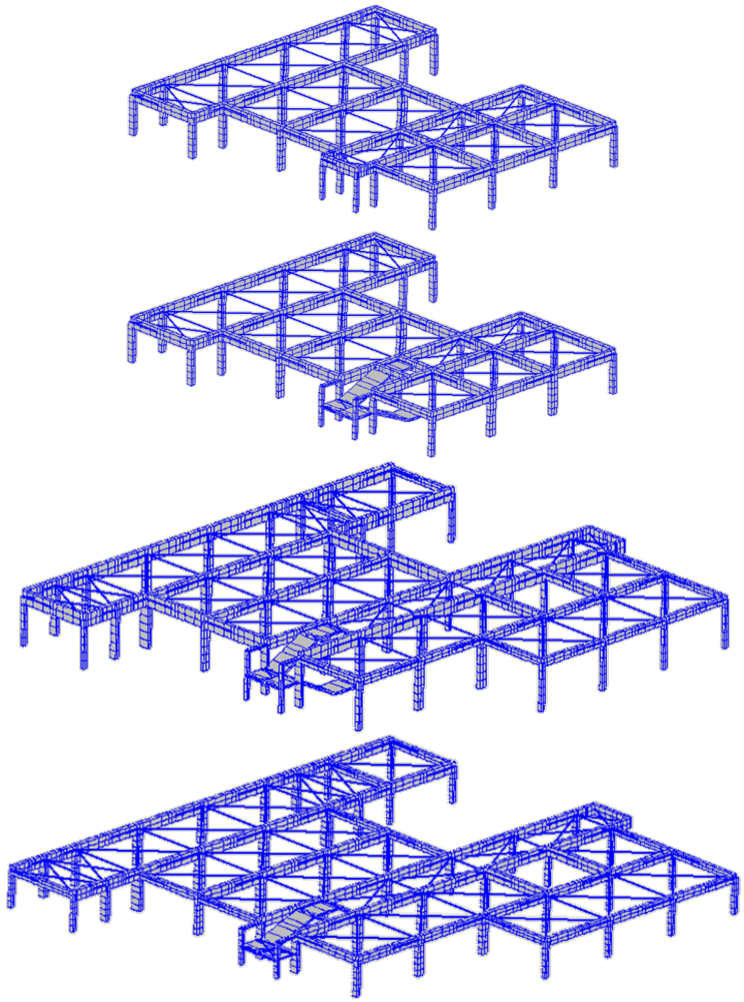

Figure 185 Partitioning strategy on the bare frame

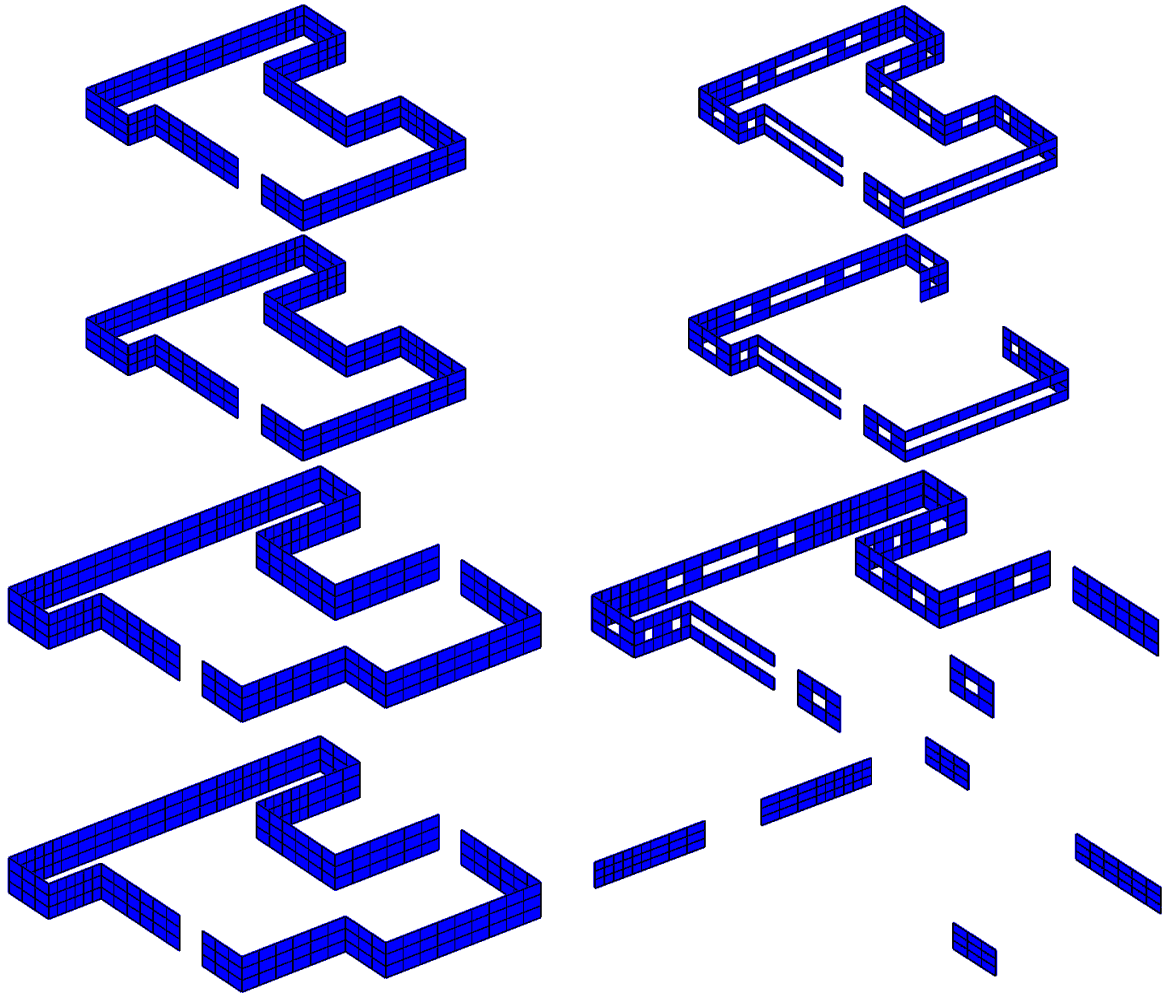

(a) (b)

Figure 186 Partitioning strategy on the case study building: masonry macroelements partitions on (a) fully and (b) partially infilled frame

7.4 Seismic assessment framework

Nonlinear dynamic analyses are conducted on the structure employing natural accelerograms selected to be spectrum-compatible with the design spectrum. These analyses involve calculating the seismic response of the structure by integrating the equations of motion, enabling the verification of potential ductile and brittle mechanisms. These advanced numerical analysis methods represent a fundamental tool for accurately evaluating the actual seismic capacity of complex structures. Their effectiveness is particularly evident when analysing existing structures with irregularities in plan and elevation. In such cases, the use of non-linear static analyses may lead to unrealistic results, discouraged from standard codes, while the use of linear dynamic analyses (response spectrum modal analysis) with a limited structural factor (for existing structures) may provide excessively conservative results.

In the current study, 7 pairs of ground motion acceleration histories are applied to the structures, in the horizontal X and Y directions. The analyses comprise two phases. Initially, a static analysis is conducted where vertical loads are applied to the structures, considering the seismic event combination factors recommended by the Italian Code (MIT, 2018). This involves the application of self-weight of both structural and non-structural components and 60% of the variable loads on the floors. Subsequently, the nonlinear dynamic analysis is executed by applying accelerograms to the base of the columns. Masses are applied as linearly distributed on columns and beams, while damping is determined following the Rayleigh formulation (Chopra, 2011), wherein the damping matrix is evaluated as a linear combination of the mass and stiffness matrices. A damping coefficient of 5% is applied for the natural frequency corresponding to the fundamental period of the structures.

7.4.1 Accelerograms

In the dynamic simulations of structural systems under earthquake loading, the selection of realistic ground accelerations is crucial. Generally, three types of acceleration time-series can be employed: artificial, synthetic, or natural accelerograms. Artificial accelerograms are created through numerical procedures, utilising power spectral density functions based on smoothed spectra or derived sinusoidal signals. Synthetic accelerograms are generated from mathematical models that consider the actual characteristics of seismological sources and soil properties. Natural accelerograms are real records obtained from data collected during previous seismic events. In the present context, natural accelerograms are adopted for the assessment.

According to Eurocode 8 (EN 1998-3, 2004) the consistency of the selected accelerograms with the elastic spectrum must be verified based on the average spectral acceleration as a function of vibration period. The average acceleration should not deviate by more than 10% compared to the elastic spectrum (determined with a damping coefficient of 5%) at any point within the larger of the two intervals for ultimate limit state checks: 0.15s ÷ 2.0s and 0.15s ÷ 2T (where T is the fundamental vibration period in the elastic condition). As for serviceability limit state checks, the deviation should be evaluated within the interval 0.15s ÷ 1.5 T. A minimum of 3 time histories must be adopted, and in this scenario, the effects on the structure are evaluated considering the most unfavourable demands. Alternatively, if at least 7 different time histories are employed, the effects on the structure are represented by the average of the seismic demands.

In the present context, a set of 7 pairs of natural accelerograms are determined, generated by using REXEL (Iervolino et al., 2009), a computer-assisted program designed for code-based seismic

structural analysis record selection. The characteristics for determining the elastic response spectrum are detailed in Table 57, while the primary features of the natural records are outlined in Table 58. Figure 187 visually illustrates the compatibility between the elastic response spectrum and the natural elastic spectra corresponding to the selected accelerograms. The combinations of the time-history ground motions are graphically displayed in Figure 188 for both the x and y directions.

Table 57 Elastic response spectrum parameters

Lon [°]	Lat [°]	Site class	Topographic category	Nominal life	Use coefficient	Limit state
13.394	42.366	C	T1	50 years	II	SLC

(*) corresponding to the Near Collapse limit state of Eurocode 8

Table 58 Main characteristic of the seven adopted two-component records

Identification	**Station ID**	**Earthquake Name**	**Date**	**M_w**	**Fault Mechanism**	**Epicentral Distance [km]**	**PGA_X [m/s^2]**	**PGA_Y [m/s^2]**
170	ST46	Basso Tirreno	15/04/1978	6.0	oblique	18	0.719	1.585
199	ST67	Montenegro	15/04/1979	6.9	thrust	16	3.680	3.557
292	ST98	Campano Lucano	23/11/1980	6.9	normal	25	0.5878	0.5878
333	ST121	Alkion	24/02/1981	6.6	normal	20	2.257	3.036
600	ST223	Umbria Marche	26/09/1997	6.0	normal	22	1.685	1.041
6331	ST2486	South Iceland (aftershock)	21/06/2000	6.4	strike-slip	22	0.513	0.386
6335	ST2557	South Iceland (aftershock)	21/06/2000	6.4	strike-slip	15	1.248	1.132

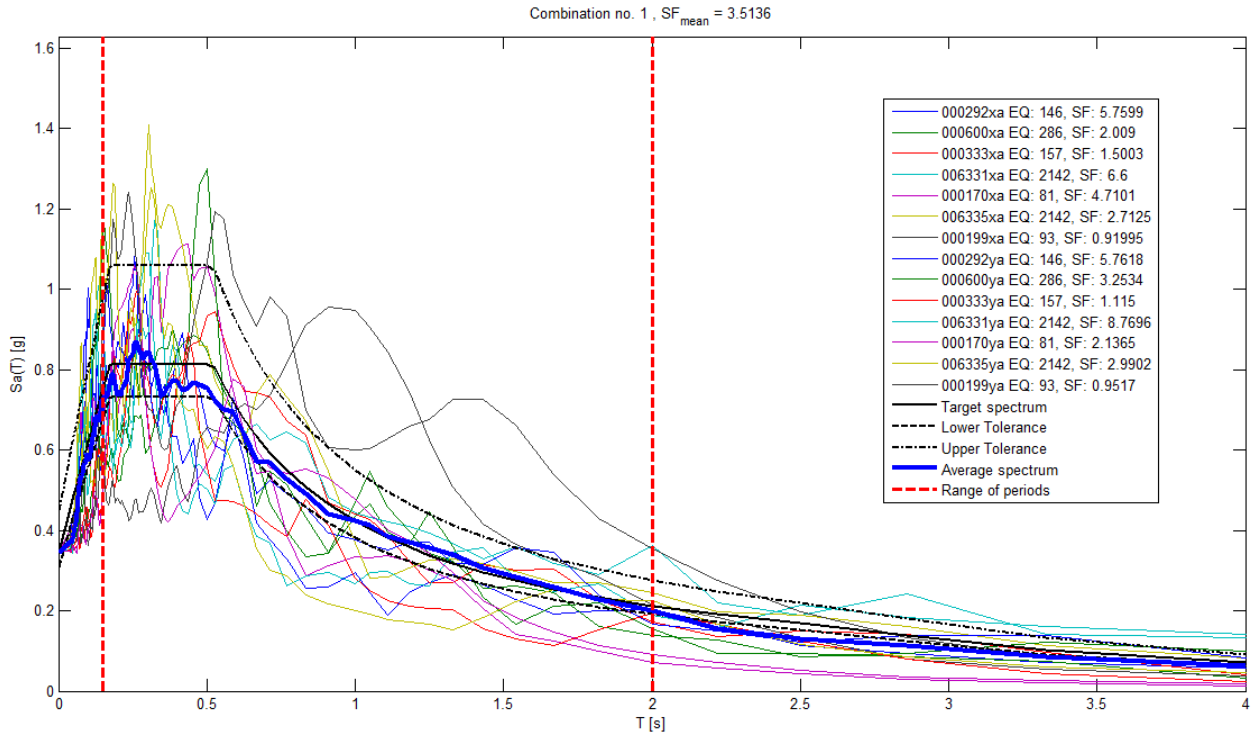

Figure 187 Evaluation of the spectrum compatibility

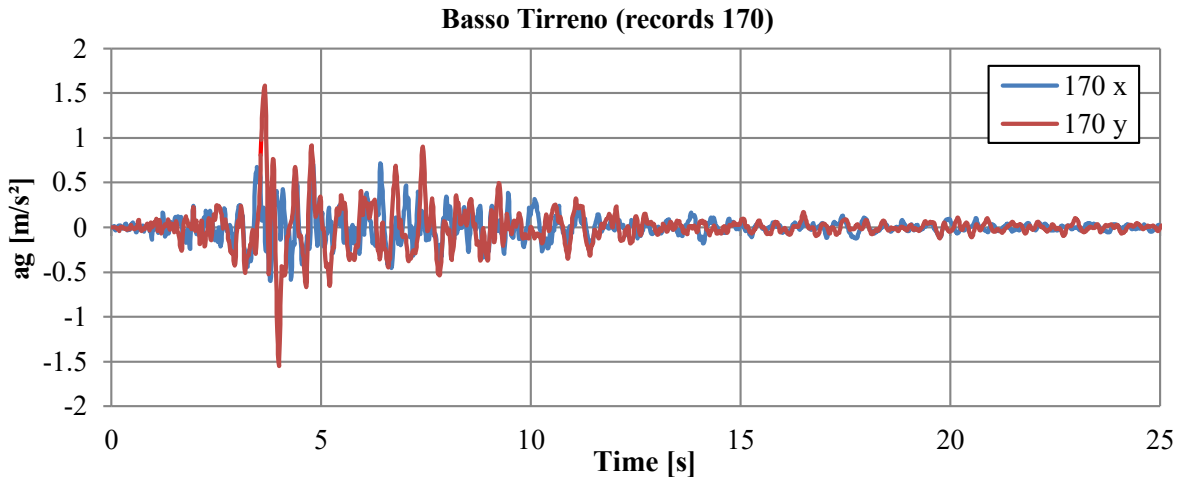

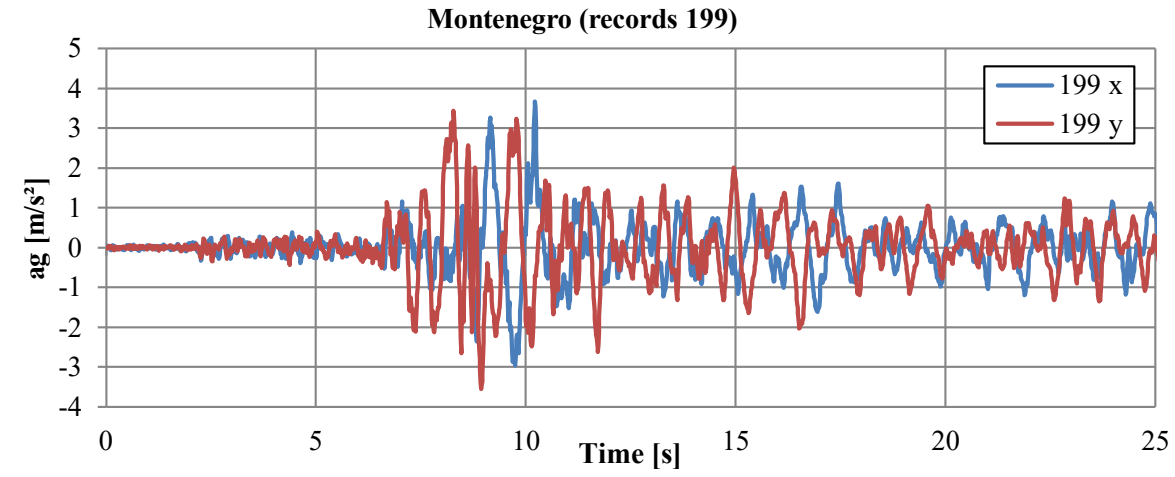
Montenegro (records 199)
ag [m/s²]
Time [s]
199 x
199 y

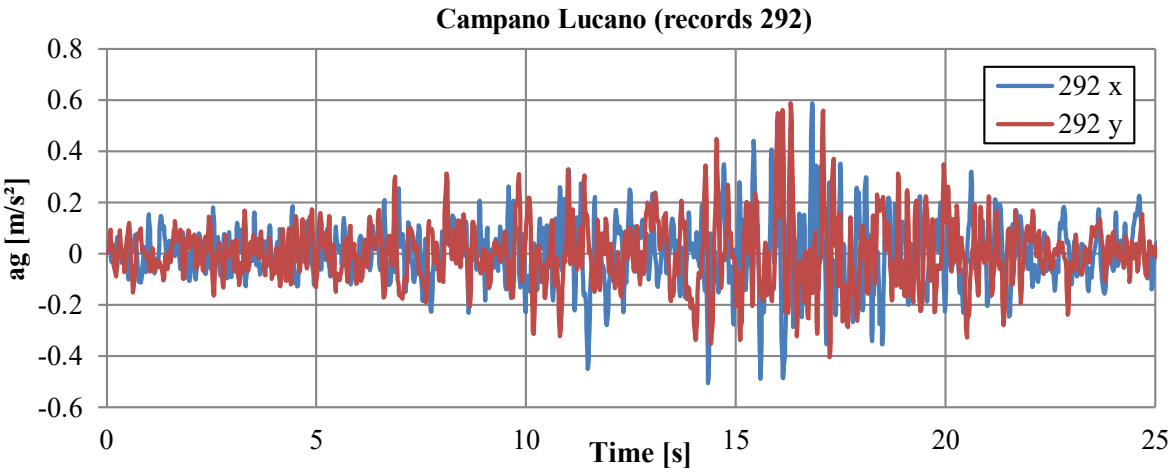
Campano Lucano (records 292)
ag [m/s²]
Time [s]
292 x
292 y

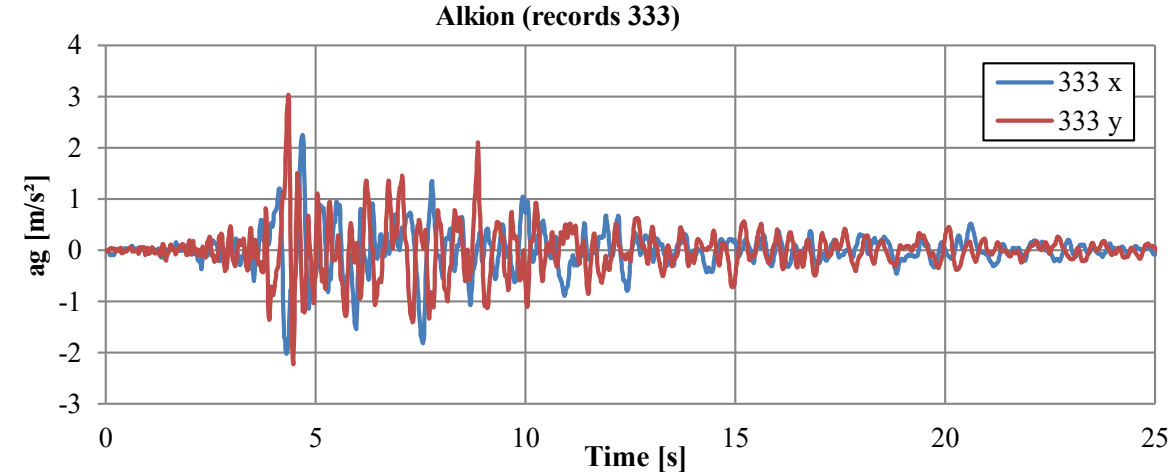
Alkion (records 333)
ag [m/s²]
Time [s]
333 x
333 y

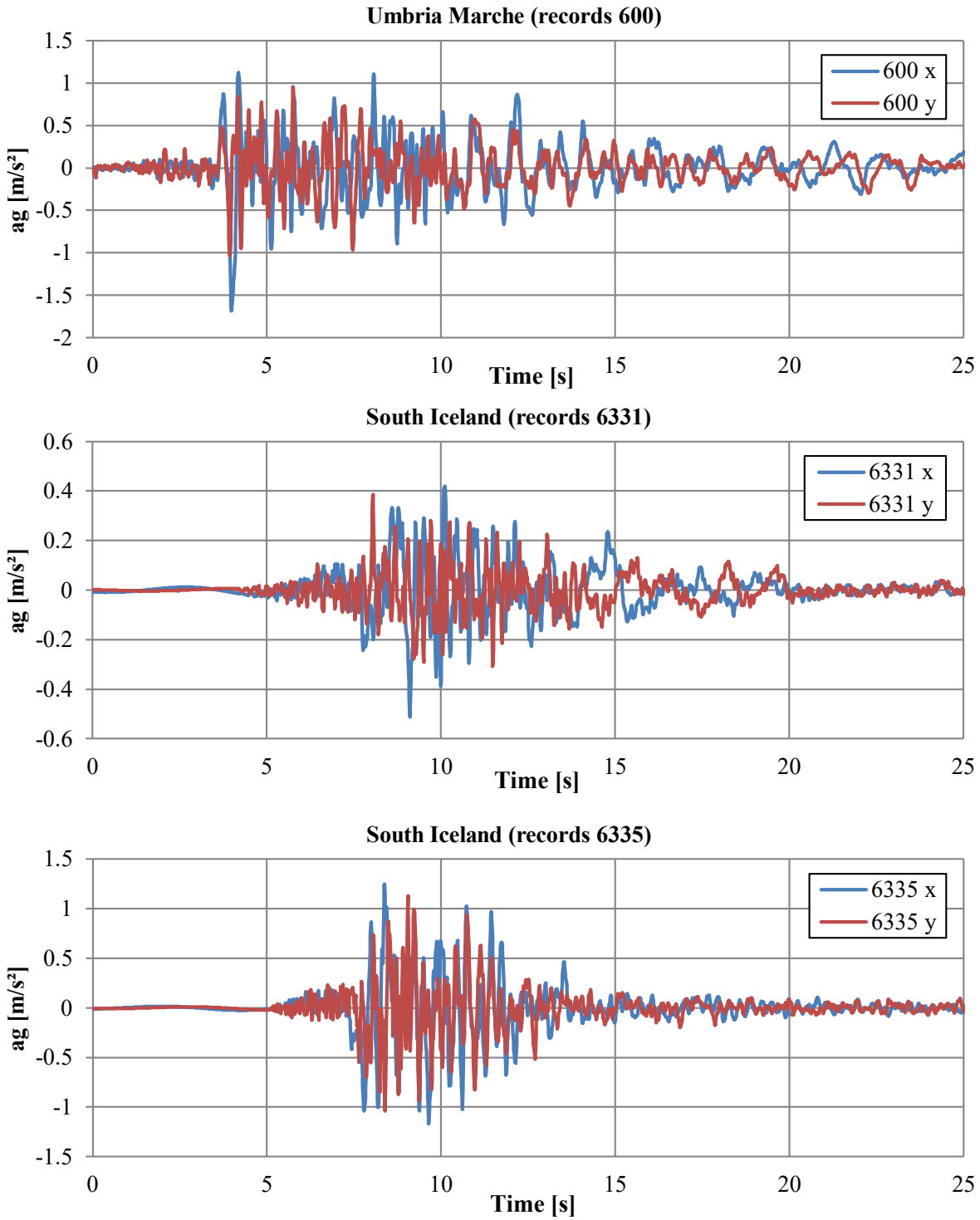

Figure 188 Pairs of selected accelerograms

7.4.2 Verification of ductile mechanisms

In accordance with current codes of practice (EN 1998-3, 2004; MIT, 2018), the seismic assessment involves verifying potential local failures at the members level. This is achieved by comparing specific

demands with capacity values, specifically checking for the occurrence of eventual ductile and brittle mechanisms.

Local ductile failure occurs when the ultimate rotation capacity is exceeded. This is specifically evaluated by considering the chord rotation angle, which is defined, according to Eurocode 8 (EN 1998-3, 2004), as the angle between the tangent to the axis at the yielding end and the chord connecting that end with the end of the contraflexure. Figure 189 provides a visual representation of the chord rotation definition for both beams and columns.

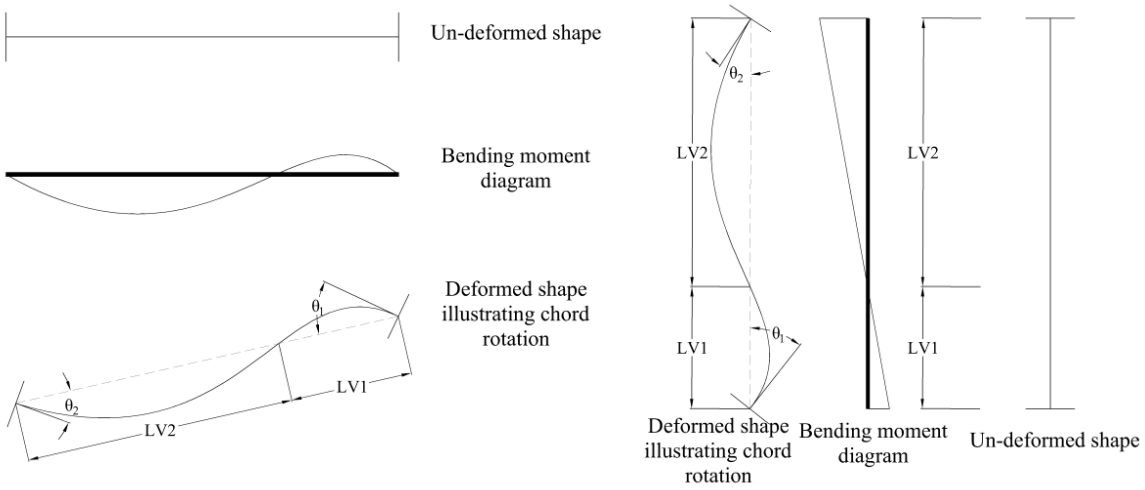

Figure 189 Chord rotation for (a) beams and (b) columns (taken from (Masjuki, 2017)

The chord rotation demands are calculated for the two extremities of each member at the end of each time step of the analysis. This calculation specifically includes contributions assessed considering both the local reference system (x, y, z) of the member (represented in Figure 190) and the global reference system (X, Y, Z). In particular, it considers the end-element rotations in the local system, the relative nodal displacements of the nodes of the end-element in the global system, and the relative nodal displacements of the extreme nodes of the entire element in the global system. Considering the distinct relationships between the two systems for columns, beams in the X direction, and beams in the Y direction, as illustrated in Figure 191, the chord rotations at the end nodes I and J of each element are evaluated using the relationships from (61) to (72).

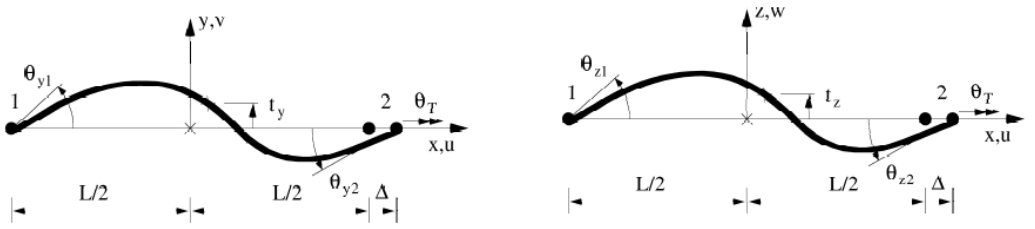

Figure 190 Degree of freedom of the beam-column elements (Izzuddin and Lloyd Smith, 2000)

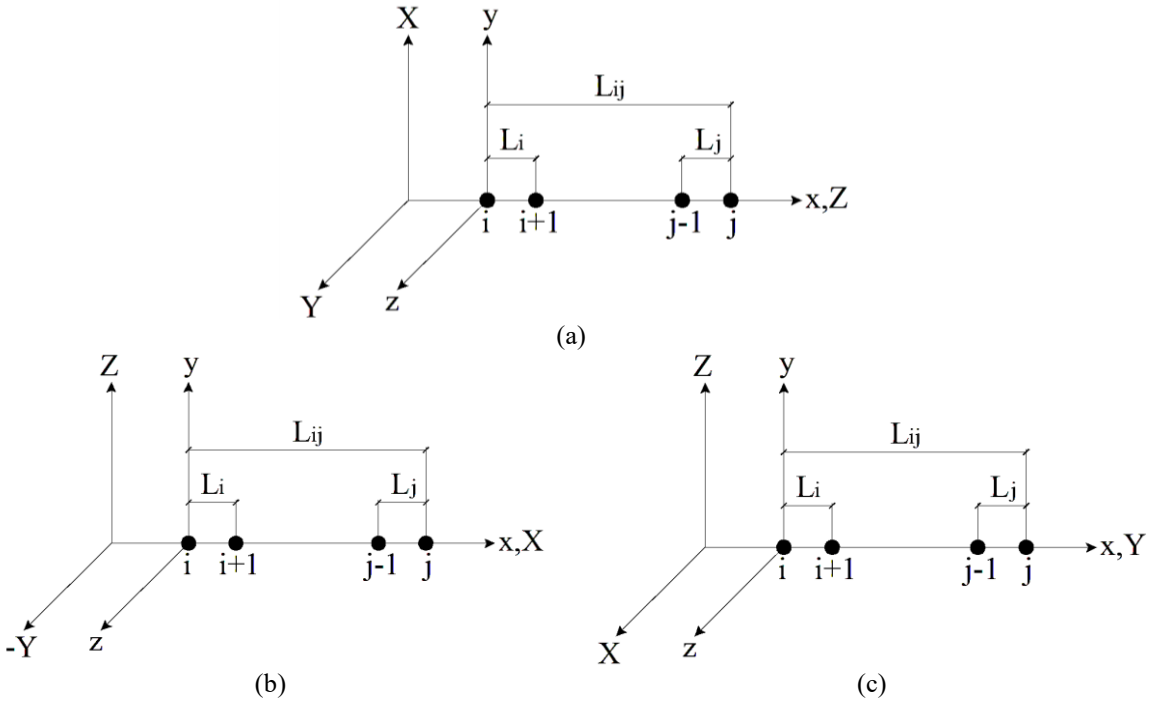

Figure 191 Orientation of (a) columns, (b) beams in X direction and (c) beams in Y direction

Columns chord rotations:

$$\widetilde{\theta_{y,i}} = \left(\frac{U_{i+1} - U_i}{L_i}\right) + \theta_{y,i} - \left(\frac{U_j - U_i}{L_{ij}}\right) \quad (61)$$

$$\widetilde{\theta_{z,i}} = \left(\frac{V_{i+1} - V_i}{L_i}\right) + \theta_{z,i} - \left(\frac{V_j - V_i}{L_{ij}}\right) \quad (62)$$

$$\widetilde{\theta_{y,j}} = \left(\frac{U_j - U_{j-1}}{L_j}\right) + \theta_{y,j} - \left(\frac{U_j - U_i}{L_{ij}}\right) \quad (63)$$

$$\widetilde{\theta_{z,j}} = \left(\frac{V_j - V_{j-1}}{L_j}\right) + \theta_{z,j} - \left(\frac{V_j - V_i}{L_{ij}}\right) \quad (64)$$

Beams along X direction chord rotations:

$$\widetilde{\theta_{y,i}} = \left(\frac{W_{i+1} - W_i}{L_i}\right) + \theta_{y,i} - \left(\frac{W_j - W_i}{L_{ij}}\right) \quad (65)$$

$$\widetilde{\theta_{z,i}} = \left(\frac{V_{i+1} - V_i}{L_i}\right) + \theta_{z,i} + \left(\frac{V_j - V_i}{L_{ij}}\right) \quad (66)$$

$$\widetilde{\theta_{y,J}} = \left(\frac{W_j - W_{j-1}}{L_j}\right) + \theta_{y,j} - \left(\frac{W_j - W_i}{L_{ij}}\right) \quad (67)$$

$$\widetilde{\theta_{z,J}} = \left(\frac{V_j - V_{j-1}}{L_j}\right) + \theta_{z,j} + \left(\frac{V_j - V_i}{L_{ij}}\right) \quad (68)$$

Beams along Y direction chord rotations:

$$\widetilde{\theta_{y,\iota}} = \left(\frac{W_{i+1} - W_i}{L_i}\right) + \theta_{y,i} - \left(\frac{W_j - W_i}{L_{ij}}\right) \quad (69)$$

$$\widetilde{\theta_{z,\iota}} = \left(\frac{\mathrm{U}_{i+1} - \mathrm{U}_i}{L_i}\right) + \theta_{z,i} - \left(\frac{\mathrm{U}_j - \mathrm{U}_i}{L_{ij}}\right) \quad (70)$$

$$\widetilde{\theta_{y,J}} = \left(\frac{W_j - W_{j-1}}{L_j}\right) + \theta_{y,j} - \left(\frac{W_j - W_i}{L_{ij}}\right) \quad (71)$$

$$\widetilde{\theta_{z,J}} = \left(\frac{\mathrm{U}_j - \mathrm{U}_{j-1}}{L_j}\right) + \theta_{z,j} - \left(\frac{\mathrm{U}_j - \mathrm{U}_i}{L_{ij}}\right) \quad (72)$$

where θ represent the end-element rotations in the local system, while U, V and W are the nodal displacements along the global reference axis X, Y and Z.

As regards the capacity, the ultimate capacity rotation θ_u for each beam and column in the model is calculated using the formula (73) specified in Eurocode 8 (EN 1998-3, 2004):

$$\theta_u = \frac{1}{\gamma_{el}} 0.016\ (0.3^{\nu}) \left[\frac{max(0.01; \omega')}{max(0.01; \omega)} f_c\right]^{0.225} \left(\frac{L_v}{h}\right)^{0.35} 25^{\left(\alpha\, \rho_{sx} \frac{f_{yw}}{f_c}\right)} (1.25^{100\rho_d}) \quad (73)$$

where:

γ_{el} is equal to 1.5 for primary seismic elements and 1.0 for secondary seismic elements;

L_v is the shear span;

h is the section height;

$\nu = N/(A_c f_c)$ is the average normal compression stress, with f_c being the concrete compressive strength;

$\omega = A_s f_y/(A_c f_c)$ and $\omega' = A_s' f_y/(A_c f_c)$ are the mechanical percentages of longitudinal reinforcement in tension and compression respectively, with f_y being the steel reinforcement yield strength;

f_{yw} is the stirrup yield strength;

$\rho_{sx} = A_{sx}/(b_w s)$ is the percentage of transversal reinforcement, with *s* being the stirrup spacing and b_w the minimum section width;

ρ_d is the steel ratio of diagonal reinforcements, in each diagonal direction;

α confinement effectiveness factor that may be taken as equals to:

$$\alpha = \left(1 - \frac{s}{2b_0}\right)\left(1 - \frac{s}{2h_0}\right)\left(1 - \frac{\sum b_i^2}{6\, h_0 b_0}\right) \tag{74}$$

where b_0 and h_0 are the dimensions of the confined core, b_i are the distances between longitudinal bars laterally restrained by tie rods or stirrups.

Ultimately, the final verification is conducted by concurrently considering demands and capacities corresponding to the two directions within a circular interaction domain (according to AIJ, 1994). The final ratio ρ_c for each member is determined as the maximum between the two ends, as reported in (75).

$$\rho_c = max\left[\left(\frac{\widetilde{\theta_{y,i}}}{\theta_{u,y,i}}\right)^2 + \left(\frac{\widetilde{\theta_{z,i}}}{\theta_{u,z,i}}\right)^2 ; \left(\frac{\widetilde{\theta_{y,j}}}{\theta_{u,y,j}}\right)^2 + \left(\frac{\widetilde{\theta_{z,j}}}{\theta_{u,z,j}}\right)^2\right] \tag{75}$$

7.4.3 Verification of brittle mechanisms

According to Eurocode 8 (EN 1998-3, 2004), typical brittle failure in RC frames can occur either at the member level or at the beam-column joints. In the current context, the verification focuses only on shear failure in columns and beams. The shear force demand is directly obtained from the simulation at the end of each time step, while the shear capacity is assessed using the expressions provided by Eurocode 2 (BS EN, 2004, p. 2). The shear strength of elements with transversal reinforcement is evaluated as the minimum between a shear-tension value, calculated using relation (64) associated with the failure of transversal reinforcement, and a shear-compression value, determined using (65) related to the failure of the concrete core. The ultimate shear strength is then determined as the minimum of these two values.

$$V_{c,s} = 0.9\, d\, \frac{A_{sx}}{s}\, f_{yw}(\cot\alpha + \cot\theta)\sin\alpha \tag{76}$$

$$V_{c,c} = 0.9\, d\, b_w\, \alpha_c\, f'_{cd}\, (\cot\alpha + \cot\theta)/(1 + cot^2\theta) \tag{77}$$

$$V_c = min(V_{c,s}; V_{c,c}) \tag{78}$$

where, in addition to parameters introduced with relation (73):

d is the effective section height;

b_w is the minimum section width;

s is the spacing between two consecutive transverse reinforcements;

$\sigma_{cp} = N/f_c \leq 0.2 f_c$ is the average compressione stress on the section;

α is the angle of inclination of the transverse reinforcement with respect to the axis of the beam;

β is the angle of inclination of the compressed strut (taken as 45°);

$f_c^{'}$ is the reduced compressive strength of the core concrete (taken as 0.5 f_c);

α_c is a augmentation factor equal to:

- 1 for not compressed elements
- $1 + \sigma_{cp}/f_c$ if $0 \leq \sigma_{cp} \leq 0.25 f_c$
- 1.25 if $0.25 f_c \leq \sigma_{cp} \leq 0.5 f_c$
- $2.5\left(1 - \sigma_{cp}/f_c\right)$ if $0.5 f_c \leq \sigma_{cp} \leq f_c$

Given the presence of bent rebars, these are taken into account by considering equivalent stirrups characterised by the spacing s, calculated through equations (67), (68) e (69):

$$S_{st} = \frac{\pi \frac{\varphi_{st}^2}{4} n_{b,st} f_{yw}}{i_{st}} \tag{79}$$

$$S_{br} = \frac{\pi \frac{\varphi_{br}^2}{4} n_{b,br} f_{yw}}{i_{br}} \tag{80}$$

$$s = \frac{\pi \frac{\varphi_{st}^2}{4} n_{b,st} f_{yw}}{S_{st} + S_{br}} \tag{81}$$

where:

S_{st} is the slip force per unit length due to stirrups;

S_{br} is the slip force per unit length due to bent rebars;

i_{st}, φ_{st}, $n_{b,st}$ are the spacing, diameter, and arms of the stirrups;

i_{br}, φ_{br}, $n_{b,br}$ are the spacing, diameter, and arms of the bent rebars;

The final verification is determined by considering demands and capacities in the two bending planes:

$$\rho_V = \left(\frac{V_{y,d}}{V_{y,c}}\right)^2 + \left(\frac{V_{z,d}}{V_{z,c}}\right)^2 \tag{82}$$

7.5 Seismic vulnerability and impact of the infills presence

This section examines the results of the analyses conducted to assess the seismic responses of both bare and infilled frame structures. Initially, the focus is on the structural behaviour in terms of modal response, aiming to highlight variations in vibration period and mode characteristics resulting from the inclusion of infills within the frame. Subsequently, dynamic nonlinear analyses are conducted, considering the set of ground accelerations introduced in Section 7.4.1. The seismic vulnerabilities of the structures are discussed and evaluated in terms of shear-displacement cycles, global failure mechanisms, and verification of brittle and ductile behaviours in beams and columns.

7.5.1 Modal Analysis

Modal analysis is performed on the three structures (bare frame, real infilled frame and full infilled frame). Periods and participating masses of the first three modes are presented in Table 59, and the corresponding deformed shapes are illustrated in Figure 192. The outcomes reveal the notable influence of the infills presence. In particular, the fundamental period of the real infilled frame is approximately 30% of that observed in the bare frame and results closer to that of the full infilled frame case. Moreover, the introduction of infills induces a shift in the characteristics of the vibration modes. Indeed, while the fundamental period of the bare frame is essentially towards Y direction, the stiffening effects induced by infills in this direction result in the first period of the infilled frames being along the X direction. Additionally, the bare frame exhibits rotational components within the 2nd and 3rd periods, with a significant participating mass in the X direction. In contrast, the infilled frame is characterised by the majority of translational mass in both the X and Y directions within the first two periods, which are purely translational, while the third period is purely rotational. Overall, the presence of infills regularises the modal response of the structures, even considering the real irregular distribution of infills. However, the reduction in periods may lead to higher seismic actions.

Table 59 Modal analysis results

Mode	Period [s]	Participating mass [%]	
		X	Y
Bare frame			
1	0.869	0.0	75.5
2	0.585	33.9	0.6
3	0.499	41.7	0.4
Real Infilled frame			
1	0.263	86.8	0.0
2	0.233	0.1	85.4
3	0.129	0.0	0.9
Full Infilled frame			
1	0.199	82.7	0.1
2	0.176	0.1	80.0
3	0.110	0.0	0.3

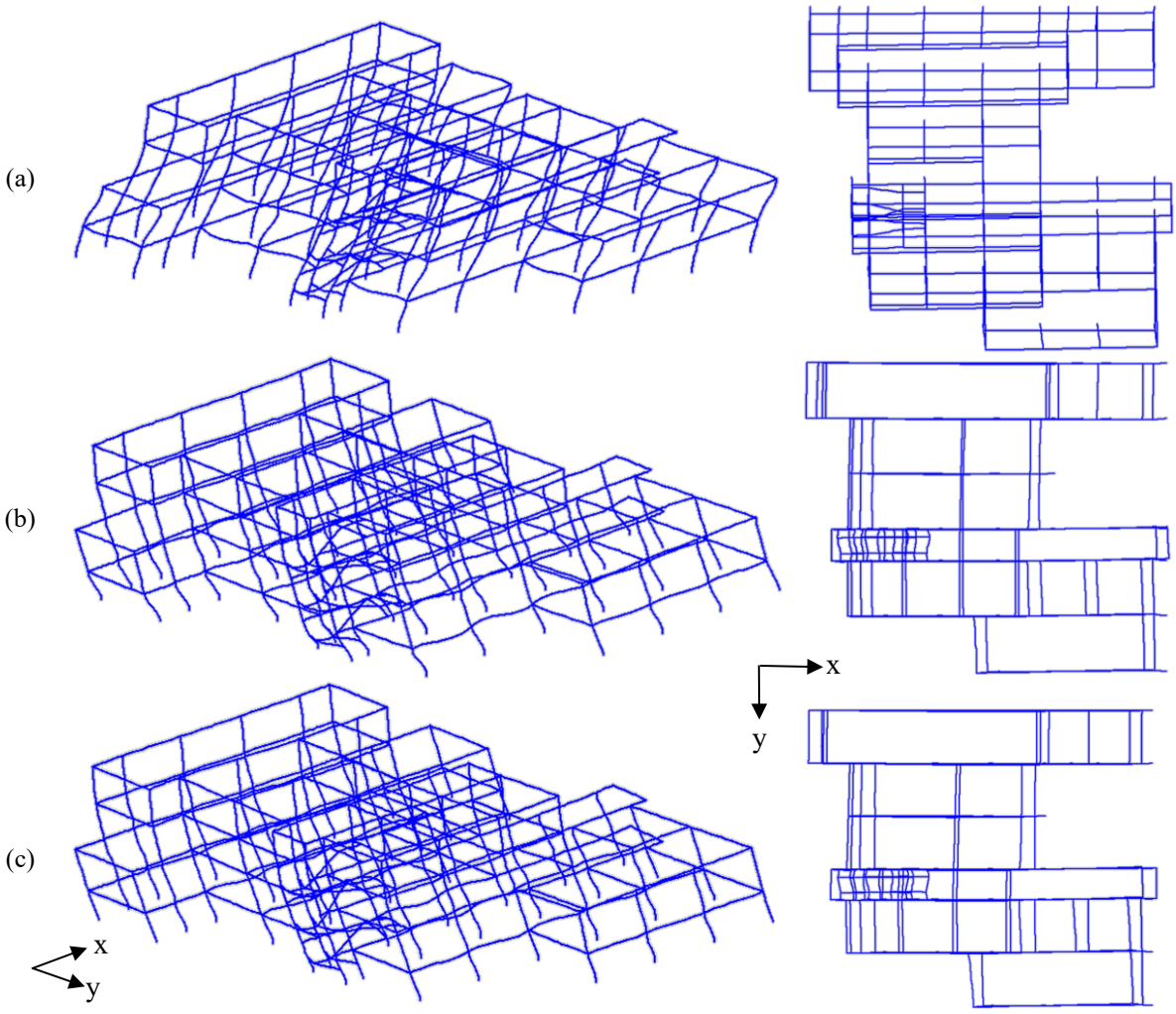

Figure 192 Deformed shapes corresponding to fundamental vibration modes: (a) bare frame; (b) real infilled frame; (c) full infilled frame

7.5.2 Nonlinear dynamic analyses

Nonlinear dynamic analyses are firstly performed on all the three structures subjecting them to the Montenegro Earthquake (records 199, Figure 188). This earthquake is represented by the records with the highest Peak Ground Acceleration (PGA) in both directions, among the accelerograms provided in section 7.4.1.

As regards the bare frame, the outcomes highlight a poor structural response, characterised by low lateral strength and stiffness, entering the plastic phase right from the beginning of the analysis. Figure 193 presents the cycles of base shear versus relative horizontal displacement (calculated as the difference between the displacement in a control node at the centre of the top floor and the

corresponding one at the base) in both the X and Y directions. Additionally, Figure 194 provides the deformed shapes of the structure at maximum displacements in the two directions (equal to 203 mm and 385 mm in X and Y, respectively), revealing notable deformability especially on the third floor. The decoupled motion of the last two floors from the first two results in the highly irregular shear-displacement cycles.

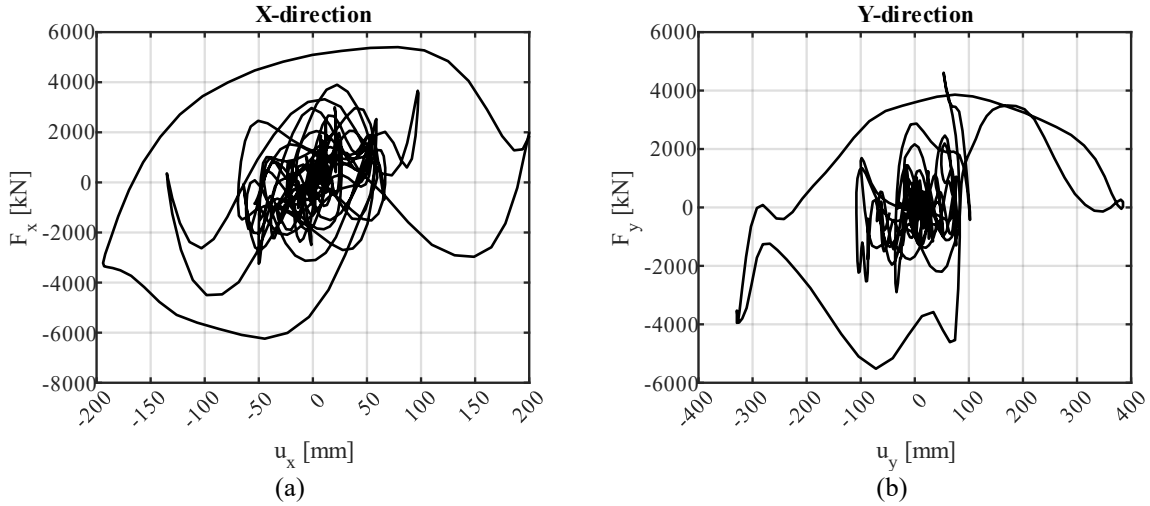

Figure 193 Base shear vs. horizontal relative displacement cycles for bare frame in (a) X-direction and (b) Y-direction, with the structure subjected to the Montenegro earthquake (records 199).

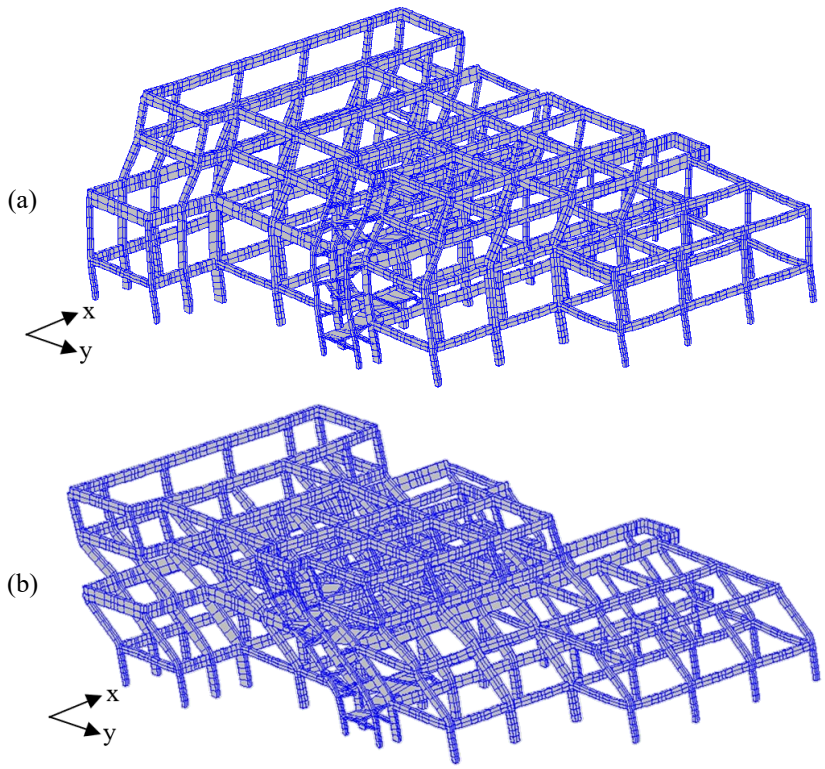

Figure 194 Deformed shape corresponding to the maximum displacement in X and Y directions (Montenegro earthquake-records 199; deformed shape x20)

The seismic response dramatically changes when masonry infills are included in the analyses. The impact is evident in Figure 195, where the responses of the analysed structures, including the bare frame response, are compared in terms of shear base versus relative displacement cycles. The increase in strength and stiffness due to the presence of infills is substantial. The real infilled frame attains a maximum force that is nearly three times that of the bare frame in both directions. Additionally, the full infilled frame remains substantially in the elastic phase throughout the entire duration of the analysis, demonstrating significantly higher stiffness and strength compared to the real infilled structure. The real infilled frame, however, exhibits very low ductility, evidenced by the sudden collapse of the ground floor at around 40% of the time-history, resulting in the termination of the analysis. Remarkably, the soft story mechanism, observed in the deformed shape of the structure at the last step reached, reported in Figure 196, is triggered by the collapse of several infill macroelements at the ground floor, as depicted in Figure 197.

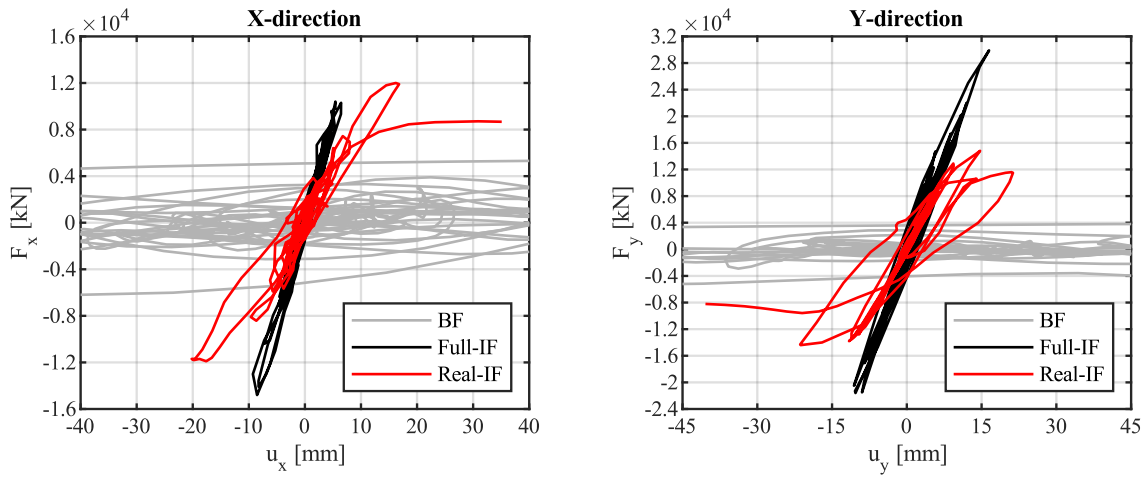

Figure 195 Base shear vs. horizontal relative displacement cycles for bare frame (BF), full infilled frame (Full-IF) and real infilled frame (Real-IF) in (a) X-direction and (b) Y-direction, with the structures subjected to the Montenegro earthquake (records 199)

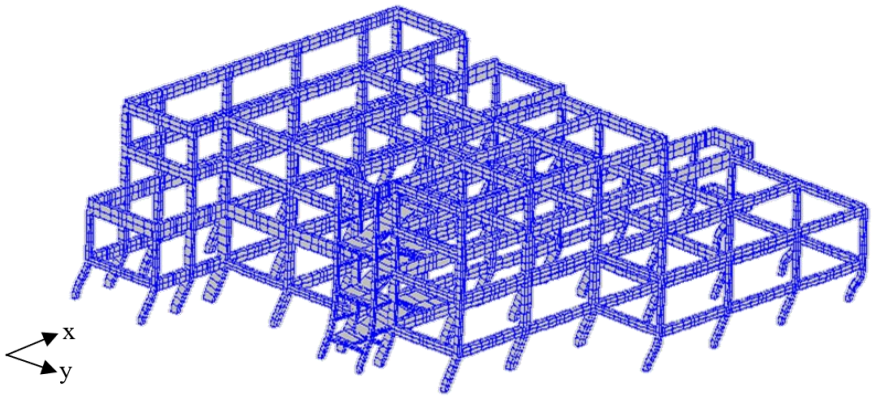

Figure 196 Deformed shape at the last step reached (Montenegro earthquake-records 199; deformed shape x20)

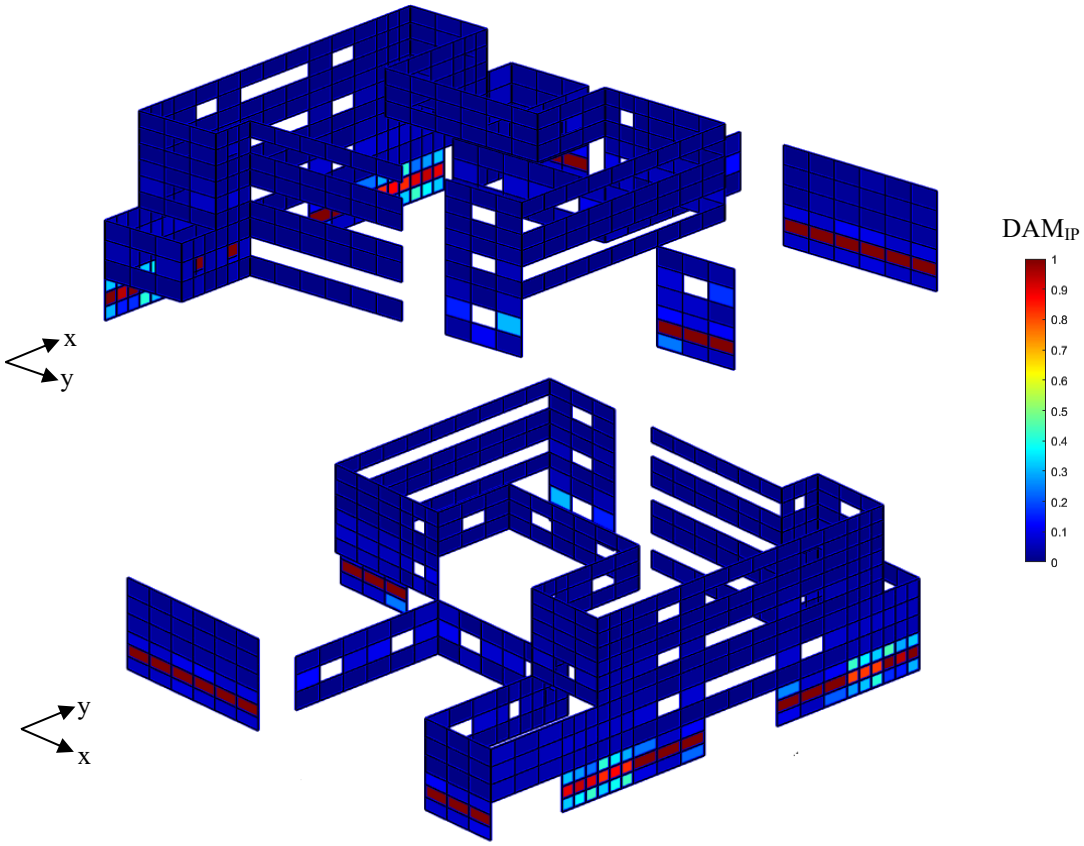

Figure 197 Axonometric views of macroelements diagonal spring damage at the last step reached on the real configuration of infills (Montenegro earthquake-records 199)

Maximum chord rotation and shear demand/capacity ratios within RC members, along with the maximum lateral drifts, are presented in Figure 198 to Figure 202 for comparisons between the bare frame and the real infilled frame.

Concerning the bare frame, demand/capacity ratios for chord rotation of columns (Figure 198) consistently exceed 1 for the second and third-floor elements, in some elements for the first storey, and none on the fourth storey. In contrast, for the infilled structure, the values are consistently lower than those of the bare frame, and they are significant only on the first floor, with six elements having a ratio close to one, while on the other storeys, the ratios are quasi-zero.

Regarding the shear ratios of columns (Figure 199), the situation is different. On the first floor, every element is not verified in both the bare and infilled structure. Remarkably, the highest ratio, equal to 9.5, is registered within the real infilled-frame, while the maximum ratio recorded within the bare frame is 7.9. The ratios generally tend to decrease on the upper floors, with generally lower ratios observed for the infilled-frame.

Lateral drift values (Figure 200) follow the same trend as column chord rotations, with significant drift observed only at the ground floor for the infilled frame and notably large values, especially on the second and third storey, within the bare frame, reaching up to 5%.

For the beams, the situation is satisfactory concerning chord rotation ratios (Figure 201), as no elements fail to meet verification in both structures. However, several elements are not verified for shear (Figure 202) in both structures, with verification ratios generally higher for the bare frame.

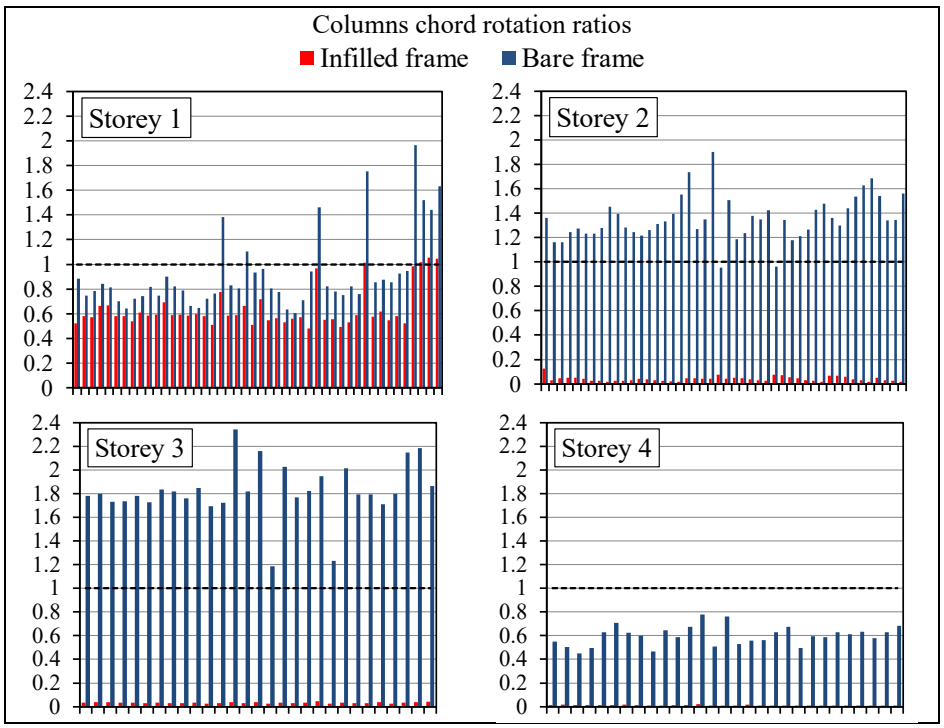

Figure 198 Columns chord rotation verification ratios for bare and real infilled frames (Montenegro earthquake-records 199)

Figure 199 Columns shear verification ratios for bare and real infilled frames (Montenegro earthquake-records 199)

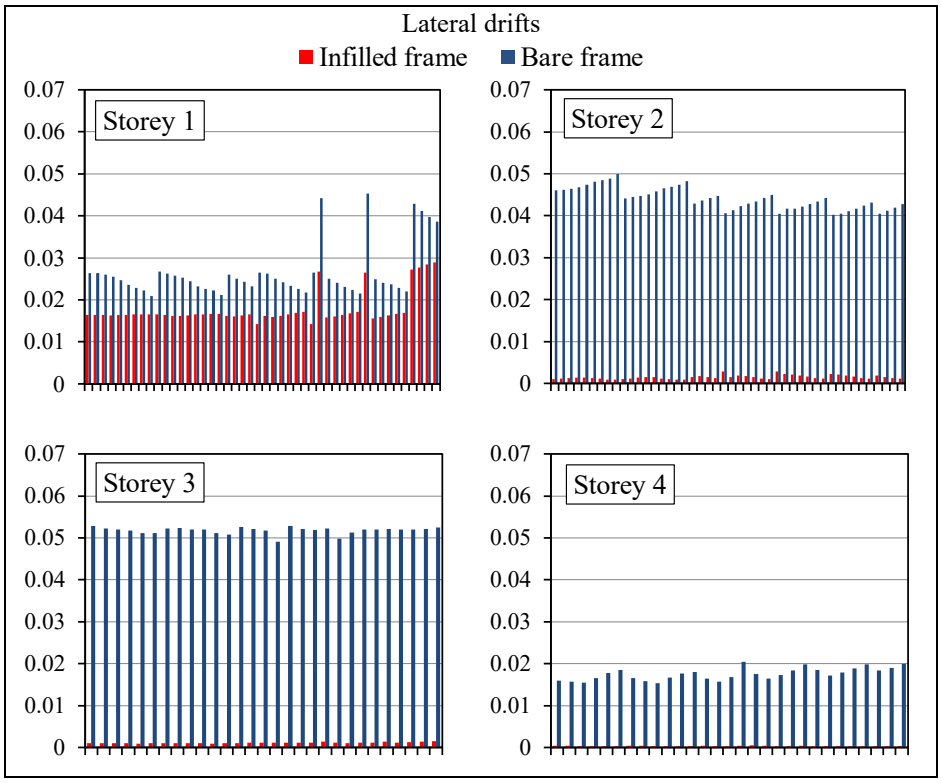

Figure 200 Lateral drifts for bare and real infilled frames (Montenegro earthquake-records 199)

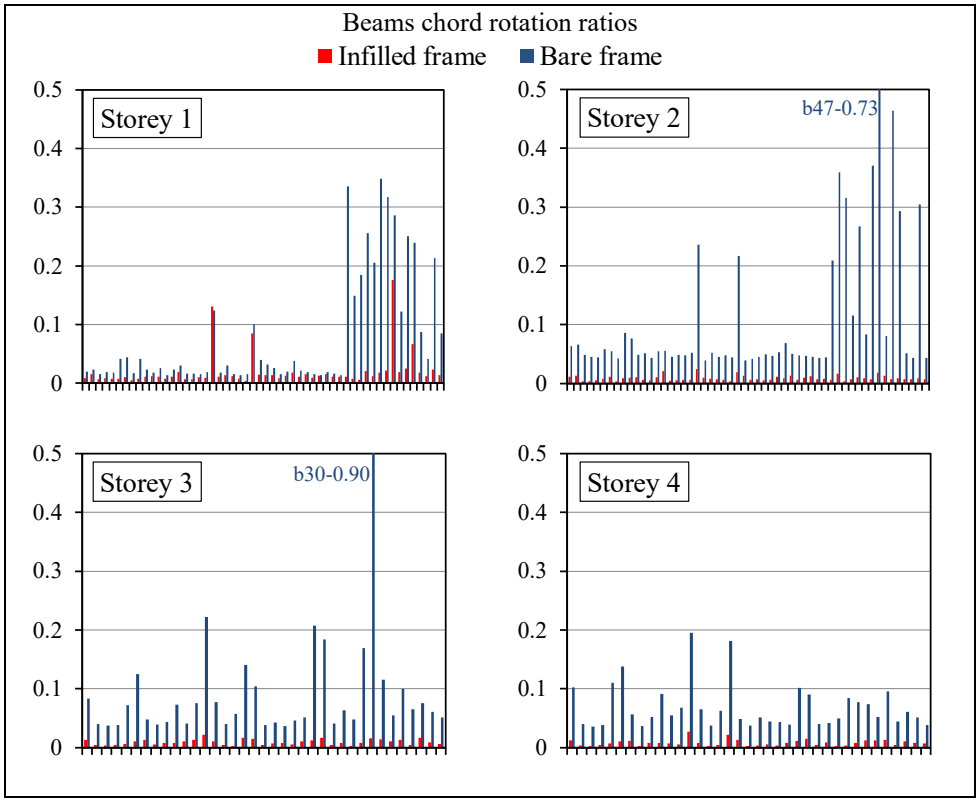

Figure 201 Beams chord rotation verification ratios for bare and real infilled frames (Montenegro earthquake-records 199)

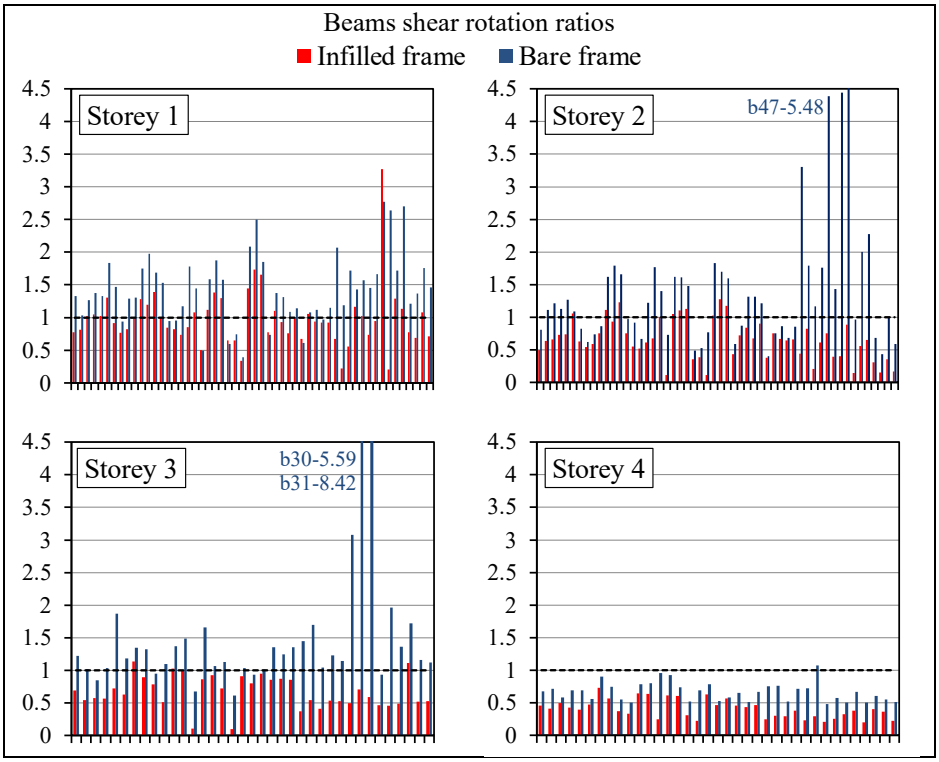

Figure 202 Beams shear verification ratios for bare and real infilled frames (Montenegro earthquake-records 199)

The remaining analyses are then conducted by subjecting the bare frame and real infilled frame to the rest of the accelerograms, characterised by lower PGAs. For each analysis, the averages of the ratios are calculated and reported from Figure 203 to Figure 207, since the final seismic assessment must be made on the overall response from all the accelerograms (as outlined in Chapter 7.4.1). Notably, all the ratios are significantly lower than those of the Montenegro earthquake alone, as the rest of the accelerograms have a significantly lower impact on the seismic responses.

Specifically, each column results verified for the chord rotation (Figure 203) in both bare and infilled frame. However, it is noteworthy that many columns are not verified for shear (Figure 204). Particularly, for the infilled frame, the ratios on the first storey are notably high, with a maximum of 6.7 for column 46, while the maximum value in the bare frame is 3.2 on column 31. Additionally, at the higher storeys, many other elements are not verified.

Regarding the lateral drifts (Figure 205), significant values are observed in the infilled frame only at the ground storey (maximum value of 0.6%), while and larger drifts are observed for the bare frame, especially on the second and third storeys (maximum value of 1.3%).

Moreover, similarly to the analysis with the single Montenegro earthquake, the situation for the beams is generally better, featuring low ratios for the chord rotation verification (Figure 206), with a maximum of 0.2 for the bare frame and 0.04 for the infilled frame.

However, higher shear values (Figure 207) are observed, and many beams do not meet verification criteria in both structures. The maximum shear ratio within the bare frame is 3.54 for beam 31 at the third storey, while the maximum ratio for the infilled frame is 1.54 for beam 28 at the first storey.

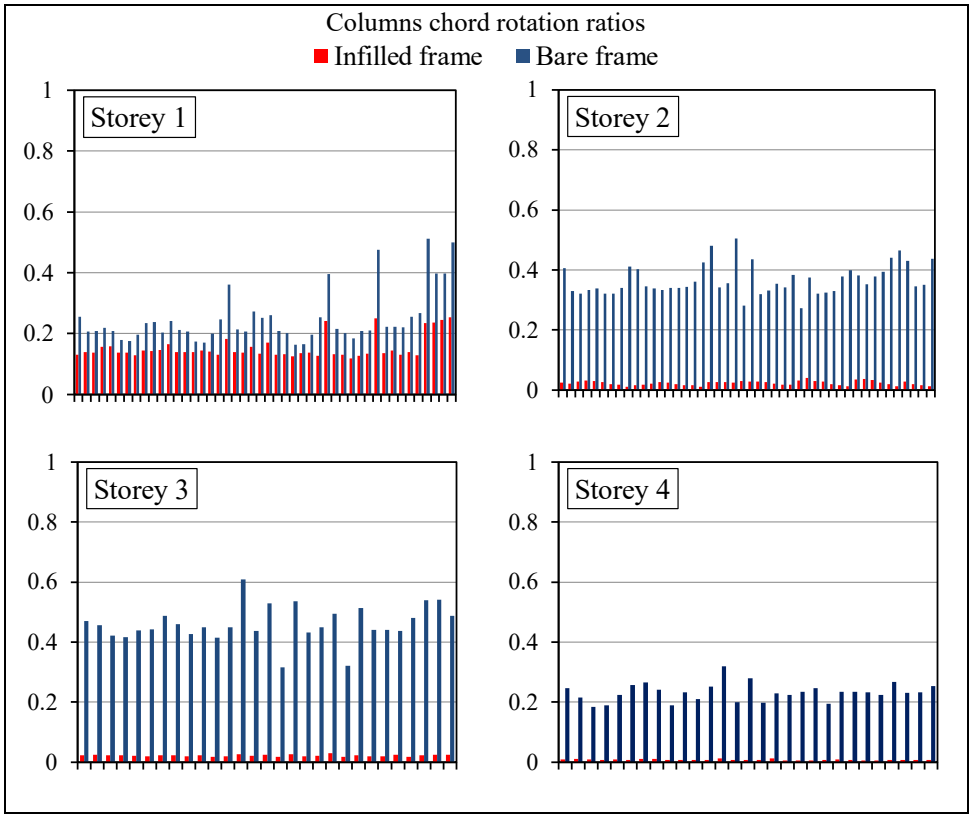

Figure 203 Average columns chord rotation verification ratios for bare and real infilled frames

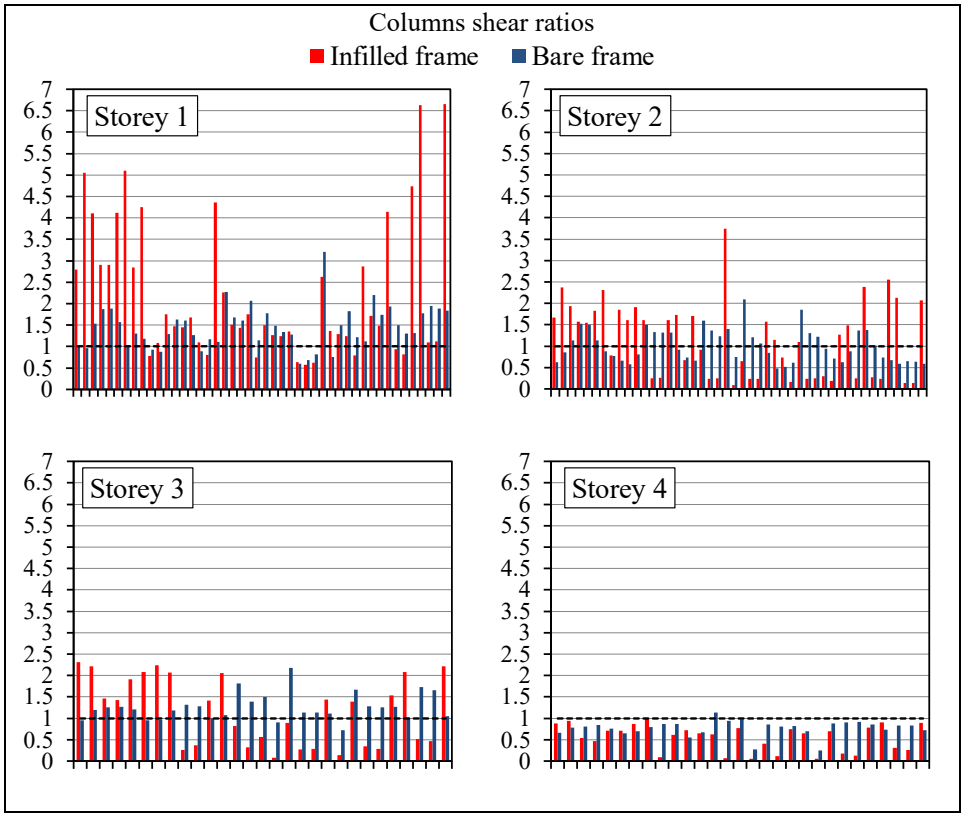

Figure 204 Average columns shear verification ratios for bare and real infilled frames

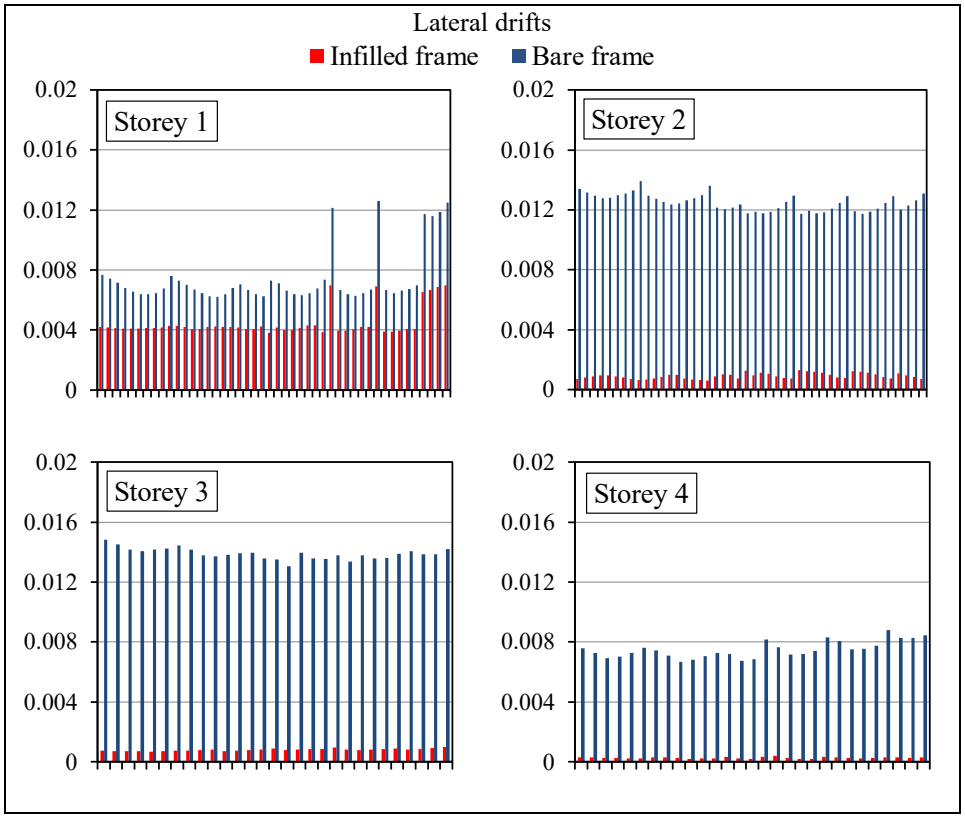

Figure 205 Average lateral drifts for bare and real infilled frames.

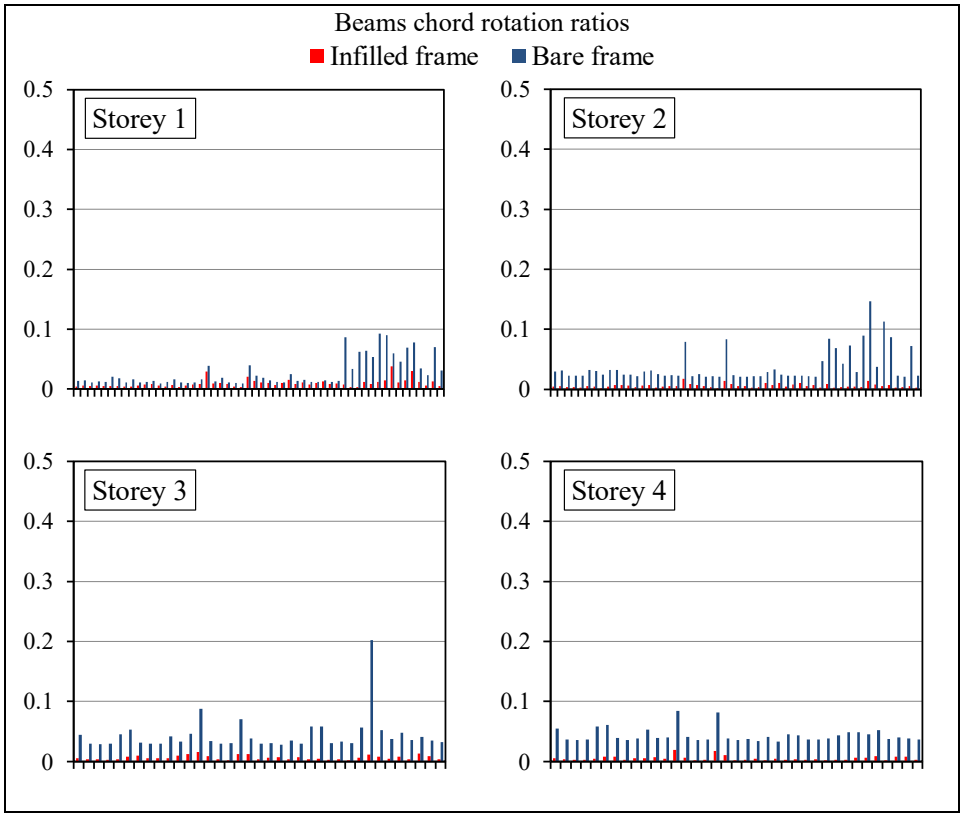

Figure 206 Average beams chord rotation verification ratios for bare and real infilled frames

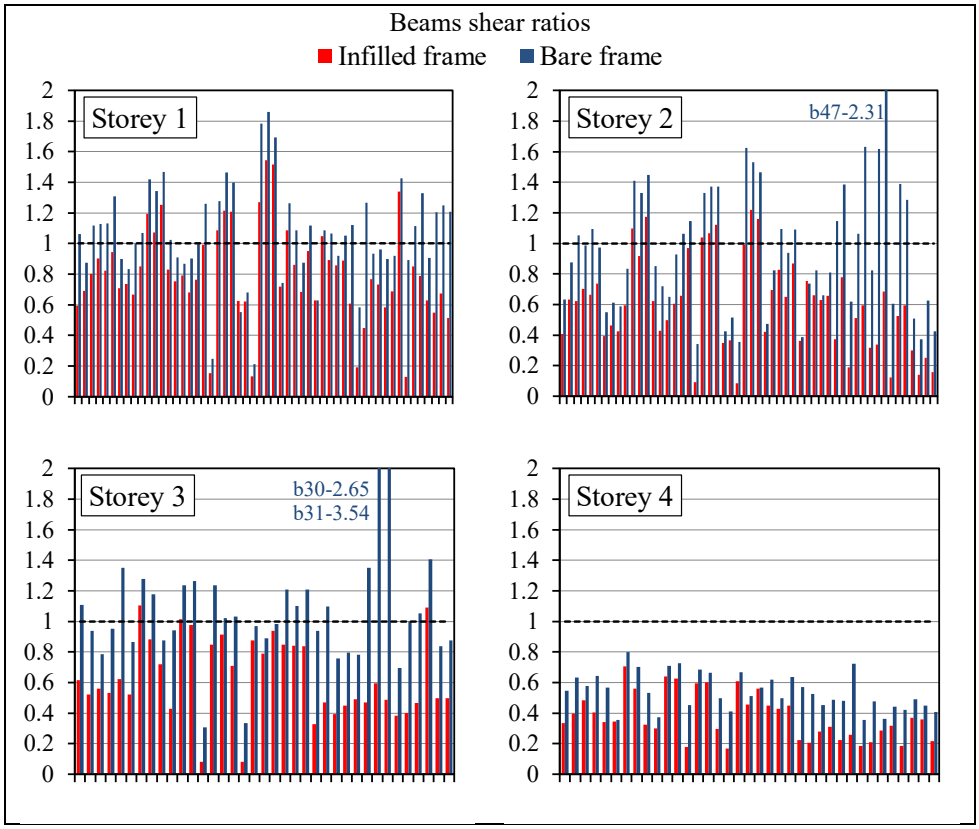

Figure 207 Average beams shear verification ratios for bare and real infilled frames

Overall, substantial differences exist in the responses between the bare and infilled frames also in terms of local member responses. The primary vulnerabilities of the structure, whether considering the bare frame or the real infilled frame, are associated with the shear capacities of the members. Notably, a significant concern pertains to the shear response of the columns at the first storey, more within the infilled frame than the bare frame, evidenced by the higher shear verification ratios. The irregular infill configuration results in a particular weakness at this level, leading to the onset of the soft-storey mechanism after the failure of masonry infills and to high force demands on the columns. Situations related to the shear response of the columns in the upper storeys can be comparable between the bare frame and the infilled frame. On the contrary, regarding the shear response of the beams, the presence of infill appears to have a beneficial effect, resulting in lower verification ratios. This is also observed in the chord rotation verifications of each member.

7.6 Summary and conclusions

In this chapter, the enhanced macroelement strategy has been applied to a realistic scenario involving the seismic assessment of an irregular RC structure, designed primarily to withstand vertical loads but

not horizontal ones. A detailed 3D numerical description has been developed, incorporating the macroelement strategy for the infill modelling, elastic-plastic beam-column elements based on a fibre plasticity approach for RC members, and a system of elastic links for floors. To enhance computational efficiency, the partitioning approach utilised throughout the thesis has been employed.

The structure has been evaluated under different conditions, considering it as a bare structure, with the actual configuration of infills, and, as a limiting case, with infills completely covering it. These configurations have been examined through nonlinear dynamic analyses, considering natural spectrumcompatible accelerograms.

The analysis results have highlighted how the presence of masonry infill significantly affects the dynamic response, impacting modal characteristics, shear-displacement curves, global failure mechanisms, and member capacities. While masonry infill panels generally have a positive impact on the response of infilled frames by increasing the overall strength, this must be considered alongside potential structural irregularities arising from an uneven distribution of infills. Indeed, these irregularities may, in turn, lead to brittle failure and soft-storey mechanisms, triggered by failures of infill panels.

Therefore, it is emphasised that for an accurate description of the response in existing RC structures not originally designed to withstand earthquakes, these components should not be treated merely as non-structural elements, as commonly practiced in the profession, since they strongly influence the structural behaviour. Instead, they must be thoroughly considered in the seismic assessment through the adoption of a reliable modeling strategy. The enhanced macroelement modeling represents a valuable tool, allowing for the representation of infills within a highly reliable and computationally efficient strategy. It is capable of precisely accounting for the various sources of irregularities that may arise due to the distribution of infills, such as portions of structures with solid infills, infills with openings of various characteristics, or parts with no infills.

CHAPTER 8

CONCLUSIONS AND FUTURE WORK

8.1 Summary

This thesis was driven by a dual objective: to examine advanced finite element modelling strategies for masonry wall structures and to provide a reliable yet efficient tool that can accurately capture the actual seismic response of real-sized structures subjected to earthquake loading. The research focused on evaluating the responses of both unreinforced masonry (URM) and masonry-infilled frame structures.

The first part of the work involved a detailed comparison between mesoscale and macroscale approaches for representing masonry structures. The aim was to assess their ability to predict the hysteretic responses of URM structures under in-plane cyclic loading, with focus on the objective calibration of mechanical parameters to evaluate ease, accuracy, and computational demand of the modelling strategies.

Subsequently, advanced strategies were examined for the modelling of masonry-infilled frames under horizontal actions, employing a multi-dimensional partitioned strategy. Considerable attention was dedicated again to the material characterisation, further assessed through parametric analyses, considering the specific features of this structural typology. The influence of openings was also examined by assessing openings with varying configurations and dimensions.

Finally, to provide a more efficient and reliable tool, ensuring an accurate representation of the actual response of masonry wall structures, a novel enhanced three-dimensional macroelement was developed. A comprehensive validation, covering applications on both URM and masonry-infilled frame structures, was carried out. The macroelement strategy was also applied in a real-world scenario,

evaluating the seismic vulnerability of a 4-story irregular reinforced-concrete structure designed without seismic provisions.

8.2 Conclusions

8.2.1 Mesoscale and macroscale modelling for cyclic analysis of URM structures

The mesoscale approach proposed in (Macorini and Izzuddin, 2011; Minga et al., 2018) and a continuum macroscale approach utilising the concrete damage plasticity material law developed in (Chisari et al., 2020), were assessed for their ability to predict the hysteretic response under in-plane cyclic loading simulating earthquake actions. The results indicated that, despite its computational robustness, the macroscale approach led to widely variable results, while the mesoscale results were less scattered, although with a greater computational burden. The main findings are summarised below.

Regarding the mesoscale approach:

- it allows for a straightforward calibration, aligning capacity curves (compared with the experimental shear-displacement cycles envelopes), load-displacement diagrams (considering the completed part of the analyses), and damage progression with experimental results, without needs for additional material calibration refinement.
- it results in low response variability with changes in less-known parameters;
- it is characterised by a high computational cost, making the analysis of larger structures challenging, even with the use of a partitioning strategy.

Concerning the continuum finite element macroscale modelling:

- a “standard calibration”, as an initial attempt to calibrate the material parameters, may results in simulations significantly distant from experimental outcomes in terms of capacity curve, load-displacement cycles, failure mode predictions, and dissipated energy;
- the variation of not easily quantifiable parameters can substantially impact the response of the models;
- a refined material calibration may lead to a good prediction of the hysteretic behaviour of real structures, such as the analysed façade with openings.
- capturing the S-shaped typical flexural load-displacement cycles of a slender panel is challenging;

- analyses are moderately time-consuming and exhibit greater numerical robustness compared to mesoscale models, enabling the completion of the entire cyclic analyses for panels and façade with openings.

Hence, the utilisation of a macroscale strategy, even with sophisticated material laws, to assess the cyclic response of masonry structures in the absence of experimental characterisation at the macroscale level—particularly for shear response and determining global tensile strength—should be approached cautiously. It is advisable to calibrate a macroscale model by initially employing a more reliable small-sized mesoscale model, within a multiscale strategy as suggested by Chisari et al. (2020) and Pantò et al. (2022). The mesoscale model can be validated based on non-invasive tests on mortar joints (such as triplet shear tests or cross tension tests), coupled with compression strength evaluation (which could be conducted with a moderately invasive flat-jack test), and subsequently used for the calibration of the macroscale model.

8.2.2 Advanced modelling of masonry-infilled frame structures

The response of masonry-infilled frames under monotonic horizontal actions was analysed by adopting a multi-dimensional partitioned strategy, employing both mesoscale and continuum macroscale approaches for the modelling of the infill.

The analyses outcomes show that the adopted modelling strategies produce an accurate response when compared to experimental outcomes, effectively representing both the global response and the local behaviour. The global response, i.e. the capacity curve, is accurately captured with precise predictions of initial stiffness, progressive stiffness decrease after frame-infill detachment, maximum strength, and post-peak phase. The local behaviour is correctly reproduced, encompassing failure mechanisms in the infill (such as diagonal cracking, leading to progressive pre-peak stiffness decrease, and corner crushing, resulting in maximum strength attainment), frame (development of plastic hinges), and frame-infill interfaces (frame-infill detachment resulting from opening and sliding of the edge interfaces, leading to the development of diagonal struts).

Notably, unlike cyclic analyses of URM structures, the utilisation of the continuum macroscale strategy for modelling masonry infill allows for the correct prediction of the infilled frame response (noteworthy, in this phase, infilled frames were investigated only under horizontal monotonic actions). This is likely because the response of the infill, especially its maximum strength, is primarily governed by compression strength and is less dependent on tensile strength, which governs more the pre-peak phase.

The compressive strength, known experimentally for the vertical direction (perpendicular to the bed-joint), is utilised in the model to estimate the horizontal compressive strength, with the same value adopted for the vertical interfaces of the mesoscale model. As a result, the predictions of the two models are consistent, and the corner crushing mechanism is accurately represented.

Several sensitivity analyses, conducted on both the models, allow to recognise the most influential parameters, specifically highlighting the strength parameters for the frame-infill interfaces (cohesion, friction coefficient and tensile bond strength) and the compression strength characteristics (compression strength and crushing energy) of the infills.

Finally, it is shown how openings can significantly influence the response of infilled frames, impacting the capacity curve by reducing pre-peak stiffness and maximum strength. Furthermore, the presence of openings affects the progression of the stress state and damage, which may vary significantly compared to the solid infill case. Notably, there is a distinct impact on the response between window infills and door infills. Remarkably, the response of window-infilled frames is notably affected by window dimensions—larger openings lead to a higher decrease in pre-peak stiffness and maximum strength. Conversely, the responses of door-infilled frames show no significant variation with changing opening dimensions, maintaining maximum strength consistently close to the residual strength of the solid infilled frame. Furthermore, in both cases, the presence of openings affects the decrease of pre-peak stiffness more than the decrease of maximum strength.

8.2.3 A novel enhanced 3D macrolement for URM and infilled frame structures modelling

The second part of the thesis regarded the development of an enhanced macro-element model, building upon the foundation established by the element introduced in a prior study (Minga et al., 2020). The novel macroelement incorporates a more sophisticated constitutive law for both in-plane and out-of-plane springs, through the implementation of the cyclic hysteretic model of (Tomaževič and Lutman, 1996), which allows to more realistically capture shear strength and stiffness degradation. Another noteworthy advancement involves the definition of the post-peak branch in the skeleton curve, in such a way to ensure the mesh objectivity. Furthermore, to realistically predict the actual interaction between frame and infill in the infilled frames, the possibility to differentiate mechanical properties between external, generally weaker, and internal frame-infill interfaces was introduced.

The enhanced macroelement underwent comprehensive validation against several experimental outcomes, demonstrating its potential to accurately predict structural responses while maintaining high

computational efficiency. In-plane tests on URM structures, including two single panels and the façade with openings, as well as out-of-plane tests on walls subjected to two-way bending with or without openings and vertical loads, were accurately reproduced. The numerical-experimental alignment regarding base shear vs. lateral displacement monotonic and cyclic responses, as well as damage patterns, was consistently precise. Additionally, a 3D URM model, representing half of a full-scale URM building experimentally tested under earthquake loading, underwent nonlinear dynamic analyses. The obtained response was accurate and consistent with results from more sophisticated mesoscale and macro models, but with significantly lower computational demands. The macroelement strategy was also validated for masonry-infilled frame structures, evaluating both solid and perforated infilled frames. The approach for infilled frames modelling demonstrated its reliability, effectively capturing every typical mechanism and providing excellent simulation of monotonic and cyclic experimental tests.

Given its reliability, the enhanced macroelement strategy was also employed to assess the seismic vulnerability of a real 4-story irregular RC existing building, originally not designed to withstand earthquake loading. The aim was to examine the influence of the presence of masonry infills on the seismic response of the structure. The analysis results highlighted the significant impact of the infills, emphasising the importance of properly considering them in the assessment of existing RC frames through the utilisation of a reliable modelling strategy. Indeed, the presence of infills may represent a significant source of irregularity, potentially triggering detrimental torsional vibration components and ultimately leading to dangerous soft-story mechanisms, as observed in the analysis carried out. Irregularities can arise from an irregular configuration of masonry infills, as well as from the presence of openings. Moreover, even modifications to non-structural element configurations during the service life of a building may lead to unexpected structural responses. Therefore, infill presence should always be considered and not neglected, as is common in professional practice nowadays. The macroelement strategy represents a valuable approach for this aim, given its excellent balance between accuracy and efficiency.

8.3 Future works

Future developments dealing with the first part of the research, which focused on comparing mesoscale and macroscale strategies within cyclic analysis of brick masonry walls, will primarily aim to develop further robust multiscale relationships (as already proposed by Chisari et al., 2020, and Pantò et al.,2022). The focus is to consider low-invasive material tests whose outcomes enable the calibration of small-scale mesoscale models, serving as virtual experimental tests. These, in turn, will enable the

calibration of a more computationally efficient macroscale model, applicable to large-sized structures. Additionally, conducting further analyses on larger structures within the macroscale framework can offer valuable insights into how the variability observed in individual components influences their overall hysteretic response. Moreover, the analyses conducted highlighted that the concrete damage plasticity model, despite being widely used for masonry structures, has deficiencies that still provide opportunities for the development of more accurate models.

Regarding advanced modelling of masonry-infilled frames, future developments will delve into further evaluating the influence of opening presence. This analysis will consider other significant variables, including the eccentricity of the openings, the presence of reinforcements, the confinement level of the infill, and the ratio between frame stiffness and infill stiffness, as well as the height-to-width ratio of the frame.

The enhanced macroelement strategy, which has demonstrated its great reliability in modelling both URM and masonry-infilled frames, can be further deepened and improved. This could include:

- Further investigation into the relationship between the ultimate displacement of the diagonal spring, which defines the post-peak branch, and masonry characteristics.
- Evaluation of the correlation between interface characteristics and the adopted mesh discretisation.
- Development of a calibration strategy for the out-of-plane spring that is independent of a mesoscale model, deemed as virtual test.
- Implementation of a co-rotational approach to consider geometric nonlinearity, aiming to accurately assess the out-of-plane behaviour, especially for slender masonry panels often found in masonry infills; this approach would also help to evaluate the crucial interaction between in-plane and out-of-plane responses, which can have a significant impact under extreme loading conditions.
- In-depth assessment of modelling infills as macroelements, comparing the results with more sophisticated mesoscale and continuum macroscale strategies, and evaluating different conditions (e.g., position and dimensions of openings, presence of reinforcements, confinement level).
- Further enhancement by exploring the possibility of connecting multiple masonry leaves in parallel, particularly beneficial for representing infills with interstitial space.

Finally, the conducted analyses demonstrate that considering infills as non-structural elements is misleading, resulting in inaccurate predictions of the structural response. In general, this represents a point on which the scientific community is increasingly in agreement. Therefore, even from a regulatory perspective, a step forward should be taken by making their inclusion in safety assessments mandatory. Within this context, the macroelement could offer a valuable approach and thus should be considered for implementation in specialised structural software.

REFERENCES

ABAQUS Inc, 2014. Abaqus analysis User's guide, v. 6.14. Providence, RI, USA.

AIJ, 1994. Architechtural Institute of Japan : Standard for Structural Calculation of Reinforced Concrete Structures.

Al-Chaar, G., Issa, M., Sweeney, S., 2002. Behavior of Masonry-Infilled Nonductile Reinforced Concrete Frames. Journal of Structural Engineering 128. https://doi.org/10.1061/(ASCE)0733-9445(2002)128:8(1055)

Ali, S.S., Page, A.W., 1987. Finite Element Model for Masonry Subjected to Concentrated Load. Proceedings of the American Society of Civil Engineers, Journal of Structural Engineering, 114, 1761–1784.

Anthoine, A., Capéran, P., 2008. Earthquake tests and analysis of the experimental results. Ispra, Italy: Italy: European Laboratory for Structural Assessment.

Anthoine, A., Magonette, G., Magenes, G., 1995. Shear compression testing and analysis of brick masonry walls. Presented at the Proceedings of the 10th European Conference on Earthquake Engineering, Vienna, Austria.

Applied Technology Council, 1996. ATC-40 - Seismic Evaluation and Retrofit of Concrete Buildings.

ASCE/SEI 41-13, 2013. Seismic Rehabilitation of Existing Buildings, American Society of Civil Engineers.

ASCE/SEI 41-17, 2017. Seismic Evaluation and Retrofit of Existing Buildings, American Society of Civil Engineers.

Asteris, P., Antoniou, S., Sophianopoulos, D., Chrysostomou, C., 2011. Mathematical Macromodeling of Infilled Frames: State of the Art. Journal of Structural Engineering 137, 1508–1517. https://doi.org/10.1061/(ASCE)ST.1943-541X.0000384

Asteris, P., Giannopoulos, I., Chrysostomou, C., 2012. Modeling of Infilled Frames With Openings. The Open Construction and Building Technology Journal 6, 81–91. https://doi.org/10.2174/1874836801206010081

Asteris, P.G., Cavaleri, L., Di Trapani, F., Sarhosis, V., 2016. A macro-modelling approach for the analysis of infilled frame structures considering the effects of openings and vertical loads. Structure and Infrastructure Engineering 12, 551–566. https://doi.org/10.1080/15732479.2015.1030761

Berto, L., Saetta, A., Scotta, R., Vitaliani, R., 2002. An orthotropic damage model for masonry structures. International Journal for Numerical Methods in Engineering 55, 127–157. https://doi.org/10.1002/nme.495

Bertolesi, E., Milani, G., Lourenço, P.B., 2016. Implementation and validation of a total displacement non-linear homogenization approach for in-plane loaded masonry. Computers & Structures 176, 13–33. https://doi.org/10.1016/j.compstruc.2016.08.001

Binda, L., Tiraboschi, C., Mirabella Roberti, G., Baronio, G., Cardani, G., 1995. Measuring masonry material properties: detailed results from an extensive experimental research. Experimental and Numerical Investigation on a brick Masonry Building Prototype, Report 5.0 - G.N.D.T.

Bomben, L., Rinaldin, G., Fasan, M., Amadio, C., 2022. Survey on non-linear cyclic responses of Unreinforced Masonry buildings by means of commercial finite-element codes. Structural Integrity Procedia.

Bracchi, S., Galasco, A., Penna, A., 2021. A novel macroelement model for the nonlinear analysis of masonry buildings. Part 1: Axial and flexural behavior. Earthquake Engineering & Structural Dynamics 50, 2233–2252.

Bracchi, S., Penna, A., 2021. A novel macroelement model for the nonlinear analysis of masonry buildings. Part 2: Shear behavior. Earthquake engineering & structural dynamics. 50, 2212–2232.

Brencich, A., Gambarotta, L., Lagomarsino, S., 1998. A macroelement approach to the three-dimensional seismic analysis of masonry buildings. 11th European Conference on Earthquake Engineering 6–11.

BS EN, 2004. Eurocode 2: Design of Concrete Structures Part 1-1–General Rules and Rules for Buildings.

Calderoni, B., Cordasco, E.A., Sandoli, A., Onotri, V., Tortoriello, G., 2015. Problematiche di modellazione strutturale di edifici in muratura esistenti soggetti ad azioni sismiche in relazione all'utilizzo di software commerciali. Anidis XVI Conference, L'Aquila.

Caliò, I., Marletta, M., Pantò, B., 2012. A new discrete element model for the evaluation of the seismic behaviour of unreinforced masonry buildings. Engineering Structures 40, 327–338. https://doi.org/10.1016/j.engstruct.2012.02.039

Caliò, I., Pantò, B., 2014. A macro-element modelling approach of Infilled Frame Structures. Computers & Structures 143, 91–107. https://doi.org/10.1016/j.compstruc.2014.07.008

Casolo, S., Peña, F., 2007. Rigid element model for in-plane dynamics of masonry walls considering hysteretic behaviour and damage. Earthquake Engineering & Structural Dynamics 36, 1029–1048. https://doi.org/10.1002/eqe.670

Cattari, S., Camilletti, D., D'Altri, A.M., Lagomarsino, S., 2021. On the use of continuum Finite Element and Equivalent Frame models for the seismic assessment of masonry walls. Journal of Building Engineering 43, 102519. https://doi.org/10.1016/j.jobe.2021.102519

Cattari, S., Camilletti, D., Magenes, G., Manzini, C.F., Morandi, P., 2017. Comparative analysis of benchmark case studies for assessing the reliability of software packages targeted to the seismic assessment of URM buildings. Presented at the Anidis, Pistoia.

Cattari, S., Ottonelli, D., Degli Abbati, S., Magenes, G., Manzini, C.F., 2019. Uso dei codici di calcolo per l'analisi sismica nonlineare di edifici in muratura: confronto dei risultati ottenuti con diversi software su un caso studio reale. Presented at the Anidis.

Chen, X., Liu, Y., 2015. Numerical study of in-plane behaviour and strength of concrete masonry infills with openings. Engineering Structures 82, 226–235. https://doi.org/10.1016/j.engstruct.2014.10.042

Chieffo, N., Marius, M., Formisano, A., Lourenco, P., Milani, G., 2021. The effect of ground motion vertical component on the seismic response of historical masonry buildings: The case study of the Banloc Castle in Romania. Engineering Structures 249, 113346. https://doi.org/10.1016/j.engstruct.2021.113346

Chisari, C., Macorini, L., Izzuddin, B., 2021. Mesoscale Modeling of a Masonry Building Subjected to Earthquake Loading. Journal of Structural Engineering 147. https://doi.org/10.1061/(ASCE)ST.1943-541X.0002823

Chisari, C., Macorini, L., Izzuddin, B.A., 2023. An anisotropic plastic-damage model for 3D nonlinear simulation of masonry structures. International Journal for Numerical Methods in Engineering 124, 1253–1279. https://doi.org/10.1002/nme.7162

Chisari, C., Macorini, L., Izzuddin, B.A., 2020. Multiscale model calibration by inverse analysis for nonlinear simulation of masonry structures under earthquake loading. International Journal for Multiscale Computational Engineering 18. https://doi.org/10.1615/IntJMultCompEng.2020031740

Chopra, L., 2011. Dynamics of Structures: theory and applications to earthquake engineering, 4th ed, Prentice Hall Int. Series in Civil Engineering and Engineering Mechanics. Pearson.

Chrysostomou, C., 1991. Effects of degrading infill walls on the nonlinear seismic response of two-dimensional steel frames /.

Chrysostomou, C.Z., Gergely, P., Abel, J.F., 2002. A six-strut model for nonlinear dynamic analysis of steel infilled frames. International Journal of Structural Stability and Dynamics 2, 335–353. https://doi.org/10.1142/S0219455402000567

Code_Aster, 2013. Law of behavior BETON-DOUBLE_DP with double Drucker-Prager criterion for the cracking and the compression of the concrete.

Comitè Euro-International du Béton, 1996. RC Frames under Earthquake Loading, State pf the Art. Rep. London, UK.

Comitè Euro-International du Béton, 1994. Behaviour and Analysis of Reinforced Concrete Structures under Alternate Actions Inducing Inelastic Response. Bulletin d'information No. 220 2, 310–380.

Comité Euro-International du Béton, 1993. Model Code 90.

Crisafulli, F., Carr, A., 2007. Proposed macro-model for the analysis of infilled frame structures. Bulletin of the New Zealand Society for Earthquake Engineering 40, 69–77. https://doi.org/10.5459/bnzsee.40.2.69-77

Crisafulli, F.J., 1997. Seismic behaviour of reinforced concrete structures with masonry infills.

Crisafulli, F.J., Carr, A.J., Park, R., 2000. Analytical modelling of infilled frame structures: A general review. Bulletin of the New Zealand Society for Earthquake Engineering 33, 30–47. https://doi.org/10.5459/bnzsee.33.1.30-47

Croce, P., Beconcini, M.L., Formichi, P., Cioni, P., Landi, F., Mochi, C., De Lellis, F., Mariotti, E., Serra, I., 2018. Shear modulus of masonry walls: a critical review, in: Procedia Structural Integrity, XIV International Conference on Building Pathology and Constructions Repair. Florence, Italy, pp. 339–346. https://doi.org/10.1016/j.prostr.2018.11.044

Da Porto, F., Modena, C., Prota, A., 2016. Report fotografico relativo ad alcuni edifici in muratura delle frazioni di Arquata del Tronto (AP). ReLUIS.

Da Silva, L., Lourenço, P.B., Milani, G., 2017. Nonlinear Discrete Homogenized Model for Out-of-Plane Loaded Masonry Walls. Journal of Structural Engineering 143. https://doi.org/10.1061/%28ASCE%29ST.1943-541X.0001831

D'asdia, P., Viskovic, A., 1995. Analyses of a masonry wall subjected to horizontal actions on its plane employing a non-linear procedure using changing shape finite elements. Transactions on Modelling and Simulation 10, 519–5626.

Dawe, J.L., Liu, Y., Seah, C.K., 2001. A parametric study of masonry infilled steel frames. Can. J. Civ. Eng. 28, 149–157. https://doi.org/10.1139/l00-084

Dawe, J.L., Yong, T.C., 1985. An Investigation of Factors Influencing the Behaviour of Masonry Infill in Steel Frames Subjected to In-Plane Shear, in: Proceedings of the Seventh International Brick Masonry Conference. pp. 803–814.

De Falco, A., Guidetti, G., Mori, M., Sevieri, G., 2017. Model uncertainties in seismic analysis of existing masonry buildings: the Equivalent-Frame Model within the Structural Element Models approach. Proceedings of the XVII Anidis Conference, Pistoia.

Decanini, L., Liberatore, L., Mollaioli, F., 2014. Strength and stiffness reduction factors for infi lled frames with openings. Earthquake Engineering and Engineering Vibration 13, 437–454. https://doi.org/10.1007/s11803-014-0254-9

Decanini, L., Mollaioli, F., Mura, A., Saragoni, R., 2004. Seismic performance of masonry infilled R/C frames. Presented at the 13th World Conference on Earthquake Engineering, Vancouver, B.C., Canada.

Demetrios, K., Karayannis, C., 2007. Experimental Investigation of infilled R/C frames with eccentric Openings. Structural engineering & mechanics 26, 231–250. https://doi.org/10.12989/sem.2007.26.3.231

Dhanasekar, M., Page, A.W., Kleeman, P.W., 1985. The Behaviour of the Brick Masonry under Biaxial Stress with Particular Reference to Infilled Frames, in: Proceedings of the Seventh International Brick and Masonry Conference. Melbourne, Australia, pp. 815–824.

Dhir, P.K., Tubaldi, E., Ahmadi, H., Gough, J., 2021. Numerical modelling of reinforced concrete frames with masonry infills and rubber joints. Engineering Structures 246. https://doi.org/10.1016/j.engstruct.2021.112833

Di Trapani, F., Vizzino, A., Tomaselli, G., Sberna, A.P., Bertagnoli, G., 2022. A new empirical formulation for the out-of-plane resistance of masonry infills in reinforced concrete frames. Engineering Structures 266, 114422. https://doi.org/10.1016/j.engstruct.2022.114422

Dipartimento della Protezione Civile, 2009. Linee guida per la riduzione della vulnerabilità di elementi non strutturali, arredi e impianti. Roma.

Dolsek, M., Fajfar, P., 2008. The Effect of Masonry Infills on the Seismic Response of a Four-Storey Reinforced Concrete Frame – A Deterministic Assessment. Engineering Structures 30, 1991–2001. https://doi.org/10.1016/j.engstruct.2008.01.001

Durrani, A.J., Luo, Y.H., 1994. Seismic retrofit of flat-slab buildings with masonry infills, in: Proceedings from the NCEER Workshop on Seismic Response of Masonry Infills. pp. 1–8.

El-Dakhakhni, W.W., 2000. Non-linear finite element modeling of concrete masonry-infilled steel frame (M.S. thesis). Civil and Architectural Engineering Dept., Drexel Univ., Philadelphia.

El-Dakhakhni, W.W., Elgaaly, M., Hamid, A.A., 2003. Three-Strut Model for Concrete Masonry-Infilled Steel Frames. Journal of Structural Engineering 129, 177–185. https://doi.org/10.1061/(ASCE)0733-9445(2003)129:2(177)

EN 1992-1-1, 2004. Eurocode 2: Design of Concrete Structures. Part 1-1: General Rules and Rules for Buildings.

EN 1996-1-1, 1995. Eurocode 6: Design of Masonry Structures. Part 1-1: General Rules for Reinforced and Unreinforced Masonry Structures.

EN 1998-1-1, 2005. Eurocode 8: Design of structures for earthquake resistance—Part 1: General rules, seismic actions and rules for buildings.

EN 1998-3, 2004. Eurocode 8: Design of Structures for Earthquake Resistance - Part 3: Assessment and Retrofitting of Buildings.

Esteva, L., 1966. Behaviour under Alternating Loads of Masonry Diaphragms Framed by Reinforced Concrete Members. Proceedings of the International Symposium on the Effects of Repeated Loadings of Materials and Structures 5, 1–36.

Facchini, L., Betti, M., Corazzi, R., Kovacevic, V.C., 2017. Nonlinear seismic behavior of historical masonry towers by means of different numerical models. Procedia Engineering, X International Conference on Structural Dynamics, EURODYN 2017 199, 601–606. https://doi.org/10.1016/j.proeng.2017.09.103

Fardis, M., 2009. Seismic Design, Assessment and Retrofitting of Concrete Buildings Based on EN-Eurocode 8, Geotechnical, Geological and Earthquake Engineering. https://doi.org/10.1007/978-1-4020-9842-0

FEMA 274, 1974. NEHRP commentary on the guidelines for the seismic rehabilitation of buildings.

FEMA 306, 1999. Evaluation of earthquake damaged concrete and masonry wall building.

FEMA 356, 2000. Prestandard and Commentary for the Seismic Rehabilitation of Buildings, Federal Emargency Management Agency.

Foraboschi, P., Vanin, A., 2013. Non-linear static analysis of masonry buildings based on a strut-and-tie modeling. Soil Dynamics and Earthquake Engineering 55, 44–58. https://doi.org/10.1016/j.soildyn.2013.08.005

Geuzaine, C., Remacle, J.F., 2009. Gmsh: a three-dimensional finite element mesh generator with built-in pre- and post-processing facilities. Int. J. Numer. Meth. Engng.

Gregorczyk, P., Lourenço, P., 2000. A review on flat-jack testing. Engenharia Civil.

Griffith, M., Vaculik, J., Lam, N., Wilson, J., Lumantarna, E., 2007. Cyclic testing of unreinforced walls in two-way bending. Earthquake Engineering & Structural Dynamics 36, 801–821. https://doi.org/10.1002/eqe.654

Holmes, M., 1961. Steel frames with brickwork and concrete infilling. Proceedings of the Institution of Civil Engineers 19, 473–478. https://doi.org/10.1680/iicep.1961.11305

Iervolino, I., Galasso, C., Cosenza, E., 2009. REXEL: Computer aided record selection for code-based seismic structural analysis. Bulletin of Earthquake Engineering 8, 339–362. https://doi.org/10.1007/s10518-009-9146-1

Imai, H., 1989. Seismic Behavior of Reinforced Masonry Walls with Small Opening, in: Proceedings of 5◦ Jornadas Chilenas de Sismología e Ingeniería Antisísmica. Santiago, Chile.

International Conference of Building Officials, 1991. Uniform Building Code.

Izzuddin, B., 2005. An enhanced co-rotational approach for large displacement analysis of plates. International Journal for Numerical Methods in Engineering 64, 1350–1374. https://doi.org/10.1002/nme.1415

Izzuddin, B.A., 1991. Nonlinear dynamic analysis of framed structures. (Ph.D. thesis). Civil Engineering Dept., Imperial College London.

Izzuddin, B.A., Elnashai, A.S., 1993. Eulerian Formulation for Large-Displacement Analysis of Space Frames. Journal of Engineering Mechanics 119 (3). https://doi.org/10.1061/(ASCE)0733-9399(1993)119:3(549)

Izzuddin, B.A., Elnashai, A.S., 1993a. Adaptive Space Frame Analysis Part I, A Plastic Hinge Approach. Proceedings of the Institution of Civil Engineers - Structures and Buildings a(99), 303–16.

Izzuddin, B.A., Elnashai, A.S., 1993b. Adaptive Space Frame Analysis: Part II, A Distributed Plasticity Approach. Proceedings of the Institution of Civil Engineers - Structures and Buildings b(99), 317–26.

Izzuddin, B.A., Lloyd Smith, D., 2000. Efficient nonlinear analysis of elasto-plastic 3D R/C frames using adaptive techniques. Computers & Structures 78, 549–573. https://doi.org/10.1016/S0045-7949(00)00041-9

Izzuddin, B.A., Macorini, L., Rinaldin, G., 2013. Partitioned Modelling for Nonlinear Dynamic Analysis of Reinforced Concrete Buildings for Earthquake Loading. Presented at the Proceedings of the Fourteenth International Conference on Civil, Structural and Environmental Engineering Computing, pp. 1–12.

Jafari, S., Rots, J.G., Esposito, R., 2022. A correlation study to support material characterisation of typical Dutch masonry structures. Journal of Building Engineering 45, 1–14. https://doi.org/10.1016/j.jobe.2021.103450

Jokhio, G.A., 2012. Mixed dimensional hierarchic partitioned analysis of nonlinear structural systems (Ph.D. thesis). Civil and Environmental Engineering Dept., Imperial College London.

Jokhio, G.A., Izzuddin, B.A., 2015. A Dual Super-Element Domain Decomposition Approach for Parallel Nonlinear Finite Element Analysis. International Journal for Computational Methods in Engineering Science and Mechanics 16, 188–212. https://doi.org/10.1080/15502287.2015.1043163

Jokhio, G.A., Izzuddin, B.A., 2013. Parallelisation of nonlinear structural analysis using dual partition super elements. Advances in Engineering Software s 60–61, 81–88. https://doi.org/10.1016/j.advengsoft.2012.10.004

Kakaletsis, D.J., Karayannis, C.G., 2007. Experimental Investigation of infilled R/C frames with eccentric Openings. Structural engineering & mechanics 26, 231–250. https://doi.org/10.12989/sem.2007.26.3.231

Kareem, K., Abdulla, K., Pantò, B., Cunningham, L., 2022. Numerical simulation of the in-plane lateral response of RC infill frames using a FEM-DMEM modelling approach. Journal of Building Engineering 51, 104305. https://doi.org/10.1016/j.jobe.2022.104305

King, G.J.W., Pandey, P.C., 1978. The Analysis of Infilled Frames Using Finite Elements. Proceedings of the Institution of Civil Engineers 65, 749–760.

Klingner, R.E., Bertero, V.V., 1976. Infilled frames in earthquake-resistant construction, Report, University of California, Berkeley. Earthquake Engineering Research Center.

Koutromanos, I., Stavridis, A., Shing, P.B., Willam, K., 2011. Numerical modeling of masonry-infilled RC frames subjected to seismic loads. Computers & Structures, Computational Fluid and Solid Mechanics 2011 89, 1026–1037. https://doi.org/10.1016/j.compstruc.2011.01.006

Kurmi, P.L., Haldar, P., 2022. Modeling of opening for realistic assessment of infilled RC frame buildings. Structures 41, 1700–1709. https://doi.org/10.1016/j.istruc.2022.05.110

Lagomarsino, S., Penna, A., Galasco, A., Cattari, S., 2013. TREMURI program: An equivalent frame model for the nonlinear seismic analysis of masonry buildings. JEST Engineering Structures 56, 1787–1799.

Lee, J., Fenves, G.L., 1998. Plastic-Damage Model for Cyclic Loading of Concrete Structures. Journal of Engineering Mechanics 124, 892–900. https://doi.org/10.1061/(ASCE)0733-9399(1998)124:8(892)

Liauw, T.C., Kwan, K.H., 1984. Nonlinear behaviour of non-integral infilled frames. Computers & Structures 18, 551–560. https://doi.org/10.1016/0045-7949(84)90070-1

Lourenço, P.B., 1996a. A user/programmer's guide for the Micro-modelling of Masonry Structures (Report nº 03.21.1.31.35). Delft University of Technology, Delft, The Netherlands - Universidade do Minho, Guimarães, Portugal.

Lourenço, P.B., 1996b. Computational Strategy for Masonry Structures (Ph.D. thesis). Delft University.

Lourenço, P.B., Gaetani, A., 2022. Finite Element Analysis for Building Assessment: Advanced Use and Practical Recommendations. Routledge. https://doi.org/10.1201/9780429341564

Lubliner, J., Oliver, J., Oller, S., Oñate, E., 1989. A plastic-damage model for concrete. International Journal of Solids and Structures 25, 299–326. https://doi.org/10.1016/0020-7683(89)90050-4

Macorini, L., Izzuddin, B.A., 2014. Nonlinear Analysis of Unreinforced Masonry Walls under Blast Loading Using Mesoscale Partitioned Modeling. Journal of Structural Engineering 140. https://doi.org/10.1061/(ASCE)ST.1943-541X.0000931

Macorini, L., Izzuddin, B.A., 2013a. Nonlinear analysis of masonry structures using mesoscale partitioned modelling. Advances in Engineering Software 60–61, 58–69. https://doi.org/10.1016/j.advengsoft.2012.11.008

Macorini, L., Izzuddin, B.A., 2013b. Enhanced Mesoscale Partitioned Modelling for Unreinforced Masonry Structures. Proceedings of the fourteenth International Conference on Civil, Structural and Environmental Engineering Computing 102. https://doi.org/10.4203/ccp.102.63

Macorini, L., Izzuddin, B.A., 2011. A non-linear interface element for 3D mesoscale analysis of brick-masonry structures. International Journal for Numerical Methods in Engineering 85, 1584–1608. https://doi.org/10.1002/nme.3046

Magenes, G., Calvi, G.M., 1997. In-plane Seismic Response of Brick Masonry Walls. Earthquake engineering & structural dynamics. 26, 1091.

Magenes, G., Kingsley, G.R., Calvi, G.M., 1995. Seismic testing of a full-scale, two-story masonry building: test procedure and measured experimental response. University of Pavia Dept. of Structural Mechanics, Pavia, Italy.

Mainstone, R.J., 1974. Supplementary note on the stiffness and strengths of infilled frames. Building Research Station, Garston, UK.

Mainstone, R.J., Weeks, G.A., 1970. The influence of bounding frame on the racking stiffness and strength of brick walls. Proceedings 2nd International Brick Masonry Conference 165–171.

Mallick, D., Garg, R., 1971. Effect of openings on the lateral stiffness of infilled frames. Proceedings of the Institution of Civil Engineers 49, 193–209. https://doi.org/10.1680/iicep.1971.6263

Mallick, D., Severn, R.T., 1967. The Behaviour of Infilled Frames under Static Loading. Proceedings of the Institution of Civil Engineering 38, 639–656.

Mann, W., Müller, H., 1980. Failure of shear-stressed masonry - An enlarged theory, tests and application to shear-walls, in: Proceedings of the International Symposium on Load Bearing Brickwork. London, UK, pp. 1–13.

Mansouri, A., Marefat, M.S., Khanmohammadi, M., 2014. Experimental evaluation of seismic performance of low-shear strength masonry infills with openings in reinforced concrete frames with deficient seismic details. The Structural Design of Tall and Special Buildings 23, 1190–1210. https://doi.org/10.1002/tal.1115

Masjuki, S.A., 2017. Assessment and retrofitting of reinforced concrete buildings with shear walls subject to earthquake loading. https://doi.org/10.25560/67713

MathWorks, 2022. MATLAB.

Mehrabi, A.B., 1994. Behavior of masonry infilled reinforced concrete frames subjected to lateral loadings (Ph.D.). University of Colorado at Boulder, United States -- Colorado.

Mehrabi, A.B., Benson Shing, P., Schuller, M.P., Noland, J.L., 1996. Experimental Evaluation of Masonry-Infilled RC Frames. J. Struct. Eng. 122, 228–237. https://doi.org/10.1061/(ASCE)0733-9445(1996)122:3(228)

Mehrabi, A.B., Shing, P.B., 1997. Finite Element Modeling of Masonry-Infilled RC Frames. Journal of Structural Engineering 123, 604–613. https://doi.org/10.1061/(ASCE)0733-9445(1997)123:5(604)

Mehrabi, A.B., Shing, P.B., 1994. Performance of Masonry-Infilled R/C Frames under In-Plane Lateral Loads: Analytical Modelling, in: Proceedings from the NCEER Workshop on Seismic Response of Masonry. San Francisco, California, pp. 45–50.

Michel, C., Zapico, B., Lestuzzi, P., Molina, F.J., Weber, F., 2011. Quantification of fundamental frequency drop for unreinforced masonry buildings from dynamic tests. Earthquake Engineering & Structural Dynamics 40, 1283–1296. https://doi.org/10.1002/eqe.1088

Midas FEA, 2016. Advanced nonlinear and detail analysis program. Analysis and Algorithm.

Minga, E., 2017. 3D meso- and macro-scale models for nonlinear analysis of masonry systems (Ph.D. thesis). Civil and Environmental Engineering Dept., Imperial College London.

Minga, E., Macorini, L., Izzuddin, B.A., 2018. A 3D mesoscale damage-plasticity approach for masonry structures under cyclic loading. Meccanica 53, 1591–1611. https://doi.org/10.1007/s11012-017-0793-z

Minga, E., Macorini, L., Izzuddin, B.A., Caliò, I., 2020. 3D macroelement approach for nonlinear FE analysis of URM components subjected to in-plane and out-of-plane cyclic loading. Engineering Structures 220, 110951. https://doi.org/10.1016/j.engstruct.2020.110951

MIT, 2019. Circolare applicativa NTC 2018.

MIT, 2018. Norme tecniche per le costruzioni 2018.

MIT, 2008. NTC 2008 e Circolare Applicativa - Norme sismiche per le costruzioni.

Mohammadi, M., Nikfar, F., 2013. Strength and stiffness of masonry-infilled frames with central openings based on experimental results. Journal of Structural Engineering (United States) 139, 974–984. https://doi.org/10.1061/(ASCE)ST.1943-541X.0000717

Mohyeddin, A., Goldsworthy, H., Gad, E., 2013. FE modelling of RC frames with masonry infill panels under in-plane and out-of-plane loading. Engineering Structures 51, 73–87. https://doi.org/10.1016/j.engstruct.2013.01.012

Mondal, G., Jain, S.K., 2008. Lateral Stiffness of Masonry Infilled Reinforced Concrete (RC) Frames with Central Opening. Earthquake Spectra 24, 701–723. https://doi.org/10.1193/1.2942376

Moretti, M., 2015. Seismic Design of Masonry and Reinforced Concrete Infilled Frames: A Comprehensive Overview. American Journal of Engineering and Applied Sciences 8, 748–766. https://doi.org/10.3844/ajeassp.2015.748.766

Mosalam, K., Gergely, P., White, R., Zawilinski, D., 1993. The Behaviour of Frames with Concrete Block Infill Walls, in: Proceedings of the First Egyptian Conference on Earthquake Engineering. pp. 283–292.

Mosalam, K., White, R., Gergely, P., 1997. Static Response of Infilled Frames Using Quasi-Static Experimentation. Journal of Structural Engineering-ASCE 123. https://doi.org/10.1061/(ASCE)0733-9445(1997)123:11(1462)

NBC-201, 1994. Nepal National Building Code.

Nwofor, T., 2012. Shear Resistance of Reinforced Concrete infilled Frames. International Journal of Applied Science and Technology 2, 148–163.

NZSEE, 2017. The Seismic Assessment of Existing Buildings (New Zealand Technical Guidelines for Engineering Assessments) - Part C - Unreinforced Masonry Buildings.

NZSEE, 2006. Assessment and Improvement of the Structural Performance of Buildings in Earthquake.

Page, A.W., 1992. Modelling the In-Plane Behaviour of Solid Masonry under Static Loading, in: Proceedings of the International Workshop on Unreinforced Hollow Clay Tile. pp. 2–5.

Pantò, B., Caliò, I., Lourenco, P., 2018a. A 3D discrete macro-element for modelling the out-of-plane behaviour of infilled frame structures. Engineering Structures 175, 371–385. https://doi.org/10.1016/j.engstruct.2018.08.022

Pantò, B., Cannizzaro, F., Caddemi, S., Caliò, I., 2016. 3D macro-element modelling approach for seismic assessment of historical masonry churches. Advances in Engineering Software 97, 40–59. https://doi.org/10.1016/j.advengsoft.2016.02.009

Pantò, B., Cannizzaro, F., Caliò, I., Lourenco, P., 2017. Numerical and Experimental Validation of a 3D Macro-Model for the In-Plane and Out-Of-Plane Behavior of Unreinforced Masonry Walls. International Journal of Architectural Heritage 1–19. https://doi.org/10.1080/15583058.2017.1325539

Pantò, B., Chisari, C., Macorini, L., Izzuddin, B.A., 2022. A hybrid macro-modelling strategy with multi-objective calibration for accurate simulation of multi-ring masonry arches and bridges. Computers & Structures 265, 106769. https://doi.org/10.1016/j.compstruc.2022.106769

Pantò, B., Silva, L., Vasconcelos, G., Lourenco, P., 2018b. Macro-modelling approach for assessment of out-of-plane behavior of brick masonry infill walls. Engineering Structures 181, 529–549. https://doi.org/10.1016/j.engstruct.2018.12.019

Park, Y.J., Reinhorn, A.M., Kunnath, S.K., 1987. IDARC: Inelastic Damage Analysis of Reinforced Concrete Frame - Shear-Wall Structures. Department of Civil Engineering, State University of New York at Buffalo.

Paulay, T., Pristley, M.J.N., 1992. Seismic design of reinforced concrete and masonry buildings. Wiley, New York, USA.

Penava, D., Sigmund, V., Kožar, I., 2016. Validation of a simplified micromodel for analysis of infilled RC frames exposed to cyclic lateral loads. Bulletin of Earthquake Engineering 14, 2779–2804. https://doi.org/10.1007/s10518-016-9929-0

Polyakov, S.V., 1960. On the interaction between masonry filler walls and enclosing frame when loading in the plane of the wall. construction in seismic regions. translation in Earthquake Engineering, Earthquake Engineering Research Institute, Moscow 36–42.

ReLUIS, 2020. Progetto DPC-ReLUIS 2019-2021 – WP10 TASK 10.3 – Uso dei software di calcolo nella verifica sismica degli edifici in muratura v1.0.

ReLUIS, 2013. Schede illustrative dei principali meccanismi di collasso locali negli edifici esistenti in muratura e dei relativi modelli cinematici di analisi. Dipartimento di Protezione Civile.

ReLUIS, Eucentre, 2023. Missione congiunta di ricognizione danni Turchia 8-13 maggio 2023.

Rinaldin, G., Amadio, C., Macorini, L., 2016. A macro-model with nonlinear springs for seismic analysis of URM buildings. Earthquake Engineering & Structural Dynamics 45, 2261–2281. https://doi.org/10.1002/eqe.2759

Rinaldin, G., Fasan, M., Noè, S., Amadio, C., 2019. The influence of earthquake vertical component on the seismic response of masonry structures. Engineering structures. 185, 184–193.

Sachanski, S., 1960. Analysis of Earthquake Resistance of Frame Buildings taking into consideration the carrying capacity of the Filling Masonry, in: Proceedings of the 2nd World Conference on Earthquake Engineering. Tokyo and Kyoto, Japan.

Sánchez, T.A., Flores, L., Bello, F.L., Alcocer, S.M., Meli, R., 1991. Respuesta sismica de muros de mampostería confinada con diferentes grados de acoplamiento a flexión. Centro Nacional de Prevención de Desastres, Mexico.

Schuller, M., Mehrabi, A., Noland, J.L., Shing, P.B., 1994. Performance of masonry - infilled R/C frames under in - plane lateral loads: Experiments, in: Proceedings from the NCEER Workshop on Seismic Response of Masonry Infills. pp. 27–32.

Selby, R., Vecchio, F., 1993. Three-dimensional Constitutive Relations for Reinforced Concrete. Tech. Rep. 93–02. Univ. Toronto, dept. Civil Engineering, Toronto, Canada.

Shing, P.B., Mehrabi, A.B., 2002. Behaviour and analysis of masonry-infilled frames. Structural Engineering Materials 4, 320–331.

Smith, B.S., 1967. Methods for predicting the lateral stiffness and strength of multi-storey infilled frames. Building Science 2, 247–257. https://doi.org/10.1016/0007-3628(67)90027-8

Smith, B.S., 1966. Behavior of Square Infilled Frames. Journal of the Structural Division 92(1).

Smith, B.S., 1962. Lateral stiffness of infilled frames. Journal of the Structural Division 88(6), 183–199.

Smith, B.S., Carter, C., 1969. A method of analysis for infilled frames. Proceedings of the Institution of Civil Engineers 44, 31–48. https://doi.org/10.1680/iicep.1969.7290

Stylianidis, K.C., 1988. Cyclic behaviour of Infilled R/C Frames, in: Proceedings of the Eighth International Brick and Masonry Conference. Dublin, pp. 792–799.

Tasnimi, A.A., Mohebkhah, A., 2011. Investigation on the behavior of brick-infilled steel frames with openings, experimental and analytical approaches. Engineering Structures 33, 968–980. https://doi.org/10.1016/j.engstruct.2010.12.018

Thiruvengadam, V., 1985. On the natural frequencies of infilled frames. Earthquake Engineering & Structural Dynamics 13, 401–419. https://doi.org/10.1002/eqe.4290130310

Thomas, F.G., 1953. The strength of brickwork. The Structural Engineer 31(2), 44–46.

Tiedeman, H., 1980. A statistical evaluation of the importance of non-structural damage to buildings, in: Proceedings of the Seventh World Conference on Earthquake Engineering. International Association of Earthquake Engineering (IAEE), Tokyo, Japan, pp. 617–624.

Tomaževič, M., Lutman, M., 1996. Seismic Behavior of Masonry Walls: Modeling of Hysteretic Rules. Journal of Structural Engineering-ASCE 122. https://doi.org/10.1061/(ASCE)0733-9445(1996)122:9(1048)

Turnsek, V., Cacovic, F., 1971. Some Experimental Results on the Strength of Brick Masonry Walls, in: Proc. of the 2nd Int. Brick Masonry Conference. Stoke-on-Trent, pp. 149–156.

Turnsek, V., Sheppard, P., 1980. The shear and flexural resistance of masonry walls. Proceedings of the International research conference on earthquake engineering, June 30 - July 3, 1980, Skopje, Yugoslavia 517–573.

Valiasis, T.N., Stylianidis, K.C., 1989. Masonry Infilled R/C Frames under Horizonal Loading. Experimental Results. European Earthquake Engineering 3, 10–20.

Van der Pluijm, R., 1999. Out-of-Plane Bending of Masonry: Behaviour and Strength (Ph.D. thesis). Eindhoven University of Technology. https://doi.org/10.6100/IR528212

Van der Pluijm, R., 1993. Shear behaviour of bed joints. 6th North American Masonry Conference, 6-9 June 1993, Philadelphia, Pennsylvania, USA 125–136.

Van der Pluijm, R., 1992. Material properties of masonry and its components under tension and shear. Proceedings 6th Canadian Masonry Symposium, 15-17 June 1992, Saskatoon, Canada 675–686.

Wood, R.H., 1958. The stability of tall buildings. Proceedings of the Institution of Civil Engineers.

Xavier, F.B., 2015. The role of masonry infill in progressive collapse mitigation of multi-storey buildings (Ph.D. thesis). Civil and Environmental Engineering Dept., Imperial College London.

Xavier, F.B., Macorini, L., Izzuddin, B.A., 2014. Robustness of Multistory Buildings with Masonry Infill. Journal of Performance of Constructed Facilities 29, B4014004. https://doi.org/10.1061/(ASCE)CF.1943-5509.0000684

Yettram, A.L., Husain, H.M., 1966. Plane-Framework Methods for Plates in Extension. Journal of the Engineering Mechanics Division 92(1), 157–68.

Zarnic, R., Gostič, S., Crewe, A.J., Taylor, C.A., 2001. Shaking table tests of 1:4 reduced-scale models of masonry infilled reinforced concrete frame buildings. Earthquake Engineering & Structural Dynamics 30, 819–834. https://doi.org/10.1002/eqe.39

Zarnic, R., Tomazevic, M., 1988. An experimentally Obtained Method for Evaluation of the Behaviour of Masonry Infilled R/C Frames, in: Proceedings of the Ninth World Conference on Earthquake Engineering. Tokyo, Japan, pp. 163–168.

Zizi, M., Campitiello, F., De Matteis, G., 2021. A retrofitting technique using steel grids for existing masonry panels: a numerical and analytical study. Bulletin of Earthquake Engineering 19. https://doi.org/10.1007/s10518-020-01030-8

Zizi, M., Chisari, C., Rouhi, J., De Matteis, G., 2022. Comparative analysis on macroscale material models for the prediction of masonry in-plane behavior. Bulletin of Earthquake Engineering 20, 963–996. https://doi.org/10.1007/s10518-021-01275-x